

The Pennsylvania State University  
The Graduate School  
Department of Materials Science and Engineering

**MICROWAVE PLASMA CHEMICAL VAPOR DEPOSITION OF HOMOEPITAXIAL  
DIAMOND FOR M-I-P DIODES:**

**A STUDY OF REACTOR DESIGN, GROWTH KINETICS, AND SURFACE  
MORPHOLOGY**

A Thesis in  
Materials Science and Engineering

by  
Michael S. Bresnehan

© 2010 Michael S. Bresnehan

Submitted in Partial Fulfillment  
of the Requirements  
for the Degree of

Master of Science

December 2010

The thesis of Michael S. Bresnehan was reviewed and approved\* by the following:

Joan M. Redwing  
Professor of Materials Science and Engineering  
Chair of Graduate Program in Materials Science and Engineering  
Thesis Co-Advisor

David W. Snyder  
Adjunct Professor of Chemical Engineering  
Head of Electronic Materials and Devices Department – Electro Optics Center  
Thesis Co-Advisor

Joshua Robinson  
Assistant Professor of Materials Science and Engineering  
Research Associate – Electro Optics Center

James H. Adair  
Professor of Materials Science and Engineering

\*Signatures are on file in the Graduate School

## ABSTRACT

Due to its excellent electronic properties and ability to be used in high temperatures and harsh environments, there is significant interest in the use of diamond to replace silicon for high power, high frequency electronics. This interest is accelerating as large area single crystal substrates become commercially available.

The diamond M-i-P (Metal – intrinsic diamond – P++ diamond) Schottky barrier diode takes advantage of intrinsic diamond's extremely high hole mobility ( $3800\text{cm}^2/\text{Vs}$ ) that permits very high forward current densities (up to  $100\text{A}/\text{cm}^2$  at 5V). However, the performance of this structure depends on the crystalline quality and purity of the intrinsic region. Defect and impurity centers act as traps, capturing charge carriers passing through the intrinsic region. This leads to power loss and degraded device efficiency. Therefore, a growth process is required that produces a thick, high quality, high purity intrinsic diamond layer.

This thesis studies the effect of microwave plasma chemical vapor deposition (MPCVD) reactor design, process conditions, and pre-growth surface treatments on the quality, surface morphology, and growth rate of single crystal intrinsic diamond. A vertical bell-jar MPCVD reactor was purchased for homoepitaxial diamond growth. Several geometry modifications were explored to take full advantage of the growth kinetics of MPCVD diamond. By altering the reactor geometry, the plasma could be manipulated to provide a high plasma density, sufficient contact to the substrate, decreased plasma etching of the quartz chamber walls, and increased dissociation of gas species (as observed with optical emission spectroscopy). As part of the reactor study, the susceptor was adapted to enhance cooling of the substrate, allowing for high microwave input powers at low substrate temperatures. In this regime, growth rates approaching  $20\mu\text{m}/\text{hr}$  were achieved in a high purity hydrogen-methane plasma. These films were verified

with Raman spectroscopy and secondary ion mass spectrometry (SIMS) to be of high crystalline quality and purity.

The effects of pre-growth surface etching and substrate misorientation on the surface morphology were also studied. Dislocations and surface defects can lead to macroscopic growth features (such as growth hillocks) that degrade device performance, encourage non-uniform p-type doping, and induce strain, defects, and impurities. Here, pre-growth reactive ion etching (RIE) is shown to remove surface damage and improve substrate surface roughness ( $R_a$ ) from 0.795nm to 0.478nm. Substrate misorientation is shown to supply a high density of favorable nucleation sites in the form of crystallographic step edges. Both techniques are shown to suppress hillock formation and improve overall film quality.

An initial study of nanocrystalline diamond growth is also reported. Grain size of polycrystalline diamond films was controlled in an attempt to deposit nanocrystalline diamond. This thesis studies the effects of argon concentration on the growth rate, grain size, and crystalline phase (as observed with Raman spectroscopy) of diamond films approaching nanocrystalline material. It was shown that argon concentrations from 90- 95% can yield diamond films with grain sizes below 1  $\mu\text{m}$  and growth rates around 1  $\mu\text{m/hr}$  in the current reactor configuration.

## TABLE OF CONTENTS

LIST OF FIGURES .....	vii
LIST OF TABLES.....	xiv
LIST OF EQUATIONS .....	xv
ACKNOWLEDGEMENTS.....	xvi
Chapter 1: Introduction / Literature Review .....	1
1.1: Diamond as a material for high-power diodes and neutron detection .....	1
1.2: Growth Mechanisms of Single Crystal Diamond .....	6
1.3: Origin of Defects .....	10
1.4: Off-axis Growth.....	13
1.5: Effect of Growth Parameters on Quality and Growth Rate .....	16
1.6: Plasma Etching and Pre-growth Surface Treatment .....	18
1.7: Focus of this Study .....	22
Chapter 2: Equipment and Experimental Procedures .....	23
2.1: Experimental Materials and Substrate Cleaning Process.....	23
2.2: Lambda Technologies MPCVD Reactor .....	25
2.2.1: Reactor Profiling Results – Susceptor Configuration 1 .....	28
2.2.2: Reactor Profiling Results – Susceptor Configuration 2.....	35
2.2.3: Reactor Profiling Results – Susceptor Configuration 3.....	38
2.3: Characterization .....	43
Chapter 3: Reactor Kinetics and Geometry Considerations .....	45
3.1: Growth Rate Study – Susceptor Configuration 1 .....	47
3.2: Growth Rate Study – Susceptor Configuration 2 .....	55
3.3: Growth Rate Study – Susceptor Configuration 3 .....	63
3.4: Optical Emission Spectroscopy Comparison.....	72
3.5: Summary of Results.....	79
3.5.1: Kinetic Explanation of Susceptor Geometry Effects.....	79
3.5.2: Explanation of Growth Rate Behavior .....	85
3.5.3: Surface Morphology Comparison.....	88
3.5.4: Raman Comparison .....	95

Chapter 4: Effect of Substrate Misorientation and Reactive Ion Etching on Surface Morphology .....	99
4.1: Off-axis Growth.....	99
4.2: Reactive Ion Etching.....	106
4.3: Summary of Results.....	121
Chapter 5: Effect of Argon Concentration on Grain Size of Polycrystalline Films.....	127
5.1: Background.....	127
5.2: Growth Rate vs. Argon Concentration.....	128
5.3: Effects of Argon Concentration on Grain Size and Morphology.....	132
5.4: Raman Characterization and Summary of Results.....	137
Chapter 6: Conclusions .....	142
6.1: Growth Kinetics and Optimal Reactor Geometry .....	143
6.2: Secondary Ion Mass Spectrometry Analysis.....	146
6.3: Off-axis vs. On-axis Growth and RIE Surface Treatment .....	149
6.4: Control of Polycrystalline Grain Size .....	151
6.5: Future Work .....	152
REFERENCES .....	154
Appendix A: Lambda Technologies MPCVD Reactor Schematics .....	158
Appendix B: Molybdenum Susceptor Schematics and Configuration Images .....	160
Appendix C: Wyko Optical Profiler Images: Off-axis Etching Study.....	163
Appendix D: Optical Images: Off-axis Etching Study .....	170
Appendix E: Raman Spectroscopy Quantitative Results: Off-axis Etching Study.....	179
Appendix F: Raman Results: Pre-etch, Post-etch, and Post-growth comparison .....	180
Appendix G: Reactor Operation and Growth Procedure .....	183

## LIST OF FIGURES

Figure 1-1: Diamond m-i-p (metal - intrinsic diamond - p++ diamond) Schottky diode structure.....	3
Figure 1-2: Hole mobility vs. boron concentration. The hole mobility decreases significantly as boron concentration is increased due to the high activation energy of boron. ....	4
Figure 1-3: Diamond detector structure with relevant detection reactions for thermal neutrons (left) and fast neutrons (right).....	5
Figure 1-4: Typical monoradical sites (Left) and biradical sites (right) created during CVD on a (100) diamond surface.....	7
Figure 1-5: Density vs. distance from substrate (z) profile for gas species in a hydrogen-methane plasma. Parameters: 200 mbar pressure, 3 kW input power, 850°C substrate temperature, 4% CH <sub>4</sub> concentration. ....	9
Figure 1-6: 200x optical images of a pyramidal hillock (left) and a flat-top hillock (right). Both macroscopic defects propagate in the [100] direction from dislocations and form (111) facets that propagate laterally. Pyramidal hillocks have a twinned crystal about the (111) plane that enhances growth rate in the [100] direction leading to the pyramid shape.....	12
Figure 1-7: Dependence of substrate misorientation on as-grown surface morphology. For the nominally “on-axis” case, growth hillocks are observed. As the misorientation angle is increased, the film becomes macroscopically smooth. ...	15
Figure 1-8: RIE etching of diamond, pressure vs. etch rate. An ideal pressure (peak of curve) is established when the concentration of species is high enough to contribute to etching yet low enough to avoid collisions with each other. ....	20
Figure 2-1: Cross section schematic of the MPCVD reactor. The microwave cavity is a 17.8cm diameter brass cylinder. The process is contained within a 12.5cm diameter quartz bell jar. The microwave probe, substrate stage, and sliding short are fully tunable to achieve the desired plasma power distribution and are indicated with red font.....	25
Figure 2-2: Left: Microwave and process cavity; Right: Full MPCVD system.....	27
Figure 2-3: Cross section of Susceptor Configuration 1 which consists of the stock 3” wafer holder on top of a molybdenum support plate and cooling stage.....	29

Figure 2-4: Temperature vs. Microwave power – Configuration 1. Substrate: 3” (111) Silicon. Gap between susceptor and cooling stage: 0mm. ....	30
Figure 2-5: Temperature vs. Microwave power – Configuration 1. Substrate: 3” (111) Silicon. Gap between susceptor and cooling stage: 2mm. ....	30
Figure 2-6: Temperature vs. Microwave power – Configuration 1. Substrate: 3” (111) Silicon. Gap between susceptor and cooling stage: 5mm. ....	31
Figure 2-7: Temperature vs. Microwave power – Configuration 1. Substrate: 3” (111) Silicon. Microwave power: 2000W.....	31
Figure 2-8: Temperature vs. Microwave power – Configuration 1. Substrate: 3” (111) Silicon. Microwave power: 2600W.....	32
Figure 2-9: Temperature vs. Flow Rate – Configuration 1. Substrate: 3” (111) Silicon. ....	33
Figure 2-10: Temperature vs. Microwave power – Configuration 1. Substrate: (100) single crystal. ....	34
Figure 2-11: Cross section of Susceptor Configuration 2. The addition of a ½” diameter raised and tapered molybdenum seed holder was added to raise the substrates into contact with the plasma.....	35
Figure 2-12: Temperature vs. Microwave power – Configuration 2. Seed holder height: 5mm. ....	36
Figure 2-13: Temperature vs. Microwave power – Configuration 2. Seed holder height: 10mm. ....	37
Figure 2-14: Cross section of Susceptor Configuration 3. The susceptor support plate was replaced by a new plate with a ½” diameter cut-out for insertion of the ½” raised and tapered molybdenum seed holder.....	39
Figure 2-15: Temperature vs. Microwave power – Configuration 3. Seed holder height: 5mm. ....	40
Figure 2-16: Temperature vs. Microwave power – Configuration 2. Seed holder height: 7mm. ....	40
Figure 2-17: Temperature vs. Microwave power – Configuration 2. Seed holder height: 10mm. ....	41
Figure 2-18: Temperature vs. Microwave power – Comparison of Susceptor Configurations. ....	42
Figure 3-1: 50x Optical Micrograph of an as-received (100) on-axis CVD seed. The substrate is mirror polished and feature-less. ....	46

Figure 3-2: Growth Rate vs. Pressure – Configuration 1. Constants: Methane concentration: 2%, Temperature: 1050°C. ....	48
Figure 3-3: Optical Micrographs – Growth Rate vs. Pressure – Configuration 1. Constants: Methane concentration: 2%, Temperature: 1050°C. ....	50
Figure 3-4: Growth Rate vs. CH <sub>4</sub> Concentration – Configuration 1. Constants: Pressure: 120 Torr, Temperature: 1050°C. ....	52
Figure 3-5: Optical Micrographs – Growth Rate vs. CH <sub>4</sub> Concentration – Configuration 1. Constants: Pressure: 120 Torr, Temperature: 1050°C. ....	53
Figure 3-6: Growth Rate vs. Pressure – Configuration 2. Constants: Methane concentration: 4%, Temperature: 1100°C. ....	56
Figure 3-7: Optical Micrographs – Growth Rate vs. Pressure – Configuration 2. Constants: Methane concentration: 4%, Temperature: 1100°C. ....	58
Figure 3-8: Growth Rate vs. CH <sub>4</sub> Concentration – Configuration 2. Constants: Pressure: 100 Torr, Temperature: 1100°C. ....	60
Figure 3-9: Optical Micrographs – Growth Rate vs. CH <sub>4</sub> Concentration – Configuration 2. Constants: Pressure: 100 Torr, Temperature: 1100°C. ....	61
Figure 3-10: Growth Rate vs. Pressure – Configuration 3. Constants: Methane concentration: 4%, Temperature: 1100°C. ....	64
Figure 3-11: Optical Micrographs – Growth Rate vs. Pressure – Configuration 3. Constants: Methane concentration: 4%, Temperature: 1100°C. ....	66
Figure 3-12: Growth Rate vs. CH <sub>4</sub> Concentration – Configuration 3. Constants: Pressure: 120 Torr, Temperature: 1100°C. ....	68
Figure 3-13: Optical Micrographs – Growth Rate vs. CH <sub>4</sub> Concentration – Configuration 3. Constants: Pressure: 120 Torr, Temperature: 1100°C. ....	70
Figure 3-14: OES Spectra for Various Pressures – Configuration 1. Constants: Methane concentration: 2%, Temperature: 1050°C. ....	73
Figure 3-15: OES Spectra for Various Pressures – Configuration 2. Constants: Methane concentration: 4%, Temperature: 1100°C. ....	74
Figure 3-16: OES Spectra for Various Pressures – Configuration 3. Constants: Methane concentration: 4%, Temperature: 1100°C. ....	74
Figure 3-17: OES Spectra for Various CH <sub>4</sub> Concentrations – Configuration 1. Constants: Pressure: 120 Torr, Temperature: 1050°C. ....	75

Figure 3-18: OES Spectra for Various CH <sub>4</sub> Concentrations – Configuration 2. Constants: Pressure: 100 Torr, Temperature: 1100°C.....	76
Figure 3-19: OES Spectra for Various CH <sub>4</sub> Concentrations – Configuration 3. Constants: Pressure: 120 Torr, Temperature: 1100°C.....	76
Figure 3-20: C2/H $\alpha$ Peak Ratios vs. Pressure for all three susceptor configurations. ....	77
Figure 3-21: C2/H $\alpha$ Peak Ratios vs. CH <sub>4</sub> Concentration for all three susceptor configurations. ....	78
Figure 3-22: Growth Rate vs. Pressure – Susceptor configuration comparison. Growth rates were averaged from the two measurement techniques. Error bars indicate the standard deviation of the data.....	85
Figure 3-23: Growth Rate vs. CH <sub>4</sub> Concentration – Susceptor configuration comparison. Growth rates were averaged from the two measurement techniques. Error bars indicate the standard deviation of the data. ....	87
Figure 3-24: Optical micrographs – Susceptor configuration comparison. Constants: Pressure: 120 Torr, Methane concentration: 8%, Temperature: 1100°C.....	89
Figure 3-25: OES Spectra – Susceptor configuration comparison. Constants: Pressure: 120 Torr, Methane concentration: 8%, Temperature: 1100°C. ....	90
Figure 3-26: 50x optical images of diamond samples grown under the low plasma density regime (susceptor configuration 2) at 4% CH <sub>4</sub> (left image) and 8% CH <sub>4</sub> (right image). In this regime, lower methane concentrations are preferred as hillock growth is more probable at high methane concentrations .....	92
Figure 3-27: 50x optical images of diamond samples grown under the high plasma density regime (susceptor configuration 3) at 4% CH <sub>4</sub> (left image) and 8% CH <sub>4</sub> (right image). In this regime, high methane concentrations are preferred as step-flow growth is promoted and hillock growth is suppressed .....	93
Figure 3-28: Raman Spectra – Susceptor Configuration 1. Here the 488nm laser was focused on the center of one of the growth hillocks .....	96
Figure 3-29: Raman Spectra – Susceptor Configuration 2. Here the 488nm laser was focused on the center of one of the growth hillocks .....	96
Figure 3-30: Raman Spectra – Susceptor Configuration 3. Here the 488nm laser was focused between macroscopic steps on one of the terrace flats.....	97
Figure 4-1: 50x Optical Micrograph of (100) Off-axis CVD diamond substrate .....	100

Figure 4-2: Growth Rate vs. Methane Concentration – Off-axis and On-axis samples. Misoriented substrates having a higher density of crystallographic steps results in a higher growth rate. Growth rates were averaged from the two measurement techniques. Error bars indicate the standard deviation of the data. ....	102
Figure 4-3: 200x Post-growth Optical Images – Left: On-axis sample, Right: Off-axis sample. Step-flow growth was achieved by mis-orienting the substrate 3-4°. ....	103
Figure 4-4: 500x Post-growth Optical Images – Effect of CH <sub>4</sub> % on Morphology. From Left to Right: 1%, 2%, 3%, 4%, 8% CH <sub>4</sub> . Higher methane concentrations promote a step-flow growth morphology. ....	104
Figure 4-5: Wyko Images – Left: 1% CH <sub>4</sub> , Right: 2% CH <sub>4</sub> . Confirmation of etch pits rather than hillock nucleation. ....	105
Figure 4-6: Surface Roughness (Ra) vs. Etch Pressure – Off-axis substrates. Ra values were averaged from three wyko scans and one AFM scan over a 5µm by 5µm area. Error bars indicate the standard deviation of the data. ....	109
Figure 4-7: RIE Etch Rate vs. Etch Pressure – Off-axis substrates. Etch rate was determined by AFM of etch steps ....	109
Figure 4-8: Post-etch Wyko surface images and Ra values for etching study – Off-axis substrates ....	110
Figure 4-9: Wyko Image of Step Edge etched at 25mtorr for 1 hour – Off-axis substrate. ....	111
Figure 4-10: Off-axis 50x and 500x Images – Constants: Methane concentration: 4% CH <sub>4</sub> , Pressure: 120 Torr, Input power: 2300W – Left: No Etch, Right: 25mtorr Etch. ....	112
Figure 4-11: Off-axis 50x and 500x Images – Constants: Methane concentration: 8% CH <sub>4</sub> , Pressure: 120 Torr, Input power: 2300W – Left: No Etch, Right: 25mtorr Etch. ....	113
Figure 4-12: On-axis 50x and 200x Images – Constants: Methane concentration: 4% CH <sub>4</sub> , Pressure: 120 Torr, Input power: 2300W – Left: No Etch, Right: 25mtorr Etch. ....	114
Figure 4-13: On-axis 50x and 200x Images – Constants: Methane concentration: 8% CH <sub>4</sub> , Pressure: 120 Torr, Input power: 2300W – Left: No Etch, Right: 25mtorr Etch. ....	115
Figure 4-14: Wyko surface profilometer images of step edges – (a): Off-axis substrate: Masked side R <sub>a</sub> : 0.84nm, Etched side R <sub>a</sub> : 0.49nm, Etch Rate: 1.74µm/hr. (b): On-axis substrate: Masked side R <sub>a</sub> : 0.71nm, Etched side R <sub>a</sub> : 0.98nm, Etch rate: 1.21µm/hr. Etch pits are formed on the etched side of the on-axis sample. ....	117

- Figure 4-15: Optical Images of etch steps – (a) 50x images: Left: Off-axis, Right: On-axis. (b) 100x images: Left: Off-axis, Right: On-axis. No degradation in surface morphology occurs with etching of the off-axis surface. However, hillocks of a larger size are observed on the etched side of the on-axis film, indicating RIE etching negatively affects the post-growth surface morphology of on-axis diamond growth ..... 119
- Figure 4-16: Crystallographic Terrace Steps – Left: On-axis, Right: Off-axis. Terrace length of nominally on-axis substrates is between 20-50nm while misorientation of 3-4° results in a decrease of the terrace length to 5.1-6.8nm ..... 123
- Figure 4-17: Raman peaks of an off-axis sample. From right to left: Pre-etch, post-etch (25 mtorr etch for 1 hour), and post-growth (120 Torr, 8% CH<sub>4</sub>, and 2300W input power)..... 125
- Figure 5-1: Nanocrystalline Diamond Growth Rate vs. Argon Concentration. The increase in growth rate up to 70% Ar is due to the enhanced dissociation of methane by argon ions. Above 70% Ar however the growth rate drops off significantly due to detachment of the plasma from the substrate. Growth rate was averaged from the two measurement techniques. Error bars indicate the standard deviation of the data..... 130
- Figure 5-2: OES Spectra at Different Argon Concentrations. As the Ar concentration is increased the C2 peak increases while the H $\alpha$  peak decreases, leading to reduced contributions from atomic hydrogen etching and promoting secondary nucleation. .... 131
- Figure 5-3: OES C2/H $\alpha$  Peak Ratios vs. Argon Concentration. .... 131
- Figure 5-4: Optical Images of morphology development. Left: 500x, Right: 1000x. Grain increases in size with increasing argon concentration up to 70% Ar due to columnar grain growth. Above 85% Ar, grain size decreases significantly due to secondary nucleation. At 98% and 99% however, NCD did not nucleate onto the surface. .... 133
- Figure 5-5: Carbon Deposition on Susceptor. Left: 98% Ar, Right: 99% Ar..... 136
- Figure 5-6: Raman Spectra for Varying Argon Concentrations. The intensity of the G-band increases significantly as the argon concentration increases above 70%. This is attributed to the increasing concentration of grain boundary containing sp<sup>2</sup> carbon phases as grain size is reduced..... 138
- Figure 5-7: Raman Spectra for 98% and 99% Argon. The sharp diamond peak and weak G-band may be due to the signal from the polycrystalline diamond substrate..... 138

- Figure 5-8: Effect of plasma-substrate contact on the deposition of nanocrystalline diamond. Point “A” indicates a region where the plasma was in contact with the substrate. Here the Raman spectra suggests nanocrystalline diamond deposition with a weak D-peak, large G-band, and a peak at  $1140\text{cm}^{-1}$ . In regions where the plasma was not in contact with the substrate, the  $1140\text{cm}^{-1}$  peak disappears and the D-peak becomes more intense, indicating microcrystalline diamond deposition ..... 140
- Figure 6-1: Susceptor configuration comparison. The increased substrate cooling combined with the confinement of the plasma volume over the substrate resulted in susceptor configuration 3 being the ideal configuration for high plasma density and high growth rates ..... 145
- Figure 6-2: 50x optical images of samples sent out for SIMS analysis. Right: CVD-05 used an on-axis substrate, susceptor configuration 1, 120 Torr, 2500W ( $1050^\circ\text{C}$ ), and 4%  $\text{CH}_4$ . Left: OA-13 was etched at 25mTorr for 1 hour, used an off-axis substrate, susceptor configuration 3, 120 Torr, 2300W ( $1100^\circ\text{C}$ ), and 8%  $\text{CH}_4$ . The step flow morphology of OA-13 (Left image) is expected to incorporate fewer impurities than the hillocks observed in CVD-05 (Right image)..... 147
- Figure 6-3: SIMS profiles of nitrogen and silicon impurities in CVD-05 (top plot) and OA-13 (bottom plot). CVD-05 used an on-axis substrate, susceptor configuration 1, 120 Torr, 2500W ( $1050^\circ\text{C}$ ), and 4%  $\text{CH}_4$ . OA-13 was etched at 25mTorr for 1 hour, used an off-axis substrate, susceptor configuration 3, 120 Torr, 2300W ( $1100^\circ\text{C}$ ), and 8%  $\text{CH}_4$ . The off-axis and etched sample (OA-13) shows slightly lower impurity levels ..... 148

## LIST OF TABLES

Table 1-1: Electronic properties of diamond compared to 4H-SiC and Silicon. ....	2
Table 2-1: Substrate Cleaning Process. ....	24
Table 3-1: Growth Rate vs. Pressure - Conditions and Results – Configuration 1.....	47
Table 3-2: Growth Rate vs. CH <sub>4</sub> - Conditions and Results – Configuration 1. ....	51
Table 3-3: Growth Rate vs. Pressure - Conditions and Results – Configuration 2.....	56
Table 3-4: Growth Rate vs. CH <sub>4</sub> - Conditions and Results – Configuration 2. ....	59
Table 3-5: Growth Rate vs. Pressure - Conditions and Results – Configuration 3.....	64
Table 3-6: Growth Rate vs. CH <sub>4</sub> - Conditions and Results – Configuration 3. ....	68
Table 3-7: Approximation of free electron density from Equation 3-2 as a function of microwave input power. Growth rates and C2/H $\alpha$ ratios are shown to correlate the free electron density to the plasma dissociation and growth rate. Contact area was estimated and u <sub>a</sub> was assumed constant based on text. ....	81
Table 4-1: Growth rate results for etched and non-etched off-axis samples as well as on- axis samples for comparison. Growth rates were averaged from the two measurement techniques. ....	101
Table 4-2: RIE Process Parameters.....	107
Table 4-3: Surface roughness results – Pre-etch, post-etch, and post-growth for off-axis and on axis samples, both etched and non-etched. Ra values were averaged from three wyko scans and one AFM scan over a 5 $\mu$ m by 5 $\mu$ m area .....	108
Table 5-1: Growth Results for Various Argon Concentrations. ....	129

## LIST OF EQUATIONS

Equation 1-1: (100) diamond growth rate with relevant surface reactions.....	8
Equation 3-1: Energy of a photon as it relates to frequency and wavelength.....	72
Equation 3-2: Plasma Input Power. ....	79
Equation 3-3: Dissociation Rate of Molecules. ....	80
Equation 3-4: Lorentz Force. ....	83
Equation 4-1: Surface Diffusion Length.....	121
Equation 4-2: Off-axis Angle.....	123

## ACKNOWLEDGEMENTS

I would first like to acknowledge my family; my three brothers: Eric, Adam, and Brian, my mother April, my father Steve, and also my grandparents, aunts, uncles, and cousins for their constant support and love.

I would sincerely like to thank my research advisor Dr. David Snyder for giving me an opportunity to further my education. I would especially like to thank him for the advice, guidance, support, and patience he has shown me.

I would like to sincerely thank my academic advisor Dr. Joan Redwing for her support and insight as well as the other faculty members who went out of their way to help me. I would also like to thank everyone at the EOC including: Joshua Robinson, David Snyder, Michael Labella, Kathleen Trumbull, Randy Cavalero, Mark Fanton, Jeremy Accord, Matthew Hollander, Zachary Hughes, Maxwell Wetherington, Brendan Farrell, and Casey Howsare for their assistance in terms of characterization work, insight, and support. I would especially like to thank Michael Labella for etching all those diamond samples and Kathy Trumbull for doing AFM for me.

I'd like to thank Joe Wander and Lambda Technologies for the training and support on operating the MPCVD tool. I would also like to thank Andrzej Badzian for his insight and knowledge of MPCVD diamond growth.

I'd like to thank all my fellow classmates and friends for all the laughs, good times, and memories, as well as their unwavering support. Finally I'd like to thank God for the many blessings he's given to me.

## Chapter 1

### Introduction / Literature Review

Due to its extraordinary properties, diamond is a material of great interest for a broad range of technical applications. However, several key technological limitations have held back commercialization of many diamond-based devices. One such limitation is the quality and purity of the active intrinsic region of diamond-based Schottky diode structures. This thesis aims to investigate growth process techniques, reactor design, and pre-growth sample preparation techniques as they correlate to the crystalline quality, surface morphology, purity, and growth rate of single crystal intrinsic diamond films.

#### 1.1: Diamond as a material for high-power diodes and neutron detection

As the demand for increased efficiency in high frequency, high power devices pushes traditional electronic materials (such as silicon) to their theoretical limits, a research focus on wide band gap materials becomes more and more important. Silicon p-i-n diodes (commonly used for high frequency applications) exhibit significant switching loss due to their bi-polar conduction [1]. Schottky barrier diodes exhibit uni-polar conduction, eliminating this drawback. Schottky barrier diodes utilizing wide band gap semiconductors such as SiC, GaN, ZnO have already shown improvements over silicon for applications such as short-wavelength lasers, LEDs, radiation detectors, UV photodetectors, and biosensors [1]. Diamond, having superior electronic properties to other wide band gap materials, theoretically would be an ideal material for increased efficiency and capability of high power, high frequency electronic devices. Several key electronic properties are compared to SiC and silicon in Table 1-1.

Table 1-1: Electronic properties of diamond compared to 4H-SiC and Silicon. [2]

<b>Property</b>	<b>Effects</b>	<b>Application</b>	<b>Diamond</b>	<b>4H-SiC</b>	<b>Si</b>
<b>Band Gap (eV)</b>	<i>Power Handling</i>	Diodes	5.47	3.36	1.12
<b>Thermal Conductivity (W/cm<sup>2</sup>·°C)</b>	<i>Heat Dissipation</i>	Diodes	21.9	3.6	1.5
<b>Breakdown Field (V/cm)</b>	<i>Current Leakage, higher applied voltages</i>	Diodes / Detectors	$2 \times 10^7$	$2.7 \times 10^6$	$3 \times 10^5$
<b>Resistivity (Ω-cm)</b>	<i>Noise, Switching Voltages</i>	Diodes / Detectors	$10^{14}$	$10^{11}$	$2.3 \times 10^5$
<b>Electron Mobility (cm<sup>2</sup>/V-s)</b>	<i>Conductivity, response time</i>	Diodes / Detectors	660	981	1450
<b>Hole Mobility (cm<sup>2</sup>/V-s)</b>	<i>Conductivity, response time (active layer)</i>	Diodes / Detectors	1650	120	370
<b>Displacement Energy (eV/atom)</b>	<i>Radiation Hardness</i>	Detectors	43	25	13-20

However, p-type diamond presents a very low concentration of free charge carriers at room temperature due to the high activation energies required for p-type dopants (boron – 0.37eV) and n-type dopants (phosphorus – 0.6eV) [1]. This would lead to a high resistance in a traditional Schottky diode structure. To overcome this limitation, an intrinsic drift layer is used in conjunction with a highly boron-doped p++ layer to create an M-i-P (metal – intrinsic diamond – p++ diamond) Schottky diode structure [1], shown in Figure 1-1. Intrinsic diamond exhibits an extremely high hole mobility (up to 3800 cm<sup>2</sup>/Vs) allowing for super-linear space charge limited current flow and large forward current densities at low voltage and limited Schottky contact areas.

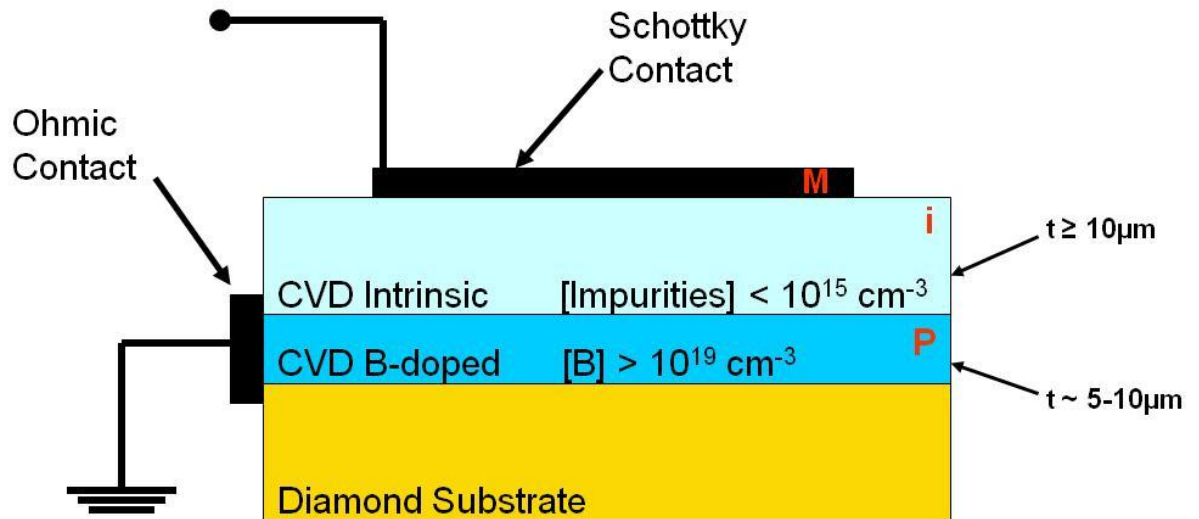


Figure 1-1: Diamond m-i-p (metal - intrinsic diamond - p++ diamond) Schottky diode structure.

Since operation of this device is based on space-charge limited current flow, the performance and efficiency of this structure is highly dependent on the purity and crystalline quality of the intrinsic drift layer. Impurities and defects act as traps, impeding the flow of electrons through the drift region. In addition, the hole mobility is severely reduced (especially at room temperature) with increasing concentration of boron impurities due to boron's high activation energy. This dependence is shown in Figure 1-2. Therefore, great care must be taken when depositing the intrinsic layer onto the boron-doped layer so that boron is not introduced into the intrinsic region. In order for diamond based m-i-p Schottky structures to be a viable replacement for silicon p-i-n diodes and a strong competitor to other wide band gap based structures (such as SiC and GaN based diodes), the purity and crystalline quality of the diamond intrinsic layer must be improved.

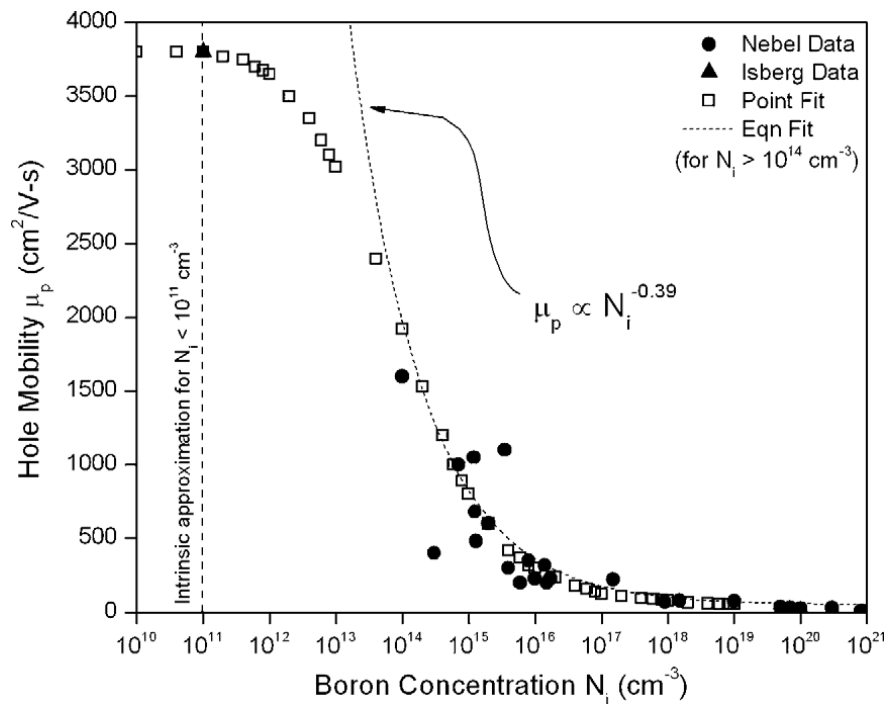


Figure 1-2: Hole mobility vs. boron concentration. The hole mobility decreases significantly as boron concentration is increased due to the high activation energy of boron. [3]

Besides high-power, high-frequency Schottky diodes, the diamond-based Schottky structure can be employed as a high-energy particle detector. Detection of neutrons and gamma radiation is an increasingly important issue as the demand for nuclear technology increases. Due to the high fluencies of these high energy particles and the high working temperature of the detectors, traditional silicon and scintillation detectors breakdown rapidly and are not ideal for practical use [6-17].

Diamond has the highest radiation hardness of any material, making it last many times longer than traditional detectors. Diamond directly detects fast neutrons (high energy neutrons with  $E=KT > 500\text{keV}$ ) via a  $^{12}\text{C}(n,\alpha_0)^9\text{Be}$  reaction [4, 5]. Fast neutrons are usually associated with radiation from nuclear weapons. For nuclear reactor monitoring, thermal neutrons are the primary detected particles. Thermal neutrons, which have lower energies ( $\sim 25\text{meV}$ ), are much slower and

do not penetrate the extremely hard diamond efficiently and must be detected with a “converter” layer, such as  ${}^6\text{LiF}$  [4, 5, 12].

A typical diamond-based detector structure is almost identical to the Schottky barrier diode structure, with the exceptions of a thicker intrinsic region ( $\sim 200\mu\text{m}$  compared to  $10\text{-}20\mu\text{m}$ ) and the addition of a converter layer. The device structure starts with a commercially available High Pressure High Temperature (HPHT) or a CVD grown substrate. A thin boron-doped diamond layer is then homoepitaxially grown on the substrate to act as a conductive layer. The thick high purity intrinsic layer is then deposited on top of the B-doped layer. This layer is the active layer for fast neutron detection and the purity and quality of this layer is essential (as discussed before) [4, 5, 6, 7]. An aluminum contact is then deposited over the intrinsic region and the LiF converter layer (for thermal neutrons) is then deposited over the contact [4, 5]. The detector structure is shown with relevant detection reactions for both fast and thermal neutrons in Figure 1-3.

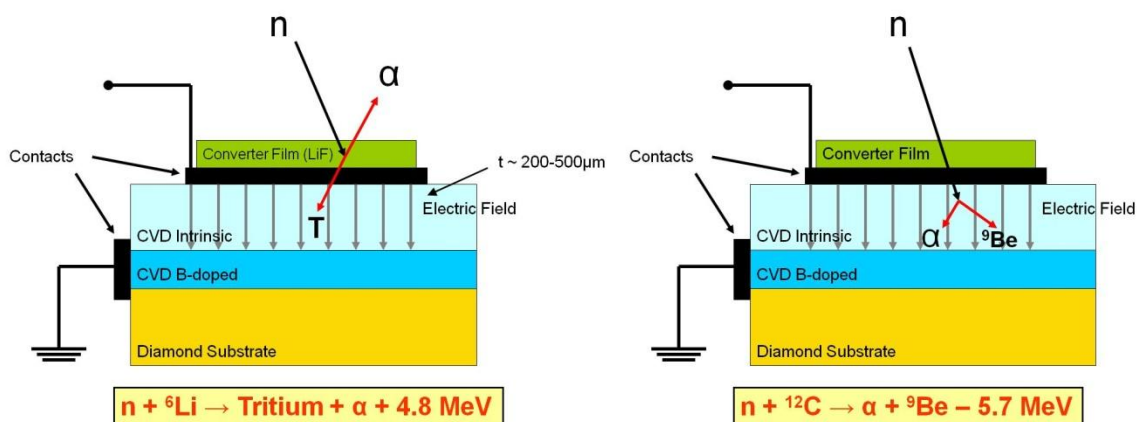


Figure 1-3: Diamond detector structure with relevant detection reactions for thermal neutrons (left) and fast neutrons (right).

For thermal neutrons, the incoming particle does not have enough energy to react with the  $sp^3$  bonded carbon atoms of diamond, so they react with  ${}^6\text{Li}$  in the LiF converter layer. This reaction creates tritium (2.73 MeV) and an  $\alpha$ -particle (2.06 MeV) [4, 5]. Tritium and the  $\alpha$ -particle are emitted at  $180^\circ$ , so only the tritium or  $\alpha$ -particle is detected. Fast neutrons have enough energy to directly interact with the  ${}^{12}\text{C}$  in the diamond sensing layer. This reaction creates beryllium (6.34 MeV) and an  $\alpha$ -particle (2.06 MeV) [4, 5].

The commercial HPHT and CVD single crystal diamond substrate usually cannot be used for detection purposes due to their nitrogen content. The substitutional nitrogen has a fast recombination and degrades the response of the detectors [10]. Defects and grain boundaries (in polycrystalline devices) in the intrinsic region of the device cause the response time of alpha particles (formed from the  ${}^{12}\text{C}(n,\alpha_0){}^9\text{Be}$  reaction) to degrade significantly [5, 6, 10]. Deep level traps are also believed to be associated with device degradation, holding charge carriers and delaying response times [15, 17].

## **1.2: Growth Mechanisms of Single Crystal Diamond**

MPCVD diamond growth proceeds via the microwave-assisted ionization of hydrogen and methane into a plasma containing atomic hydrogen and carbon radicals. The accepted mechanisms for single crystal (100) diamond growth via MPCVD involve the abstraction reactions of adsorbed surface hydrogen atoms by gas phase atomic hydrogen [18-21]. In other words, since the gas phase is  $>90\%$  hydrogen, the diamond surface is almost completely saturated with adsorbed atomic hydrogen. When another atomic hydrogen ion arrives at the site of an adsorbed hydrogen, it reacts to form  $\text{H}_2$ , thus desorbing and leaving a new reactive surface site [18-21]. Two main types of surface radical sites are created on the diamond surface: monoradical

sites (a single dangling bond on a surface carbon) and biradical sites (two surface radical sites on adjacent carbons) [19]. These radical sites (as well as common variants) are illustrated in Figure 1-4. These sites can either be re-occupied by another H atom, (which is most probable), or react with a carbon radical,  $\text{CH}_3$  being the most common diamond growth species [18-21].

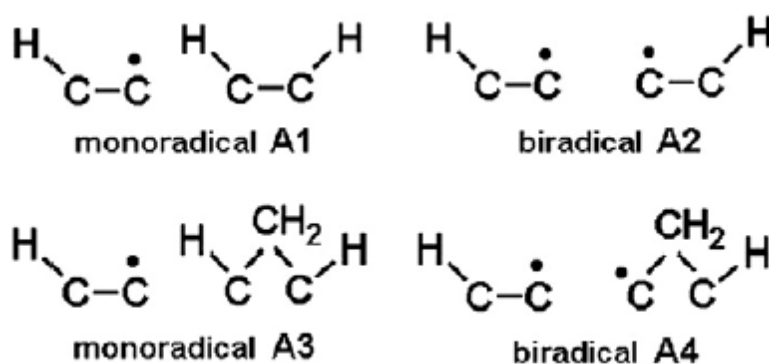


Figure 1-4: Typical monoradical sites (Left) and biradical sites (right) created during CVD on a (100) diamond surface. [19]

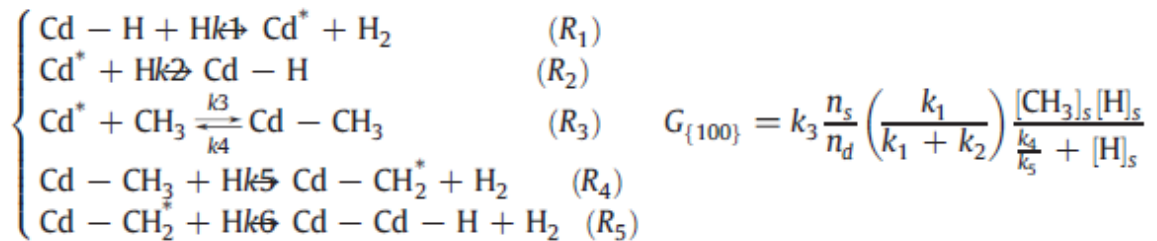
The attachment of a reactive hydrocarbon species to an active site can then result in two possibilities. First, the adsorbate may be removed from the surface by thermal desorption or by etching from atomic hydrogen [20]. This case is likely if the carbon species is adsorbed far from a step edge. Since surface migration is not favorable due to the strength of C-C bonds and the termination of the surface with hydrogen, the adsorbed radical will most likely return to the gas phase. Alternatively, the hydrocarbon species may be incorporated into the diamond lattice by the abstraction reactions of the remaining hydrogen atoms on the adsorbed species by atomic hydrogen [18-20].

Though many hydrocarbon radicals are believed to contribute, the dominant precursor to CVD diamond growth is  $\text{CH}_3$  [18-21]. This hydrocarbon radical can adhere to both monoradical

and biradical reactive surface sites. In the case of biradical adsorption, CH<sub>3</sub> does not have to wait for an abstraction reaction to occur for it to link into the lattice since an adjacent dangling bond is already present [19]. Since CH<sub>3</sub> seems to dominate growth, most growth modeling studies only focus on this species for simplification [18-21].

Modeling of CVD diamond growth has produced growth rate expressions to illustrate the growth process quantitatively. Growth rate is dependent on the concentrations of CH<sub>3</sub> and atomic hydrogen at the surface of the substrate as well as the concentration of reactive sites [18, 19].

Equation 1-1 shows equations describing the growth rate on (100) diamond surfaces and the relevant surface chemistry reactions (R<sub>1</sub> through R<sub>5</sub>), where Cd is an occupied surface site, Cd\* is an active surface site, [CH<sub>3</sub>]<sub>s</sub> and [H]<sub>s</sub> is the concentrations of CH<sub>3</sub> and atomic hydrogen at the substrate surface, respectively, n<sub>s</sub> is the surface site density, n<sub>d</sub> is the molar density of diamond, and k<sub>1</sub>, k<sub>2</sub>, k<sub>3</sub>, k<sub>4</sub>, and k<sub>5</sub> are the rate constants for reactions 1, 2, 3, 4, and 5, respectively.



Equation 1-1: (100) diamond growth rate with relevant surface reactions. [18]

Obviously, in order for this model to be viable, the surface densities of CH<sub>3</sub> and atomic hydrogen must be determined. Figure 1-5 shows a model expressing the concentration of typical gas phase species in a hydrogen-methane plasma as a function of distance from the substrate;

0mm being in contact with the substrate [18]. Notice that the concentration of  $\text{CH}_3$  radicals increases abruptly at the substrate surface.

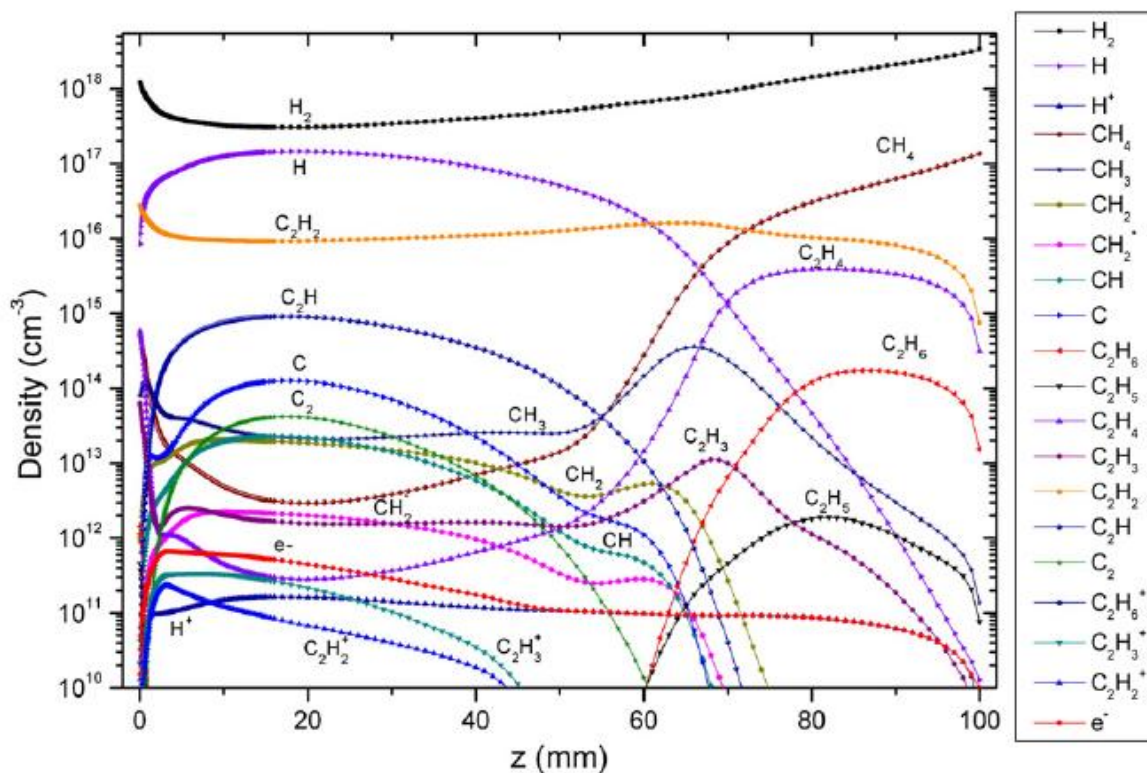


Figure 1-5: Density vs. distance from substrate ( $z$ ) profile for gas species in a hydrogen-methane plasma. Parameters: 200 mbar pressure, 3 kW input power, 850°C substrate temperature, 4%  $\text{CH}_4$  concentration. [18]

Obviously, the exact mechanisms of CVD diamond growth are very complex and cannot be summarized easily. Surface chemistry and methyl radical incorporation also are influenced greatly by temperature. Incorporation mechanisms can be altered (such as influence of monoradical sites vs. biradical sites) by slight changes of factors such as high or low atomic hydrogen content, pressure, and temperature fluxes with increasing diamond thickness [18]. Explanations of such mechanisms, as well as incorporation mechanisms of hydrocarbon radicals other than  $\text{CH}_3$  ( $\text{CH}_2$ ,  $\text{C}_2\text{H}_2$ , ect.) are detailed in the literature [18-21].

### 1.3: Origin of defects

One of the main limitations to the development and further improvement of diamond-based devices and applications is the fact that CVD diamond films rarely exhibit smooth, defect-free surfaces. High defect densities and macroscopic defect features can render a CVD diamond film useless for applications, as they lead to local areas of degraded material as well as local areas of non-uniform doping for the p-type layer [22]. In order to increase the range of technological applications and improve the performance and reproducibility of single crystal diamond films, the crystalline quality as well as the purity of the CVD films must be enhanced and the defect density must be decreased. However, before one can begin to improve the surface morphologies and crystalline quality of CVD single crystal diamond, it is important to gain a better understanding of how these surface defects are formed.

There are essentially three different types of defects that are commonly observed on homoepitaxial CVD diamond films: unepitaxial crystals, hillocks with flat tops, and pyramidal hillocks [23]. Unepitaxial crystals seem to be isolated, randomly orientated diamond crystallites that can be on the surface or embedded in the CVD layer. Pyramidal hillocks are 4-fold symmetry defects with laterally propagating (111) facets that are almost always topped with a non-epitaxial diamond crystal [23]. Flat-topped hillocks consist of a square (100) facet on top of four (111) lateral facets. These defects usually lead to the incorporation of impurities, crystalline imperfections, strain, and graphitic and non-diamond phases within the film [22, 23]. Surface roughness is also increased significantly when these defects are present, which adds additional polishing and etching steps to device fabrication and is undesirable for device-grade material. A higher concentration of boron dopants is usually incorporated into hillocks when depositing a p-type layer [24]. This leads to non-uniform conduction and short-circuiting, unsuitable for device grade material.

Unepitaxial crystals, having no apparent relation to the diamond layer, are believed to be formed randomly. Their nucleation may be catalyzed by a contaminant impurity at the surface and mainly depend on the growth and plasma conditions [23]. Hillock formation seems to occur in the initial stages of growth and metal impurities appear to play a role in their formation [23]. The density and sizes of hillocks increases as the thickness of the film increases. Thin films show very small hillocks with smooth areas in between while thicker films show coalescing hillocks where the strongest step sources dominate [25]. Therefore, it can be concluded that hillock formation is started at the initiation of diamond growth [25].

Both pyramidal and flat-topped hillock formation is believed to be caused by stacking faults or dislocations that: (i) nucleate at the interface between the surface and the epitaxial layer from lattice disruptions; or (ii) propagate from the substrate into the CVD layer [22]. Dislocations nucleating at the substrate-layer interface can be caused by impurity contamination or by surface and subsurface substrate damage [22]. Dislocations always propagate parallel to the direction of growth, and thus continue through the layer throughout the entire growth [22, 23]. Hillocks have a higher growth rate than the surrounding areas, leading to a rough surface. This is because dislocations have easily breakable C-C bonds and dangling bonds, creating step edges. Therefore, incorporation of incoming methyl radicals is enhanced compared to a defect-free diamond surface. These defects thus behave as growth centers, explaining the increased growth rate and development of hillocks [23]. As the (100) surface growth rate is locally enhanced at hillock locations, (111) facets will develop simultaneously and propagate laterally in the  $\langle 110 \rangle$  direction, giving hillocks their pyramid-like appearance. Since the  $\langle 110 \rangle$  direction is the direction of minimum free energy [25], the growth conditions will usually be such that the (111) facets propagate faster than the (100) surface, forming a flat-topped hillock [18]. If twinning occurs (the  $180^\circ$  rotation of the crystal lattice about the  $\langle 111 \rangle$  axis forming a mirror image of the lattice about the (111) plane [22]), a small twinned crystal in the center of the (100) face of a flat-topped

hillock will form on top of the propagating dislocation. The growth rate of this feature would be higher than the surrounding (100) face, due to weaker C-C bonds and dangling bonds. (111) facets will be generated from the twin and will rapidly grow towards the lateral sides of the hillock, thus becoming a pyramidal hillock [23]. Hillocks without any apparent (111) lateral faces have also been observed [23]. In these cases, the sides of the hillock exhibit a round shape. This is usually observed under growth conditions utilizing high methane concentrations (>6%) or high nitrogen concentrations [23]. An example of a pyramidal and flat topped hillock is shown in Figure 1-6.

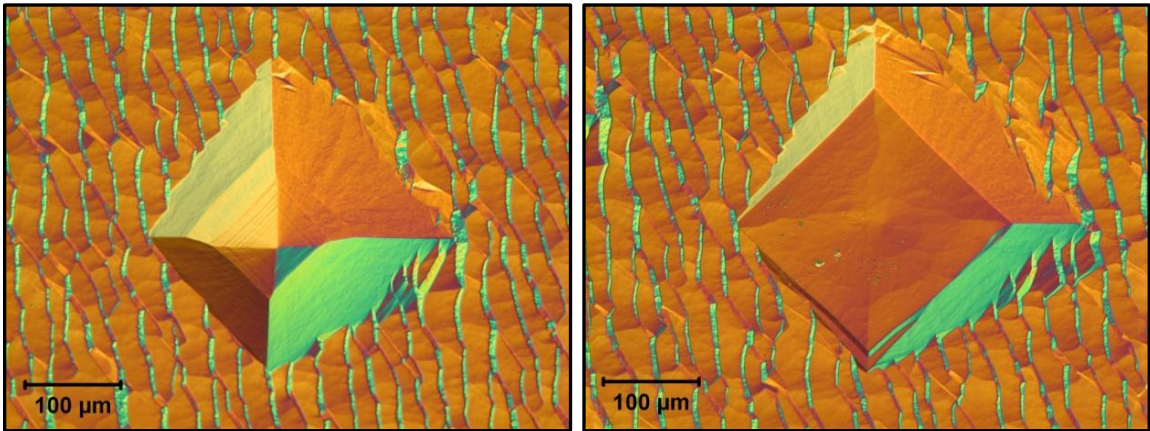


Figure 1-6: 200x optical images of a pyramidal hillock (left) and a flat-top hillock (right). Both macroscopic defects propagate in the [100] direction from dislocations and form (111) facets that propagate laterally. Pyramidal hillocks have a twinned crystal about the (111) plane that enhances growth rate in the [100] direction leading to the pyramid shape.

Stacking faults are also known to occur in single crystal diamond and are common in HPHT synthesis [22]. These are planar defects which only occur on  $\{111\}$  planes. Therefore, these defects are not common for (100)-oriented CVD diamond growth [22]. Vacancy clusters are another defect that form in CVD diamond. These defects are believed to be the cause of the brown coloration sometimes observed in natural and CVD diamonds [22]. This brown coloration is usually only observed in CVD films when grown with a high level of nitrogen incorporation ( $>0.1$ ppm within the film) [22]. The increased growth rate associated with nitrogen addition is believed to lead to growth errors and degraded quality, leading to this type of defect [22].

#### **1.4: Off-Axis Growth**

During CVD growth of diamond, deposition proceeds via a “layer by layer” mechanism adsorbing onto steps. On a perfectly on-axis diamond face with no defects, steps would only be generated by the formation of critical nuclei on the surface, which would require a large supersaturation of carbon radicals [25]. Obviously, no crystal is perfect and growth usually proceeds at lower supersaturations on steps caused by foreign particles, screw dislocations, and other imperfections. This leads to the formation of local areas of enhanced growth rate at these step edges and consequently, the formation of macroscopic defects such as hillocks [25]. On-axis growth (where there are few atomic steps from misorientation) almost always leads to hillock formation [22-28], although some low-growth-rate conditions utilizing very low methane concentrations ( $<0.1\%$ ) and an acid based pre-growth cleaning process have produced hillock-free growth with on-axis substrates [29]. However, it is possible to provide steps uniformly across the entire surface of the crystal by using a substrate which is slightly misoriented, or “off-axis”

[25-28]. Therefore, it is possible to increase growth rate and crystalline quality by creating a high concentration of atomic steps via the utilization of off-axis substrates.

After initial nucleation of carbon onto a step edge, the step will advance laterally over the surface in the  $\langle 110 \rangle$  direction (the direction of minimum free energy) parallel to the (100) surface [25]. As growth continues, these steps can pile up and form bunches or macrosteps, giving the step-growth appearance. Growth rates are substantially higher at atomic steps and proportional to the density of steps times their propagation velocity [25]. Sources of steps are hillocks (or other dislocations or defects), crystal edges (from substrate imperfections, microfractures, and strain caused by mechanical cutting and polishing), and misorientation of the substrate [25]. By increasing the misorientation of the substrate, a higher density of these steps will compete and beat out most unwanted steps (dislocations, crystal edges, etc.) [25, 28]. Therefore, both growth rate and crystalline quality are influenced by the degree of misorientation.

If the off-axis orientation is small, the step densities will be low. Carbon radicals will be incorporated into the lateral growth from the steps [25-28]. However, at high methane concentrations, a surplus of carbon radicals which cannot participate in the lateral growth may grow from an unwanted step source, such as a dislocation, and form a hillock. Therefore, at low off-axis angles, the methane concentration must be very low to prevent any hillock formation [28]. This is consistent with low methane studies showing microscopically smooth growth at the expense of growth rate on on-axis substrates [29]. On the other hand, when the off-axis orientation is large, the step density will also be very high. In this case, the increased density of steps is large enough to accommodate larger concentrations of carbon radicals and lateral growth rate can be enhanced significantly. This rapid lateral growth can overcome undesired growth originating from defect-associated step sources, leading to negligible hillock formation [28]. Therefore, it is important to control the degree of misorientation, and thus the density of steps on the surface of the diamond substrate to produce films with macroscopically smooth surfaces.

Also, using the same argument, the methane concentration must be manipulated for each misorientation angle so that it is low enough to prevent hillock formation, but high enough to obtain optimal growth rates [28].

Growth rates have been shown to increase approximately linearly with increasing off-angle, and do not seem to saturate even at angles as large as  $5^\circ$  [28]. The roughness of the film also seems to decrease as the misorientation is increased, as shown in Figure 1-7. To quantify these theories, photoluminescence spectroscopy and free-exciton emission spectroscopy were conducted in one study [28] and show that the crystalline quality is indeed improved as the off-angle is increased, up to  $5^\circ$  in this case.

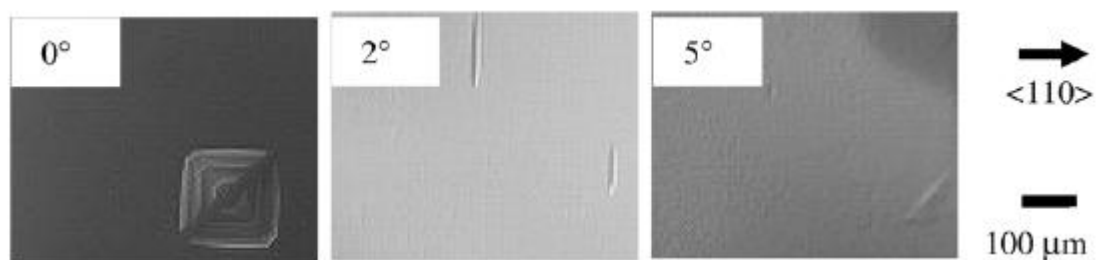


Figure 1-7: Dependence of substrate misorientation on as-grown surface morphology. For the nominally “on-axis” case, growth hillocks are observed. As the misorientation angle is increased, the film becomes macroscopically smooth. [28]

### 1.5: Effect of Growth Parameters on Quality and Growth Rate

The quality of single crystal diamond films grown by various CVD methods (most commonly MPCVD) is determined by several different mechanisms. Some of the major factors that control the quality, as well as growth rate, of CVD diamond are the growth parameters. These parameters include substrate temperature [30, 31], methane concentration [30-33], microwave power density [31, 33, 34], and pressure [35].

The temperature regime of the deposition process has a large effect on the properties of the deposited diamond film. It has been shown that increasing the substrate temperature leads to an increase in growth rate due to an increase in the surface reaction rates and the mobility of the absorbed species [30, 31]. However, the quality of the films varies over this temperature and is quite sensitive. At high temperatures ( $>1000^{\circ}\text{C}$ ) large pyramidal hillocks (observed by optical microscopy) form on the surface with non-epitaxial crystallites usually present on the tops [31]. The higher growth rates and rough morphology may also cause non-diamond carbon to be buried in the film creating compressive stresses, which may lead to defects [36]. Lower growth temperatures ( $<750^{\circ}\text{C}$ ) result in much lower growth rates and produce rough films with a high density of etch pits [30, 31]. The ideal temperature for high-quality growth appears to be around  $850^{\circ}\text{C}$ . At this temperature, very smooth films are deposited with minimal hillock formation and no observable non-epitaxial crystallites [30, 31].

An increase in methane concentration directly leads to an increase in the growth rate of the diamond films. This is due to an increase in the ratio of  $\text{CH}_3$  radicals to ionized hydrogen [31-33]. Interestingly, the variation of methane concentrations (from 2%-7.2%) does not seem to have an effect on the crystalline quality of CVD diamond [31]. The density of atomic hydrogen is believed to be high enough at high microwave power densities to etch away any non-diamond

phase formations even at high methane concentrations [31]. At lower concentrations however, some etch pits were observed due to an excess of hydrogen ions.

As expected, the growth rate of single crystal diamond films also increases with increasing microwave power density due to an increase of  $\text{CH}_3$  radicals and atomic hydrogen densities [31, 33, 34]. However, high concentrations of atomic hydrogen can lead to etching of the diamond surface and compete with growth at low methane concentrations. This can lead to the formation of etch pits. Therefore, an increase in microwave power density must be coupled with an increase in methane concentration to compensate for etching related to increased atomic hydrogen concentrations [31]. The increase in etching due to increased concentrations of atomic hydrogen at higher MW power densities ( $>100 \text{ W/cm}^3$ ) can also lead to etching of the quartz walls of the reactor, incorporating Si into the film [31]. Literature reports that the quality of the film seems to be independent of MW power density [31, 35]. MW power density is also associated with reactor pressure. Therefore, an increase in pressure would lead to an increase in MW power density and increase growth rate with minimal effect on crystalline quality [35].

Other growth regimes have been used which utilize low methane concentrations ( $<2\%$ ) at low temperatures ( $\sim 750^\circ\text{C}$ ) and pressures ( $<100 \text{ Torr}$ ). The growth rates in this case are small, but quality and reproducibility can be controlled to a greater degree [37]. The power density can also be increased in this case without raising the pressure by water cooling the substrate holder to allow for increased input power [37].

Nitrogen addition is a well established technique used to increase the growth rates of diamond films [30, 31, 32, 35]. However, incorporation of nitrogen into diamond films can induce defects and increase dislocation densities [38]. Also, an increase in Si incorporation seems to be associated with nitrogen addition, possibly from enhanced quartz etching [31].

## 1.6: Plasma Etching and Pre-growth Surface Treatment

Low surface damage and microscopically smooth surfaces are a key requirement for technological applications of single crystal CVD diamond films. It is very difficult and uncommon to produce as-grown diamond films that are free of macroscopic surface features, such as hillocks, facets, and macroscopic steps. Therefore, bulk planarization is almost always required for device fabrication. However, mechanical polishing inevitably leads to microfractures, cracks, and residual metal particles on the diamond substrate surface [22], which in turn leads to the propagation of defects during homoepitaxial growth throughout the CVD film. These surface and sub-surface flaws must therefore be removed prior to growth.

Using a plasma etching (or dry etching) technique prior to homoepitaxial growth can remove these residual defects and particles and greatly improve the quality of the deposited CVD diamond film [22]. Traditionally, oxygen/hydrogen mixtures (usually >90% hydrogen) have been used to etch mechanically induced defects. Because defects have weaker C-C bonding, this plasma etching process removes defective areas preferentially, creating etch pits of size and density comparable to the level of surface and sub-surface damage [22]. The creation of etch pits (especially in high densities) will lead to a very rough surface, undesirable for device-grade material. Therefore, if exceptionally low surface roughness is to be obtained, the etch process should remove damaged areas, non-damaged areas, and areas around extended defects at the same etch rate [22]. Thus, oxygen containing plasmas are generally not suitable for highly smooth surface processing.

There are several different etching processes utilizing many different mixtures of gases, types of reactors, pressures, and temperatures. Gas chemistries consist of many different combinations including process gases such as H<sub>2</sub>, O<sub>2</sub>, Ar, N<sub>2</sub>, SF<sub>6</sub>, Kr, and Cl. Most of the successful etching processes use plasma processing techniques such as electron cyclotron

resonance (ECR), inductively coupled plasma (ICP), or parallel plate reactive ion etching (RIE) [22, 39, 40]. These techniques utilize very low pressures (in the mTorr range) to remove material via bombardment (as well as chemical reaction) rather than chemical surface reactions only (as is the case for higher pressures). Operating pressures this low are unrealistic for traditional MPCVD systems, such as the Lambda Technologies system and require specialized reactors.

Plasma etching techniques are comprised of two related mechanisms; chemical reactive etching and physical sputtering. Chemical reactive etching is the main mechanism involved in most dry etching techniques, but is isotropic and leads to pits. The sputtering mechanism is anisotropic but has a lower etch rate. Controlling the contributions of each of these mechanisms is the key to realizing a good etch morphology [41]. Varying pressure is an important factor to achieve an adequate proportion of these two mechanisms. In order to optimize the etching process, the coupled effects of reactor pressure, RF power, and reactant flow rate must be taken into consideration. For example, one study [41] showed that when the RF power was 120W, and the reactant flow (oxygen in this case) was 80 sccm, the optimal pressure range was between 80-100 mTorr (shown in Figure 1-8). Within this range, the etch rate was highest and the surface was smooth. Deviating from this pressure range resulted in a decrease in etch rate as well as a rougher surface. This can be explained by a reduction of the total chemical species at pressures lower than the optimal range, leading to lower etch rates. At higher pressures, the concentration of chemical species will be increased and the number of collisions of activated species will greatly increase and be annihilated, leading to an overall reduction in concentration of activated species, causing the etch rate to decrease [41]. It was shown that as reactant flow rate and RF power are increased; the optimal pressure range will shift towards higher pressures [41].

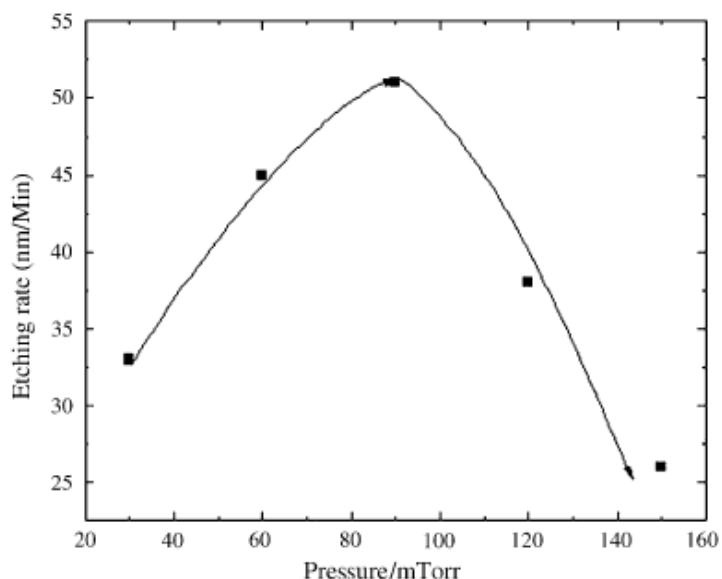


Figure 1-8: RIE etching of diamond, pressure vs. etch rate. An ideal pressure (peak of curve) is established when the concentration of species is high enough to contribute to etching yet low enough to avoid collisions with each other. [41]

Parallel plate reactive ion etching (RIE) is one of the most common dry etching techniques for diamond films. One example from the literature [42] uses a  $\text{CF}_4\text{-O}_2$  plasma to obtain highly smooth surface morphologies at high etch rates ( $\sim 9 \mu\text{m/hr}$ ). This study showed that the optimal pressure was 15 mTorr for gas mixtures of 25%  $\text{CF}_4/\text{O}_2$  [42]. Small variations in  $\text{CF}_4$  concentration influenced the morphology and etch rates significantly.

A variation of traditional “parallel plate” RIE is a reactor configuration called inductively coupled plasma (ICP). This method uses induction to increase the density of ionized species in the plasma. One study [22, 39] used an ICP technique utilizing an  $\text{Ar/Cl}$  plasma chemistry to etch (100) single crystal diamond after mechanical polishing. When compared to the  $\text{Ar/O}_2$  plasma etch, which preferentially etched surface pits, it was found that the  $\text{Ar/Cl}$  plasma produced a very smooth surface completely free of macroscopic features. Therefore, it was shown that this plasma

chemistry etches non-preferentially, etching defective areas and non-defective areas at the same rate. The Ar/Cl plasma chemistry also has a lower etch selectivity (defined as the diamond etch rate to the etch rate of photoresist [39]) compared to Ar/O<sub>2</sub> chemistries, creating greater possibilities for patterning of features and fabrication of micro-structures [39]. This study was done at a pressure of 5 mTorr and resulted in etch rates of 40-100 nm/min. During this process, Ar ions are used for sputtering of the diamond surface and enable the chemical reaction of the chlorine ions with the carbon atoms, resulting in CCl<sub>x</sub> etch products [39]. This plasma chemistry has not been extensively studied in traditional parallel plate RIE or ECR reactor configurations.

Another study [40] used an electron cyclotron resonance (ECR) technique which allowed for very high etching rates (up to 16 μm/hr for single crystal diamond) by incorporating a magnetic field. ECR plasma discharges generate very high plasma densities at low pressures (< 100 mTorr) and temperatures. When combined with substrate biasing, this technique enables excellent anisotropic etching at high rates [26]. This study used a mixture of Ar, O<sub>2</sub>, and SF<sub>6</sub> at 45 mTorr. The addition of SF<sub>6</sub> resulted in etched films with smoother surfaces [40].

All three RIE plasma etching variations are similar in the fact that they use high density plasma discharges at low pressures to create both atomic bombardment and chemically reactive etching at the surface of the diamond film to remove surface and sub-surface defects, most of which are induced during bulk planarization, i.e. mechanical or chemical-mechanical polishing. ICP is a common etching technique and is readily available at the MRI facilities. The literature results of chlorine-based ICP etching [22, 39] show very smooth surface morphologies at high etch rates.

### **1.7: Focus of this Study**

The literature review has shown the basic dependencies of growth parameters on the growth rate, surface morphology, and crystalline quality of single crystal MPCVD diamond films. This thesis will use the current fundamental knowledge of MPCVD diamond growth and attempt to expand upon it in an effort to improve the intrinsic region of high-power diode structures. Focus is directed toward an understanding of the plasma density and the dissociation of the gas precursors by the manipulation of the susceptor geometry and substrate cooling. It will be shown that by controlling the behavior of the plasma, the growth rate can be increased significantly and hillock formation can be suppressed by promotion of the step-flow growth mode, leading to thick high-quality (100) single crystal diamond films.

In addition, substrate misorientation and ICP reactive ion etching were shown in literature to improve the starting surface of the substrates and further improve the morphology of the as-grown diamond film. Therefore, these techniques were employed in the current study to further improve the surface morphology of as-grown diamond films in an attempt to suppress the formation of growth hillocks.

## Chapter 2

### Equipment and Experimental Procedures

Homoepitaxial diamond films were grown in a microwave plasma chemical vapor deposition system that has several features that proved to be beneficial for enhancing growth rate and improving morphology. This chapter will detail the MPCVD reactor as well as study the temperature dependence of the 3mmx3mm single crystal diamond substrate on microwave power and reactor pressure. Samples characterization is also discussed using several techniques including: Raman spectroscopy, optical microscopy, atomic force microscopy, optical profilometry, and secondary ion mass spectrometry. Pre-growth substrate preparation is also discussed in this chapter. A standard cleaning process was applied for all samples and a reactive ion etching process was used on select samples.

#### 2.1: Experimental Materials and Substrate Cleaning Process

Single crystal (100) oriented CVD synthetic diamond plates (3mmx3mmx0.5mm) were used for all experiments except where specified. Initial reactor profiling studies used 3" diameter (111) oriented silicon wafers, seeded ultrasonically with a mixture of 0.25 $\mu$ m diamond powder and ethanol (3g : 100mL). Off-axis CVD diamond substrates were also used for specified experiments. These substrates were type 3A (100) oriented CVD synthetic diamond plates (3mmx3mmx0.3mm). Nitrogen concentrations were <1ppm for these substrates. All CVD diamond plates were purchased from Element 6.

All substrates were cleaned with a standard two step cleaning process, utilizing a solvent cleaning step and an acid cleaning step [29]. Substrates were cleaned prior to etching and prior to growth. The cleaning process is detailed in Table 2-1.

Table 2-1: Substrate Cleaning Process [29].

<b>Solvent Cleaning Step</b>	
<b>Solvent and sample place in ultrasonic bath for 10 minutes</b>	
<b>Solvent</b>	<b>Grade</b>
Methanol	Electronic Grade
Acetone	Electronic/Cleanroom Grade
Ethanol	Reagent Alcohol HPLC Grade
<b>Acid Cleaning Step</b>	
<b>Sample placed in ~40mL of acid mixture for 15 minutes</b>	
<b>Acids</b>	<b>Ratio</b>
Nitric Acid ( $\geq 90\%$ ) : Sulfuric Acid (95-98%)	1 : 1
Nitric Acid ( $\geq 90\%$ ) : Hydrochloric Acid (37%)	1 : 3
Hydrofluoric Acid (48%)	N/A

All chemicals were purchased from Sigma-Aldrich. Substrates were rinsed with de-ionized water and blown dry with nitrogen between each step. Following the final HF step, substrates were placed in a beaker containing de-ionized water and heated to  $\sim 200^\circ\text{C}$  for 15 minutes to remove any residual HF.

Etching was performed with the Tegal 6540 HRe cluster etch system. This ICP etching tool features dual-frequency RF power technology and magnetic plasma confinement for high-density plasma etching. Available process gases include:  $\text{Cl}_2$ ,  $\text{BCl}_3$ ,  $\text{SF}_6$ ,  $\text{O}_2$ , Ar, and  $\text{CF}_4$ .

## 2.2: Lambda Technologies MPCVD Reactor

Homoeptaxial deposition of intrinsic single crystal diamond was performed in a commercial microwave plasma chemical vapor deposition (MPCVD) reactor. The system was purchased from Lambda Technologies of Morrisville, NC in the spring of 2009.

The MPCVD reactor came with several features that offered a valuable upgrade from traditional home-made tube reactors. A cross section schematic showing the basic parts of the reactor is shown in Figure 2-1 and a more detailed schematic is given in Appendix A.

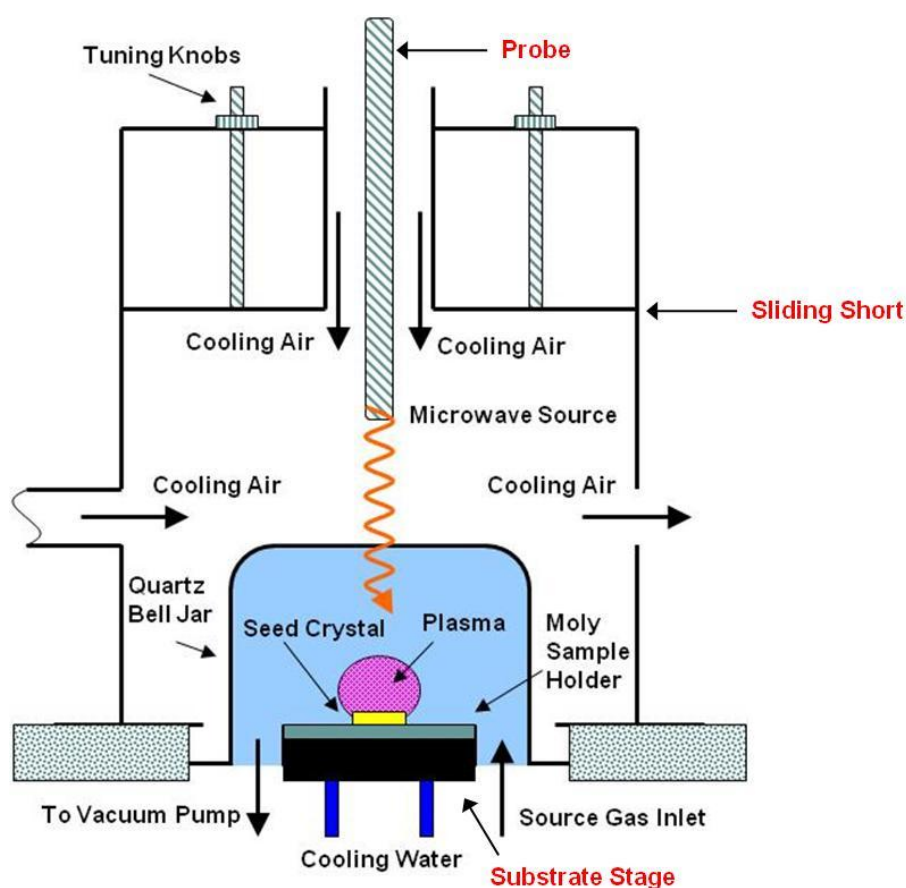


Figure 2-1: Cross section schematic of the MPCVD reactor. The microwave cavity is a 17.8cm diameter brass cylinder. The process is contained within a 12.5cm diameter quartz bell jar. The microwave probe, substrate stage, and sliding short are fully tunable to achieve the desired plasma power distribution and are indicated with red font.

The system is equipped with a 6kW 2.45 GHz microwave generator for an increased range of power input, plasma density, and substrate temperature control. A fully adjustable and tunable microwave cavity is contained within a 17.8cm diameter brass cylinder which produces a  $TM_{013}$  electromagnetic power distribution mode. The microwave cavity features three independently tunable sections: the substrate stage, microwave probe, and sliding short to achieve adequate microwave power match. This means that the majority of the forward microwave power will be efficiently coupled into the plasma to maintain consistent temperature and plasma density. The MPCVD system also features a water cooled stage to reduce substrate temperature, allowing for higher microwave input power. This, consequently, leads to enhanced plasma power density and improved ionization of gas precursors. The process cavity includes a 12.5cm diameter quartz bell jar and a three inch molybdenum susceptor capable of holding a three inch silicon wafer for polycrystalline deposition. The large area bell-jar leads to reduced silicon etching from plasma-quartz interaction. A turbo pump was installed for efficient evacuation of impurity gases (such as nitrogen, oxygen, and water vapor) prior to deposition. Images of the Lambda Technologies MPCVD reactor are shown in Figure 2-2 and cross sectional schematics of the microwave cavity and a block diagram of the system can be found in **Appendix A**. Operation of the reactor as well as the standard run procedures are detailed in **Appendix G**.

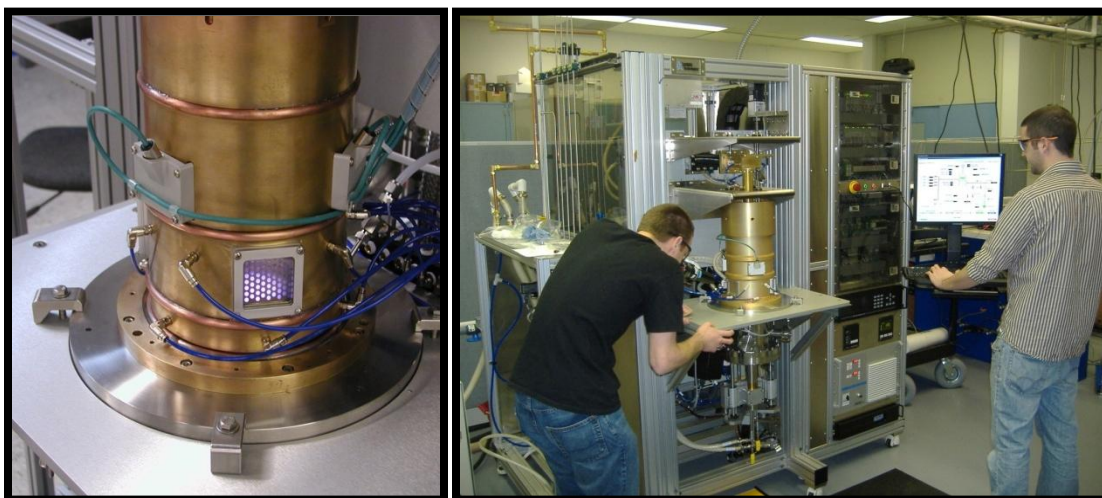


Figure 2-2: Left: Microwave and process cavity; Right: Full MPCVD system.

Molybdenum susceptors were used as substrate holders. Different reactor configurations (detailed in the following sections) used different susceptor designs. Schematics of the molybdenum susceptors used for each reactor configuration can be found in **Appendix B**. Custom made molybdenum susceptors were fabricated either in house or by Diamond Ground Products, Inc. The molybdenum source material used had a purity of 99.5%.

Hydrogen and methane were the only precursors used for intrinsic diamond growth. Argon was used in the nano-crystalline growth studies. Only UHP source gases were used; UHP hydrogen had a purity of 5N (99.999%), UHP methane had a purity of 3.7N (99.97%), and UHP argon had a purity of 5N (99.999%). During growth, the plasma chemistry and ionization behavior were studied using an Avantes AvaSpec-2048 Optical Emission Spectrometer (OES).

The system is controlled by a custom designed HMI (human-machine-interface) program called DiamoTech. Four mass flow controllers (MFC) came with the system: a 1000 sccm hydrogen MFC, a 50 sccm methane MFC, a 20 sccm carbon dioxide MFC, and a 5000 sccm argon MFC. No CO<sub>2</sub> source was connected to the system at the time however.

Before any growths could be attempted in the newly acquired Lambda Technologies MPCVD reactor, it was important to understand the substrate temperature behavior at different pressures for a range of forward input powers. These reactor profiling experiments would prove to be valuable in understanding and choosing deposition processes and geometry configurations for future growth studies. It was quickly discovered that the as-received substrate holders were less than ideal for single crystal growth and more suited to polycrystalline growth on three inch silicon wafers. Therefore, several modifications were made to the susceptor geometry to enhance the growth process of single crystal diamond. Three susceptor configurations were used and will be detailed in the following sections.

### **2.2.1: Reactor Profiling Results – Susceptor Configuration 1**

The first susceptor configuration was simply the as-received standard three inch wafer holder design. Here, temperature vs. forward power profiles were taken for both three inch (111) silicon wafers as well as 3mmx3mmx0.5mm (100) CVD single crystal seeds. Temperature vs. flow rate was also studied for (111) Si wafers to determine any changes associated with flow rate. The temperature of the substrates was measured with a Mikron M770S one and two color pyrometer.

Figure 2-3 shows the cross sectional depiction of susceptor configuration 1. In this configuration, a molybdenum support plate is placed on top of a stainless steel cooling stage and quartz support tube. The quartz support tube can be adjusted to raise the molybdenum support plate off of the stainless steel cooling stage if the operator desires less cooling to the substrate. On top of the molybdenum support plate sits the three inch molybdenum wafer holder. A 3mm x 3mm CVD seed (or three inch Si wafer) is then placed on top of the as-received molybdenum

wafer holder. Schematics detailing all of the susceptor parts and images of the three different susceptor configurations are shown in **Appendix B**.

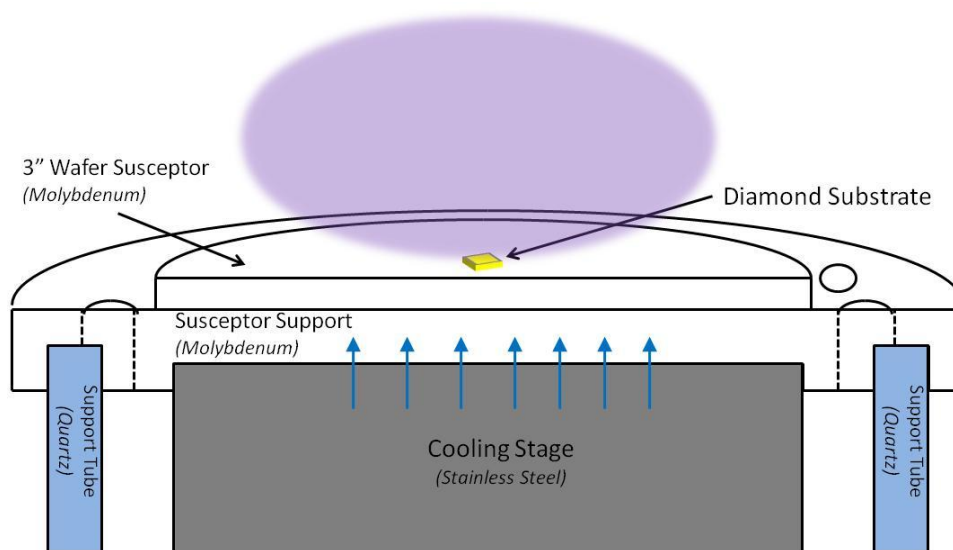


Figure 2-3: Cross section of Susceptor Configuration 1 which consists of the stock 3" wafer holder on top of a molybdenum support plate and cooling stage.

Temperature vs. forward power profiles were taken for three different gap spacings between the susceptor support plate and the cooling stage: 0mm (in contact), 2mm, and 5mm. The pressure was varied between 40 Torr and 160 Torr in 20 Torr increments (where applicable). The forward power was increased in increments of 200W for each pressure setting until the temperature leveled out or a maximum temperature of 1200°C was reached. A constant flow rate of 294 sccm of H<sub>2</sub> and 6 sccm of CH<sub>4</sub> maintained a constant methane concentration of 2%. Geometry settings were held constant for all three susceptor configurations: Probe: 1.00, Short: 22.15, Lower Bellows: -1.30. The following plots show the results of the profiling experiments for the three inch (111) Si wafer.

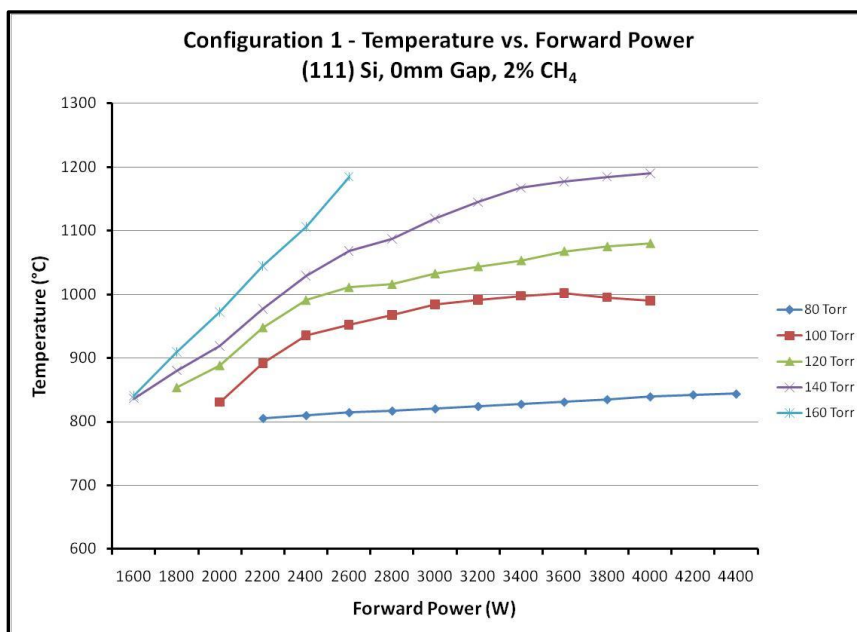


Figure 2-4: Temperature vs. Microwave power – Configuration 1. Substrate: 3” (111) Silicon. Gap between susceptor and cooling stage: 0mm.

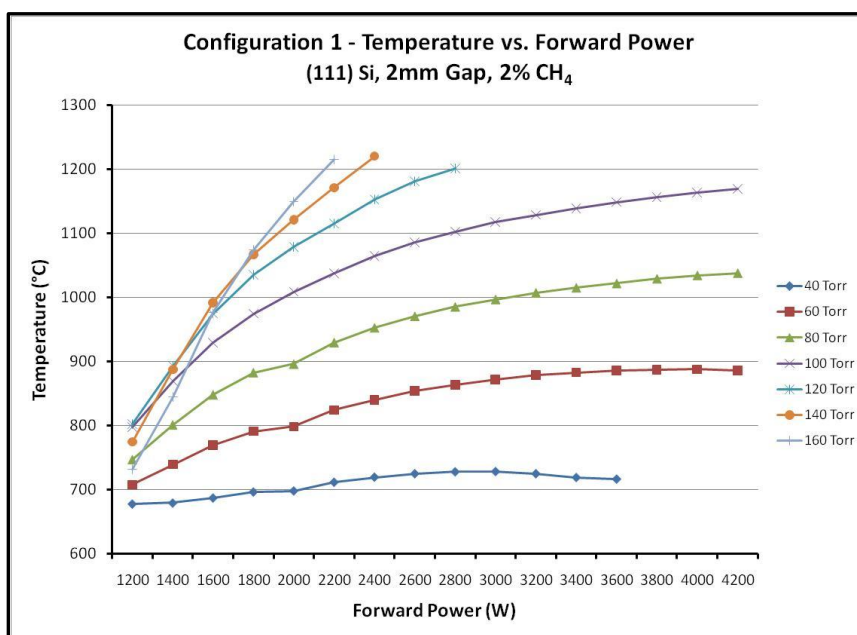


Figure 2-5: Temperature vs. Microwave power – Configuration 1. Substrate: 3” (111) Silicon. Gap between susceptor and cooling stage: 2mm.

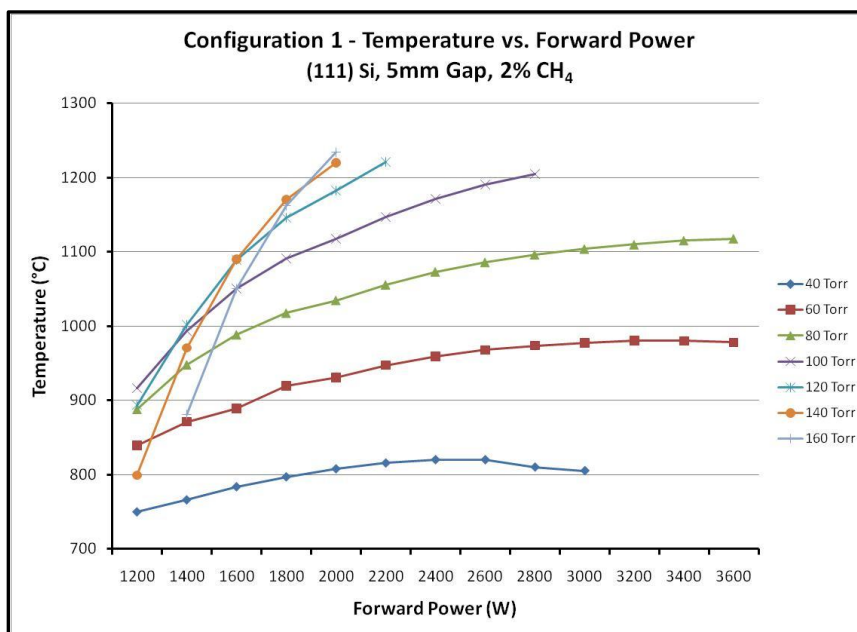


Figure 2-6: Temperature vs. Microwave power – Configuration 1. Substrate: 3” (111) Silicon. Gap between susceptor and cooling stage: 5mm.

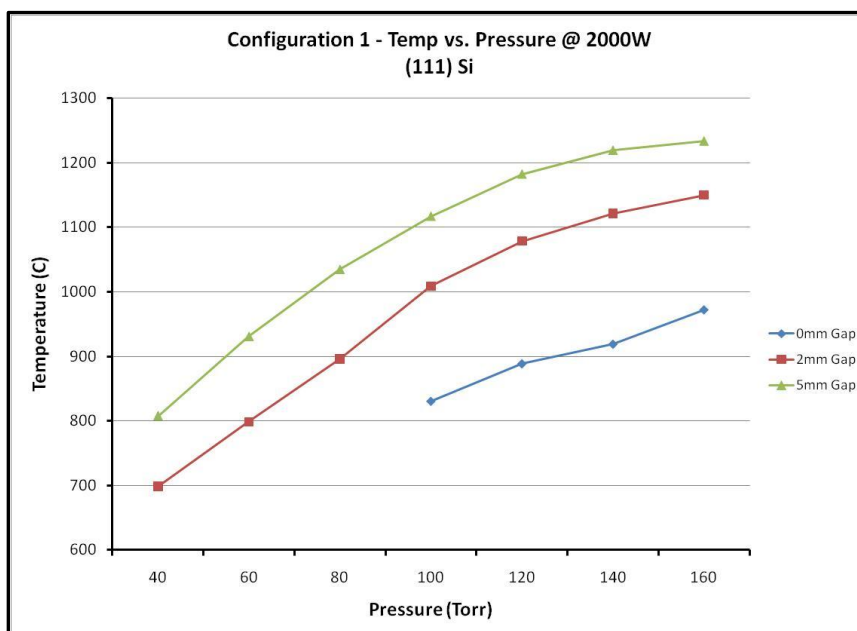


Figure 2-7: Temperature vs. Microwave power – Configuration 1. Substrate: 3” (111) Silicon. Microwave power: 2000W.

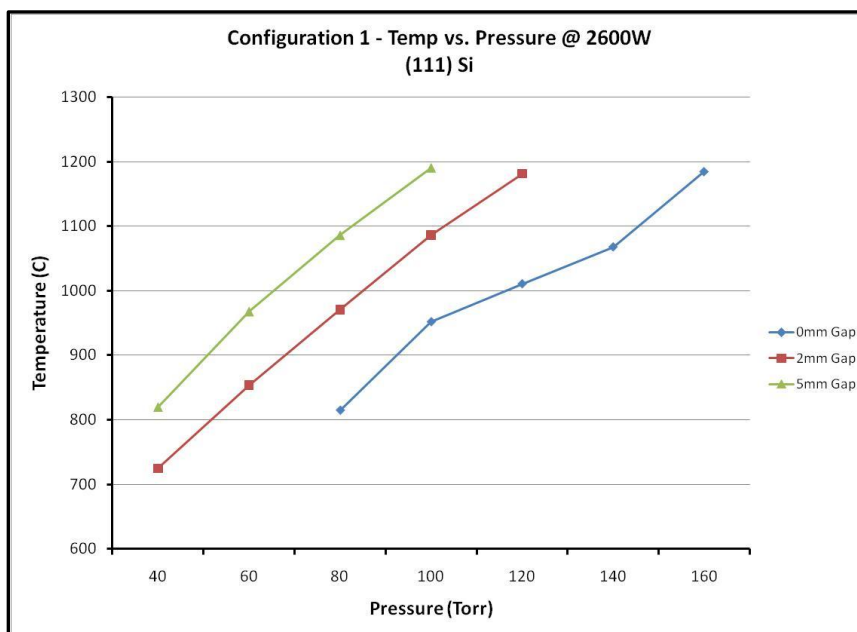


Figure 2-8: Temperature vs. Microwave power – Configuration 1. Substrate: 3” (111) Silicon. Microwave power: 2600W.

As expected the slopes of the temperature vs. power curves increased as the pressure was increased. Increasing the gaps between the susceptor support plate and the cooling stage resulted in similar curvature; however the profiles are translated to higher temperatures. This can clearly be seen in the temperature vs. pressure graphs (Figures 2-7 and 2-8).

Next, temperature vs. flow rate profiles were taken for three different gap spacings (0mm, 2mm, and 5mm). The pressure was maintained at 100 torr, CH<sub>4</sub> concentration was 2%, and the power was set so that the temperature was 1000°C for the nominal gas flow rate of 300 sccm H<sub>2</sub>. The gas flow rate was then varied from 25% to 200% of the nominal flow and the temperatures were recorded. Figure 2-9 shows the results of this experiment.

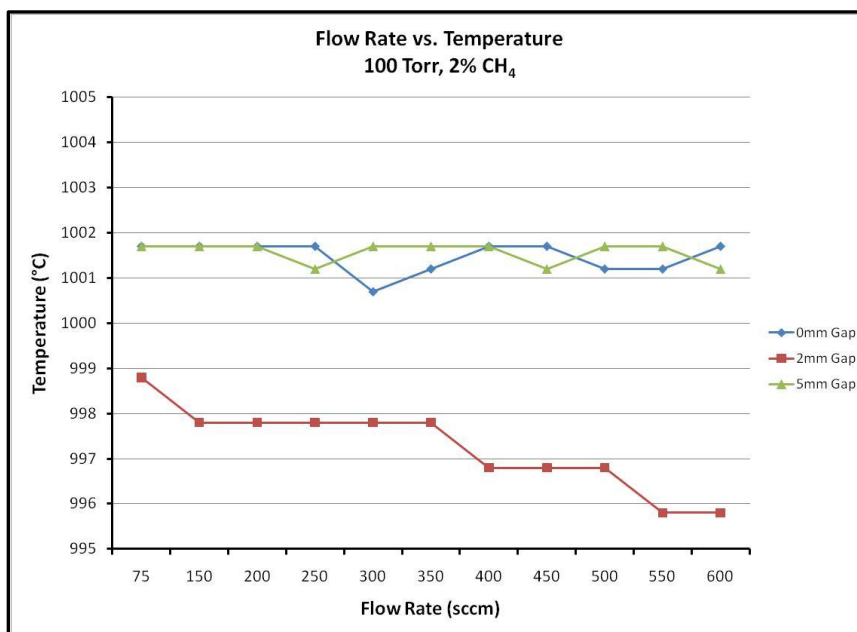


Figure 2-9: Temperature vs. Flow Rate – Configuration 1. Substrate: 3” (111) Silicon.

As shown in Figure 2-9, there seems to be no correlation between temperature and flow rate as temperatures fluctuate no more than three degrees. This may be due to the geometry of the system and the constant pressure being maintained in the bell jar.

Temperature vs. forward power was also profiled for (100) 3mm x 3mm x 0.5mm CVD single crystal diamond substrates. Temperatures were recorded at three different pressures: 80 Torr, 100 Torr, and 120 Torr. The forward power was increased in increments of 200W for each pressure setting until the temperature leveled out or a maximum temperature of 1200°C was reached. The gas flow rate was set at 294 sccm H<sub>2</sub> and 6 sccm CH<sub>4</sub>, methane concentration was 2%, and the gap spacing between the cooling stage and substrate was 2mm. Figure 2-10 shows the results.

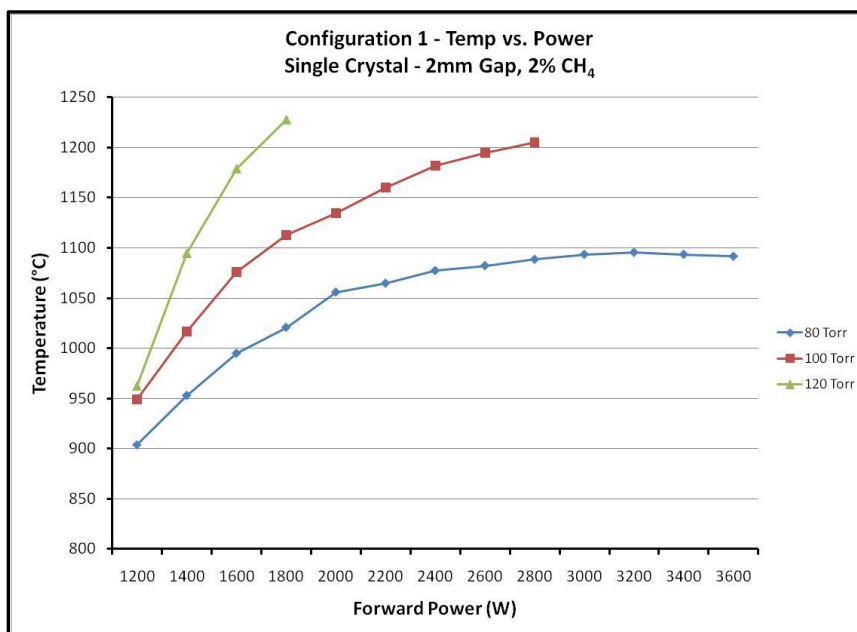


Figure 2-10: Temperature vs. Microwave power – Configuration 1. Substrate: (100) single crystal.

The temperature vs. power profile for single crystal diamond is similar to the ones for polycrystalline diamond, except the slopes are even steeper and the temperatures are translated significantly higher at lower pressures compared to the Si wafers.

Initial growth runs (detailed in Chapter 3) showed very low growth rates for this susceptor configuration. Results were not comparable to literature using similar conditions. After close observations during the temperature vs. power profiling of single crystal diamond seeds for susceptor configuration 1, it became apparent that the plasma was not interacting very well with the substrate. In addition, the plasma volume over the substrate was very large. A large plasma volume is ideal for large area polycrystalline growth but undesirable for growth on small single crystal seeds. In configuration 1, it seems that the majority of the input power was being absorbed into plasma regions far from the substrate surface. Therefore the plasma density over the substrate is much lower than desired as microwave energy is wasted elsewhere.

### 2.2.2: Reactor Profiling Results – Susceptor Configuration 2

Susceptor configuration 2 was designed in an attempt to: 1) raise the single crystal seeds into better contact with the plasma; 2) confine the volume of the plasma to a smaller region over the substrate and therefore increase plasma power density and reactive ion density at the surface of the substrate. Two tapered molybdenum seed holders (1/2" diameter) were fabricated with heights of 5mm and 10 mm. Schematics of these seed holders can be found in **Appendix B** and were designed to hold substrates up to 5mm x 5mm.

The basic design of susceptor configuration 2 is identical to susceptor configuration 1, except that the 1/2" diameter tapered seed holders were placed directly on top of the three inch wafer holder. The cross sectional design of susceptor configuration 2 is shown in Figure 2-11.

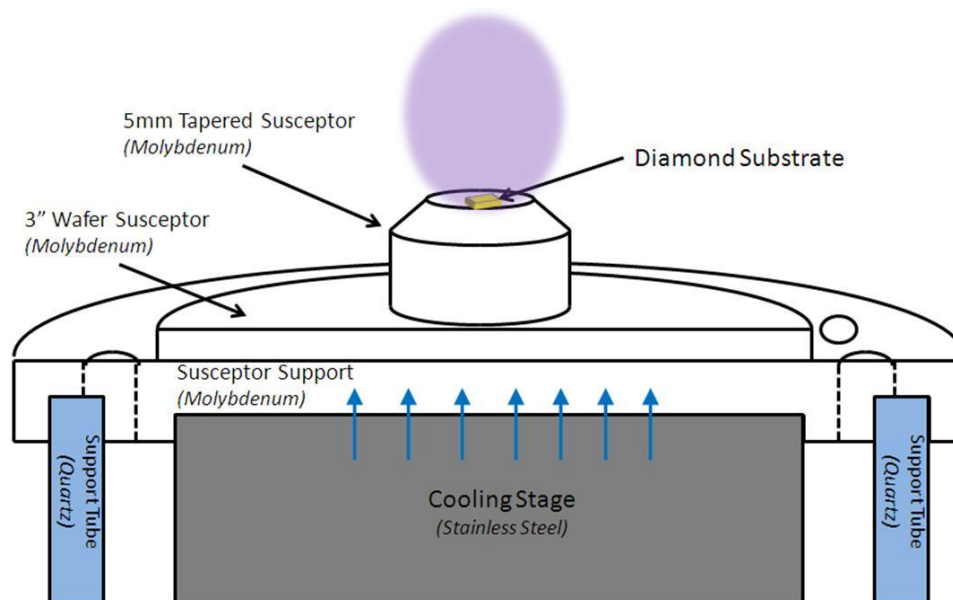


Figure 2-11: Cross section of Susceptor Configuration 2. The addition of a 1/2" diameter raised and tapered molybdenum seed holder was added to raise the substrates into contact with the plasma.

For the temperature vs. power study of susceptor configuration 2, single crystal (100) seeds (3mm x 3mm x 0.5mm) were used. The pressure was varied between 80 Torr and 120 Torr in 20 Torr increments (where applicable). The forward power was increased in increments of 50W for each pressure setting until the temperature leveled out or a maximum temperature of 1200°C was reached. A constant flow rate of 196 sccm of H<sub>2</sub> and 4 sccm of CH<sub>4</sub> maintained a constant methane concentration of 2%. No gap between the stainless steel cooling stage and the molybdenum support plate was used. The following plots show the results of the profiling experiments.



Figure 2-12: Temperature vs. Microwave power – Configuration 2. Seed holder height: 5mm.



Figure 2-13: Temperature vs. Microwave power – Configuration 2. Seed holder height: 10mm.

From the temperature vs. power plots, it is obvious that the seeds are heating up very rapidly with minimal forward microwave power levels. For the 5mm holder (Figure 2-12), temperatures approaching 1200°C were reached at forward powers of less than 1200W, even at lower pressures. The 10mm seed holder was even worse; reaching temperatures of 1200°C at less than 700W. Pressures higher than 100 Torr were not applicable for the 10mm seed holder.

This configuration did in fact satisfy the goal of confining the plasma into contact with the substrate. Consequently however, this caused the substrate to heat up to undesirable temperatures at very low forward powers. The low power input would result in less than desirable plasma power densities over the substrate and could have a negative effect on growth. Due to this increased heating, it quickly became apparent that cooling to the substrate would be a necessity for maintaining high plasma power densities at growth temperatures (~1100°C).

Susceptor configuration 2 appears to have some benefits over susceptor configuration 1 in that the substrate is put into contact with the plasma and the plasma is confined to a smaller area, pulling it far from the quartz chamber walls. However, the low input powers required to maintain a reasonable growth temperature may not be enough to fully ionize methane into the methyl radical concentrations required for high quality diamond growth [31]. The problem is that the thickness of the molybdenum susceptor parts creates a large thermal resistance between the stainless steel cooling stage and the diamond substrate. To improve the substrate cooling, the thermal resistance between the substrate and cooling stage must be minimized.

### **2.2.3: Reactor Profiling Results – Susceptor Configuration 3**

Susceptor configuration 3 employed a custom fabricated molybdenum susceptor support designed to improve cooling to the substrate by reducing the amount of material (and thus the thermal resistance) between the stainless steel cooling stage and the diamond substrate. To accomplish this, the three inch wafer holder insert and the stock susceptor support plate were removed. A new molybdenum susceptor support plate, utilizing a cut-out for the tapered and raised seed holder inserts, was fabricated by Diamond Ground Products, Inc. Detailed schematics of the redesigned susceptor support can be found in **Appendix B**. Three different seed holder heights were used: 5mm, 7mm, and 10mm. The goal of this susceptor configuration was to use the raised and tapered design of configuration 2 (promoting enhanced substrate-plasma interaction) coupled with improved cooling to allow for increased forward input power and thus higher plasma power densities over the substrate. Figure **2-14** shows a cross-sectional representation of susceptor configuration 3.

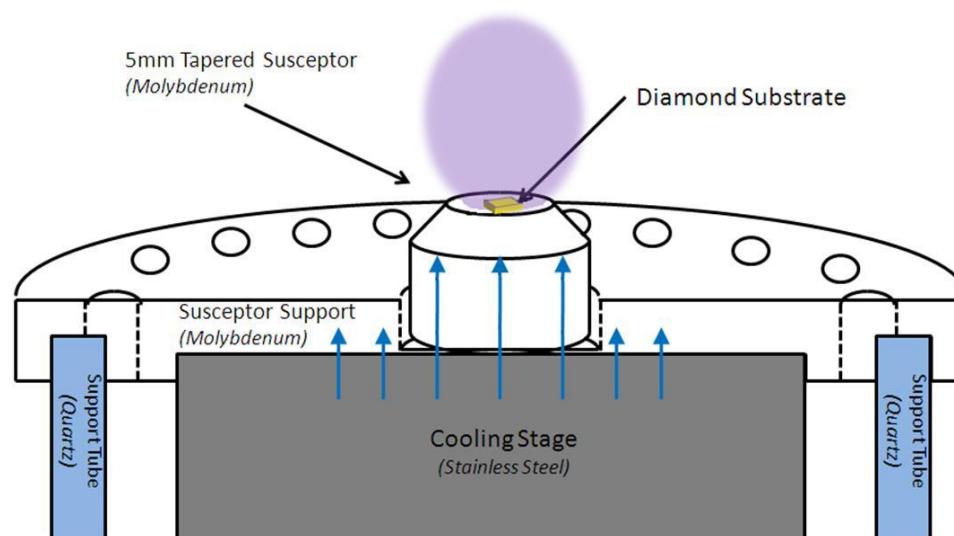


Figure 2-14: Cross section of Susceptor Configuration 3. The susceptor support plate was replaced by a new plate with a  $\frac{1}{2}$ " diameter cut-out for insertion of the  $\frac{1}{2}$ " raised and tapered molybdenum seed holder.

For the temperature vs. power study of susceptor configuration 3, single crystal (100) seeds (3mm x 3mm x 0.5mm) were used. The pressure was varied between 100 Torr and 140 Torr in 20 Torr increments (where applicable). The forward power was increased in increments of 100W for the 5mm and 7mm seed holders, and 50W for the 10mm seed holder for each pressure settings until the temperature leveled out or a maximum temperature of 1200°C was reached. A constant flow rate of 196 sccm of H<sub>2</sub> and 4 sccm of CH<sub>4</sub> maintained a constant methane concentration of 2%. No gap between the stainless steel cooling stage and the molybdenum support plate was used. Temperature vs. power profiles are shown below for this configuration.

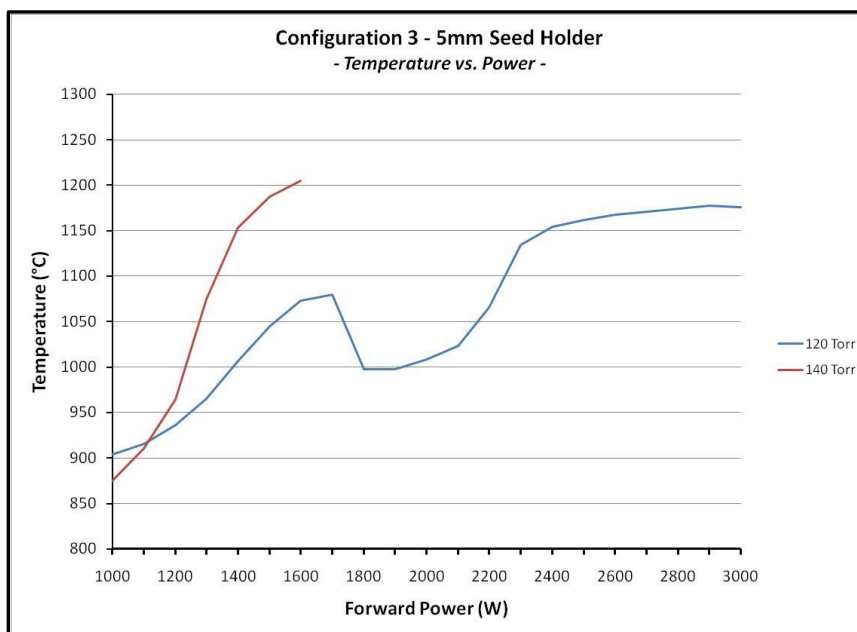


Figure 2-15: Temperature vs. Microwave power – Configuration 3. Seed holder height: 5mm.

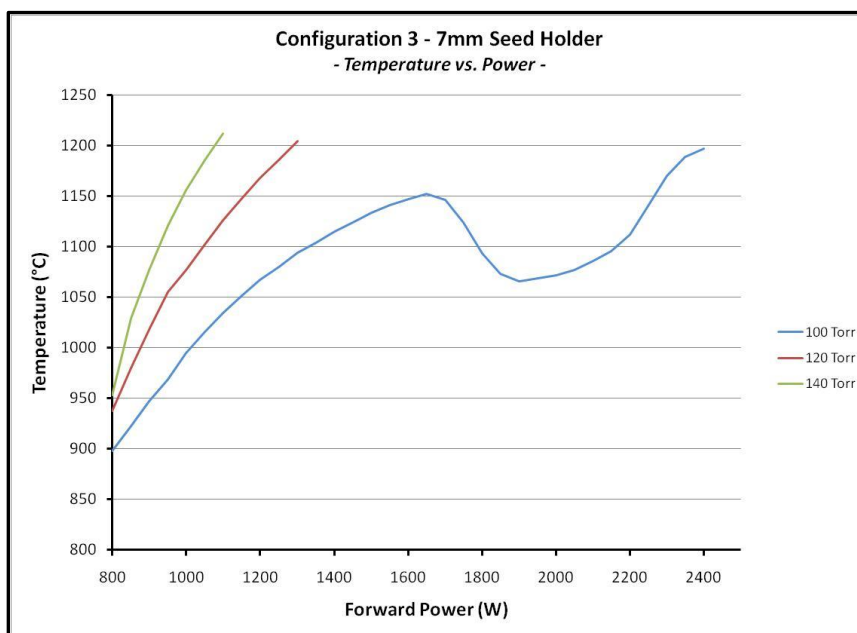


Figure 2-16: Temperature vs. Microwave power – Configuration 2. Seed holder height: 7mm.



Figure 2-17: Temperature vs. Microwave power – Configuration 2. Seed holder height: 10mm.

As expected, the improvement in cooling to the substrate allowed for increased microwave power input while maintaining low growth temperatures. From Figures 2-15 to 2-17, it is obvious that the increase in seed holder size has a direct effect on substrate temperature. Differences of only 2mm in seed holder height lead to temperature changes of several hundred degrees. Interestingly, for the 5mm and 7mm seed holders, a shift in plasma “modes” seems to occur between 1700W and 1800W for the 5mm holder and between 1600W and 1700W for the 7mm holder. In these power regions, the temperature appears to level out then suddenly drops approximately 80°C. Observed visually, the plasma “ball” seems to expand abruptly as the power is increased past this threshold. This expanding of the plasma volume seems to reduce the plasma power density over the substrate, reducing the temperature. Increasing the power input further increases the temperature, which then proceeds to follow a similar curve as the previous plasma mode. This shift in plasma mode could lead to even higher power inputs, creating higher carbon radical concentrations at reasonable growth temperatures. This shift was not observed for the

10mm seed holder because the temperature reached a maximum well before 1600W. It can be assumed that the same plasma shift may occur for susceptor configuration 2, but input powers were too low to reach this threshold.

Figure 2-18 compares the results of all three susceptor configurations. Obviously susceptor configuration 2 is undesirable due to the limitation of low power input. Configuration 1 shows a more reasonable curve, reaching growth temperatures at higher input power levels for better ionization of the gas precursors. However, this configuration has the drawback of providing poor substrate-plasma contact. Configuration 3 (5mm seed holder) provides a curve with two modes allowing for very high forward power at growth temperatures.

As a comparison, typical growth temperatures are around 1100°C. From Figure 2-18, configuration 1 reaches 1100°C at ~1500W, configuration 2 (5mm holder) reaches 1100°C at ~1100W, and due to the improved cooling to the substrate, configuration 3 (5mm holder) reaches growth temperature at ~2300W.

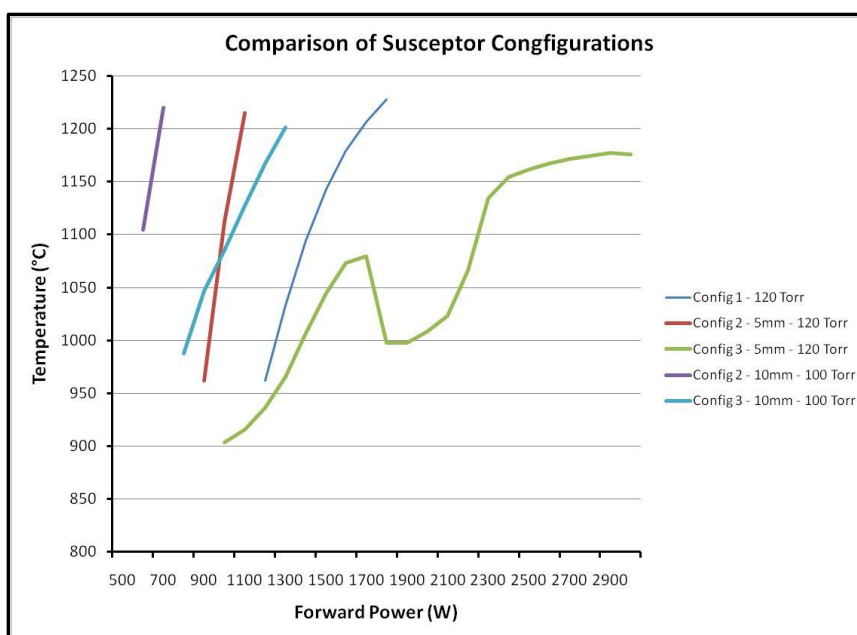


Figure 2-18: Temperature vs. Microwave power – Comparison of Susceptor Configurations.

### 2.3: Characterization

Growth rate was measured two ways. The weight change of the sample was divided by the surface area and theoretical density of diamond to determine the thickness change. The samples were weighed with an Ohaus Adventurer Pro analytical balance with readability up to 0.1 mg. Growth rate was also measured directly by determining the change in thickness with a mechanical gauge. The thickness of the samples was measured with an Ultra-Digit Mark IV digital indicator with readability up to 0.001 mm. The growth rate was then determined by averaging the results of these two methods.

To determine crystalline quality and phase, Raman microscopy was performed on the samples with a WITec CRM200 Confocal Raman microscope using a 488nm incident laser. Raman relies on inelastic scattering (Raman scattering) of monochromatic light (the 488nm laser in this case) to give information on the phonon modes of a system. For diamond, Raman gives useful information on the bonding of carbon. Both  $sp^2$  bonding for graphitic phases and  $sp^3$  bonding for the diamond phase can be observed easily with Raman spectroscopy. Impurity scattering and defect centers can also give characteristic Raman responses. The intensity and full width half maximum values can provide qualitative information on the quality of the diamond lattice and the location of the diamond peak (nominally located at 1332  $rel./cm$ ) can indicate compressive stresses (shift to the right) or tensile stresses (shift to the left) in the film based on the peaks shift from 1332  $rel./cm$  [43].

For purity analysis, select samples were sent to Evans Analytical Group (EAG) for secondary ion mass spectrometry (SIMS). SIMS is a destructive technique that relies on the sputtering of a surface by a highly focused ion beam. Sputtered atoms that are positively or negatively charged pass through a mass spectrometer which separates the ions according to their mass/charge ratio. The relative concentrations of each element can thus be measured [43]. This

technique is very useful for chemical analysis of impurity concentrations in diamond films. Concentrations of silicon, nitrogen, molybdenum, and boron were analyzed for this study. For MPCVD diamond growth, silicon is expected to be introduced through hydrogen etching of the quartz bell jar, nitrogen may be present in the source gases and become incorporated, and molybdenum may be introduced from etching of the susceptor. Boron impurity levels are of interest due to their contribution to the electrical properties of diamond as a p-type dopant. SIMS however is a very expensive characterization tool, so limited use of this technique on only select samples was employed for this thesis.

Surface morphology was characterized several ways. Optical micrographs were taken with an Olympus BX60M optical microscope to study surface features and overall morphology. Surface roughness was determined with a Wyko NT1100 optical profiler which utilized two modes: VSI for rougher samples (vertical resolution: 3nm) and PSI for very smooth samples (vertical resolution: 1Å). A VEECO Dimension 3100 atomic force microscopy (AFM) system was also used for characterization of etched samples to obtain finer resolution of surface roughness.

Optical emission spectroscopy (OES) was used to characterize the plasma chemistry in-situ during growth runs using an Avantes AvaSpec-2048 optical emission spectrometer. This technique is based off the relaxation of an electronically excited state of a molecule in a plasma. This relaxation is accompanied by the emission of a photon, giving plasmas their glow. The emitted photon's wavelength corresponds to the excited electron's energy-level drop [44]. OES is a nonintrusive *qualitative* technique for analysis of the plasma's chemical composition. This proved to be a highly beneficial technique for studying the effect of process parameters and reactor configuration on the plasma dissociation behavior. The plasma behavior and chemistry could then be correlated to growth rate, surface morphology, and suspected growth mechanisms.

## Chapter 3

### Reactor Kinetics and Geometry Considerations

Diamond growth can proceed via several different mechanisms and depends strongly on the kinetics controlled by the growth conditions. A great deal of research effort has resulted in a fundamental understanding of the effects of process parameters on the growth behavior of single crystal MPCVD diamond. Literature (summarized in Chapter 1) has shown basic dependencies of methane concentration, reactor pressure, substrate temperature, and plasma density on the growth rate and quality of CVD diamond films. While there have been many prior studies on such dependencies, this chapter focuses on single crystal growth in the Lambda MPCVD system and specifically. Here, the effect of the plasma density and precursor dissociation behavior, as it correlates to the configuration of the reactor, on the growth rate and morphology of MPCVD grown diamond films is studied.

The temperature vs. power profiles observed in the previous chapter provides valuable information on the operation and capabilities of the Lambda Technologies MPCVD reactor. It was shown that the temperature, as a function of pressure and input power, changes drastically for each susceptor configuration. It is therefore sensible to presume that the diamond growth behavior may differ considerably for each susceptor configuration as well.

To understand the influence of the geometrical design of the susceptor on the growth kinetics of single crystal (100) diamond films, growth runs were performed under a range of process conditions for all three susceptor configurations. Based on the results of this study, an understanding of the effect of susceptor geometry on growth rate, crystalline quality, and surface morphology was determined.

The following sections investigate the growth rate behavior as a function of reactor pressure and methane concentration for all three susceptor configurations. Growth rate vs. temperature was neglected as specific temperatures proved to be very hard to correlate between susceptor configurations for certain pressures.

Optical emission spectroscopy (OES) was used to characterize the plasma discharge during growth. Using OES, the dissociation behavior of carbon radicals as well as atomic hydrogen can be observed and understood. The ratio between the C<sub>2</sub> peak (related to carbon radicals) and the H $\alpha$  peak (related to atomic hydrogen) can be compared between different methane concentrations and pressures for each susceptor configuration. A better understanding of the plasma chemistry for each susceptor configuration is highly beneficial in understanding the growth behavior for a range of process conditions.

For all runs described in this chapter, 3mm x 3mm x 0.5mm (100) single crystal CVD seeds were used as substrates. These substrates were nominally on-axis ( $\pm 1^\circ$ ) and were cleaned using the standard cleaning process detailed in section 2.1. Figure 3-1 shows a 50x image of a typical substrate after cleaning.

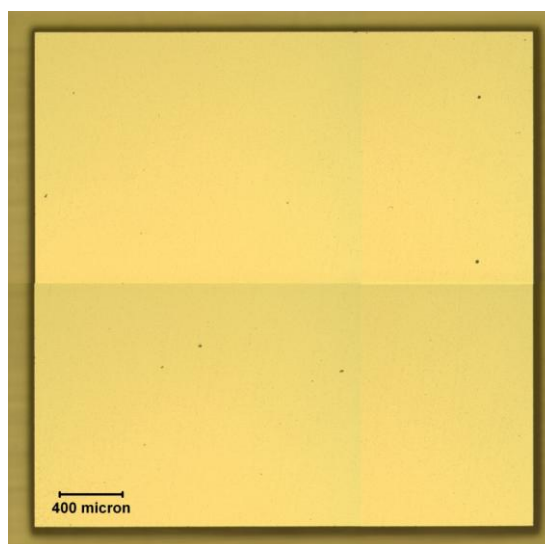


Figure 3-1: 50x Optical Micrograph of an as-received (100) on-axis CVD seed. The substrate is mirror polished and feature-less.

### 3.1: Growth Rate Study – Susceptor Configuration 1

Susceptor configuration 1, previously shown in Figure 2-2, was the as-received susceptor configuration and was designed for holding three inch silicon wafers for polycrystalline growth. Temperature vs. power profiles, detailed in section 2.3.1, show relatively high input powers at growth temperatures (i.e. – 1500W at 1100°C), however it was observed that the plasma was in poor contact with the substrate. This could lead to low growth rates due to a lower density of reactive carbon radicals and atomic hydrogen at the surface of the substrate. In addition, the plasma volume was large. This could lead to interaction and etching of the quartz bell jar walls as well as a reduced overall plasma power density.

Table 3-1: Growth Rate vs. Pressure - Conditions and Results – Configuration 1.

Sample #	Temp (°C)	Pressure (mbar/torr)	CH <sub>4</sub> (%)	Duration (hrs)	Growth Rate - weight (µm/hr)	Growth Rate – gauge (µm/hr)
MPCVD-5-CVD-14	1050	133 / 100	2	4	0.74	0.40
MPCVD-5-CVD-01	1050	160 / 120	2	4	1.09	0.95
MPCVD-5-CVD-03	1050	213 / 160	2	6	1.48	1.50

Table 3-1 shows the process parameters used for the growth rate vs. pressure study. Reactor pressures of 100 Torr, 120 Torr, and 160 Torr were used. Methane concentration was held constant at 2%. Growth temperatures were fixed at 1050°C and the growth time was 4 hours (except where specified). Growth rate is also displayed in Table 3-1 and was measured two different ways: (1) directly from a mechanical thickness gauge and (2) calculated from the theoretical density of diamond using the change in weight measured with a digital mass indicator. Tolerances and capabilities of both thickness measurement techniques are described previously in section 2.2. Figure 3-2 shows the growth rate values measured from weight and the thickness gauge vs. pressure.

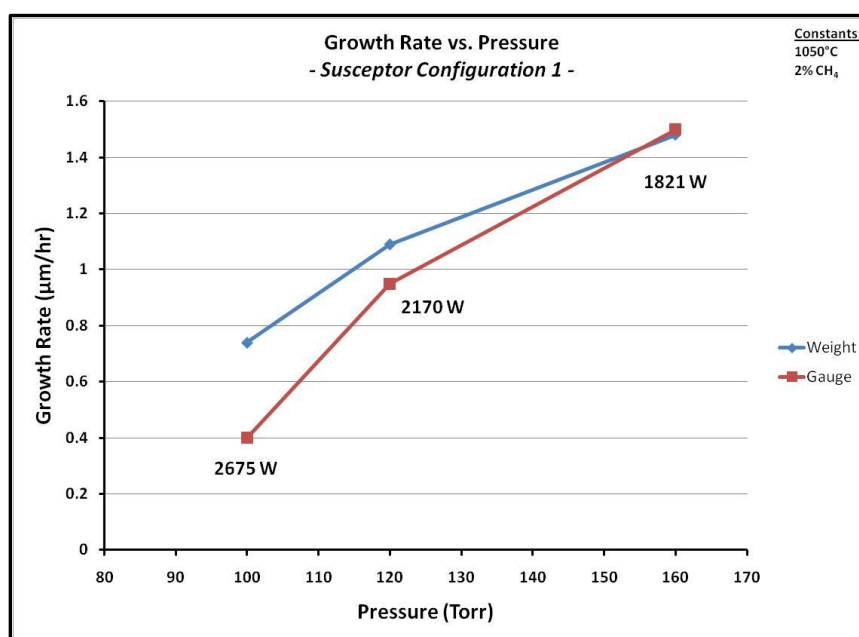
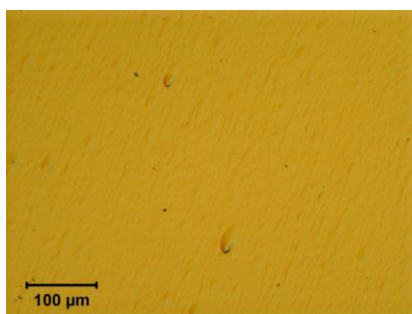
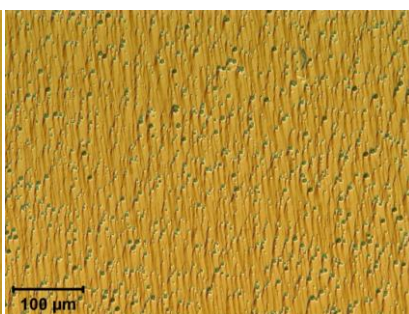


Figure 3-2: Growth Rate vs. Pressure – Configuration 1. Constants: Methane concentration: 2%, Temperature: 1050°C.

As expected, the growth rate increases with increasing pressure. These results are consistent with the trends observed in literature [30, 31]. At high pressures (>120 Torr) growth rate is expected to be enhanced significantly due to the increase of reactive carbon radical concentrations and plasma power density at the surface [30, 31, 35]. However, the growth rates are unexpectedly low and undesirable for practical application. Here, growth rates do not exceed 2 $\mu\text{m/hr}$ , which is undesirable for device fabrication, especially in the application of neutron detection where intrinsic diamond regions require thicknesses in excess of 100 $\mu\text{m}$ .

As hypothesized during the temperature vs. power study of section **2.3.1**, it seems that there is poor contact between the plasma and the substrate. The plasma may very well contain high concentrations of reactive carbon radicals and atomic hydrogen, but if those radicals are far from the substrate surface, very few will be incorporated into the film.

Figure **3-3** shows the post-growth optical images of each sample. 200x, 500x, and 1000x images were taken of the surface to determine if pressure has a significant effect on surface morphology. CVD-14 was run at 100 Torr and had an average thickness of 2.20 $\mu\text{m}$ , CVD-01 was run at 120 Torr and had an average thickness of 4.87 $\mu\text{m}$ , and CVD-03 was run at 160 Torr and had an average thickness of 8.96 $\mu\text{m}$ .

**CVD-14****100 Torr**Avg Thickness: 2.20 $\mu\text{m}$ **CVD-01****120 Torr**Avg. Thickness: 4.87 $\mu\text{m}$ **CVD-03****160 Torr**

Avg. Thickness: 8.96

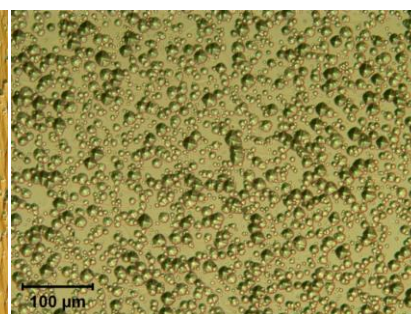
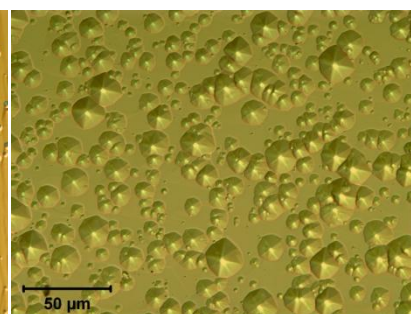
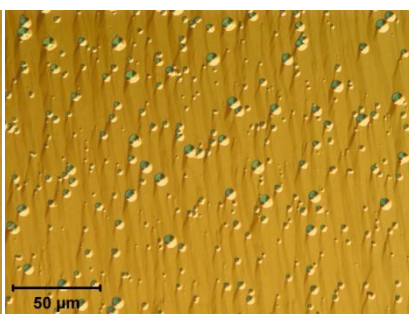
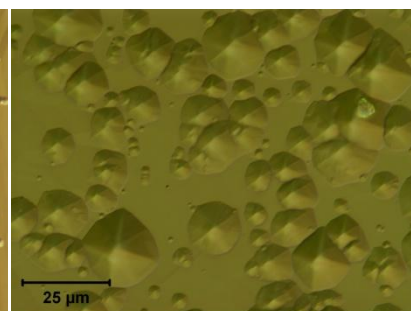
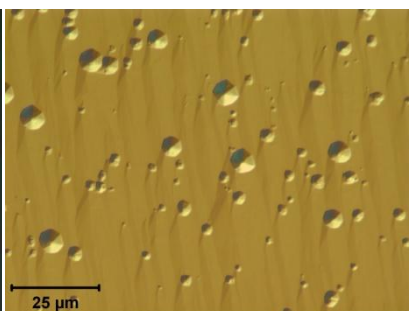
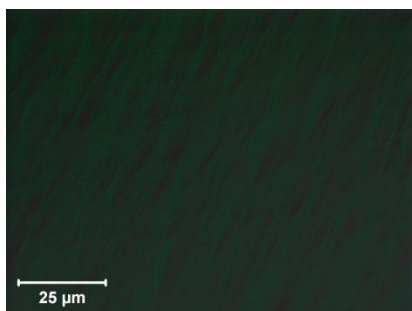
**200x Images****500x Images****1000x Images**

Figure 3-3: Optical Micrographs – Growth Rate vs. Pressure – Configuration 1. Constants: Methane concentration: 2%, Temperature: 1050°C.

Based on the optical images of the three samples, it seems at first that increasing the pressure leads to increased roughness of the surface. At 100 Torr, the film appears relatively smooth with no apparent hillocks or macroscopic features. At 120 Torr, hillocks begin to propagate out from the step-growth. At 160 Torr, hillock formation seems to dominate the surface. However, the increasing roughness cannot be correlated to pressure increases with any true accuracy. Because the films are of different thicknesses, defects such as hillocks (having locally higher growth rates) would naturally grow larger with thicker films. CVD-03 (160 Torr) was also grown for 2 hours longer than the other two samples. Consequently, growth features would have more time to develop. Therefore, it seems that no significant surface morphology degradation, or improvement for that matter, can be directly correlated to changes in growth pressure.

Table 3-2 shows the process parameters used for the growth rate vs. methane concentration study. Pressure was maintained at 120 Torr and temperature was held constant at 1050°C. Run times were 4 hours except CVD-06 which was 6 hours. Table 3-2 also shows the growth rates for each sample determined from both a mechanical thickness gauge and a mass balance scale. Figure 3-4 shows the growth rate values for each measurement technique vs. CH<sub>4</sub> concentrations.

Table 3-2: Growth Rate vs. CH<sub>4</sub> - Conditions and Results – Config 1

Run #	Temp (°C)	Pressure (mbar/torr)	CH <sub>4</sub> (%)	Duration (hrs)	Growth Rate - weight (um/hr)	Growth Rate - gauge(um/hr)
MPCVD-5-CVD-01	1050	160 / 120	2	4	1.49	0.95
MPCVD-5-CVD-36	1050	160 / 120	4	4	2.97	3.20
MPCVD-5-CVD-06	1050	160 / 120	8	6	6.82	5.43

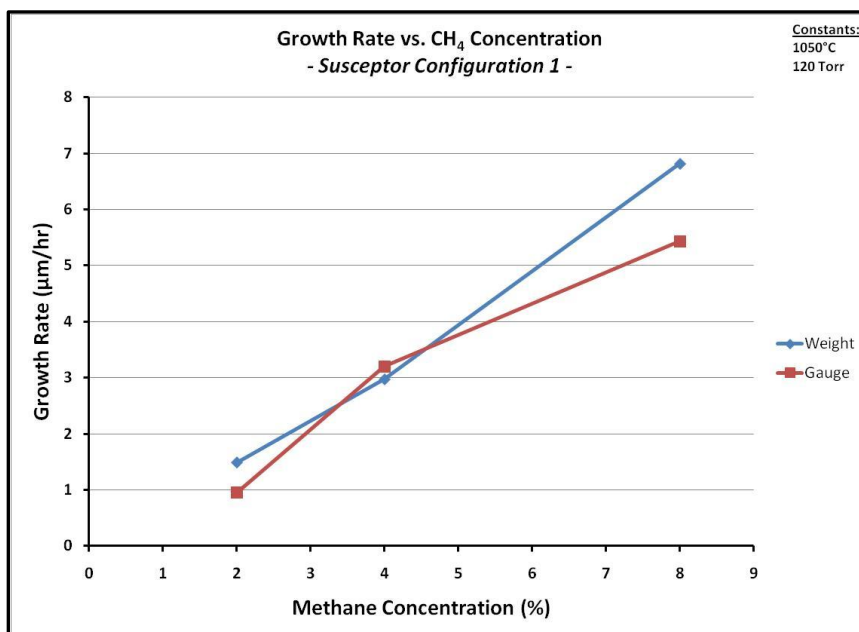
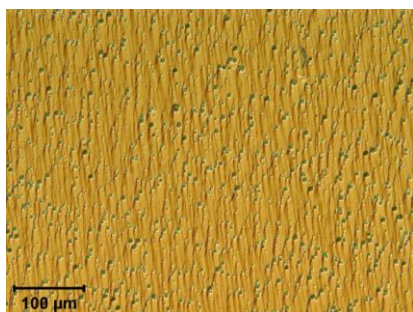
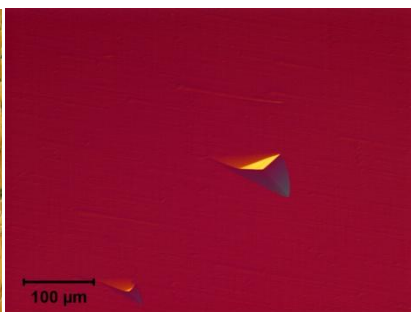
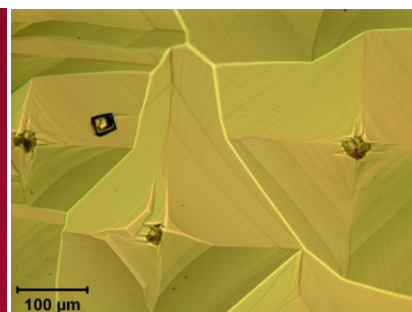
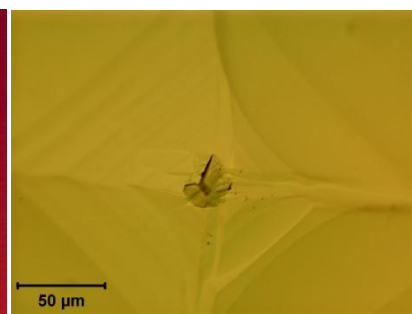
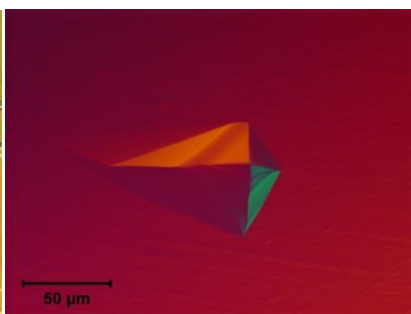
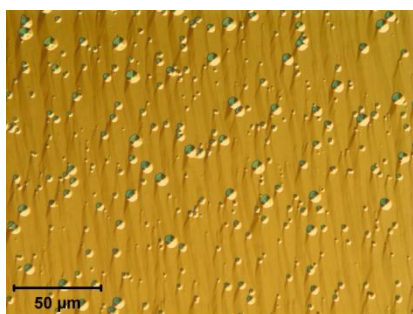
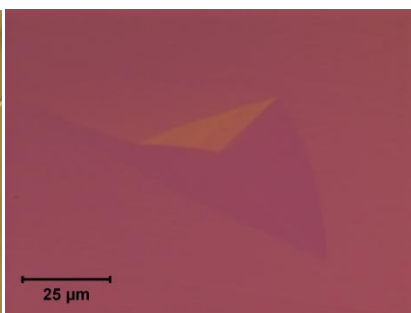
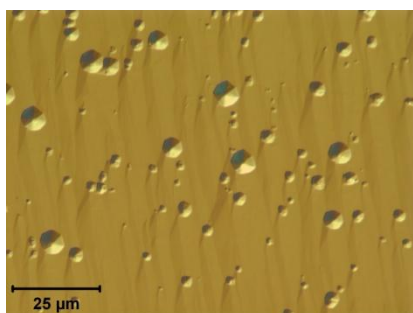


Figure 3-4: Growth Rate vs. CH<sub>4</sub> Concentration – Configuration 1. Constants: Pressure: 120 Torr, Temperature: 1050°C.

From Figure 3-4, it can be seen that an increase in methane concentration leads to an increase in growth rate, which is consistent with literature [30, 31]. A higher percent of methane in the source gas leads to a higher percent of reactive carbon radicals (such as CH<sub>3</sub>) in the plasma chemistry. This creates more carbon radicals which can contribute to growth at the surface.

Increasing the methane concentration to 8% led to growth rates higher than 6µm/hr, which is an adequate deposition rate for device fabrication. However, higher growth rates are desired.

Figure 3-5 shows the post-growth optical images of each sample. 200x, 500x, and 1000x images were taken of the surface to determine if methane concentration has a significant effect on surface morphology. CVD-01 was run at 2% CH<sub>4</sub> and had an average thickness of 4.87µm, CVD-36 was run at 4% CH<sub>4</sub> and had an average thickness of 12.34µm, and CVD-06 was run at 8% CH<sub>4</sub> and had an average thickness of 45.75µm.

**CVD-01****2% CH<sub>4</sub>**Avg Thickness: 4.87 $\mu$ m**CVD-36****4% CH<sub>4</sub>**Avg. Thickness: 12.34 $\mu$ m**CVD-06****8% CH<sub>4</sub>**Avg. Thickness: 45.75 $\mu$ m**200x Images****500x Images**

N/A

**1000x Images**

Figure 3-5: Optical Micrographs – Growth Rate vs. CH<sub>4</sub> Concentration – Configuration 1. Constants: Pressure: 120 Torr, Temperature: 1050°C.

The optical images of the surface morphology show large growth hillocks dominating at high methane concentrations. Again, this effect could be due to the differences in thicknesses between the samples. The 2% sample shows small hillocks across the surface which have not had time to develop into large pyramidal or flat topped hillocks. At 8% CH<sub>4</sub>, large hillocks completely cover the surface and coalesce with one another. For CVD-06, the surface was too rough to focus at 1000x. The smoothest surface was obtained at 4% CH<sub>4</sub>. Local areas of hillock growth can be observed, but unlike the 2% CH<sub>4</sub> run (CVD-01), hillocks do not uniformly cover the surface and are only found sparingly.

In conclusion, growth rate vs. pressure and growth rate vs. methane concentration both exhibited fundamental dependencies comparable to previous studies and literature [30, 31]. Growth rate appears to be limited by the concentration of reactive carbon radicals at the surface of the substrate. This can be controlled two different ways: (1) by directly controlling the concentration of carbon radicals in the gas phase (i.e. – increase the methane concentration), or (2) increasing the overall concentration of gas atoms in the reactor by increasing the reactor pressure. This same observation also explains why growth rates are overall lower than expected and do not correlate to studies done in other reactors (such as tube reactors at the EOC) under similar conditions. The plasma does not appear to be in contact with the substrate. The concentration of reactive carbon radicals, which was shown to limit the growth kinetics of (100) diamond, is lower at the surface than in the plasma. Therefore, growth rates are overall decreased in this geometry configuration.

### 3.2: Growth Rate Study – Susceptor Configuration 2

Susceptor configuration 2, shown previously in Figure 2-10, consists of the basic components of susceptor configuration 1 with the addition of a 0.5” diameter raised and tapered seed holder. Based on the low growth rates observed from susceptor configuration 1, this raised seed holder was designed with the goal of improving plasma contact and interaction with the substrate. In addition, the new seed holder pedestal would confine and focus the plasma to a smaller volume over the substrate. Therefore, plasma power density should be enhanced at the surface of the substrate, thus improving growth rate by increasing the concentration of reactive carbon radicals and atomic hydrogen at the diamond surface.

Table 3-3 shows the process parameters and results of the growth rate vs. pressure study carried out with susceptor configuration 2. Temperature was held constant at 1100°C, methane concentration was fixed at 4%, and growth duration was 4 hours (except CVD-09 which was 6 hours). Pressures of 80 Torr, 100 Torr, and 120 Torr were used. Temperature could not be maintained at 1100°C for pressures higher than 120 Torr due to the poor cooling observed during temperature vs. power profiling (section 2.3.2). The 5mm seed holder height was used because growth temperatures could not be maintained at high pressures when using the 10mm seed holder (see Figures 2-11 and 2-12). Growth rate vs. pressure results are plotted in Figure 3-6.

Table 3-3: Growth Rate vs. Pressure - Conditions and Results – Configuration 2.

Run #	Temp (°C)	Pressure (mbar/torr)	CH <sub>4</sub> (%)	Duration (hrs)	Growth Rate - weight (um/hr)	Growth Rate - gauge(um/hr)
MPCVD-5-CVD-15	1100	107 / 80	4	4	3.94	3.20
MPCVD-5-CVD-09	1100	133 / 100	4	6	6.51	5.37
MPCVD-5-CVD-16	1100	160 / 120	4	4	5.90	4.85

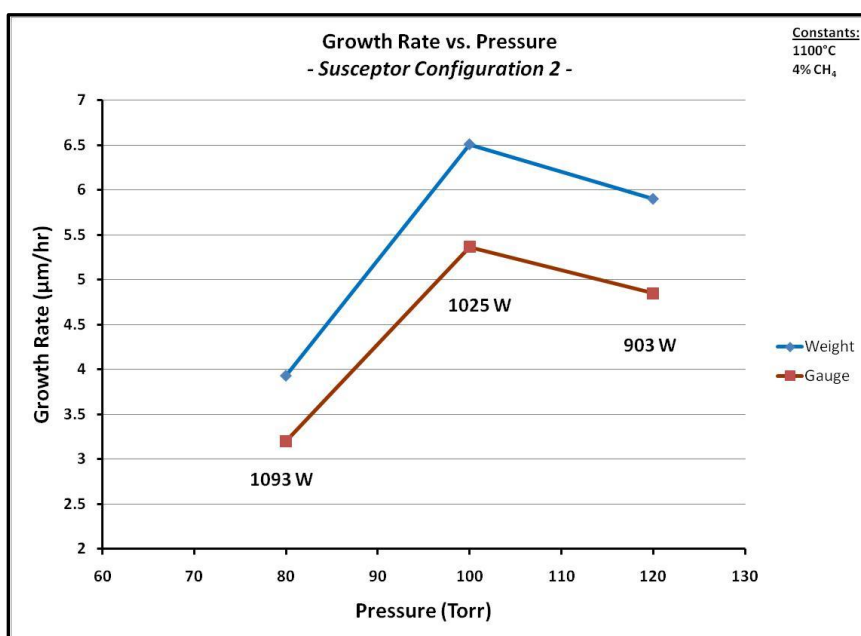


Figure 3-6: Growth Rate vs. Pressure – Configuration 2. Constants: Methane concentration: 4%, Temperature: 1100°C.

As expected, growth rates were overall improved significantly over susceptor configuration 1 due to the improved contact between the plasma and the substrate. Interestingly however, the growth rate vs. pressure results did not follow the same trend as was observed with susceptor configuration 1. From 80 Torr to 100 Torr, growth rate increased significantly. However, from 100 Torr to 120 Torr, growth rate actually decreased. This does not correlate to literature [30, 31, 35]. As pressure is increased, the total concentration of reactive carbon radicals and atomic hydrogen atoms is also increased. This being the case, it would be expected that growth rate would be enhanced at higher pressures.

One possible explanation for the decrease in growth rate at higher pressures is that the input power is not high enough to fully ionize the process gas. The average forward microwave power during each run was added to Figure 3-6 and indicates that the dissociation behavior of the plasma may be negatively affected at high pressures. However, it will be shown through optical emission spectroscopy in section 3.4, that the dissociation of gas species in the plasma is in fact *improved* at higher pressures. Therefore another mechanism must be responsible for the drop in growth rate. This will be discussed in section 3.5.2.

Figure 3-7 shows the optical images of each sample of the growth rate vs. pressure study for susceptor configuration 2. This study includes 50x compiled images of the entire sample surface as well as 200x, 500x, and 1000x images. CVD-15 was run at 80 Torr and had an average thickness of 14.27 $\mu\text{m}$ , CVD-09 was run at 100 Torr (for 6 hours instead of 4) and had an average thickness of 35.63 $\mu\text{m}$ , and CVD-16 was run at 120 Torr and had an average thickness of 21.51 $\mu\text{m}$ .

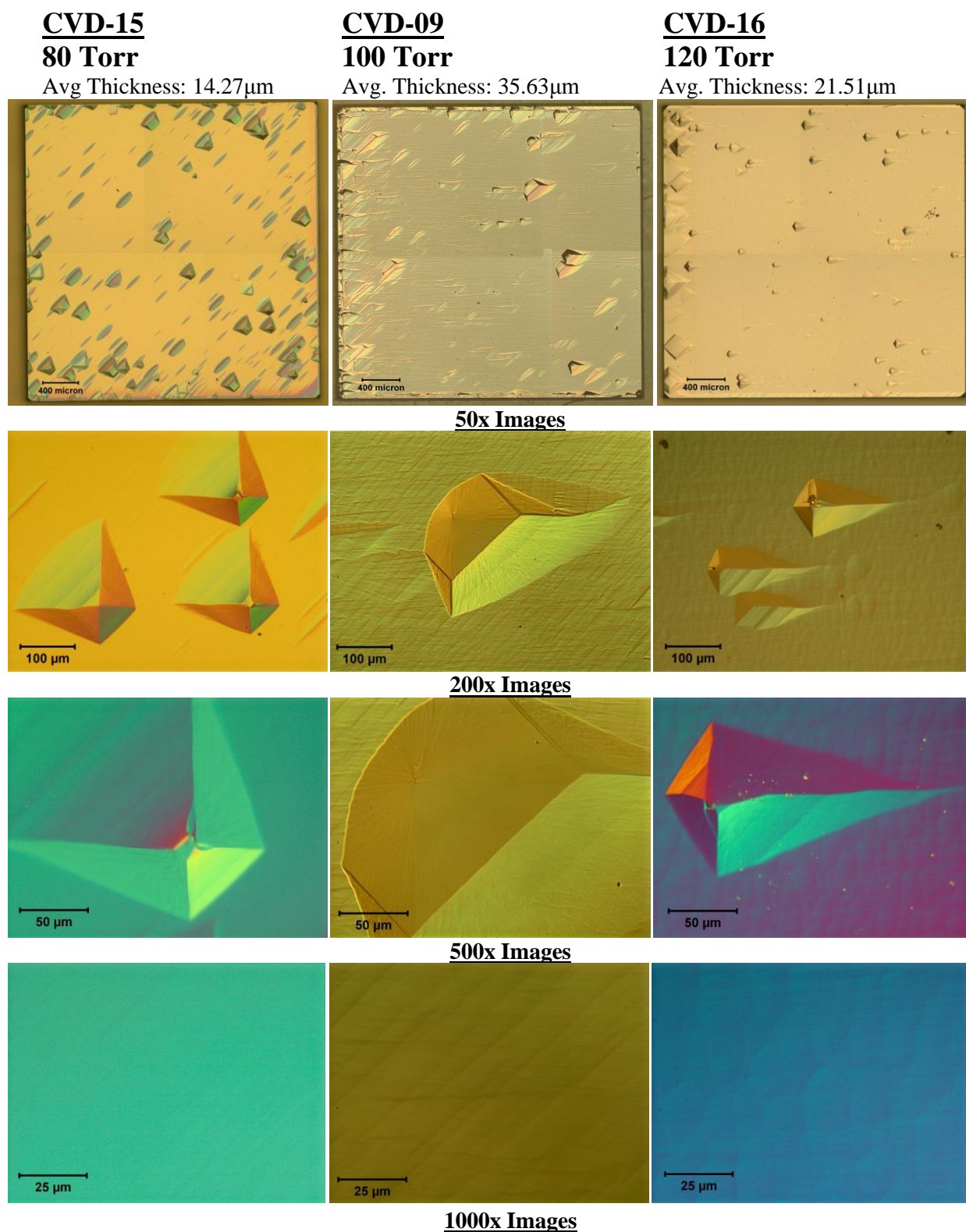


Figure 3-7: Optical Micrographs – Growth Rate vs. Pressure – Configuration 2. Constants: Methane concentration: 4%, Temperature: 1100°C.

Overall, the surface morphologies are similar from sample to sample. Growth hillocks of comparable size are spread fairly uniformly across the surface with very smooth step growth between the hillocks. It is interesting to point out that the hillocks are slightly tilted, indicating that these substrate seeds were slightly off-axis. It does appear that the density of growth hillocks seems to be higher at lower pressures. Perhaps this is due to the higher density of atomic hydrogen at the substrate surface at higher pressures. This would cause a greater degree of hydrogen etching of the surface at higher pressures and may help in suppressing hillock growth from defects.

Table 3-4 shows the process parameters and results of the growth rate vs. CH<sub>4</sub> concentration study carried out with susceptor configuration 2. Temperature was held constant at 1100°C, pressure was fixed at 100 Torr, and growth duration was 4 hours (except CVD-09 which was 6 hours). Methane concentrations of 2%, 4%, and 8% were used. The 5mm seed holder was again used for this study. Growth rate vs. CH<sub>4</sub> concentration results are plotted in Figure 3-8.

Table 3-4: Growth Rate vs. CH<sub>4</sub> - Conditions and Results – Configuration 2.

Run #	Temp (°C)	Pressure (mbar/torr)	CH <sub>4</sub> (%)	Duration (hrs)	Growth Rate - weight (um/hr)	Growth Rate - gauge(um/hr)
MPCVD-5-CVD-17	1100	133 / 100	2	4	1.40	1.55
MPCVD-5-CVD-09	1100	133 / 100	4	6	6.51	5.37
MPCVD-5-CVD-18	1100	133 / 100	8	4	11.15	9.10

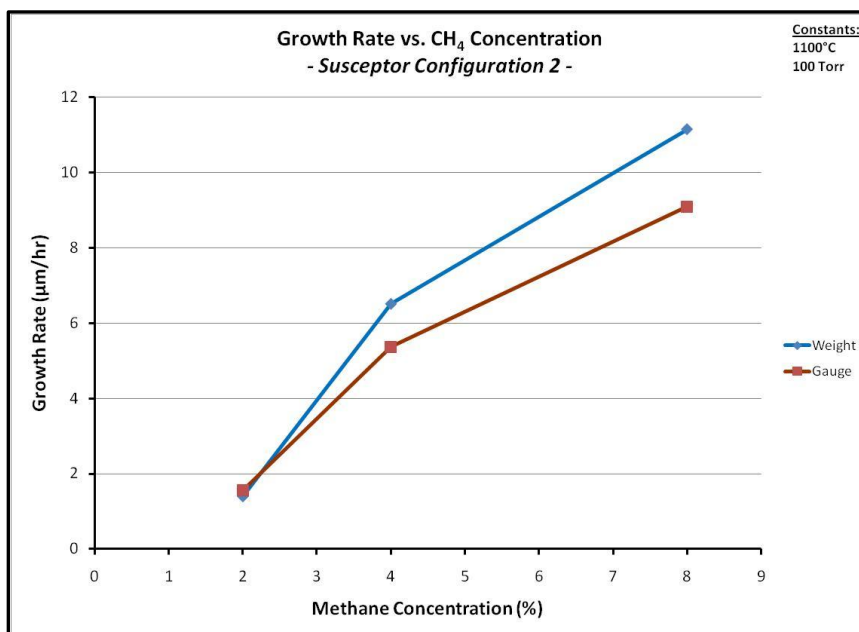


Figure 3-8: Growth Rate vs. CH<sub>4</sub> Concentration – Configuration 2. Constants: Pressure: 100 Torr, Temperature: 1100°C.

As expected, the growth rates are much higher than they were with susceptor configuration 1 due to the improved contact between the plasma and the substrate. The growth rate vs. CH<sub>4</sub> concentration curve follows a similar trend compared to susceptor configuration 1 and compares to results from literature [30, 31]. Growth rates higher than 10µm/hr are now possible with the improved geometry configuration.

Figure 3-9 shows the optical images of each sample of the growth rate vs. CH<sub>4</sub> concentration study for susceptor configuration 2. This study includes 50x compiled images of the entire sample surface as well as 200x, 500x, and 1000x images. CVD-17 was run at 2% CH<sub>4</sub> and had an average thickness of 5.89µm, CVD-09 was run at 4% CH<sub>4</sub> (for 6 hours instead of 4) and had an average thickness of 35.63µm, and CVD-18 was run at 8% CH<sub>4</sub> and had an average thickness of 40.50µm.

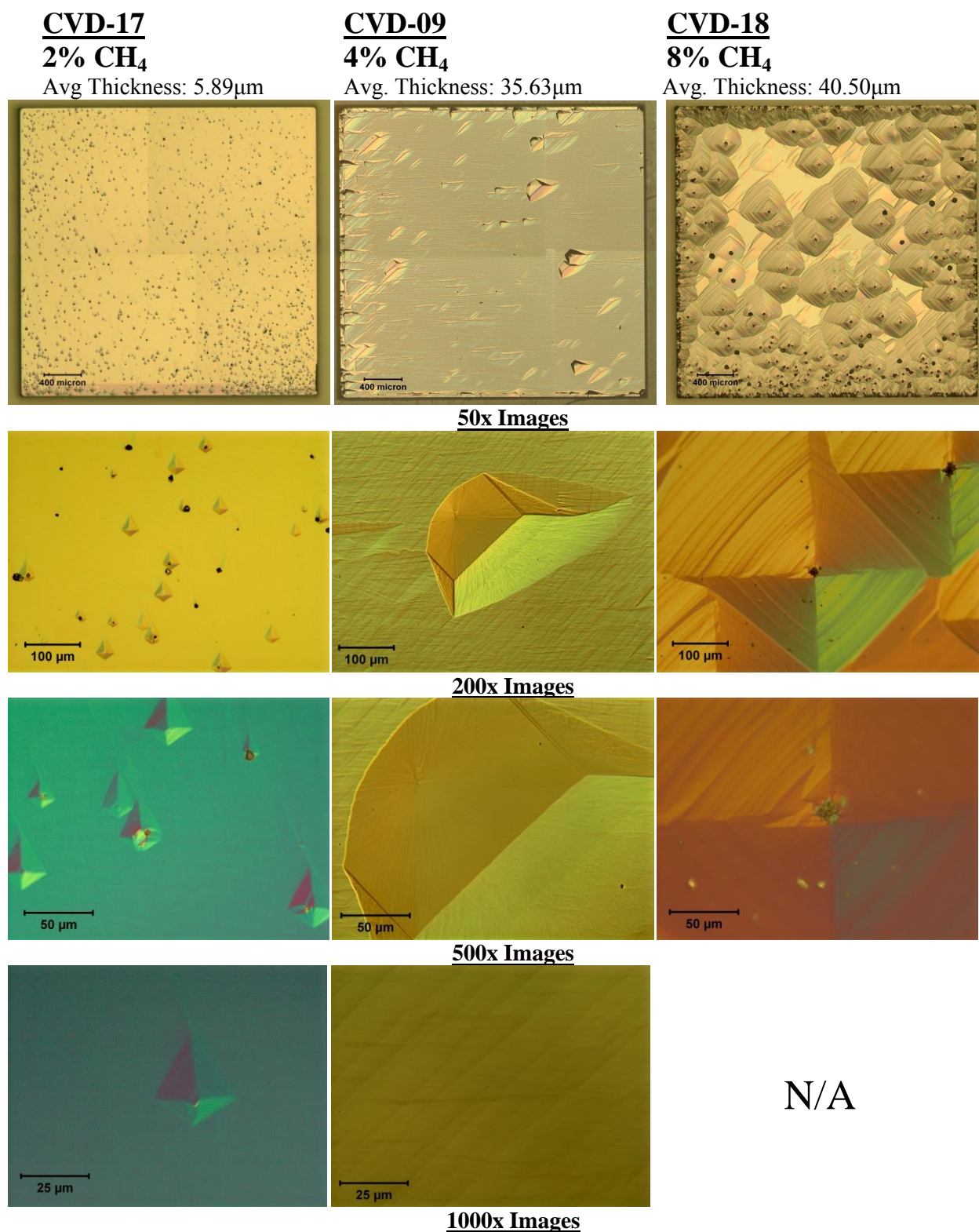


Figure 3-9: Optical Micrographs – Growth Rate vs. CH<sub>4</sub> Concentration – Configuration 2.  
Constants: Pressure: 100 Torr, Temperature: 1100°C.

At lower methane concentrations (2% and 4%), growth hillocks are randomly scattered across the surface with smooth step growth between the hillocks. At high methane concentration (8%), hillock growth seems to dominate. These results are very similar to the results observed for susceptor configuration 1. The increase in methane concentration seems to increase the size and density of growth hillocks. In this case, the disparity in film thickness between the 4% sample and 8% sample is low because CVD-09 (4%) was grown for 6 hours instead of 4. Therefore, the difference in thickness cannot be blamed for the extreme difference in morphology.

Large methane concentrations seems to over-power hydrogen etching, leading to very high growth rates, but producing films with large hillocks. As explained in section 1.3, C-C bonding at dislocation sites is much weaker than on a defect-free diamond surface lattice [23]. Therefore, hydrogen can easily etch away carbon incorporation at these sites, especially at low methane concentrations where hydrogen would have more time before other carbon radicals arrive to the site. It seems that at high methane concentrations, carbon atoms attaching readily to defects (such as dislocations) are buried immediately by newly incoming carbon atoms. Consequently, this leaves little time for hydrogen to etch away carbon incorporation at these sites, leading to a high density of large growth hillocks.

Adding a raised and tapered substrate holder to the existing susceptor configuration successfully brought the substrate into better contact with the plasma and led to significantly improved growth rates. However, it seems that the plasma power density is lower than anticipated due to the low microwave input powers required to maintain growth temperatures. This limitation seems to restrict growth at high pressures and high methane concentrations. If the cooling to the substrate can be improved, the forward microwave power (and accordingly, the plasma power density) could be considerably higher. This could lead to improved contributions from atomic hydrogen and reactive carbon radicals on the growth of (100) diamond films. Higher densities of atomic hydrogen could improve etching from dislocation sites at high methane concentrations and

improve hillock suppression. Also, higher carbon radical concentrations could improve growth rates.

### **3.3: Growth Rate Study – Susceptor Configuration 3**

Susceptor configuration 3, previously shown in Figure 2-13, was designed in an attempt to improve cooling to the substrate. This was accomplished by removing as much material between the stainless steel cooling stage and the diamond seed as possible, thereby reducing thermal resistance to the substrate. The as-received susceptor base plate and three inch wafer holder were removed and replaced with a single molybdenum base plate with a ½” diameter cut out for insertion of the ½” diameter tapered seed holder. Schematics of the redesigned base plate and ½” seed holders can be found in Appendix B.

Temperature vs. power profiles (detailed in section 2.3.3) show a significant improvement over the first two susceptor configurations in terms of microwave power input at growth temperature. This should lead to enhanced plasma power densities over the substrate and thus, improved dissociation of process gases (i.e. – hydrogen and methane).

Table 3-5 shows the process parameters and results of the growth rate vs. pressure study carried out with susceptor configuration 3. Temperature was held constant at 1100°C, methane concentration was fixed at 4%, and growth duration was 4 hours. Pressures of 100 Torr, 120 Torr, and 140 Torr were used. Based off of temperature vs. power profiles, the 5mm seed holder height was used because of the shift in plasma mode; allowing for very high microwave power inputs (see Figure 2-14). Growth rate vs. pressure results are plotted in Figure 3-10.

Table 3-5: Growth Rate vs. Pressure - Conditions and Results – Configuration 3.

Run #	Temp (°C)	Pressure (mbar/torr)	CH <sub>4</sub> (%)	Duration (hrs)	Growth Rate - weight (um/hr)	Growth Rate - gauge(um/hr)
MPCVD-5-CVD-35	1100	133 / 100	4	4	5.20	3.90
MPCVD-5-CVD-28	1100	160 / 120	4	4	6.90	7.20
MPCVD-5-CVD-34	1100	186 / 140	4	4	5.20	5.05

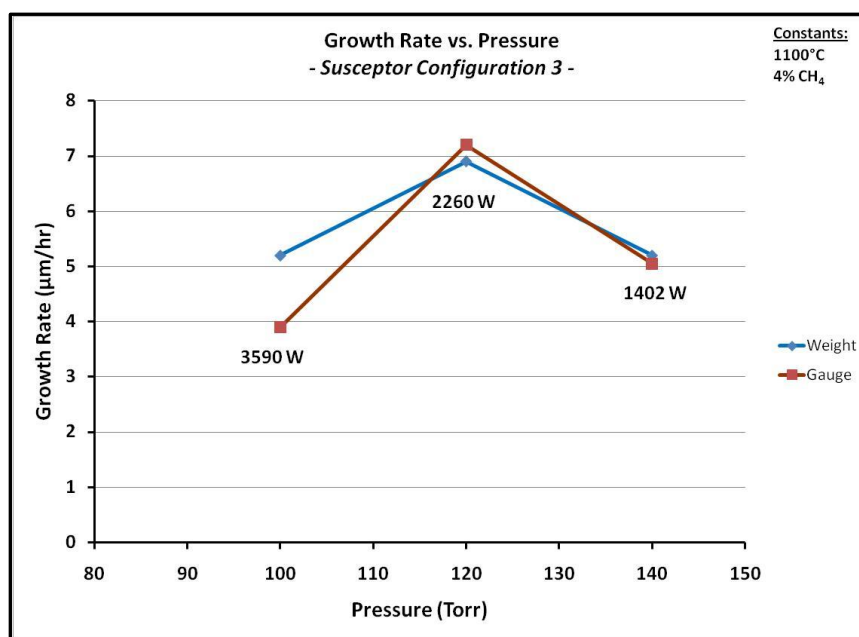


Figure 3-10: Growth Rate vs. Pressure – Configuration 3. Constants: Methane concentration: 4%, Temperature: 1100°C.

As expected, growth rates were improved overall with the higher microwave power input possible with susceptor configuration 3. As with susceptor configuration 2, at high pressures the growth rate decreases. The mechanisms for this will be discussed in detail in section **3.5.2**. Average forward microwave powers were added to the plot to show how the input power must be decreased to maintain growth temperature as pressure is increased. The peak growth pressure possible with susceptor configuration 3 was increased compared to susceptor configuration 2 (from 100 Torr to 120 Torr). A higher pressure regime could lead to higher growth rates and plasma power densities since the growth is no longer limited by microwave power input at 120 Torr.

Figure **3-11** shows the optical images of each sample for the growth rate vs. pressure study for susceptor configuration 3. This study includes 50x compiled images of the entire sample surface as well as 200x, 500x, and 1000x images. CVD-35 was run at 100 Torr and had an average thickness of 18.20 $\mu\text{m}$ , CVD-28 was run at 120 Torr and had an average thickness of 28.20 $\mu\text{m}$ , and CVD-34 was run at 140 Torr and had an average thickness of 20.50 $\mu\text{m}$ .

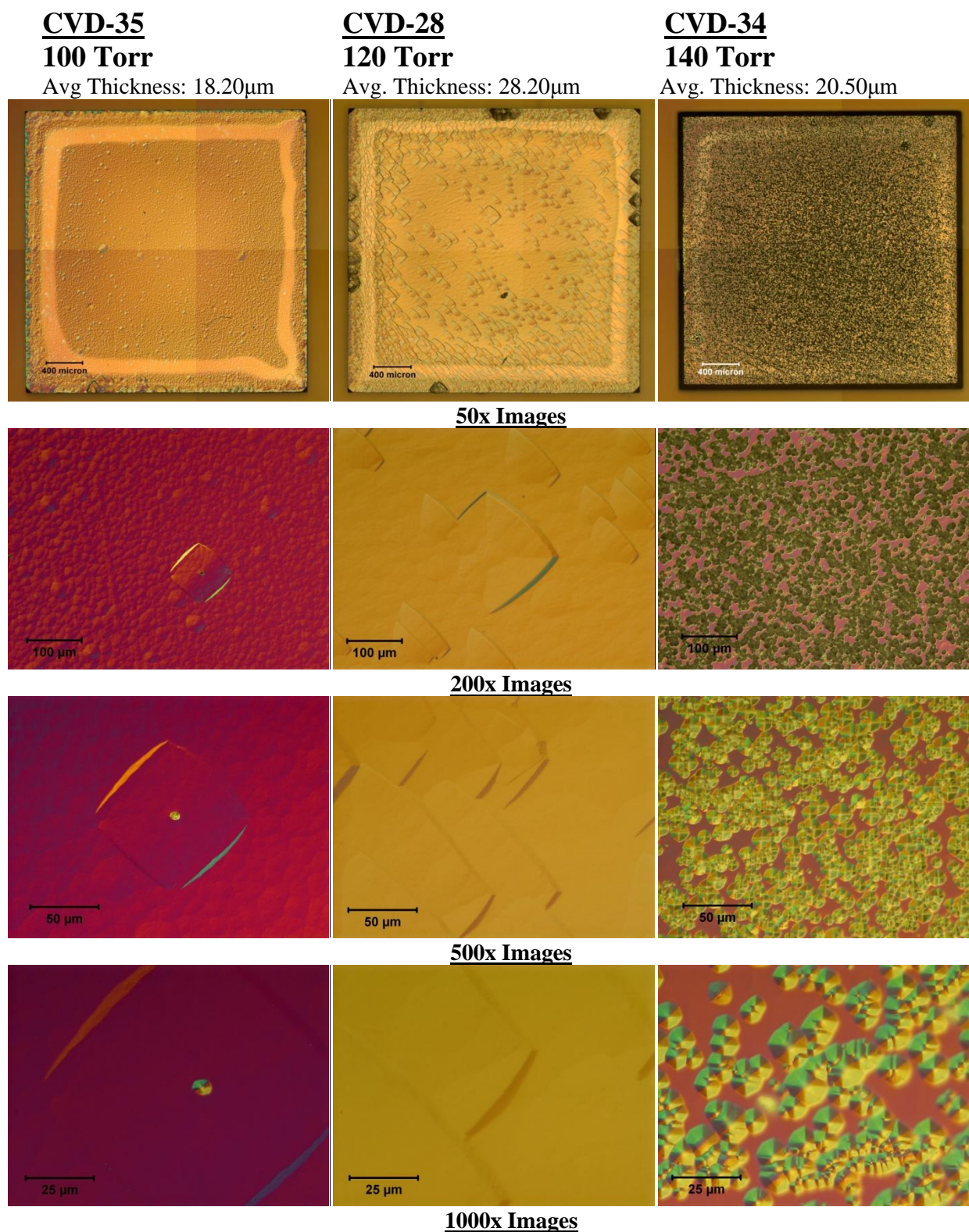


Figure 3-11: Optical Micrographs – Growth Rate vs. Pressure – Configuration 3. Constants:  
Methane concentration: 4%, Temperature: 1100°C.

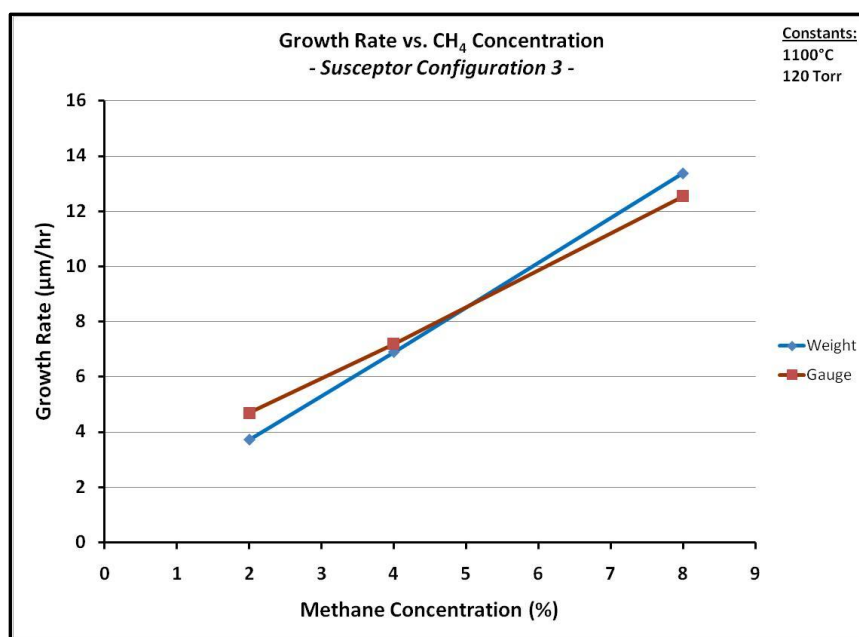
For CVD-35 and CVD-28 (100 Torr and 120 Torr, respectively), island formation dominates and local areas of hillock formation is observed. The density of hillocks increases significantly from 100 Torr to 120 Torr. This could partially be due to the higher growth rate at 120 Torr, giving hillocks the opportunity to develop at a faster rate. Also, the higher pressure would present higher concentrations of carbon radicals at the surface increasing the probability that carbon radicals will run into each other before reaching a crystallographic step. Therefore, hillocks are more likely to develop from coalescing islands at higher pressures than at lower pressures.

At 140 Torr (CVD-34) the growth morphology is much different than the previous two samples. At first glance, it appears that small hillocks have formed over the entire surface. However, upon closer inspection, these features were discovered to be etch pits rather than hillocks. This was confirmed with Wyko surface profilometry. Because susceptor configuration 3 utilizes enhanced cooling to the substrate, very high input powers are possible. These high input powers led to increased growth rates and are usually beneficial due to the enhanced dissociation of the process gases. However, under certain conditions, the very high plasma density may negatively affect the growth morphology. At this high of a pressure, a higher concentration of atomic hydrogen would be at the surface of the diamond sample. It is obvious that the methane concentration was not high enough to fully accommodate the aggressive hydrogen abstraction reactions occurring on the surface. Therefore, hydrogen etching was taking place in some areas at a higher rate than carbon incorporation; decreasing growth rate and forming etch pits.

Table **3-6** shows the process parameters and results of the growth rate vs.  $\text{CH}_4$  concentration study carried out with susceptor configuration 3. Temperature was held constant at  $1100^\circ\text{C}$ , pressure was fixed at 120 Torr, and growth duration was 4 hours. Methane concentrations of 2%, 4%, and 8% were used. The 5mm seed holder was again used for this study. Growth rate vs.  $\text{CH}_4$  concentration results are plotted in Figure **3-12**.

Table 3-6: Growth Rate vs. CH<sub>4</sub> - Conditions and Results – Configuration 3.

Run #	Temp (°C)	Pressure (mbar/torr)	CH <sub>4</sub> (%)	Duration (hrs)	Growth Rate - weight (um/hr)	Growth Rate - gauge(um/hr)
MPCVD-5-CVD-33	1100	160 / 120	2	4	3.72	4.70
MPCVD-5-CVD-28	1100	160 / 120	4	4	6.90	7.20
MPCVD-5-CVD-29	1100	160 / 120	8	4	13.38	12.55

Figure 3-12: Growth Rate vs. CH<sub>4</sub> Concentration – Configuration 3. Constants: Pressure: 120 Torr, Temperature: 1100°C.

Growth rates are further increased over susceptor configuration 1 and 2 due to the combination of improved plasma-substrate contact and improved plasma power density at the substrate surface. The growth rate vs. CH<sub>4</sub> concentration curve follows a similar trend compared to susceptor configuration 1 and 2 and compares to results from literature [30, 31]. Growth rates around 13μm/hr are now possible with the improved geometry configuration.

Figure **3-13** shows the optical images of each sample of the growth rate vs. CH<sub>4</sub> concentration study for susceptor configuration 3. This study includes 50x compiled images of the entire sample surface as well as 200x, 500x, and 1000x images. CVD-33 was run at 2% CH<sub>4</sub> and had an average thickness of 16.84μm, CVD-28 was run at 4% CH<sub>4</sub> and had an average thickness of 28.20μm, and CVD-29 was run at 8% CH<sub>4</sub> and had an average thickness of 51.86μm.

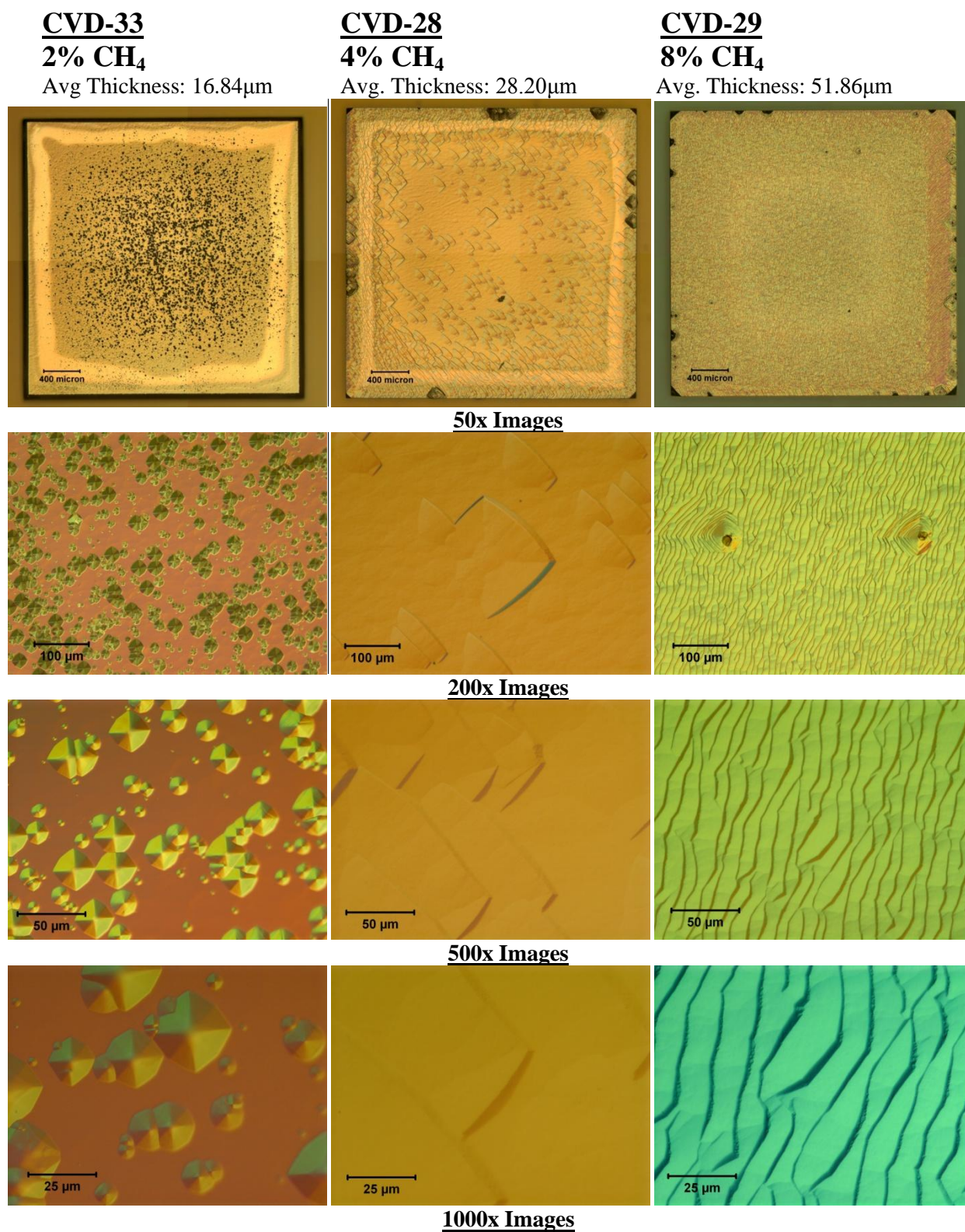


Figure 3-13: Optical Micrographs – Growth Rate vs. CH<sub>4</sub> Concentration – Configuration 3.  
 Constants: Pressure: 120 Torr, Temperature: 1100°C.

CVD-33 (2% CH<sub>4</sub>) shows a similar surface morphology as CVD-34 from the pressure study. Once again, close inspection and Wyko surface profilometry revealed that the small surface features were etch pits rather than growth hillocks. This is obvious on this sample because the features are of considerably different sizes. Growth hillocks, nucleating during the initial stages of growth, are always very similar in size. The mechanism for the formation of etch pits in this case is similar to the mechanism discussed previously for CVD-34 (grown at 140 Torr). The high plasma density creates very high concentrations of atomic hydrogen at the surface, promoting a high density of hydrogen abstraction reactions. Because the methane concentration is low (2% in this case), the concentration of carbon radicals on the surface isn't high enough to fully accommodate the abstraction reaction rate. Therefore, hydrogen etching will occur, leading to lower growth rates and the formation of etch pits.

Interestingly, at high methane concentrations (8%) step-growth almost completely dominates. This growth morphology has not been observed for nominally on-axis substrates with any of the previous susceptor configurations. For susceptor configurations 1 and 2; high methane concentrations led to high densities of large hillocks dominating the entire surface.

It is evident that high methane concentrations are preferred for susceptor configuration 3 due to the improved plasma density that is possible. Obviously the concentration of atomic hydrogen at the surface plays an important role in the growth mode. The high hydrogen abstraction reaction rate and high carbon incorporation rate on crystallographic lattice edges could lead to growth rates of lattice steps being higher than those of the defect-nucleated hillocks. This would lead to the step-flow morphology propagating faster in the [110] direction than the hillocks in the [100] direction, causing dislocations to be covered by the step-flow. The mechanisms for this shift in growth mode and stark contrast in surface morphology to samples grown under the same conditions with the other two susceptor configurations will be explained in greater detail in section **3.5.3**.

### 3.4: Optical Emission Spectroscopy Comparison

Dissociation of hydrogen and methane into atomic hydrogen, methyl radicals, and free electrons by microwave energy is the basis for MPCVD diamond growth. Based on the observed results in previous sections, it seems that the behavior of the plasma (plasma density, dissociation rate) may have a pronounced effect on the nucleation, growth behavior, and growth rate of homoepitaxial diamond films.

In plasmas, when a high-energy electron collides with a molecule, the inelastic collision results in the excitation of an electron in the target molecule. A molecule in an excited state will then undergo one of several processes. If the incident electron does not have enough kinetic energy to break bonds, the electron will relax back toward the ground state. If the energy of the incoming electron is high, then either dissociation or ionization will occur [44]. Relaxation of an electronically excited state is accompanied by the emission of a photon, giving plasmas their glow. The emitted photon's wavelength corresponds to the excited electron's energy-level drop via Equation 3-1, where  $\nu$  is the frequency,  $c$  is the speed of light, and  $h$  is the Planck constant. Therefore, each molecule or atom in the plasma gives off a characteristic emission line that can provide insight into the ionization behavior and chemical composition of the plasma [44].

$$E(eV) = h\nu = \frac{hc}{\lambda(\mu m)} = \frac{1.24}{\lambda(\mu m)}$$

Equation 3-1: Energy of a photon as it relates to frequency and wavelength [44]

Optical Emission Spectroscopy (OES) is a nonintrusive *qualitative* technique for analysis of the plasma's chemical composition. The intensity of each emission spectrum is dependent on the overall concentration of each species in the plasma. Therefore, Optical Emission

Spectroscopy can provide a good idea of the relative concentrations of specific gas species contained in the plasma. Though quantitative analysis of molecular concentrations cannot be obtained from this technique, the chemistry and behavior of the plasma can be better understood by looking at the ratios of specific ions or species.

Two peaks in particular seem to dominate the plasma associated with MPCVD diamond growth: the C2 peak and the H $\alpha$  peak. These peaks relate to CH<sub>3</sub> radicals and atomic hydrogen, respectively. Observing the behavior of these two peaks (specifically the C2/H $\alpha$  ratios) may lead to a better understanding of the ionization behavior of the plasma as related to pressure, methane concentration, and geometrical configuration.

Figures 3-14, 3-15, and 3-16 show the OES spectra for all three susceptor configurations as a function of pressure. Relevant peaks for carbon and hydrogen species are labeled.

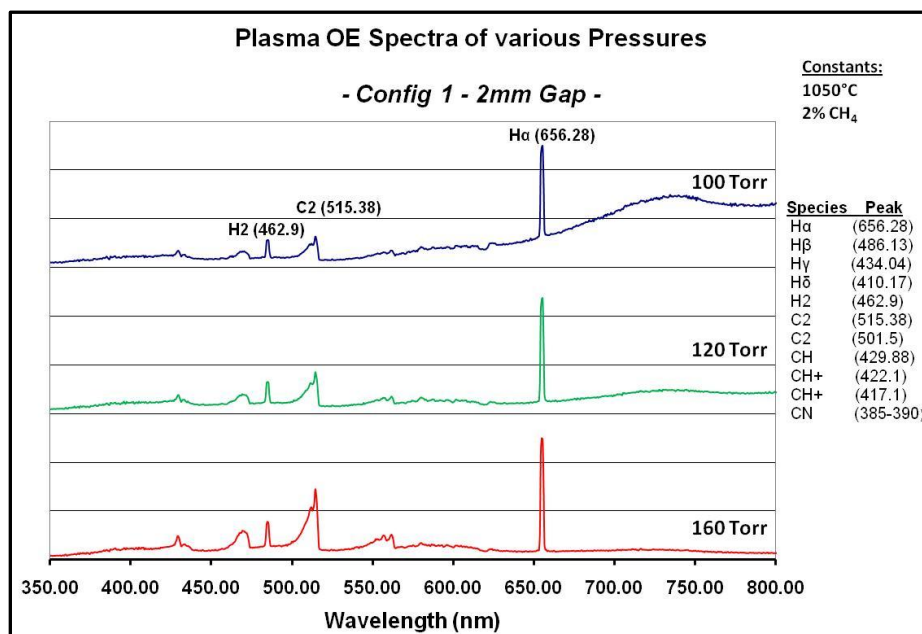


Figure 3-14: OES Spectra for Various Pressures – Configuration 1. Constants: Methane concentration: 2%, Temperature: 1050°C.

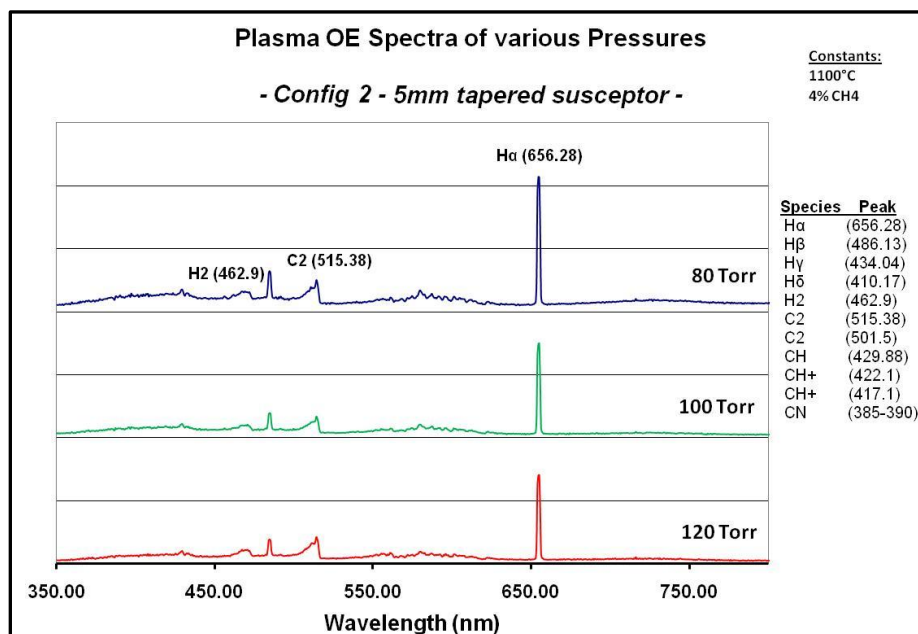


Figure 3-15: OES Spectra for Various Pressures – Configuration 2. Constants: Methane concentration: 4%, Temperature: 1100°C.

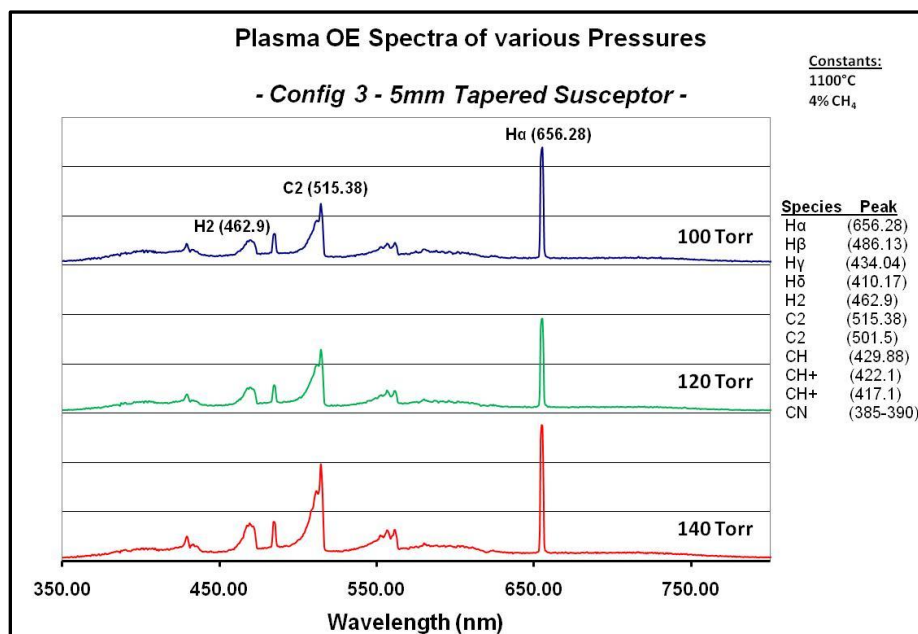


Figure 3-16: OES Spectra for Various Pressures – Configuration 3. Constants: Methane concentration: 4%, Temperature: 1100°C.

As pressure is increased, the C2/H $\alpha$  ratios increase as well. This seems to be related to a combination of two aspects. First, the total density of ions, chemical species, and electrons in the plasma would be increased with increased pressure. Therefore, a higher concentration of methane molecules would be present to be ionized at higher pressure. Second, the plasma power density is enhanced with increasing pressure due to the confinement and shrinkage of the plasma volume. Therefore, microwave energy is coupled into a smaller volume, enhancing the ionization of gas species locally. The enhanced plasma density and high gas concentrations ionize the input methane gas into CH<sub>3</sub> carbon radicals more readily, thus increasing the C2/H $\alpha$  ratios. The increased C2/H $\alpha$  ratios would indicate that the growth rate should increase with increasing pressure. However, it was observed in Figures 3-6 and 3-10 that the growth rates declined at high pressures. An explanation to the mechanisms that affect growth rate is given in section 3.5.2.

Figures 3-17, 3-18, and 3-19 show the OES spectra for all three susceptor configurations as a function of methane concentration. Relevant peaks for carbon and hydrogen species are labeled.

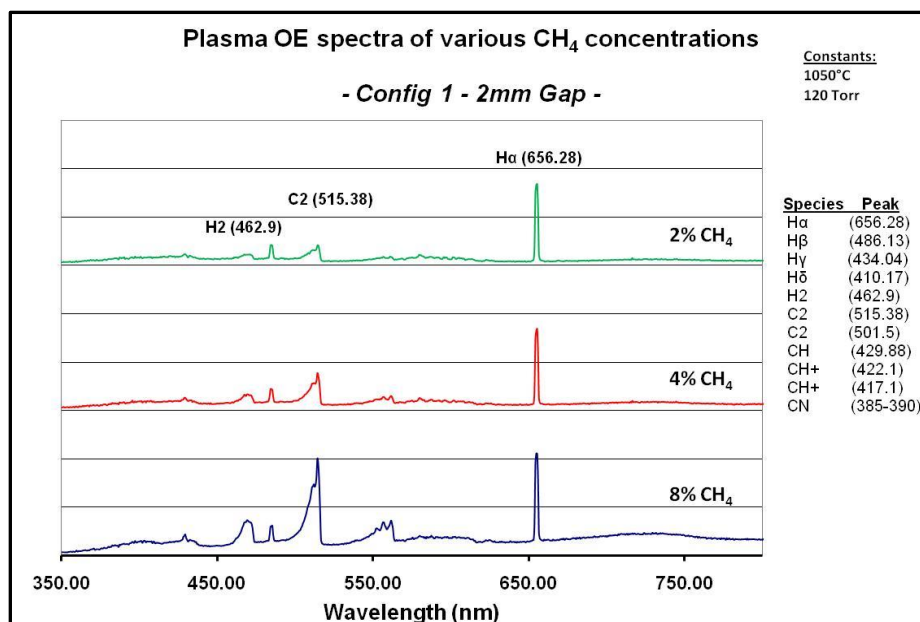


Figure 3-17: OES Spectra for Various CH<sub>4</sub> Concentrations – Configuration 1. Constants: Pressure: 120 Torr, Temperature: 1050°C.

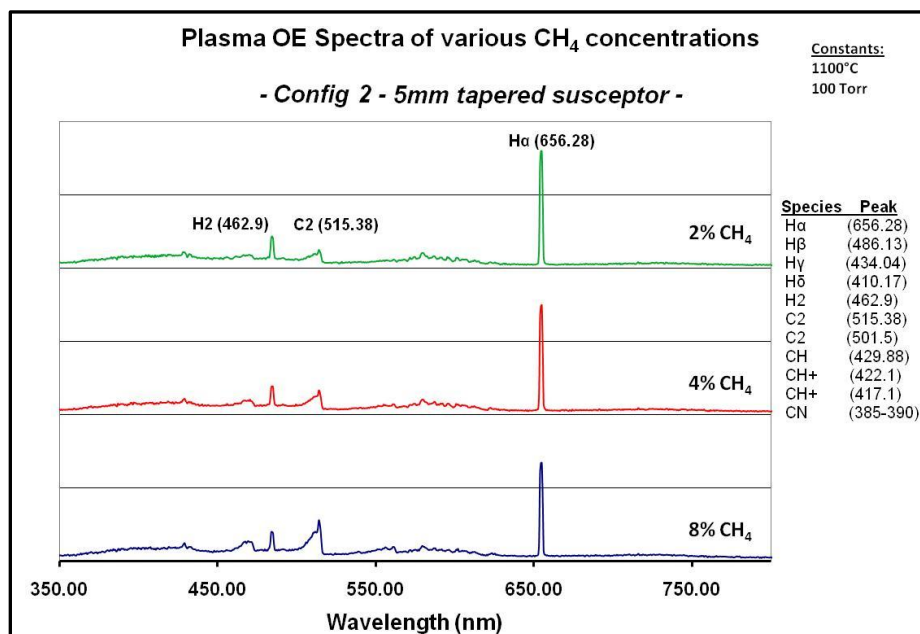


Figure 3-18: OES Spectra for Various CH<sub>4</sub> Concentrations – Configuration 2. Constants: Pressure: 100 Torr, Temperature: 1100°C.

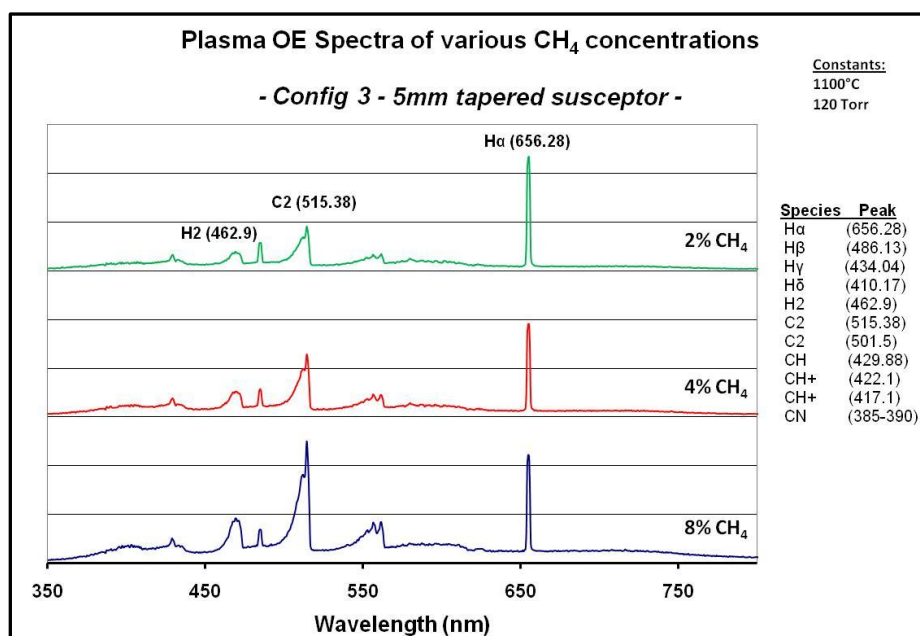


Figure 3-19: OES Spectra for Various CH<sub>4</sub> Concentrations – Configuration 3. Constants: Pressure: 120 Torr, Temperature: 1100°C.

As expected, an increase in methane concentration leads to an increase in  $C2/H\alpha$  ratio. This is similar to the case of pressure where an increase in total concentration of methane molecules in the gas phase results in an overall increase in carbon radicals in the plasma.

Configurations 1 and 3, both using high input microwave power, show large C2 peaks compared to configuration 2 where low microwave powers were used. It is therefore apparent that for configuration 2, only a small fraction of the methane present in the gas phase is being ionized due to the low input powers. On the other hand, the high input powers used in configurations 1 and 3 allow a higher percent of the methane to become ionized.

Figures 3-20 and 3-21 show the  $C2/H\alpha$  ratios vs. pressure and methane concentration, respectively. All three susceptor configurations are compared to show the degree of methane ionization and thus, the concentration of active carbon radicals.

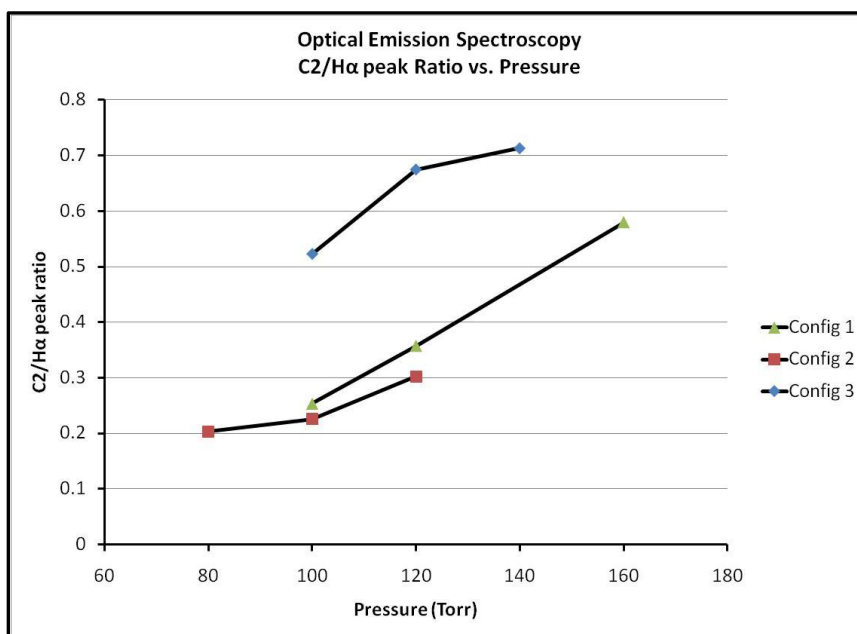


Figure 3-20:  $C2/H\alpha$  Peak Ratios vs. Pressure for all three susceptor configurations.

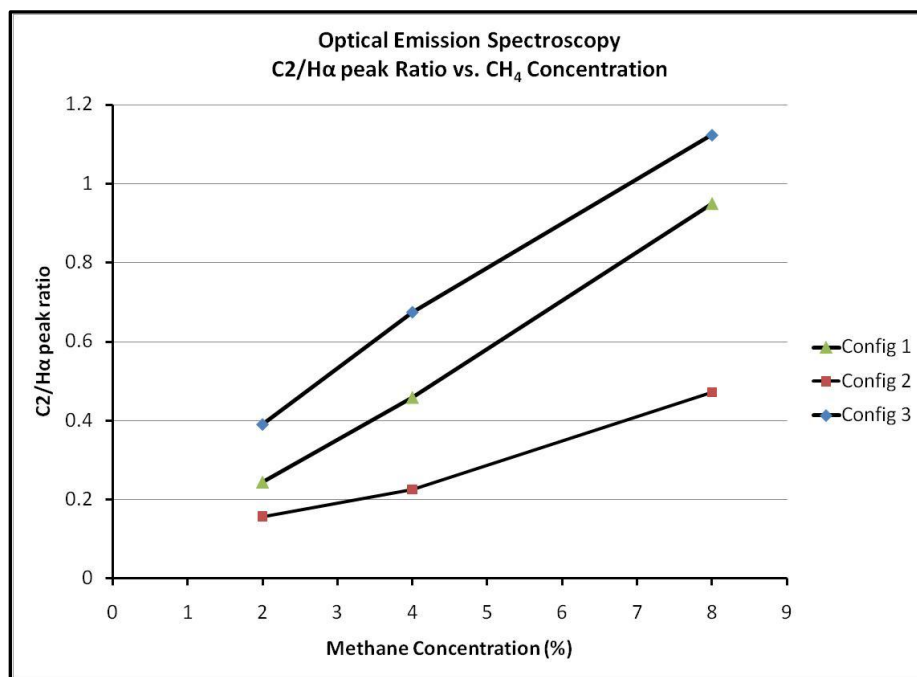


Figure 3-21: C2/H $\alpha$  Peak Ratios vs. CH $_4$  Concentration for all three susceptor configurations.

From Figures 3-20 and 3-21, the effect of susceptor configuration on the behavior of the plasma chemistry can be clearly observed. Configuration 1, being designed for a 3" wafer, allows for very high microwave input powers. Therefore, ionization of carbon radicals is high throughout the pressure range. As observed in section 3.1 however, growth rates were very low due to poor substrate-plasma interaction. Though it seems that this geometry configuration produces a plasma discharge with sufficient ionization behavior, this characteristic cannot be utilized to its full potential as the bulk of the active species are far from the substrate surface.

The raised and tapered geometry of susceptor configuration 2 successfully confined the plasma to a smaller volume. This allowed for good substrate-plasma interaction. However, because cooling to the substrate was so poor, the input microwave power had to be kept very low

(<1kW) in order to maintain growth temperature (1100°C), resulting in poor dissociation behavior and a low plasma density

Utilizing a cut-out design for substrate cooling, growth rate is enhanced significantly with susceptor configuration 3 (as shown in section 3.3) thanks to the combination of excellent substrate-plasma contact and high C<sub>2</sub>/H<sub>α</sub> dissociation. Improved cooling to the substrate has allowed for increased microwave power input and thus enhanced plasma density (and therefore reactive gas species) over the substrate.

### 3.5: Summary of Results

#### 3.5.1: Kinetic Explanation of Susceptor Geometry Effects

The results from the previous sections show that the geometrical configuration of the susceptor alters the coupling behavior of the microwave power into the plasma, and thus the growth rate and surface morphology are affected.

In the previous sections (3.1-3.4), observations for each scenario have attempted to explain the behavior of the plasma as it pertains to growth kinetics. A more detailed physical explanation of the plasma kinetics needs to be addressed. Equations 3-2 and 3-3 show the dependence of microwave input power on the plasma density, P(W), and the dissociation rate, R, of molecules within the plasma, respectively [44].

$$P(W) = j_+ A \varepsilon_L = n_e q_e u_a A$$

Equation 3-2: Plasma Input Power [44]

For Equation **3-2**,  $j_+$  is the ion flux into the plasma sheath ( $A/cm^2$ ),  $A$  is the effective area of plasma contact with its container ( $cm^2$ ),  $\epsilon_L$  is the total energy dissipated in the plasma per ion injected into the sheath (eV),  $n_e$  is the plasma power density (or the density of free electrons) ( $e/cm^3$ ),  $q_e$  is the charge of electron ( $1.6 \times 10^{-19}$  C), and  $u_a$  is the ambipolar diffusion velocity (cm/s) [44].

$$R \left( \frac{\text{molecules}}{cm^2} \right) = n_e n_{AB} c_e \sigma \times 10\% = 3.6 \times 10^{-9} n_e n_{AB}$$

Equation **3-3**: Dissociation Rate of Molecules [44]

For Equation **3-3**,  $n_e$  again is the plasma power density (density of free electrons) ( $e/cm^3$ );  $n_{AB}$  is the density of molecule AB (molecules/ $cm^3$ ), methane in this case;  $c_e$  is the speed of a typical electron in a plasma (for electrons with a typical average energy of  $\sim 9$ eV;  $c_e$  is equal to  $1.8 \times 10^8$  cm/s); and  $\sigma$  is the collision cross section of reacting molecules ( $cm^2$ ). The 10% factor is attributed to the fact that for typical MPCVD plasmas, only about 10% of the electron density,  $n_e$ , is energetic enough to dissociate the reactant molecule (methane in this case) [44].

Table **3-7** shows how the input power affects the density of free electrons in the plasma. The  $n_e$  values were approximately calculated from Equation **3-2**. The plasma contact area was approximated to be 3cm for susceptor configuration 1 and 1cm for susceptor configurations 2 and 3. The ambipolar diffusion velocity was assumed constant and taken as  $10^5$  cm/s based on text [44]. The maximum growth rate and the maximum C2/H $\alpha$  ratios were added to the table to be correlated to plasma dissociation.

Table 3-7: Approximation of free electron density from Equation 3-2 as a function of microwave input power. Growth rates and C2/H $\alpha$  ratios are shown to correlate the free electron density to the plasma dissociation and growth rate. Contact area was estimated and  $u_a$  was assumed constant based on text [44].

	<b>Average Input Power (W)</b>	<b>Approximate <math>n_e</math> (cm<sup>-3</sup>)</b>	<b>Maximum Growth Rate at 8% CH<sub>4</sub> (<math>\mu\text{m/hr}</math>)</b>	<b>C2/H<math>\alpha</math> Ratio at 8% CH<sub>4</sub></b>
<b>Configuration 1</b>	2250	$1.7 \times 10^{17}$	6.13	0.95
<b>Configuration 2</b>	973	$7.7 \times 10^{16}$	10.13	0.47
<b>Configuration 3</b>	2336	$1.9 \times 10^{17}$	15.87	1.12

Based on these functions, the results from the previous sections can be understood to a greater degree. Susceptor configuration 1 (shown in Figure 2-2) consisted of the as-received wafer holder. Here the substrate laid on a large 3" diameter molybdenum surface. In this configuration the plasma is free to spread across the entire surface area of the wafer holder, causing the input microwave power absorption to be spread throughout the plasma volume. Also, the plasma bulk is suspended above and in poor contact with the substrate. Therefore high input powers are required to heat the substrate to growth temperatures. Because  $q_e$  and  $u_a$  can be considered constants, the density of free electrons (plasma density,  $n_e$ ) is dependent only on input power and plasma contact area. From Table 3-7, the high input power results in a high density of free electrons, which in turn led to a high dissociation rate, as shown with Equation 3-3. However, the large plasma contact area observed with this configuration should lower the plasma density according to Equation 3-2. While this is true to some degree, the overall contribution from input power is greater than the effect of contact area. Therefore dissociation rates are still high. This is consistent with OES data showing high C2/H $\alpha$  peak ratios, meaning that the methane is being dissociated sufficiently (section 3.1).

However, the plasma-substrate contact for configuration 1 is poor. In a typical plasma, dissociated gas species, electrons, and ions are injected into the sheath (the region between the plasma and a surface) by ambipolar diffusion [44]. As the sheath width is increased, the dissociated molecules, ions, and electrons are more likely to recombine or be pulled back into the plasma. The probability that particles will reach the surface decreases significantly. Therefore, despite the excellent dissociation behavior observed with OES, the concentration of radicals at the surface is not nearly as high as in the plasma bulk due to the large sheath width between the plasma and the substrate. As a result, growth rate is low even though  $n_e$  is high.

The raised and tapered geometry of susceptor configuration 2 (shown in Figure **2-10**) successfully confined the plasma to a smaller volume. This allowed for good substrate-plasma interaction and an increase in plasma power density according to Equation **3-2**. However, because cooling to the substrate was so poor, the input microwave power had to be kept very low (<1kW) in order to maintain growth temperature (1100°C). Therefore, from Equations **3-2** and **3-3** and Table **3-7**, it can be seen that the overall plasma power density ( $n_e$ ) as well as the dissociation rate would be significantly reduced.

It may be worthwhile to explain the dependence of plasma power density on input power more scientifically. The low input power would produce a low electric field in the microwave cavity. The resulting Lorentz force, shown in Equation **3-4** where  $q_e(C)$  is the charge of an electron and  $E(V/m)$  is the electric field, on free electrons would produce incident electrons with their acceleration (and thus kinetic energy) lower than electrons in stronger electric fields (high input microwave powers). Therefore, even though the plasma power density is improved with susceptor configuration 2, the acceleration of electrons through the plasma is low. Therefore, a large percent (compared to higher microwave power inputs) of free electrons in the plasma do not seem to have enough incident energy to dissociate methane into carbon radicals. This explanation is consistent with OES data for susceptor configuration 2 (section **3.2**).

$$F = q_e E$$

Equation 3-4: Lorentz Force [44]

Despite the poor dissociation behavior of the plasma for configuration 2, a 65% increase in the maximum growth rate was achieved over configuration 1 (shown in Table 3-7). This may be surprising considering the fact that  $n_e$  was decreased by an order of magnitude and the  $C2/H\alpha$  ratio was consequently decreased by 50%. The increase in growth rate can therefore only be explained by the improved plasma-substrate contact obtained by the confinement of the plasma volume over the substrate with the raised and tapered susceptor insert.

The decrease and confinement of the plasma volume can be attributed to the following physical explanation: When a plasma is formed, it will diffuse outward towards its containing surfaces. Electrons (having a higher thermal velocity than the ions in the plasma) will lead the way. When the negatively charged electrons and positively charged ions come across a conductive surface with a negative surface potential (i.e. a molybdenum susceptor), the electrons will be decelerated and the ions will be accelerated into the surface (in this case the susceptor and the diamond substrate) [44].

In the case of susceptor configuration 1, the plasma expanded and contracted due to the mutual attraction between the ions and electrons in the bulk of the plasma. The containing surfaces were too far away to be in contact with the plasma, so a very small percentage of dissociated particles were able to reach the substrate (or any other surface for that matter). In configuration 2 and 3, the plasma came across a conductive, small area contact surface: the raised

and tapered susceptor insert. When this happened, the ions being injected into the sheath were attracted to and accelerated into this small area, confining the plasma over the substrate.

The plasma sheath width would be significantly decreased in this case. As a consequence, a greater percent of the ion flux into the sheath would reach the substrate and contribute to growth. Therefore, the concentration of active species at the substrate surface for configuration 2 must actually be greater than for configuration 1, even though the dissociation rate and plasma density ( $n_e$ ) is lower in the former.

The design of configuration 3 (shown in Figure **2-13**) allowed for improved cooling to the substrate. This created a “best of both worlds” scenario in which the improved plasma-substrate contact obtained from the raised and tapered geometry of configuration 2 could be used while also allowing for high input powers. Therefore, the high dissociation rates observed with configuration 1 could be utilized in conjunction with the enhanced plasma-substrate interaction of configuration 2. This led to a 159% increase over the maximum growth rate and an 18% increase in the C2/H $\alpha$  ratio of susceptor configuration 1 by creating a very high density of free electrons (from Equation **3-2** and Table **3-7**) and a small sheath width between the plasma and the substrate. Therefore, a very high concentration of free carbon radicals and atomic hydrogen at the substrate surface would be present with susceptor configuration 3. This high plasma density and excellent plasma-substrate interaction seemed to have a significant effect on the morphology and quality of the deposited films as well. This will be explained in greater detail in section **3.5.3**.

### 3.5.2: Explanation of Growth Rate Behavior

Figure 3-22 shows the effect of pressure on the growth rates for each susceptor configuration. Configuration 1 resulted in low growth rates as explained previously. Configuration 2 and 3 however show a similar trend.

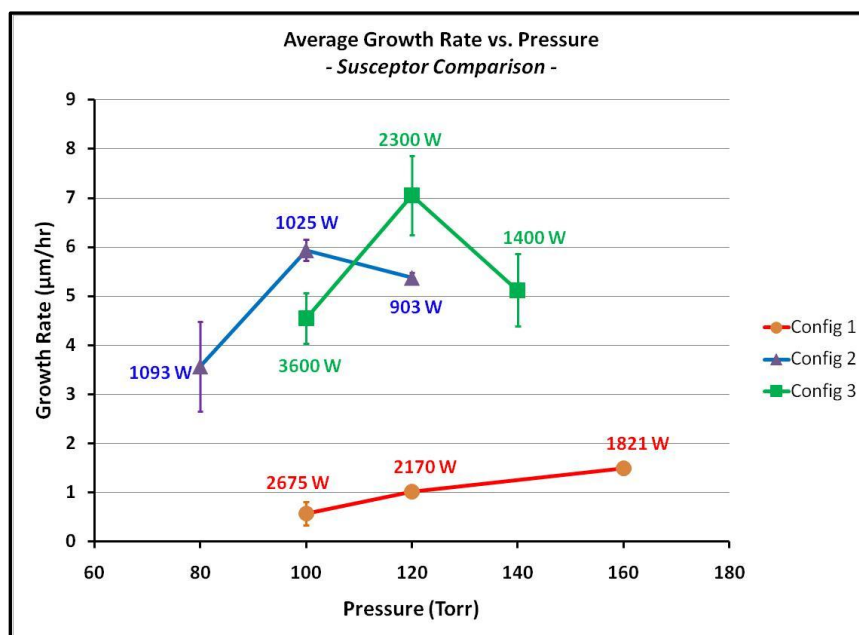


Figure 3-22: Growth Rate vs. Pressure – Susceptor configuration comparison. Growth rates were averaged from the two measurement techniques. Error bars indicate the standard deviation of the data.

The observed effect of pressure on growth rate is somewhat counter-intuitive. For configuration 2 and 3, an increase in growth rate from low pressure to high pressure was followed by a decrease in growth rate at higher pressures. It would be assumed that the cause for this decrease in growth rate at higher pressures would be due to the lower input powers required to maintain growth temperatures. According to Equation 3-2, a decrease in input power would lead to a decrease in density of free electrons. This would in turn lower the dissociation rate and explain the decrease in growth rate. However, OES data shows the dissociation of methane to actually increase at higher pressures based on the C2/H $\alpha$  ratios (Figure 3-20). This can be explained by Equation 3-3, which shows that dissociation rate is dependent not only on the density of free electrons, but also on the total density of methane molecules; which obviously would increase significantly at higher pressures. So why does the growth rate drop at higher pressures when the dissociation of methane is actually increased? One explanation could be related to the ion flux through the plasma sheath to the substrate. At low pressures, electrons and ions can cross the sheath with a low probability of encountering a collision with another molecule. At high pressures, electrons will diffuse less far from their generation region due to their decreased mean free path [44]. If the electrons cannot diffuse as far, than the heavier positively charged ions certainly will not either. Therefore, it seems that there is a point along the pressure range where the concentration of dissociated methyl radicals and atomic hydrogen reaching the substrate surface is reduced, lowering growth rate. For configuration 3, this point occurs at 120 Torr compared to 100 Torr for configuration 2, where configuration 3 benefits from higher power inputs (as observed in Figure 3-22). Configuration 1 does not show the same trend. This is probably because the plasma sheath width in this case is large to begin with, so the effect of pressure on the sheath width probably does not affect growth rate to the same degree as with the other two configurations.

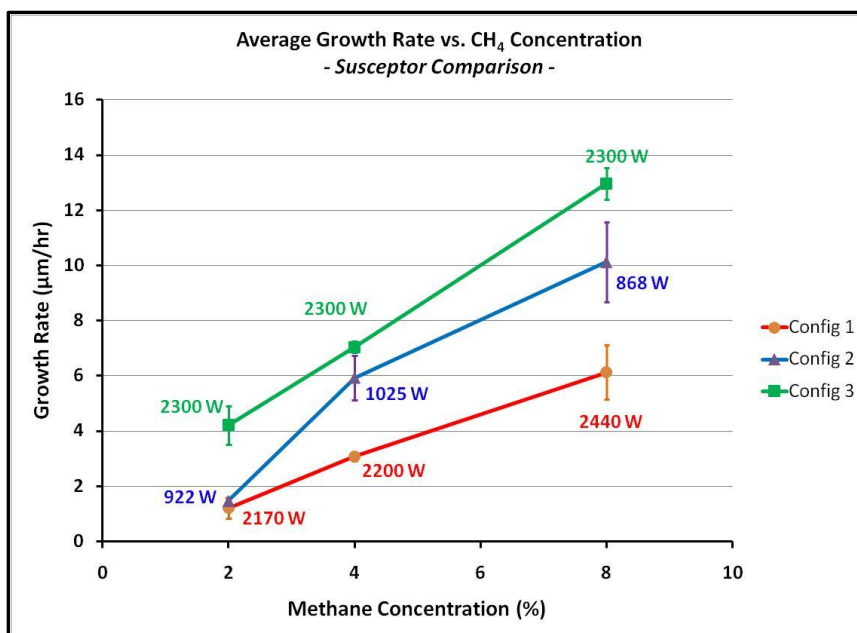


Figure 3-23: Growth Rate vs. CH<sub>4</sub> Concentration – Susceptor configuration comparison. Growth rates were averaged from the two measurement techniques. Error bars indicate the standard deviation of the data.

Figure 3-23 truly depicts the difference between susceptor configurations. At a methane concentration of 2%, Growth rates are nearly identical and do not seem to be effected by the susceptor configuration or the plasma behavior that results from each susceptor configuration. In this regime, growth is diffusion limited. The concentration gradient required for diffusion depletes the reactant over the surface and thereby limits the film-forming surface-reaction rate [44]. Therefore, even at the optimal susceptor configuration (configuration 3), there is not enough active carbon radicals at the surface to accommodate the full potential of the growth reaction rate.

As methane concentration is increased, a greater separation between growth rates starts to develop. With the bulk of the plasma far away from the substrate surface, susceptor configuration 1 would have a low concentration of active carbon radicals and atomic hydrogen at the film

surface. Configuration 2 created improved plasma-substrate contact and thus would have increased carbon species at the surface. Configuration 3 allowed for improved cooling and thus increased input powers, resulting in a high concentration of carbon radicals and atomic hydrogen at the substrate surface. The growth rate increased approximately linearly for configuration 3, showing that diamond growth at the current conditions is limited by the methane concentration.

### 3.5.3: Surface Morphology Comparison

In the previous section, it was shown that factors such as the susceptor geometry, cooling to the substrate, plasma power density, and dissociation rate of methane significantly affect the growth rate of (100) homoepitaxial diamond growth. These factors seem to affect the growth mode and surface morphology of the deposited films as well.

Figure 3-24 shows optical images of three samples, one for each susceptor configuration, that were run under identical conditions. Pressure was held at 120 Torr, methane concentration was 8%, and growth temperature was 1100°C. For configurations 2 and 3, growth time was 4 hours. Growth time was extended to 6 hours for configuration 1 to make the thicknesses of all three samples comparable.

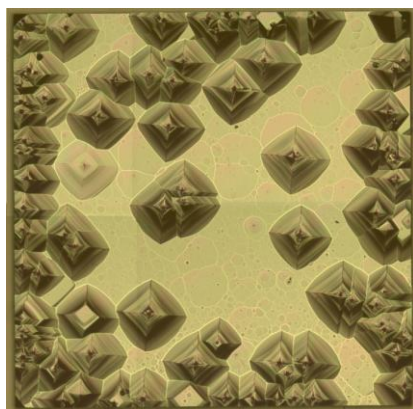
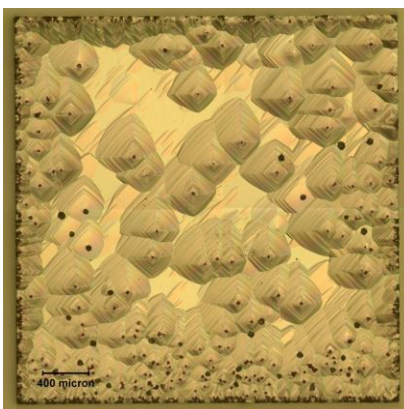
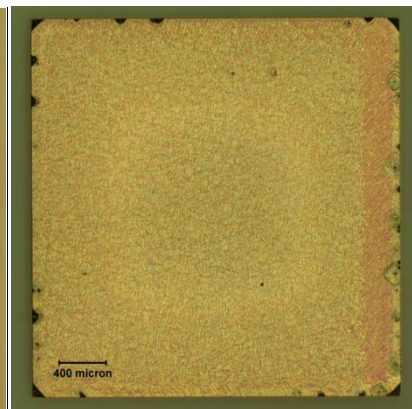
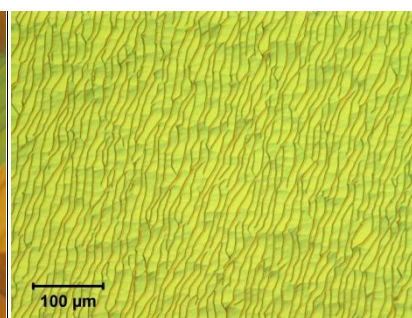
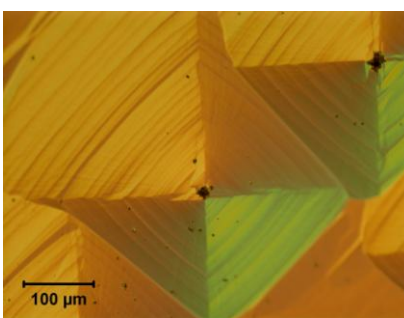
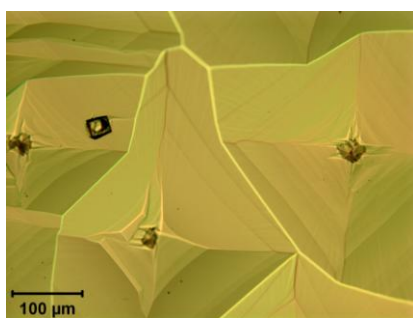
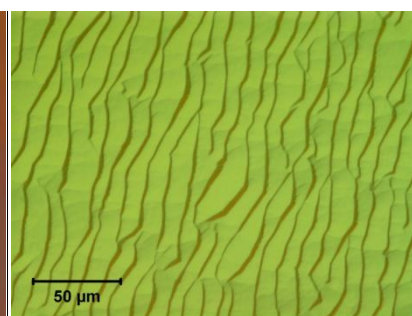
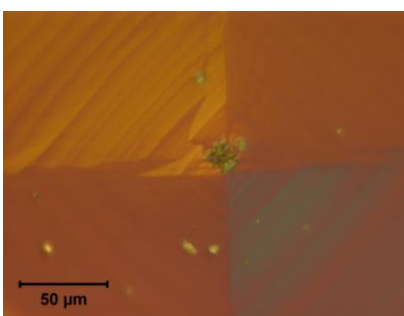
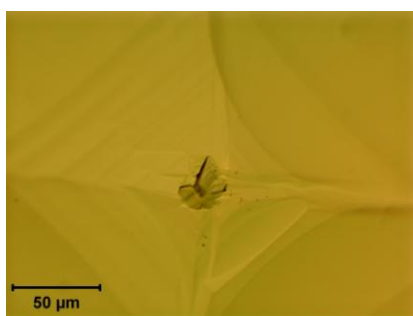
**CVD-06****Configuration 1**Avg. Thickness: 45.75 $\mu\text{m}$ **CVD-18****Configuration 2**Avg. Thickness: 40.50 $\mu\text{m}$ **CVD-29****Configuration 3**Avg. Thickness: 51.86 $\mu\text{m}$ **50x Images****200x Images****500x Images**

Figure 3-24: Optical micrographs – Susceptor configuration comparison. Constants: Pressure: 120 Torr, Methane concentration: 8%, Temperature: 1100°C.

Figure 3-25 shows the OES results for the runs shown above. The dissociation behavior can clearly be observed for each susceptor configuration under identical conditions. Configuration 3 has the highest C2/H $\alpha$  ratio and configuration 2 has the lowest. Configuration 1 has good dissociation behavior, but as explained previously, the bulk of the plasma is too far from the substrate surface for this dissociation to fully contribute.

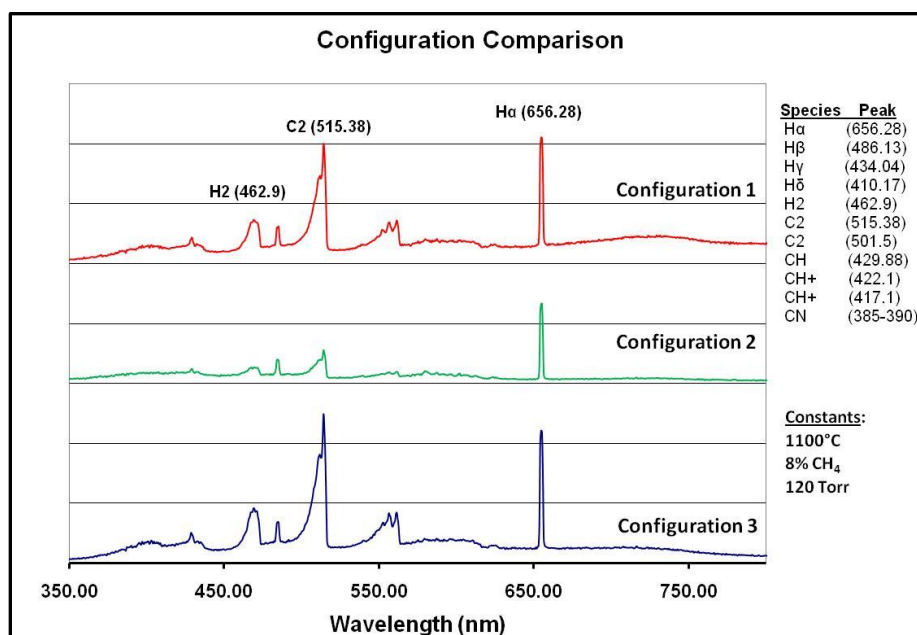


Figure 3-25: OES Spectra – Susceptor configuration comparison. Constants: Pressure: 120 Torr, Methane concentration: 8%, Temperature: 1100°C.

From Figure 3-24, it is obvious that a change in growth mode occurs with configuration 3. Configurations 1 and 2 produced films with large hillocks covering a large percent of the surface. These hillocks most likely formed by nucleating onto dislocations, or by forming new dislocations due to island growth. Since these substrates were nominally on-axis, the terrace width between each crystallographic step would be large (much larger than the surface diffusion length of carbon atoms on diamond). Therefore, there is a high probability that nucleation would occur somewhere in the middle of the terrace steps rather than on the edge of a step. Additional

carbon atoms could then adsorb onto these sites forming “islands”. If several islands are formed on the same terrace step, they will eventually collide with each other and usually form a dislocation. Hillocks would then proceed to grow from the dislocations.

Configuration 3 on the other hand, grew in step-flow mode. Step-flow growth usually occurs when the terrace length is smaller than the surface diffusion length (typical for misoriented substrate), creating a high probability that atoms will adsorb onto step edges rather than in the middle of a step. Steps will then proceed to propagate in the [110] direction. This growth mode is preferred over island growth because it does not introduce dislocations, strain, or impurity atoms to the same degree. Island growth and step-flow growth will be discussed in more detail in Chapter 4.

If all these substrates were nominally on-axis, then the terrace lengths should be very similar and the growth mode should be the same. Why does the growth mode change from island growth to step-flow mode when the susceptor configuration is altered? The only “real” difference between configuration 3 and configurations 1 and 2 is the concentration of active species at the substrate surface. Because the plasma density was so high and the plasma-substrate contact is excellent, the concentration of atomic hydrogen and carbon radicals at the substrate surface would be larger for configuration 3 than for the other two configurations. Therefore, it is apparent that there are two growth regimes occurring: a low plasma density regime (configurations 1 and 2) and a high plasma density regime (configuration 3). The low plasma density regime is the typical MPCVD process reported in most literature. Figure 3-26 shows optical images of samples grown with configuration 2. Low methane concentrations are preferred in this case because carbon radicals arriving at the surface would have more time to find a crystallographic step site before encountering another carbon radical and grouping into islands. At high methane concentrations however, there is a high probability that carbon radicals will come across other carbon radicals and form islands and eventually propagate into hillocks.

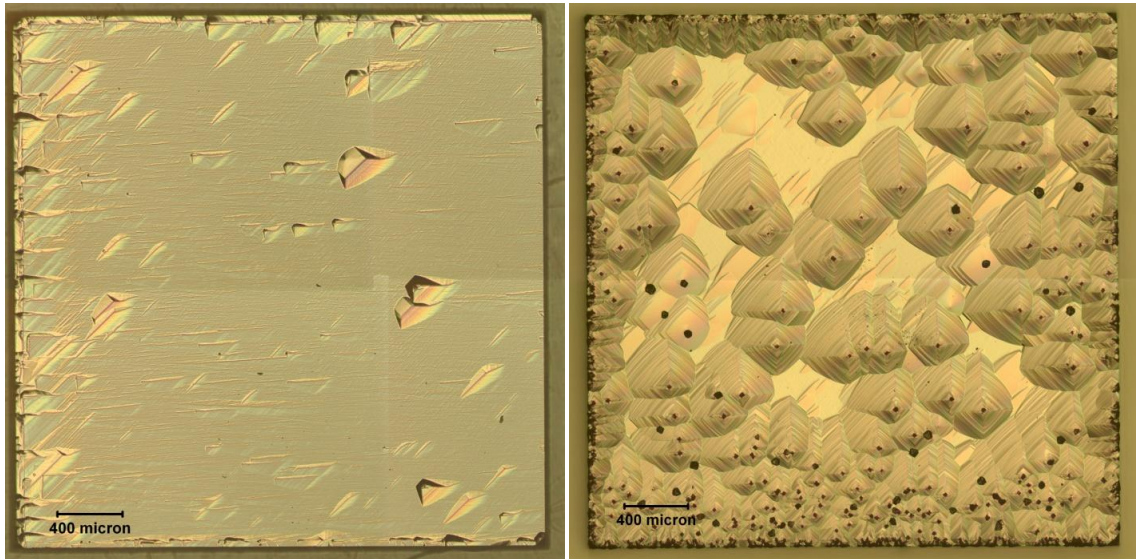


Figure 3-26: 50x optical images of diamond samples grown under the low plasma density regime (susceptor configuration 2) at 4% CH<sub>4</sub> (left image) and 8% CH<sub>4</sub> (right image). In this regime, lower methane concentrations are preferred as hillock growth is more probable at high methane concentrations.

Figure 3-27 shows optical images of samples grown with configuration 3; utilizing the high plasma density regime. Here, high methane concentrations promote step flow growth and low methane concentrations lead to hillock formation. This is completely opposite of the low plasma density regime.

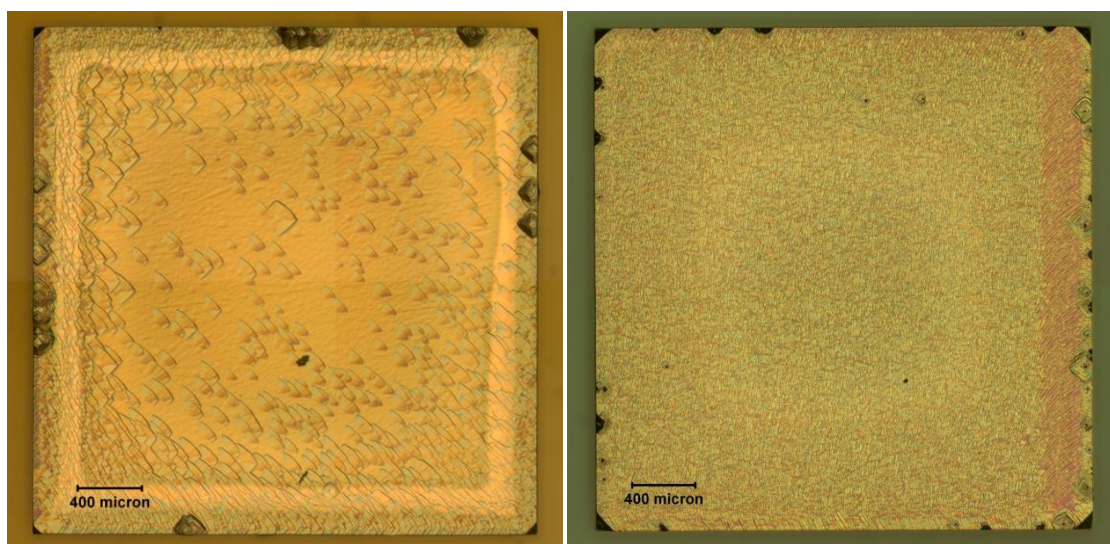


Figure 3-27: 50x optical images of diamond samples grown under the high plasma density regime (susceptor configuration 3) at 4% CH<sub>4</sub> (left image) and 8% CH<sub>4</sub> (right image). In this regime, high methane concentrations are preferred as step-flow growth is promoted and hillock growth is suppressed.

This could be due to one of several mechanisms that could be taking place in response to the increased concentrations of both atomic hydrogen and carbon radicals at the substrate surface. One explanation to the change in growth mode between plasma density regimes is that the diffusion length of carbon atoms on a diamond surface increases for the high plasma density regime. Some literature suggests that the migration length of carbon precursors increases by orders of magnitude in the presence of a large amount of atomic hydrogen [45, 46]. Hydrocarbon precursors migrate along dimer chains or dimer rows of a hydrogenated (100) diamond surface [45]. It has been proposed through numerical calculations that the average migration length under normal CVD diamond growth is around 10Å and the upper limit around 20-40Å. However, recent reports suggest that at very high concentrations of atomic hydrogen on the surface, migration lengths exceeding 100Å are possible [45]. An increased migration length would increase the

probability that hydrocarbon precursors would adsorb onto a favorable site (a crystallographic step edge) rather than nucleate randomly or onto a dislocation. However, the literature shows that this type of enhanced surface migration only occurs at very low methane concentrations (<1%) and island growth occurs at concentrations greater than 4% as carbon radicals run into each other during surface migration at high methane concentrations. Therefore, something else must be taking place.

Perhaps the explanation is based on the increased growth rate observed with configuration 3. The high concentration of carbon radicals (created by the high plasma density and observed with OES) may be saturating the surface and preferentially nucleating at crystallographic step edges. Microscopically, the  $2 \times 1 / 1 \times 2$  double domain structure at a crystallographic step presents incoming radicals with a higher density of dangling bonds than the flat terrace surface [2]. Therefore, adsorbed radicals are more stable at step edges than on terraces and growth occurs dominantly at step edges. In addition, because abstraction of terminating hydrogen from step edges is easier than from terraces, radicals are considered to adsorb at step edges in high probability. This growth model is called the trough model and would be preferred at very high concentrations of atomic hydrogen at the surface [2].

The high rate of hydrogen abstraction and subsequent carbon radical incorporation (at high methane concentrations) at step edges would allow for a large percentage of carbon radicals to be incorporated at the step site and generate a very rapid growth of steps in the [110] direction. This rapid lateral growth would overcome and cover any unwanted [100] growth such as nucleation on dislocations, pits, or micro-fractures.

Hillocks were observed at 4%  $\text{CH}_4$  in the high plasma density regime because growth from unwanted step sources in the [100] direction had more time to develop. Conversely, at 8%  $\text{CH}_4$ , growth from such sites was beaten out by the [110] propagation of lateral steps. In other words, there are two competing growth directions: hillocks in the [100] direction and steps in the

[110] direction. At high methane concentrations (8%), lateral growth in the [110] direction is fast enough to overcome hillock growth in the [100] direction, leading to the domination of step-flow growth. At lower methane concentrations (4%), hillocks had more time to develop and [100] island growth dominated.

Therefore, it is apparent that the high plasma density mode is only beneficial for high methane concentrations. In fact, because of the aggressive hydrogen abstraction, etch pits were actually observed at a methane concentration of 2% (Figure 3-13). However, when high methane concentrations are used, the high plasma density regime can produce excellent step-flow growth morphology even on substrates without any nominal misorientation. This effect was repeated and confirmed several times at these conditions using substrates that are nominally on-axis.

#### 3.5.4: Raman Comparison

Figures 3-28, 3-29, and 3-30 show the Raman spectra for configuration 1, configuration 2, and configuration 3, respectively. For configurations 1 and 2, the Raman spectra were focused in the center of the hillock defects. Here a non-epitaxial crystal almost always forms from the dislocation propagating through the film. For configuration 3, the Raman spectra was focused on one of the terrace steps propagating in the [110] direction.

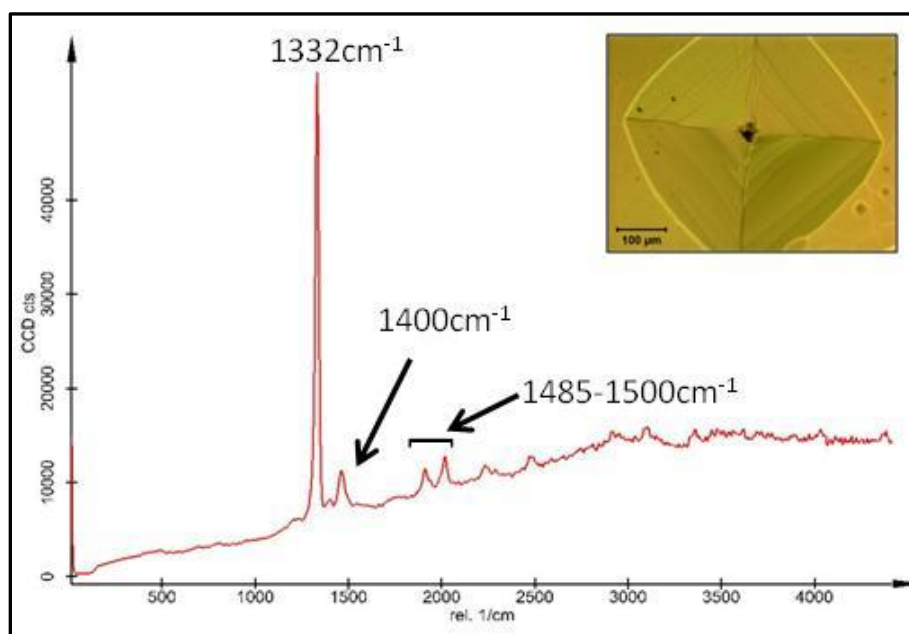


Figure 3-28: Raman Spectra – Susceptor Configuration 1. Here the 488nm laser was focused on the center of one of the growth hillocks.

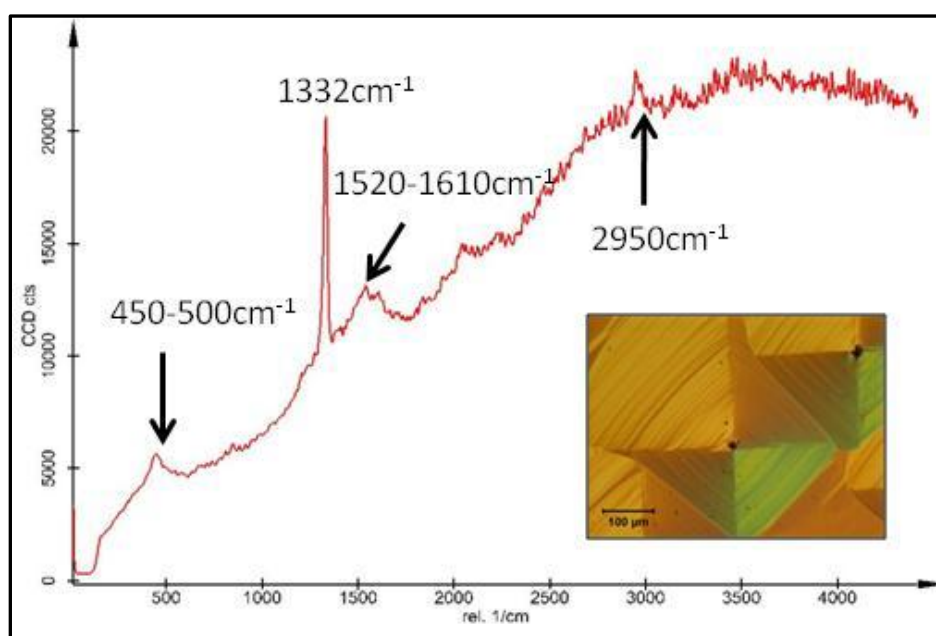


Figure 3-29: Raman Spectra – Susceptor Configuration 2. Here the 488nm laser was focused on the center of one of the growth hillocks.

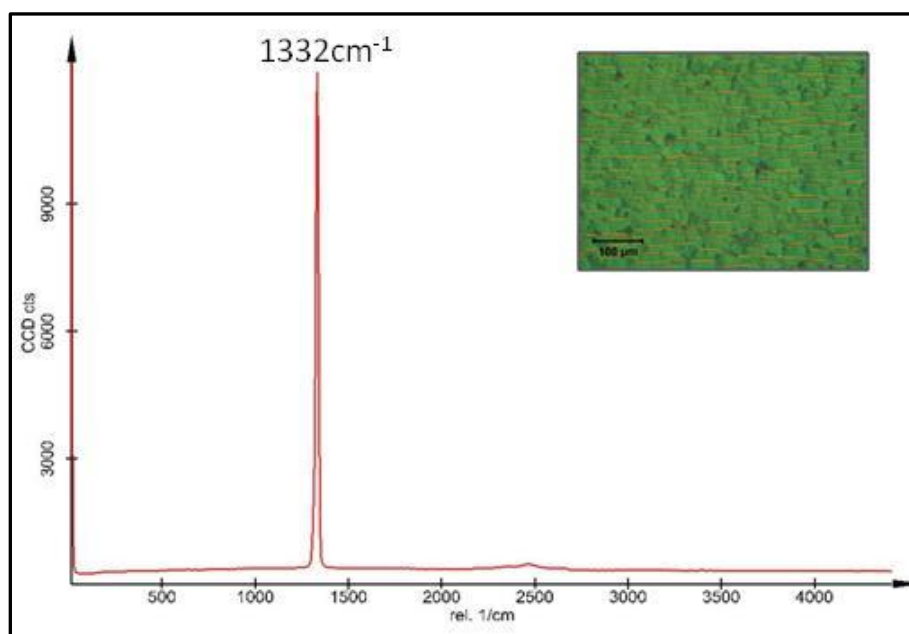


Figure 3-30: Raman Spectra – Susceptor Configuration 3. Here the 488nm laser was focused between macroscopic steps on one of the terrace flats.

The samples grown with configurations 1 and 2 contain a large density of hillocks which resulted in Raman spectra containing background peaks that are most likely a response from either defect or impurity scattering. Though most of these peaks were difficult to distinguish to any real accuracy, some obvious peaks and bands were identified and correspond to known impurity scattering centers and defective material contributions. Configuration 1 (Figure 3-28) shows a sharp peak at  $1332\text{cm}^{-1}$ , corresponding to the diamond peak. However, a distinct peak at  $1400\text{cm}^{-1}$  is indicative of regions of disordered graphite and the peaks from  $1485\text{-}1500\text{cm}^{-1}$  are associated with intrinsic point defects with  $\text{sp}^2$  hybridized carbon phases [47]. Configuration 2 (Figure 3-29) shows a clear diamond peak as well as the G-band ( $1520\text{-}1610\text{cm}^{-1}$ ). The G-band indicates this area of the film contains  $\text{sp}^2$  graphitic phases. A peak around  $450\text{-}500\text{cm}^{-1}$  is associated with a Si-Si impurity vibrational mode or scattering on acoustic phonons of a distorted

diamond lattice. Also, a sharp peak at  $2950\text{cm}^{-1}$  may correspond to oxygen impurities [47]. Configuration 3 (Figure **3-30**) however shows only the diamond peak at  $1332\text{cm}^{-1}$ , indicating excellent phase quality with no detectable graphitic phases, defect interference, or photoluminescence scattering from impurities [47]. This suggests that hillocks induce defects and impurities into the film, while step-flow growth produces defect and impurity free films.

It can therefore be concluded that susceptor configuration 3 (having improved plasma density as well as enhanced plasma-substrate contact) not only resulted in the highest growth rate, but also the highest quality film as observed with Raman spectroscopy.

## Chapter 4

### Effect of Substrate Misorientation and Reactive Ion Etching on Surface Morphology

Surface morphology plays an important role in improving crystalline quality and purity of MPCVD diamond films. Formation of macroscopic features, such as growth hillocks, can lead to the incorporation of dislocations, strain, and impurities. Literature suggests that by using a substrate surface with a slight misorientation of the crystallographic planes, growth of such hillocks can be suppressed, morphology can be improved, and crystalline quality can be enhanced [25-29, 45, 46]. Misorientation of the substrate has also been shown to increase growth rate. Further improvements in surface morphology are expected to result from pre-growth reactive ion etching (RIE) of the substrates [22, 39, 40]. Surface defects and imperfections induced by mechanical polishing and processing of the substrates can act as nucleation sites for hillocks. RIE can remove a large percent of these surface defects by etching the first few microns of surface material.

#### 4.1: Off-axis Growth

As explained in section 1.4, misorientation of the substrates creates a higher density of crystallographic steps on which incident carbon atoms can nucleate. Not only is this expected to increase growth rate, but morphology and crystalline quality can be enhanced due to the increased probability that carbon will nucleate onto step sites from misorientation rather than run into each

other and form islands or nucleate onto unwanted step sources (such as dislocations, microfractures, and foreign particles).

Growth on misoriented substrates was carried out in an attempt to improve morphology and crystalline quality of single crystal intrinsic diamond. To further improve morphology of the deposited films, pre-growth ICP reactive ion etching (RIE) was completed on several samples and will be discussed in detail in section 4.2. As observed in Chapter 3, susceptor configuration 3 provided the best growth conditions for high quality, high growth rate deposition. Therefore, all runs in this chapter utilized susceptor configuration 3. All substrates are (100) oriented single crystal diamond seeds purchased from Element Six and have dimensions of 3mm x 3mm x 0.3mm. Samples denoted with “OA” were off-axis seeds with a nominal misorientation of 3-4° according to the manufacturer. Exact misorientation could not be measured in house due to the very small size of the samples. Figure 4-1 shows a 50x optical image of a typical as-received off-axis substrate. On-axis seeds were run with and without etching as a comparison to the off-axis growth runs. On-axis seeds are denoted with “CVD” having a maximum misorientation of 0-1°.



Figure 4-1: 50x Optical Micrograph of (100) Off-axis CVD diamond substrate.

Table 4-1 details the runs performed to study the effect of off-axis substrates at different methane concentrations as well as at different etching pressures. On-axis samples (both etched and non-etched) were also used as a comparison. Wyko surface roughness data and optical images for all samples can be found in Appendices C and D, respectively. For this study, only methane concentration and etch pressure (detailed subsequently in section 4.2) were varied. For all growth runs, pressure was maintained at 120 Torr, the total flow rate was 200 sccm, and the input power was held at 2300W to give an estimated temperature of 1100°C. The exact temperature could not be measured accurately due to the small thickness of the samples, so the temperature was estimated based on previous power vs. temperature studies (detailed in section 2.3).

Table 4-1: Growth rate results for etched and non-etched off-axis samples as well as on-axis samples for comparison. Growth rates were averaged from the two measurement techniques.

Run	Etch Pressure (mTorr)	Growth CH <sub>4</sub> %	Growth Rate (μm/hr)	Standard Deviation (μm/hr)
OA-01	N/A	8	16.99	1.19
OA-02	25	8	15.26	0.56
OA-03	25	4	7.64	0.29
OA-04	25	2	4.53	0.10
OA-05	5	4	6.15	0.77
OA-06	50	4	6.37	0.45
OA-07	75	4	7.36	1.15
OA-09	25	1	1.47	0.03
OA-10	25	3	5.14	0.62
OA-11	N/A	4	7.44	0.01
CVD-28	N/A	4	4.63	0.82
CVD-29	N/A	8	12.97	0.59
CVD-30	25	4	6.00	0.98
CVD-31	25	8	12.00	0.78

Figure 4-2 shows the growth rate as a function of methane concentration for off-axis substrates (1-8%) and on-axis substrates (4% and 8%). The growth rate is enhanced with misorientation of the substrate. Deposition onto off-axis substrates results in a 1.27x increase in growth rate over on-axis growth at both 4% and 8% CH<sub>4</sub>. An increase in density of contributing step sites would lead to an increase in the overall density of growth centers. Therefore, a higher percentage of methyl radicals at the substrate surface would be able to contribute to growth. Off-axis growth would consequently proceed at higher rates than on a surface with a low density of crystallographic steps (on-axis). In addition, off-axis diamond growth usually proceeds via step-flow growth mode. Step-flow growth generally results in higher growth rates than island growth mode due to the preferential growth direction [44].

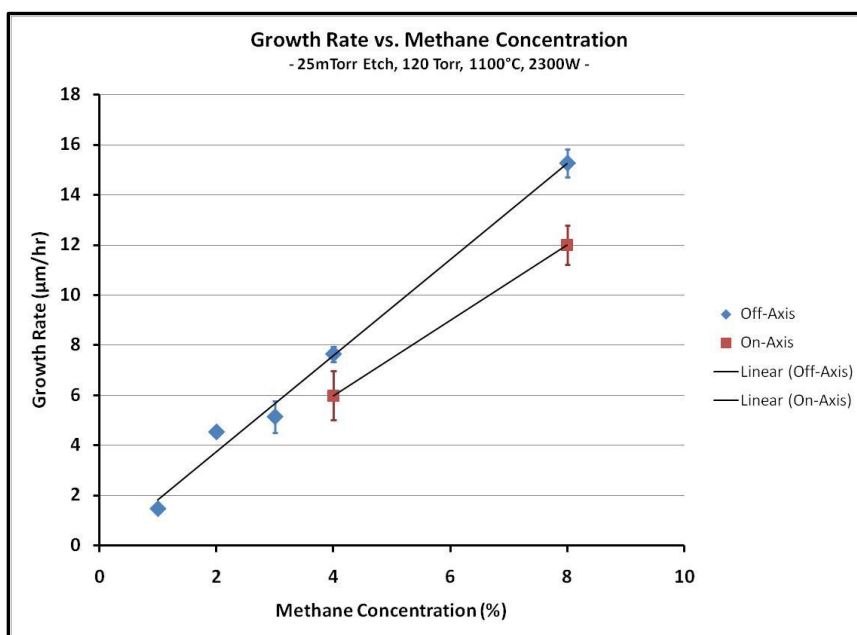


Figure 4-2: Growth Rate vs. Methane Concentration – Off-axis and On-axis samples. Misoriented substrates having a higher density of crystallographic steps results in a higher growth rate. Growth rates were averaged from the two measurement techniques. Error bars indicate the standard deviation of the data.

As expected, the growth mode for off-axis and on-axis growth can differ significantly. Figure 4-3 shows 200x optical images of an on-axis (CVD-28) and an off-axis (OA-03) film. The misoriented substrate (image on the right) resulted in step-flow growth mode while on-axis growth resulted in coalescing islands and macroscopic hillock-like facets. An explanation of the mechanisms which cause this difference in morphological growth mode will be discussed in section 4.3.

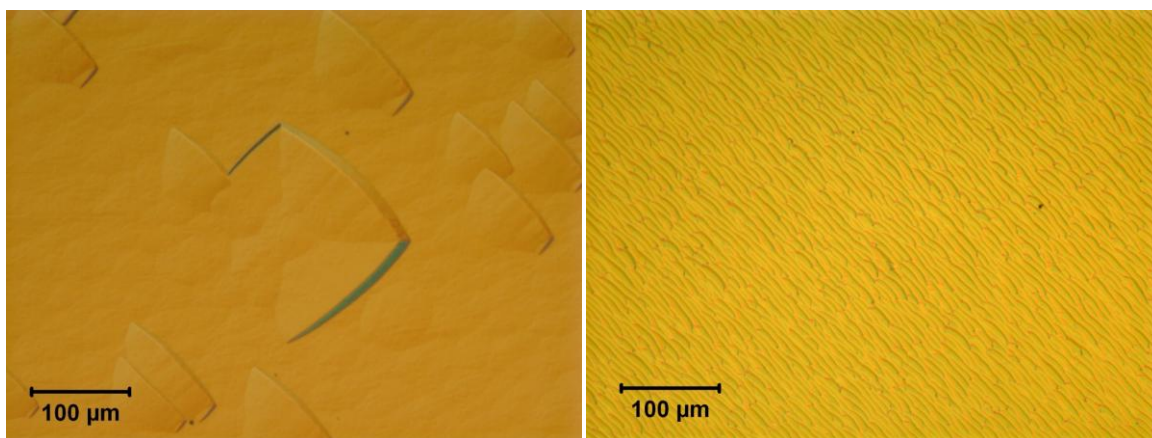


Figure 4-3: 200x Post-growth Optical Images – Left: On-axis sample, Right: Off-axis sample. Step-flow growth was achieved by mis-orienting the substrate 3-4°.

Methane concentration was the only variable besides etch pressure (discussed in section 4.2). Therefore, the effect of methane concentration on the morphology of off-axis diamond growth can be studied. Figure 4-4 shows the progression of morphology for increasing concentrations of methane in the gas phase. Starting from the top left and ending at the bottom right; methane concentrations of 1%, 2%, 3%, 4%, and 8% were used (samples OA-09, OA-04, OA-10, OA-03, and OA-02, respectively). At 1% CH<sub>4</sub>, the surface is very rough with what appears to be small hillocks completely covering the sample surface. At 2%, the density of these apparent hillocks decreases significantly and elongated oval-like steps begin to appear on the surface. At 3% CH<sub>4</sub>, it

appears that a transition to step-flow mode occurs. The hillocks become absent from the surface and steps begin to line up preferentially. At 4% CH<sub>4</sub>, step-flow mode has completely taken over. Distinct steps are now observed propagating in the [110] direction. Up to 8% CH<sub>4</sub> still results in step-flow growth mode with no apparent degradation in morphology or hillock formation.

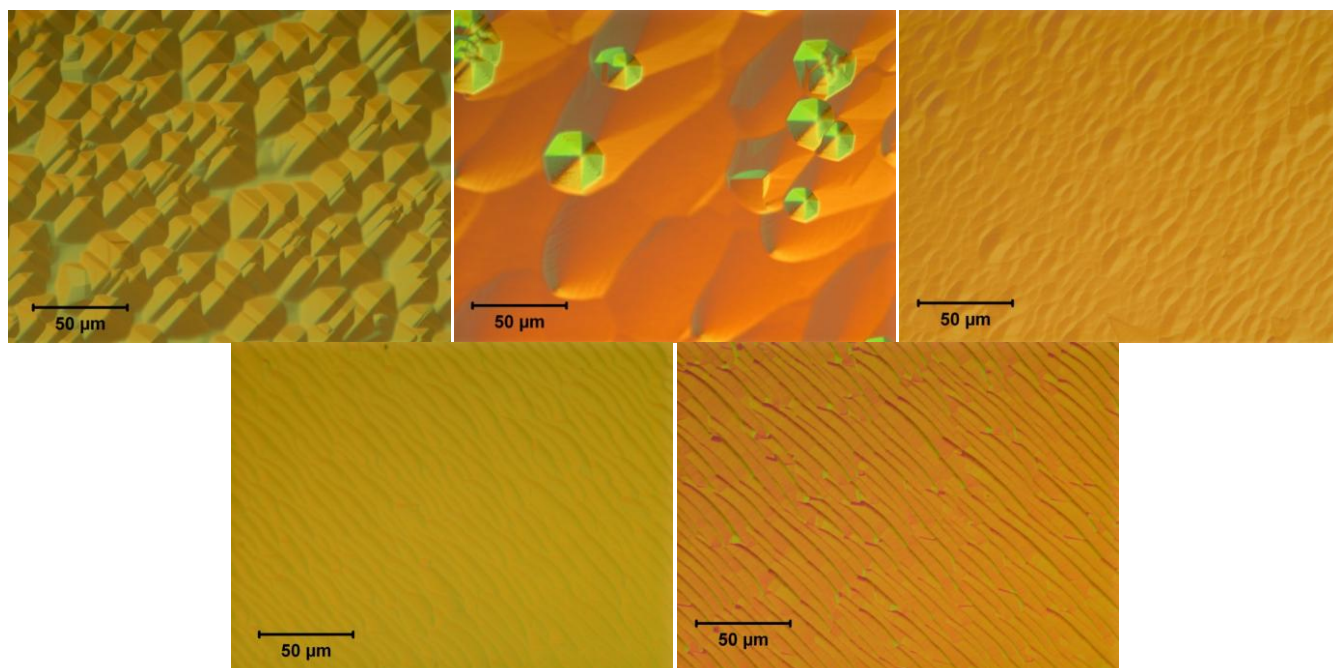


Figure 4-4: 500x Post-growth Optical Images – Effect of CH<sub>4</sub> % on Morphology. From Left to Right: 1%, 2%, 3%, 4%, 8% CH<sub>4</sub>. Higher methane concentrations promote a step-flow growth morphology.

Interestingly, these results do not conform to observations made in the literature which show step-flow growth at low concentrations of methane and hillock formation at higher methane concentrations [45]. The reasoning for this morphology dependence on methane concentration is that at lower methane concentrations and significant misorientation angle ( $>2^\circ$ ), carbon atoms have enough time to migrate across the surface to a step edge, which would most likely be a crystallographic step in the case of off-axis growth, before being buried by additional incoming

carbon atoms. This explanation seems reasonable but may not be applicable for conditions controlling growth for this study. D. Takeuchi et. al. used low growth pressures (25 Torr), low substrate temperature (800°C) and low input power (750W) [45]. The present growth conditions used high pressure (120 Torr), high temperature (1100°C), and high input power (2300W). Therefore, the plasma behavior would be completely different. Due to the enhanced susceptor configuration and higher growth parameters, the plasma power density would be much higher for the present study than for the growths described in literature. Therefore, the concentration of atomic hydrogen at the sample surface would be much higher here and may lead to etching at low methane concentrations. Consequently, the hillocks observed at 1% and 2% were suspected to not actually be hillocks at all, but instead etch pits. Wyko surface profilometry confirmed this hypothesis as shown in Figure 4-5.

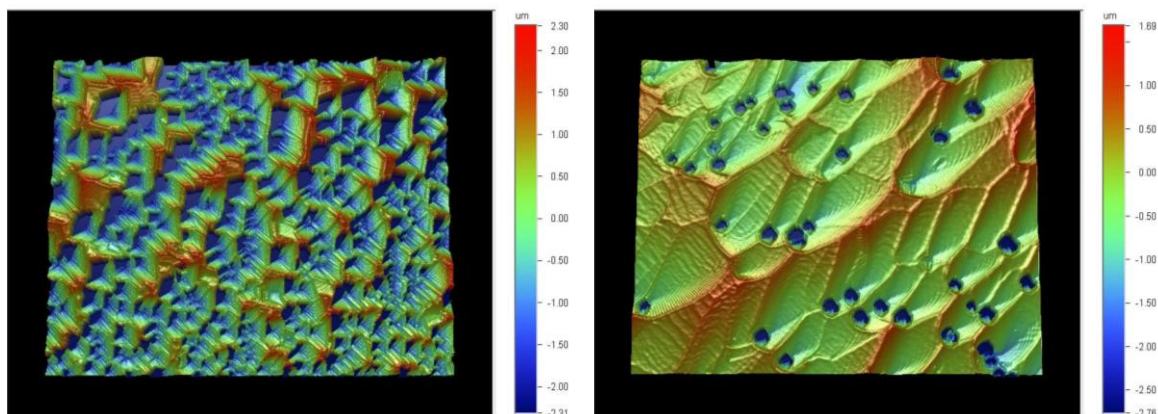


Figure 4-5: Wyko Images – Left: 1% CH<sub>4</sub>, Right: 2% CH<sub>4</sub>. Confirmation of etch pits rather than hillock nucleation.

Many times when using interference contrast in optical microscopy, the apparent depth of certain features can be misleading. Here, the optical images of the 1% and 2% CH<sub>4</sub> samples portrayed indented etch pits as raised hillocks.

## 4.2: Reactive Ion Etching

Reactive Ion Etching (RIE) has also been shown to improve the overall quality of single crystal diamond [22, 39, 40]. Mechanical polishing of the substrates almost always results in surface and subsurface damage such as dislocations, pits, and micro-fractures. These defects can act as undesired nucleation sites for incoming methyl radicals. And as explained in section 1.3, nucleation sites other than crystallographic step edges can result in the formation of hillocks or other unwanted macroscopic defects.

As detailed in section 1.6, plasma etching techniques are comprised of two related mechanisms; chemical reactive etching and physical sputtering. Chemical reactive etching is the main mechanism involved in most dry etching techniques, and is isotropic. The sputtering mechanism has a lower etch rate but is anisotropic. Controlling the contributions of each of these mechanisms is the key to realizing a smooth, pit free etch morphology [41]. Pressure seems to determine these contributions. At low pressures, the mean free path of ions and electrons is large and particles are able to accelerate to the sample easily. Here, physical sputtering dominates. At high pressures, chemical reactive etching dominates due to the large concentration of reactive species at the surface of the sample.

For this study, the Tegal 6540 HRe ICP cluster etch system (described in section 2.2) was used. Pressure was the only variable (varied from 5mTorr to 75mTorr) as it seemed to have the largest effect on etch rate and etch morphology [22, 41]. A chlorine-argon gas chemistry and input power were held constant and were taken from literature [22, 39]. A fluorine-based chemistry [42] was attempted as well; however initial tests showed insignificant etching so the chlorine-based chemistry was used exclusively. Table 4-2 shows the parameters used for etching.

Table 4-2: RIE Process Parameters.

<b>TEGAL RIE Etching Parameters</b>	
<b>Argon Flow Rate</b>	25 sccm
<b>Chlorine Flow Rate</b>	40 sccm
<b>Input Power</b>	300W
<b>Pressure</b>	5-75 mTorr
<b>Etch Time</b>	1 hour

Several experiments were performed to evaluate the etching process on the growth behavior of off-axis diamond substrates. For all samples, only methane concentration during growth and pressure during etching were varied. All growths were performed for 4 hours with a constant pressure of 120 Torr, a constant flow rate of 200 sccm, and a constant microwave input power of 2300W. The temperature could not be detected by the pyrometer due to the small thickness of the substrates, therefore 2300W was chosen based on power-temp profiles for susceptor configuration 3 (section 2.3.3) to obtain ~1100°C.

Etching was characterized primarily by surface roughness and etch rate. Pre-etch and post-etch surface roughness's were measured with optical profilometry (Wyko) and atomic force microscopy (AFM) and averaged. Post-growth surface roughness was measured with the Wyko optical profiler only. Etch rate was determined using samples that were half covered in tape and half exposed. The resulting step edge was then measured with AFM to determine etch rate after one hour. Table 4-3 shows the pre-etch, post-etch, and post-growth surface roughness's. Wyko images and optical images for all samples described in Table 4-3 can be found in Appendices C and D, respectively.

Table 4-3: Surface roughness results – Pre-etch, post-etch, and post-growth for off-axis and on axis samples, both etched and non-etched. Ra values were averaged from three wyko scans and one AFM scan over a 5 $\mu$ m by 5 $\mu$ m area.

Run	Etch Pressure (mTorr)	Growth CH <sub>4</sub> %	Avg. Pre-Etch Ra (nm) (Wyko/AFM)	Avg. Post-Etch Ra (nm) (Wyko/AFM)	Post-Growth Ra (nm) (Wyko)
OA-01	N/A	8	0.54	N/A	177.10
OA-02	25	8	0.80	0.477	148.79
OA-03	25	4	0.64	0.413	179.39
OA-04	25	2	0.82	0.558	368.96
OA-05	5	4	0.49	0.546	135.71
OA-06	50	4	0.60	0.671	159.63
OA-07	75	4	0.56	0.905	183.46
OA-09	25	1	0.66	0.611	556.33
OA-10	25	3	0.41	0.348	61.74
OA-11	N/A	4	0.69	N/A	111.59
CVD-28	N/A	4	0.74	N/A	92.07
CVD-29	N/A	8	0.75	N/A	124.72
CVD-30	25	4	0.76	2.501	195.77
CVD-31	25	8	0.65	2.815	194.59

The first study was to determine the optimal etch pressure in terms of surface roughness and etch rate to use for future studies. A large degradation in surface roughness would suggest an aggressive etch and is undesirable as it may induce more defects to the surface than were originally present. Too passive of an etch may result in a very low etch rate and would not remove much surface or subsurface damage. Therefore, an optimal etch pressure which results in a sufficient etch rate without damaging the surface is required. Figure 4-6 shows the average surface roughness (Ra) vs. etch pressure and Figure 4-7 shows the etch rate vs. etch pressure. Note that these figures pertain to off-axis substrates. Run numbers OA-05, OA-03, OA-06, and OA-07 were used for this study.

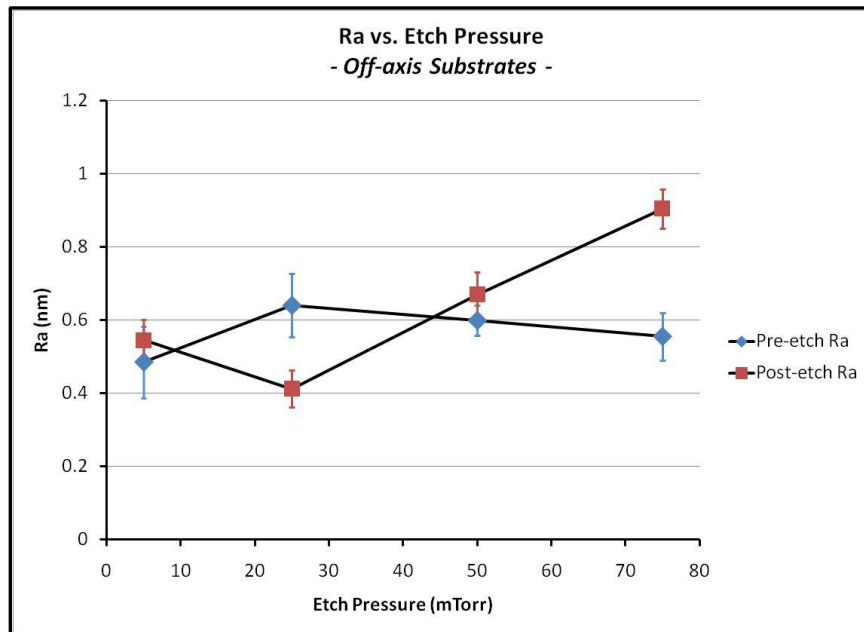


Figure 4-6: Surface Roughness (Ra) vs. Etch Pressure – Off-axis substrates. Ra values were averaged from three wyko scans and one AFM scan over a  $5\mu\text{m}$  by  $5\mu\text{m}$  area. Error bars indicate the standard deviation of the data.

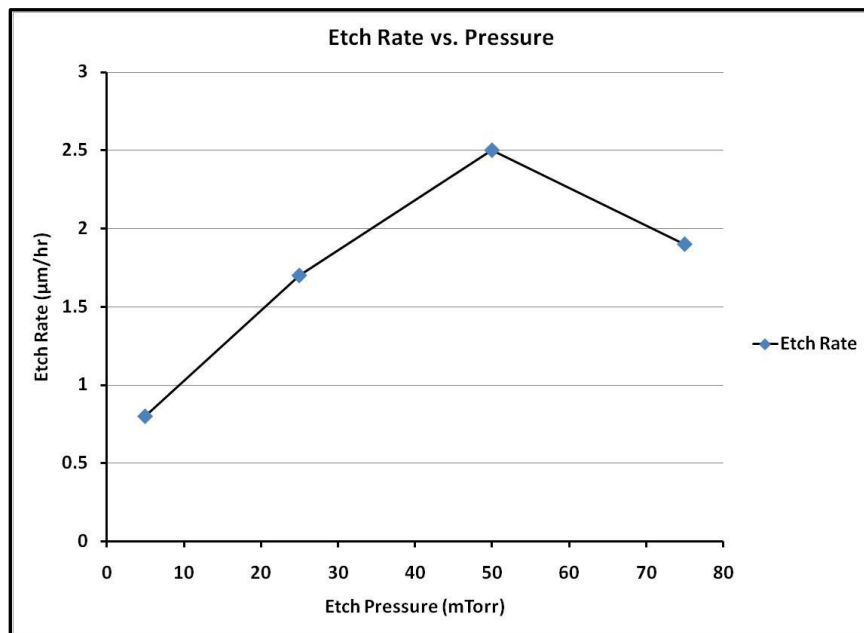


Figure 4-7: RIE Etch Rate vs. Etch Pressure – Off-axis substrates. Etch rate was determined by AFM of etch steps.

From Figure 4-6, it is obvious that at high pressures chemical reactive etching dominates, leading to an aggressive etch and high post-etch  $R_a$  values. At very low pressures (5mTorr), the  $R_a$  does not change very much, indicating a very passive etch. The optimal etching pressure for this etching chemistry was at 25mTorr. Here the surface roughness actually decreased, indicating that a smoothing effect occurs due to the harmonious contributions from physical sputtering as well as chemical etching. Figure 4-7 shows a similar trend as Figure 1-7 from literature [41]. At 25 mTorr, the etch rate is  $\sim 1.7\mu\text{m/hr}$ , which is enough to remove any surface pits or micro-fractures. Figure 4-8 illustrates the effect of etching pressure on the off-axis substrate surfaces. Here, post-etch Wyko surface profiler images and  $R_a$  surface roughness values for etch pressures of 5mTorr through 75mTorr; corresponding to Figures 4-6 and 4-7 are shown.

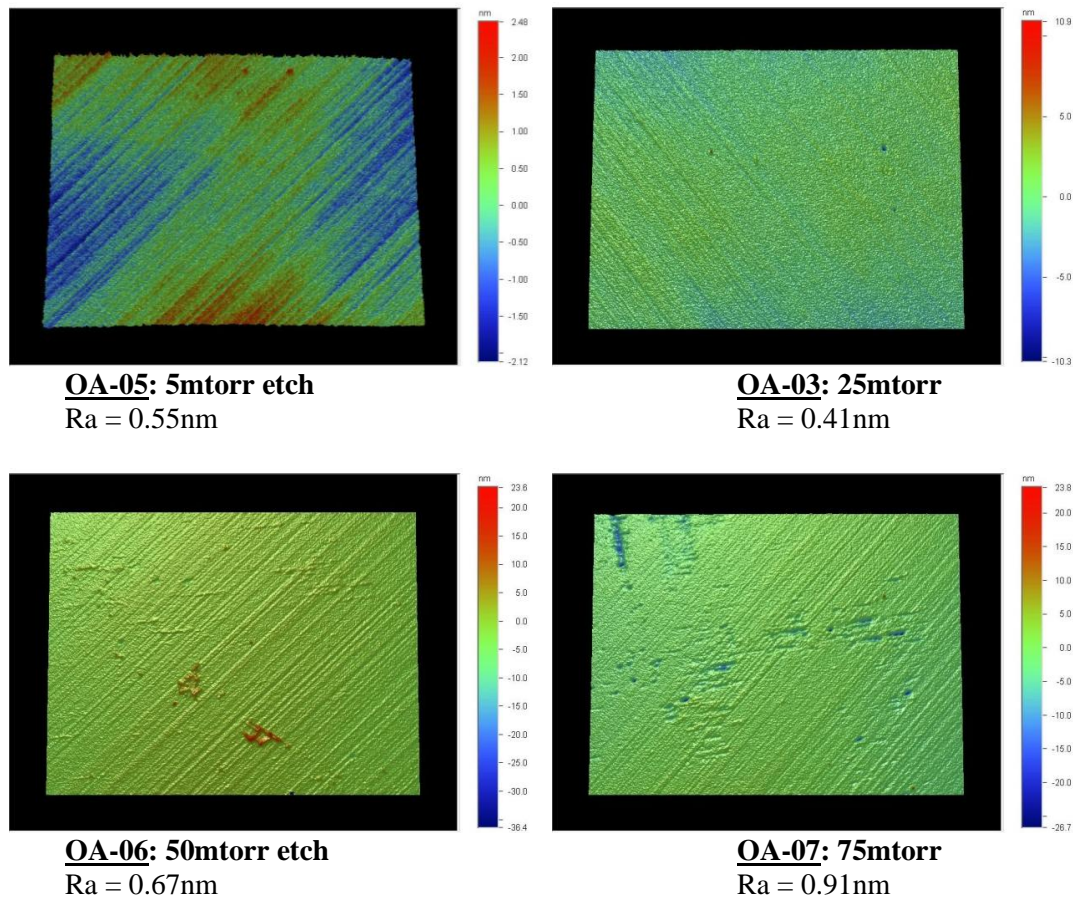


Figure 4-8: Post-etch Wyko surface images and  $R_a$  values for etching study – Off-axis substrates.

From Figure 4-8, the smoothing effect at 25mTorr and the degradation in surface roughness at high etch pressures can be observed visually. Additionally, pre-etch and post-growth wyko images can be found in Appendix C for these samples. Figure 4-9 shows an image obtained from the Wyko optical profiler of the step edge used to determine etch rate at 25mTorr on an off-axis substrate. Here, the improvements in surface quality using the 25mTorr etch can be observed visually. The higher step shows several pits that were most likely induced from micro-fracturing during mechanical polishing. The lower step shows a complete absence of these features. Based on Figures 4-6 through 4-9, it is obvious that 25mTorr is the best pressure for this etching regime for smooth etching at desirable rates.

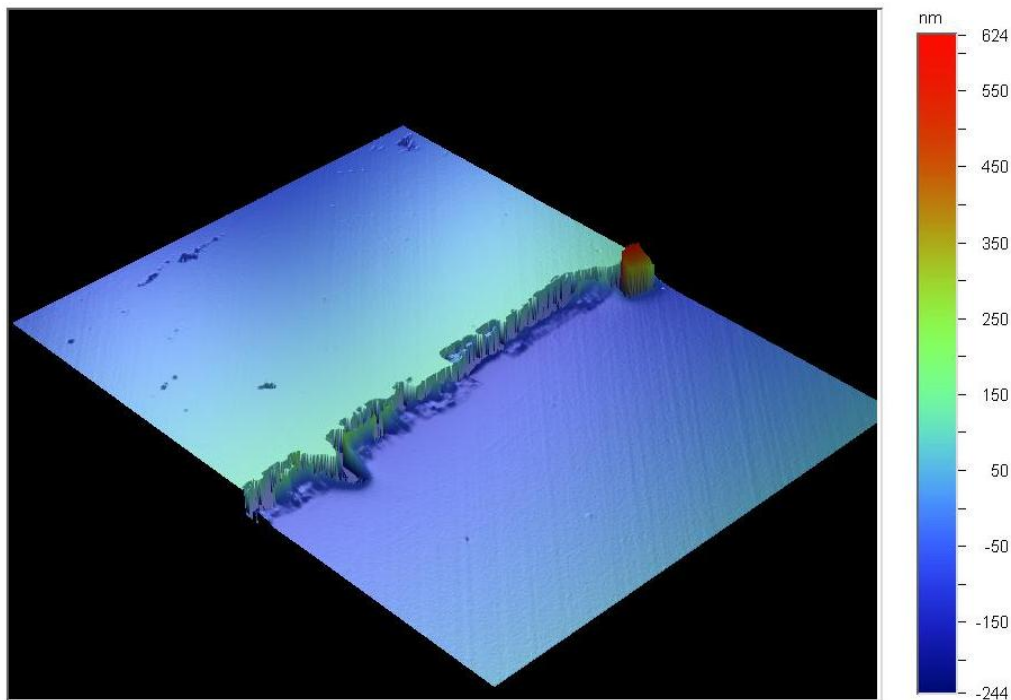


Figure 4-9: Wyko Image of Step Edge etched at 25mtorr for 1 hour – Off-axis substrate.

Now that a sufficient etch pressure has been established, surface morphologies can be compared. Figure 4-10 shows a comparison between two off-axis growths (OA-11 and OA-03) run under the same growth conditions: a pressure of 120 Torr, CH<sub>4</sub> concentration of 4%, temperature of 1100°C, input power of 2300W, and growth time of 4 hours. However, the sample on the left (OA-11) was not treated with a pre-growth etching step while the sample on the right (OA-03) was etched at 25mTorr for 1 hour. Figure 4-11 shows a similar comparison between an etched and non-etched sample (OA-01 and OA-02) ran at 8% CH<sub>4</sub>.

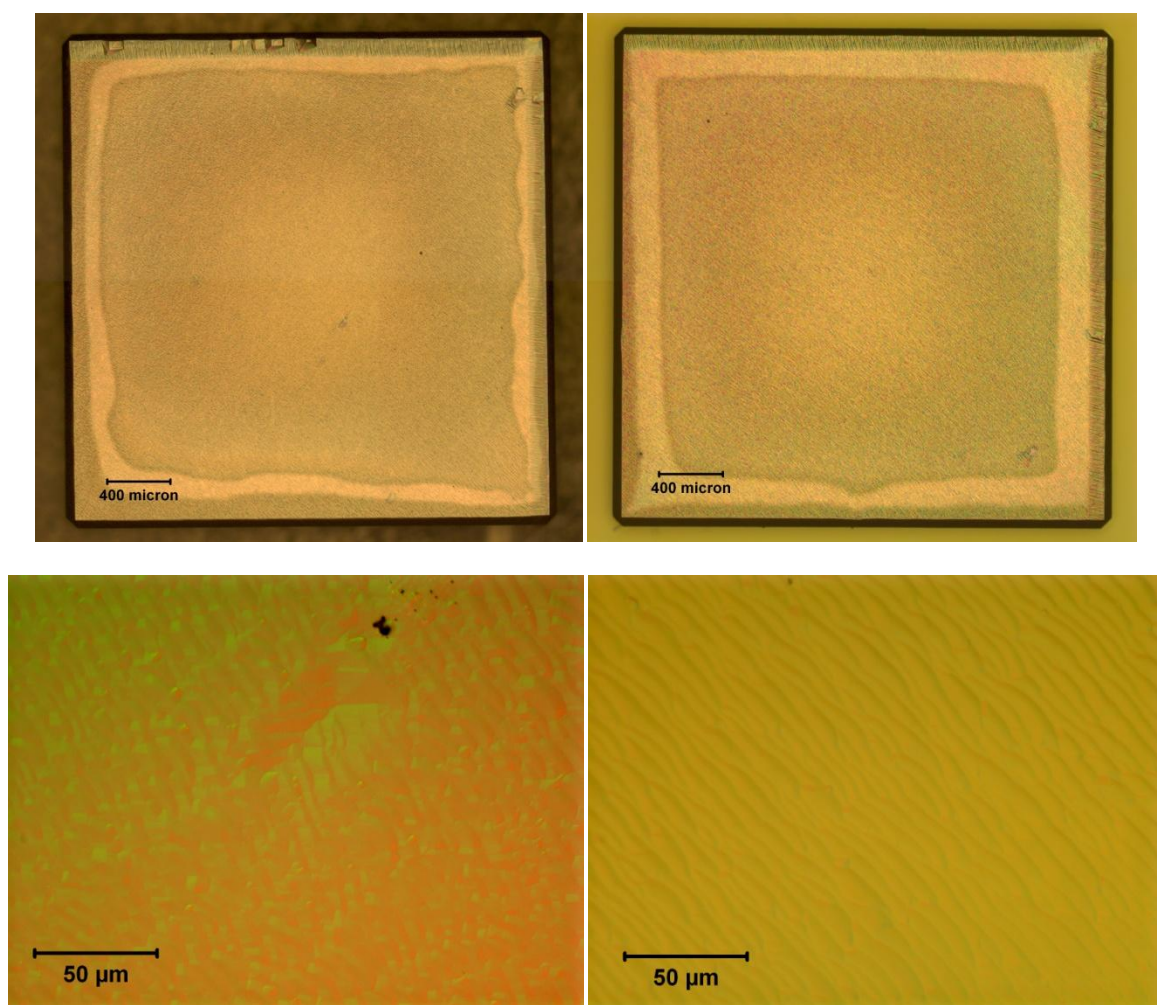


Figure 4-10: Off-axis 50x and 500x Images – Constants: Methane concentration: 4% CH<sub>4</sub>, Pressure: 120 Torr, Input power: 2300W – Left: No Etch, Right: 25mtorr Etch.

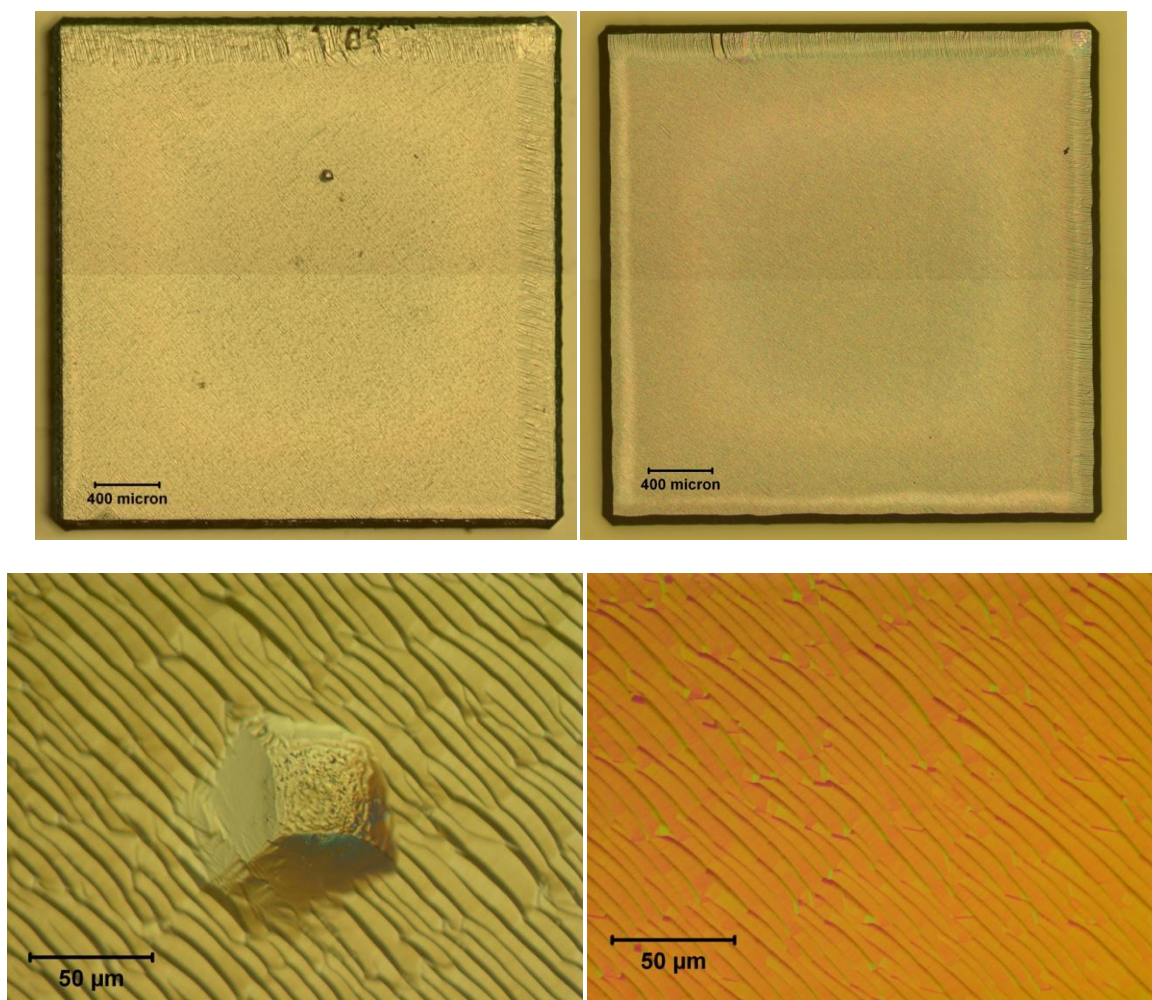


Figure 4-11: Off-axis 50x and 500x Images – Constants: Methane concentration: 8% CH<sub>4</sub>, Pressure: 120 Torr, Input power: 2300W – Left: No Etch, Right: 25mtorr Etch.

Visually, the etched samples for both 8% and 4% CH<sub>4</sub> look smoother, displaying uniform step-flow growth across the entire sample surface. The samples that were grown as-received have several small growth imperfections along the edges and a few small growth hillocks. The growth rates were comparable for etched and non-etched samples. For the 8% CH<sub>4</sub> samples, the non-etched sample had a growth rate of 16.99 $\mu\text{m/hr}$  and the etched sample had a growth rate of 15.26 $\mu\text{m/hr}$ . For the 4% CH<sub>4</sub> samples, the non-etched sample had a growth rate of 7.44 $\mu\text{m/hr}$  and the etched sample had a growth rate of 7.64 $\mu\text{m/hr}$ . The roughness values for the etched 8% CH<sub>4</sub> sample showed an improvement of almost 30nm over the non-etched sample (see Table 4-3).

This suggests that the 25mtorr etch step improves the post-growth film roughness to at least some degree, although the overall improvement in morphology is clearly due to the misorientation.

Figure 4-12 shows a comparison between two *on-axis* growths (CVD-28 and CVD-30) run under the same growth conditions: a pressure of 120 Torr, CH<sub>4</sub> concentration of 4%, temperature of 1100°C, input power of 2300W, and growth time of 4 hours. The sample on the left (CVD-28) was not treated with a pre-growth etching step while the sample on the right (CVD-30) was etched at 25mTorr for 1 hour. Figure 4-13 shows a similar comparison between an etched and unetched sample (CVD-29 and CVD-31) ran at 8% CH<sub>4</sub>.

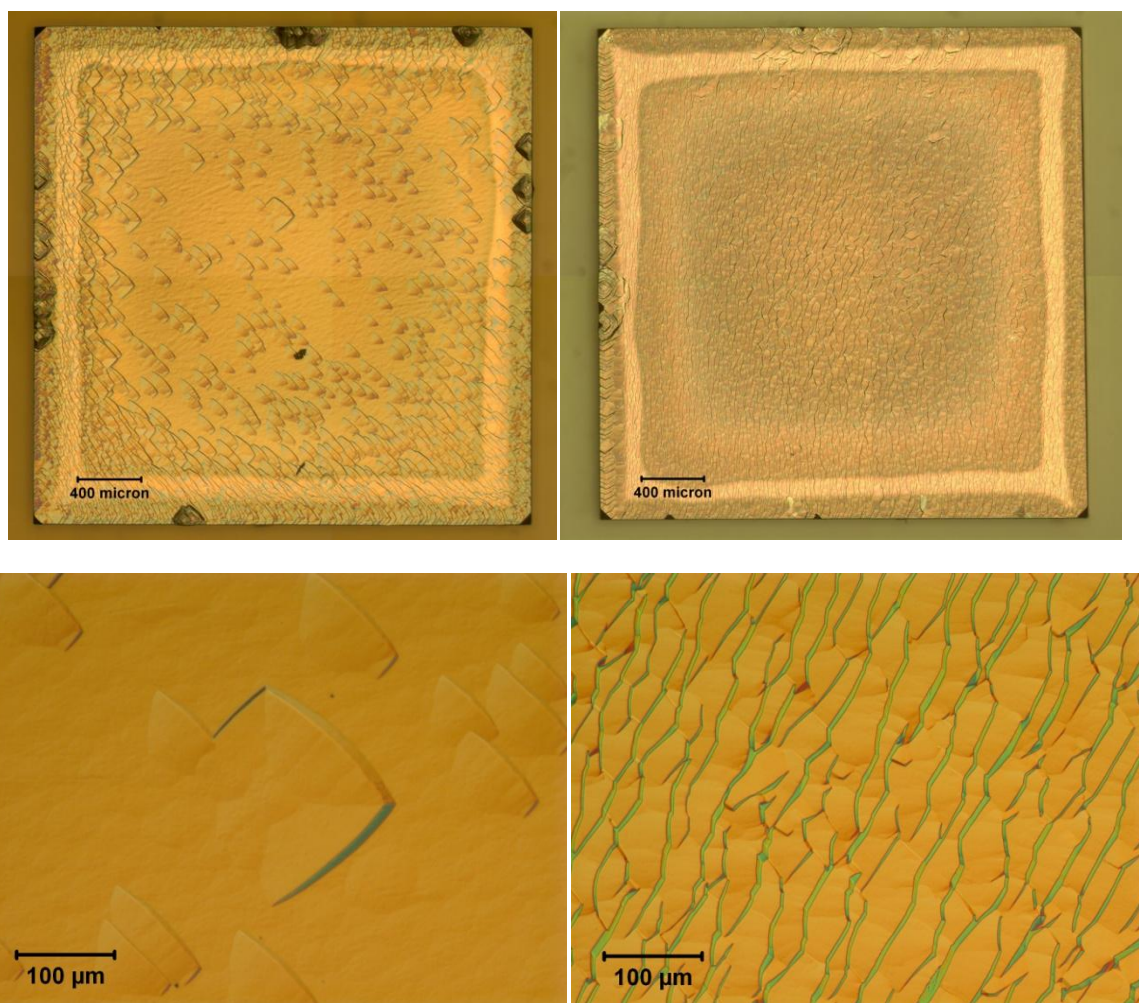


Figure 4-12: On-axis 50x and 200x Images – Constants: Methane concentration: 4% CH<sub>4</sub>, Pressure: 120 Torr, Input power: 2300W – Left: No Etch, Right: 25mtorr Etch.

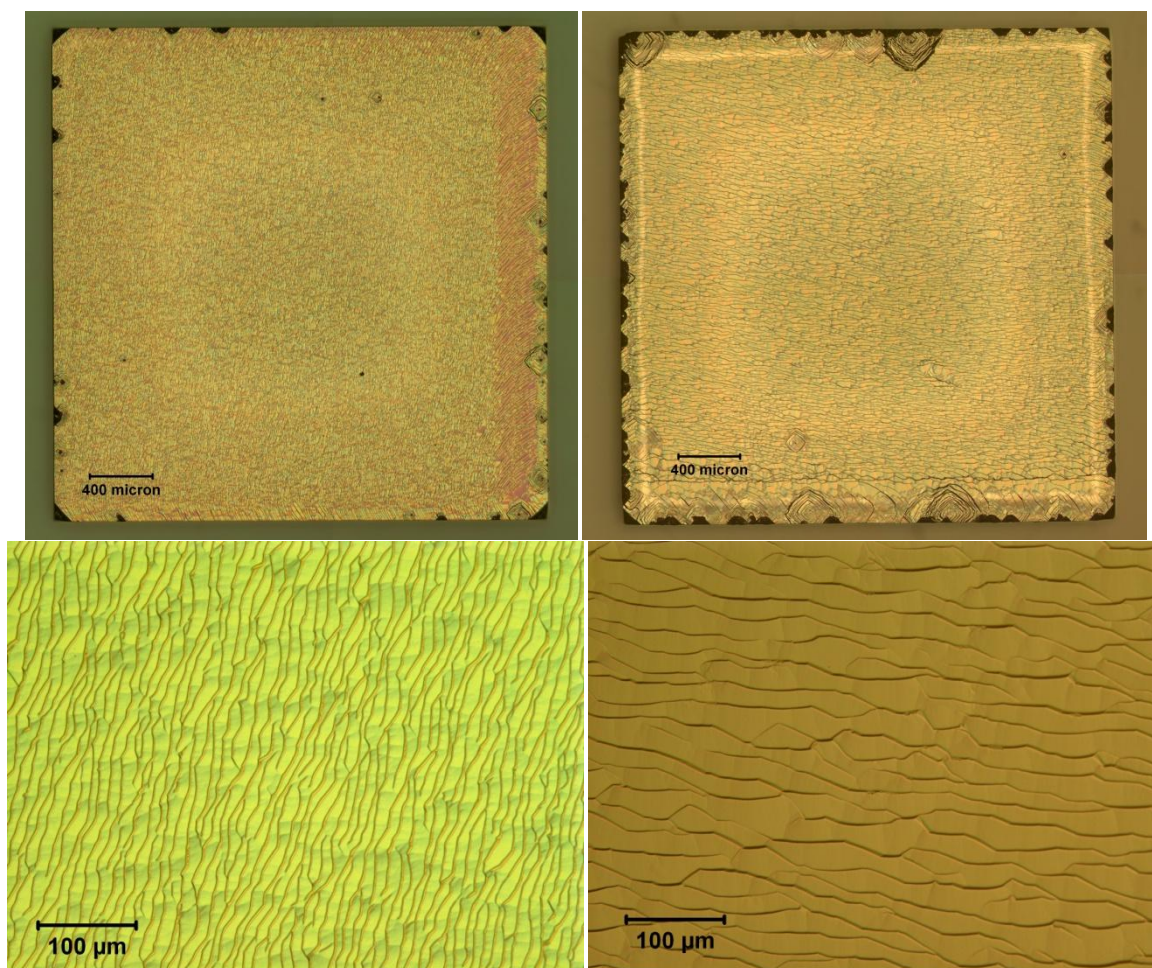


Figure 4-13: On-axis 50x and 200x Images – Constants: Methane concentration: 8% CH<sub>4</sub>, Pressure: 120 Torr, Input power: 2300W – Left: No Etch, Right: 25mtorr Etch.

For 4% CH<sub>4</sub>, the etched sample (CVD-30) shows uniform step-growth across the entire surface while the sample without etching (CVD-28) shows coalescing hillocks with island growth between the larger facets. In the case of on-axis growth, it seems that the pre-growth etch step may actually encouraged step-flow growth at this methane concentration. CVD-30 had a growth rate of 6.0μm/hr and CVD-28 had a growth rate of 4.6μm/hr, indicating that not only does the step-flow growth mode improved overall surface morphology, but it also increases growth rate. The surface roughness Ra values were actually lower for the un-etched sample however; 92.07nm

compared to 195.77nm. Though the surface roughness is lower for this sample, the coalescing islands and hillocks most likely introduce dislocations and impurities into the film. Therefore, even though step-flow growth may produce rougher films in some cases, it is usually a more preferred growth mode. Note that the RIE treatment cannot be credited to any certainty for this difference in growth mode. The contrasting morphologies could be due to a very slight misorientation difference between the two samples and may not be a direct effect of etching as this result was not observed in the subsequent run at the same conditions (See Figure 4-15).

At 8% CH<sub>4</sub> (Figure 4-13), step-flow growth was observed for both the etched and non-etched samples. Contradictory to most literature where step-flow growth only occurs at low methane concentrations, it seems that in this high plasma density growth mode, step-flow growth is favored at high methane concentrations. In addition, the surface morphology of the non-etched sample actually appears better than the etched sample. The surface roughness of the non-etched sample was 124.72nm while the surface roughness of the etched sample actually increased to 194.59nm. Therefore, while etching of *off-axis* substrates leads to a smoother starting surface and consequently a better as-grown surface morphology, etching of *on-axis* substrates leads to a roughening of the substrate surface.

The results shown in Figures 4-6 through 4-9 were based on RIE treatment of *off-axis* substrates. However, when RIE was performed on *on-axis* substrates, the smoothing effect was in fact not observed. It is shown in Table 4-3 that a roughening effect occurs with the on-axis substrates (CVD-30 and CVD-31) that were etched at 25 mTorr. The Ra values for CVD-30 and CVD-31 increased from 0.76nm to 2.50nm and from 0.65nm to 2.82nm, respectively, after etching. Figure 4-14 shows wyko images of the step edge for an off-axis sample and an on-axis sample etched at 25mTorr. Both samples were etched simultaneously to avoid any inconsistencies. The left side of the samples shown below is the etched side and the right side is the masked side.

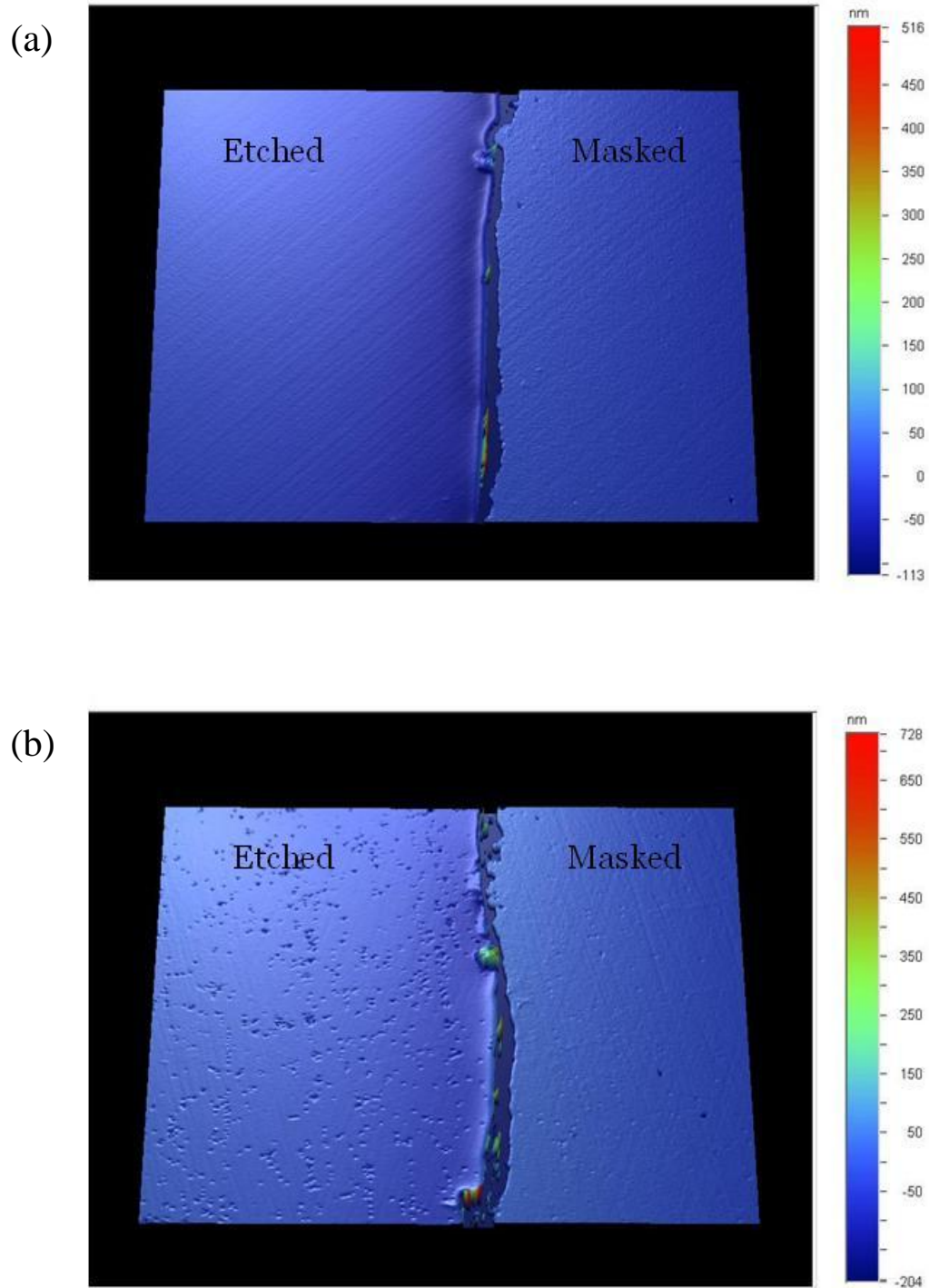


Figure 4-14: Wyko surface profilometer images of step edges – (a): Off-axis substrate: Masked side  $R_a$ : 0.84nm, Etched side  $R_a$ : 0.49nm, Etch Rate: 1.74 $\mu\text{m/hr}$ . (b): On-axis substrate: Masked side  $R_a$ : 0.71nm, Etched side  $R_a$ : 0.98nm, Etch rate: 1.21 $\mu\text{m/hr}$ . Etch pits are formed on the etched side of the on-axis sample

From Figure 4-14, it can be observed visually that a significant amount of pitting occurs on the etched surface of the on-axis substrate while there is no degradation (and in fact an improvement in Ra) of the off-axis substrate surface. This is consistent with reference [54] which shows that the density of etch pits decreases with increasing misorientation angle. In addition, the etch rate (as verified with AFM) of the on-axis seed is  $0.53\mu\text{m/hr}$  less than the etch rate of the off-axis seed. Figure 4-15 shows the post-growth morphologies of the samples shown above. Both samples were growth under identical conditions: 120 Torr, 2300W, 4%  $\text{CH}_4$ , for 4 hours. 50x and 100x optical images show the step edge and both the etched and masked sides clearly. Once again, the etched side is on the left and the masked side is on the right of the image.

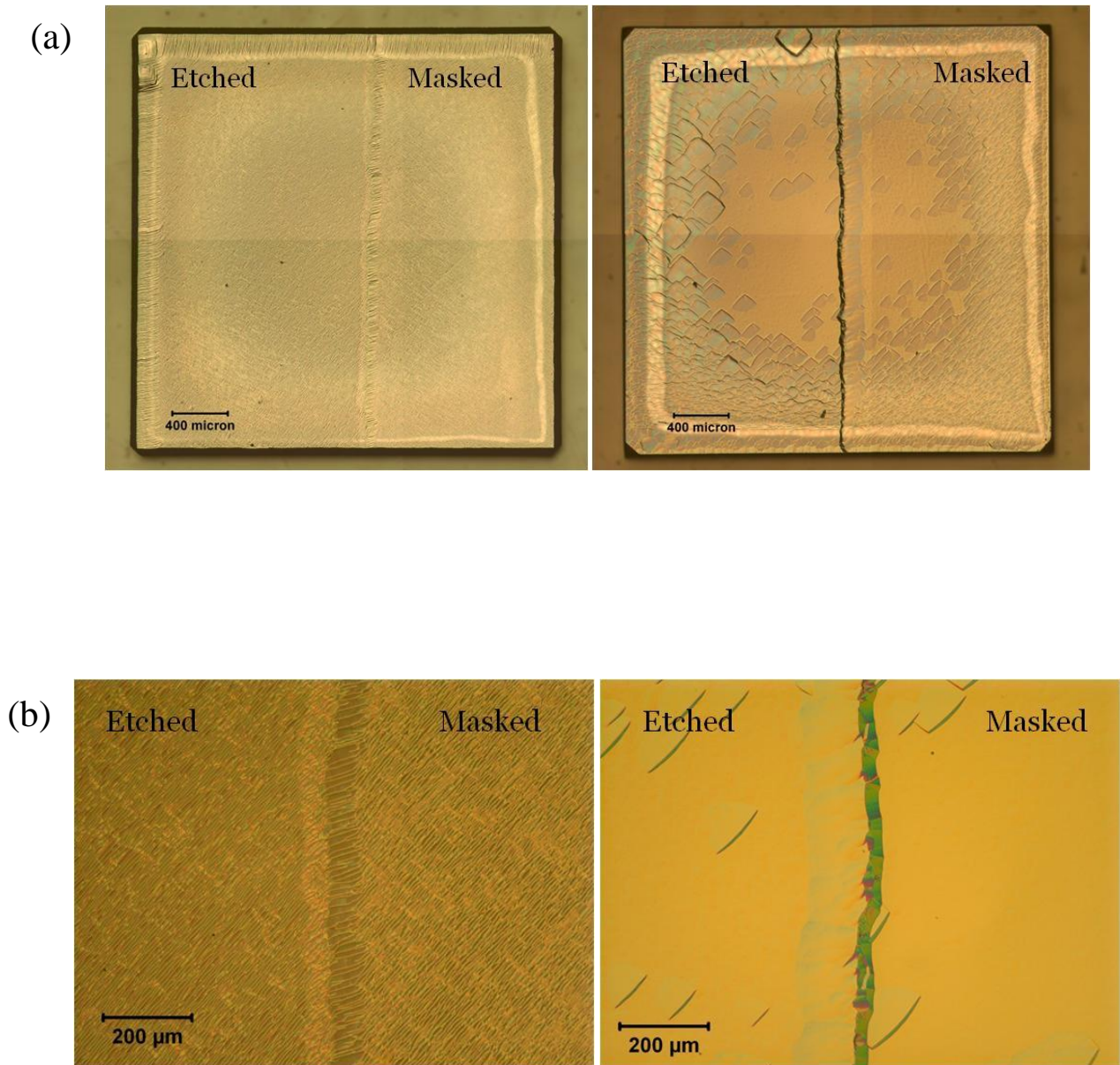


Figure 4-15: Optical Images of etch steps – (a) 50x images: Left: Off-axis, Right: On-axis. (b) 100x images: Left: Off-axis, Right: On-axis. No degradation in surface morphology occurs with etching of the off-axis surface. However, hillocks of a larger size are observed on the etched side of the on-axis film, indicating RIE etching negatively affects the post-growth surface morphology of on-axis diamond growth.

The off-axis sample shows no apparent degradation to the as-grown surface on the etched side. On the other hand, the etched side of the on-axis sample shows hillock features that are physically larger compared to the masked side.

It seems that the RIE pre-growth surface treatment can be somewhat beneficial in removing surface damage caused by mechanical polishing. However, the degree of misorientation has a significant effect on the roughness of the etched surface. Etching of on-axis or close to on-axis substrates may in fact damage the starting surface by introducing pitting, leading to a degraded as-grown epitaxial film.

The difference in etching morphology between off-axis and on-axis substrates can be explained by the etching mechanisms occurring at the diamond surface. Studies have suggested that the etching of (100) diamond surfaces can proceed two ways: (a) by regression of pre-existing steps caused by the misorientation of the substrate surface, and (b) by creation and subsequent regression of new steps in the form of etch pits [48]. In other words, the misoriented substrates provide a high density of crystallographic step sites where carbon atoms can be removed easily. These steps will then retreat during etching, leading to mechanism (a). On well-oriented substrates however, the density of crystallographic step sites is very small and these surfaces have large terraces between any such step sites. Therefore, removal of  $sp^3$  carbon on terraces between steps is much more likely than it would be on a misoriented surface. When this happens, new steps are created and further etching will take place at such sites, leading to the formation of etch pits (mechanism (b)) [48]. The etch pits can then lead to local areas of enhanced growth and form hillocks during deposition. Therefore, RIE of (100) diamond is most beneficial for substrates that have some degree of misorientation from the (100) plane.

### 4.3: Summary of Results

In order to understand the effects of misorientation and pre-growth etching on the deposited morphology of diamond films, it is important to understand what is taking place at the surface atomically. When a molecule is transported through the plasma sheath and approaches the diamond surface, it will begin to feel an attraction to the surface molecules. Van der Waals forces will pull the molecule into a weakly-adsorbed state known as physisorption, where the molecule cannot escape the potential well at the surface but can still migrate along the surface [44]. The mobile molecule will then hop (diffuse) between atomic surface sites until it either gains enough energy to break the potential well of the surface and desorb, or forms chemical bonds with surface atoms and is incorporated into the film. The latter is known as chemisorption [44]. In the case of MPCVD diamond deposition, carbon radicals migrate across dimer chains or rows of a hydrogenated diamond surface until a hydrogen abstraction reaction occurs and the carbon atom is incorporated into the film [18-20, 45, 48]. Equation 4-1 describes the diffusion on the surface of a material where  $\Lambda$  is the surface diffusion length,  $D$  is the surface diffusivity, and  $t$  is time.

$$\Lambda = 2\sqrt{Dt}$$

Equation 4-1: Surface Diffusion Length [44]

The surface diffusion that takes place prior to chemisorption is one of the most important determinants of film structure [44]. Surface diffusion allows atoms on the surface of diamond to find the most active sites for chemisorption. In some cases the most active sites are surface defects such as dislocations. Here, the weaker C-C bonds and dangling bonds at the dislocation

provide a favorable site in which atoms diffusing on the surface can easily react with chemically and become incorporated. Such incorporation however inevitably leads to local areas of enhanced growth and hillock formation. Crystallographic step edges also provide favorable chemisorption sites due to the increased density of dangling bonds at such locations. Incorporation at crystallographic edges results in step-flow growth propagating in the  $\langle 110 \rangle$  directions. As explained previously, step-flow growth is the preferred method of diamond growth for high-quality, low-impurity films. Therefore, it is desirable to increase the number of crystallographic step edges in which carbon atoms can be preferably incorporated and decrease the density of unwanted nucleation sites, such as dislocations and crystalline imperfections. One way to increase the density of crystallographic step edges is to misorient the substrate, as shown in section 4.1. To decrease the density of unwanted nucleation sites, such as crystalline imperfections, reactive ion etching was shown in section 4.2 to non-preferentially etch the first few microns of (off-axis) surface material, removing micro-fractures and imperfections caused by mechanical polishing.

Off-axis growth was shown in section 4.1 to suppress hillock formation and improve the surface morphology of the deposited films. Step-flow growth was observed on most samples except for the samples grown at low methane concentrations. On the other hand, when on-axis substrates were grown under identical conditions, island growth dominated and macroscopic hillocks and facets were observed. Such hillock growth results in the coalescing of “islands” and can induce dislocations, stress, and impurities into the film.

Figure 4-16 depicts a crystallographic view of a typical on-axis diamond surface (left) compared to an off-axis diamond surface (right).

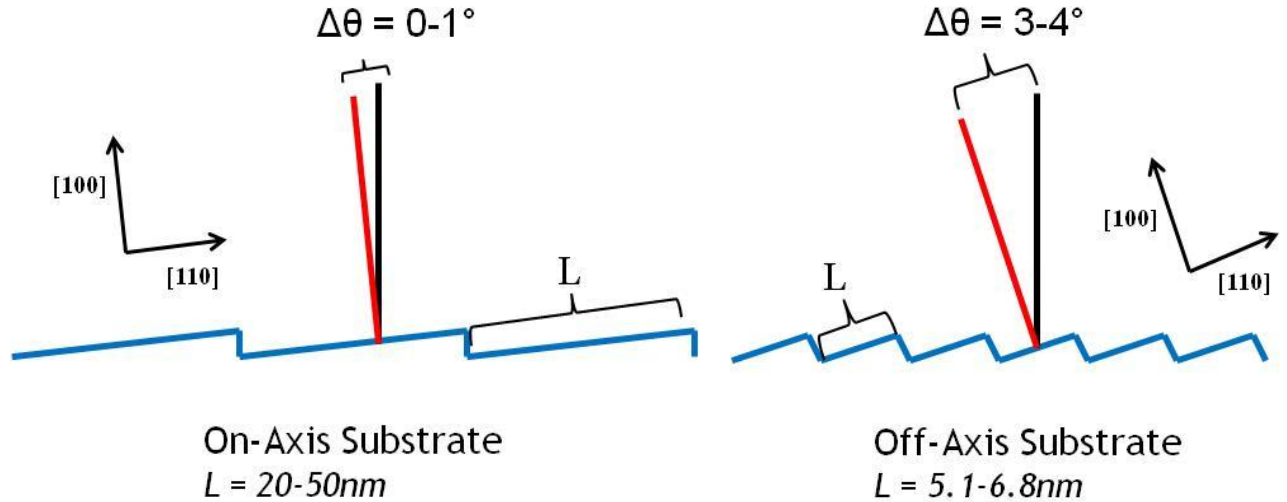


Figure 4-16: Crystallographic Terrace Steps – Left: On-axis, Right: Off-axis. Terrace length of nominally on-axis substrates is between 20-50nm while misorientation of 3-4° results in a decrease of the terrace length to 5.1-6.8nm.

The terrace length “L” is significantly shortened when the substrate is misoriented.

Equation 4-2 gives an expression for determining the terrace length, where “ $\Delta\theta$ ” is the misorientation in radians and “a” is the lattice constant (which is 3.57Å for (100) diamond). For the case of on-axis growth, where a maximum misorientation of 1° is assumed, terrace lengths are between 20 and 50nm, depending on the exact misorientation. Conversely, for misorientations of 3-4° (such as the substrates used in the present study), terrace lengths are around 5.1-6.8nm in length. Therefore, the terrace lengths are an order of magnitude smaller for off-axis substrates.

$$\Delta\theta = \frac{a}{L}$$

Equation 4-2: Off-axis Angle [44]

When  $L < \Lambda$ , atoms diffusing on the surface are more likely to diffuse to a terrace edge and nucleate there than to form new nuclei within the terraces [44]. In addition, the increased density of terrace edges creates a higher probability that the adatoms will find a terrace edge before they can migrate to a dislocation site and nucleate. This explains the differences in morphology between on-axis and off-axis substrates observed in section 4.1. There is a high probability that atoms could not diffuse to terrace edges in the case of on-axis growth. Instead, they nucleated between terrace edges (promoting island growth) or worse, came across a dislocation site and formed hillocks. For off-axis growth, atoms had a much higher probability of reaching a terrace edge and nucleating to promote step-flow growth.

Reactive Ion Etching (RIE) was shown in section 4.2 to improve post-growth morphology of both on-axis and off-axis samples. This was achieved by preferentially removing the first few microns of surface material, thus removing any crystalline imperfections such as micro-fractures from mechanical polishing of the substrates. Reactive ion etching utilizes two etching mechanisms: chemical reactive etching and physical sputtering. As explained in section 1.6, control of both these mechanisms is the key to realizing a quality etch morphology. Figure 4-6 showed that at 25 mTorr, the etching step actually had a smoothing effect on off-axis substrates. At this pressure, the contributions from chemical reactive etching and physical sputtering were similar. Therefore, this etch pressure was used for all subsequent experiments. It was shown that the ICP RIE treatment of on-axis substrates created a high density of etch pits however (see Figure 4-14). Therefore, RIE may only be suitable for misoriented substrates.

Raman was used to determine the crystalline quality and phase of the off-axis samples used in the etch study. Figure 4-17 shows the Raman peaks obtained from the as-received substrate (pre-etch), the substrate after RIE treatment (post-etch), and the deposited film (post-growth).

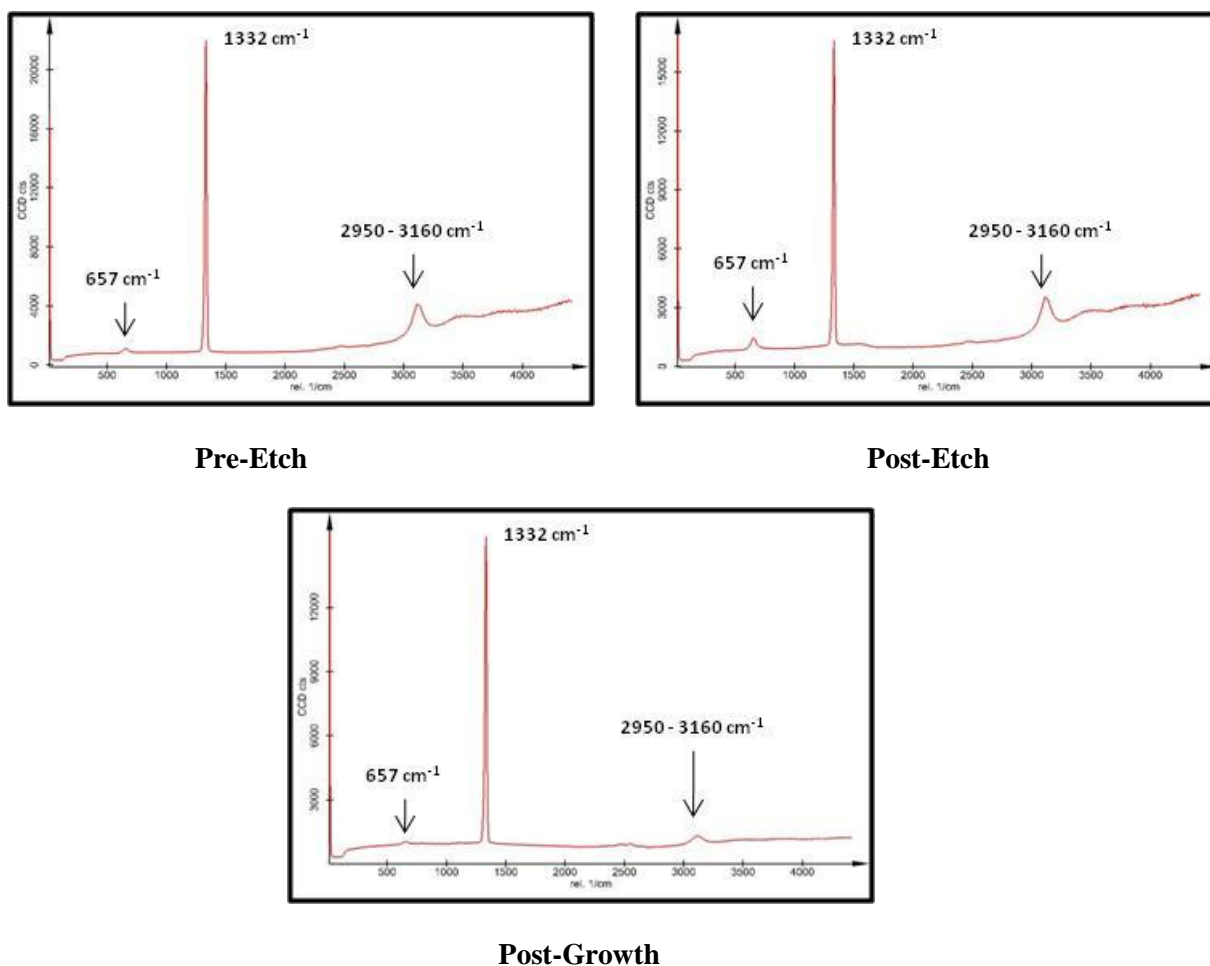


Figure 4-17: Raman peaks of an off-axis sample. From right to left: Pre-etch, post-etch (25 mtorr etch for 1 hour), and post-growth (120 Torr, 8% CH<sub>4</sub>, and 2300W input power).

The diamond peak is located at  $1332\text{ cm}^{-1}$  and the graphitic peak (G-Band) is observed between  $1520\text{-}1610\text{ cm}^{-1}$  [47]. The pre-etch Raman peak and the post-etch Raman peak look very similar, showing a strong  $\text{sp}^3$  diamond peak and containing no  $\text{sp}^2$  graphitic phases. Therefore, it is apparent that there is no degradation in film quality from the RIE treatment. Post-growth Raman shows a strong diamond peak similar to the substrate. Additionally, two background peaks (one at  $657\text{ cm}^{-1}$  and one from  $2950\text{-}3160\text{ cm}^{-1}$ ) observed in the pre-etch and post-etch scans are significantly reduced after growth. The peak at  $657\text{ cm}^{-1}$  is common in the spectra of

CVD diamond films treated by transition metals at high temperatures [47]. This could have been induced during mechanical polishing of the commercial substrates by the manufacturer. The peak from 2950-3160 $\text{cm}^{-1}$  is observed in the spectra of CVD diamond grown with a small amount of oxygen or nitrogen in the process gas mixture [47]. The manufacturer of the substrate material probably added one or both of these gases to the process to increase growth rate. Some additional bands are observed beyond 3200 $\text{cm}^{-1}$  and may be attributed to 3<sup>rd</sup> order Raman scattering [47]. The decrease in the intensity of the two background peaks after growth indicates that the deposited film is of a higher quality than the substrate. Appendix F shows Raman spectra for off-axis and on-axis growths that were etched at 25 mTorr. Here, the effect of methane concentration on the post-growth Raman spectrum can be observed. It seems that for off-axis and on-axis growth, the peak from 2950-3160 $\text{cm}^{-1}$  decreases as methane concentration is increased. This suggests that higher methane concentrations lead to higher crystalline quality; at least for the present growth conditions.

Quantitative Raman results are given in Appendix E. Here, 10 $\mu\text{m}$  line scans were taken for each sample; pre-etch, post-etch, and post-growth. The full width half maximum (FWHM) as well as the center of mass (COM) values of the diamond peaks were averaged over the entire line scan and the standard deviation is shown for the data. FWHM values are generally used as an indicator of overall quality, where a low FWHM is of high quality. COM values are used to determine if any stress has been incorporated into the film, where a shift to the right (upward shift) of the theoretical center of mass indicates a compressive stress and a shift to the left (downward shift) indicates a tensile stress [43]. Appendix E shows that for all etching conditions and growth conditions studied in Chapter 4, there were no conditions which resulted in a significant change in either FWHM or COM values. This indicates that the crystalline quality was preserved throughout the etching treatment as well as the film deposition. Also, no induced stress was observed following etching or film deposition.

## Chapter 5

### **Effect of Argon Concentration on Grain Size of Polycrystalline Films**

The following chapter will deviate somewhat from the focus of the rest of this thesis. Until now, this thesis has attempted to understand the growth mechanisms and reactor kinetics of (100) single crystal diamond in an effort to improve the crystalline quality and purity of intrinsic homoepitaxial diamond for use in high power, high frequency devices and detection applications. However, additional research attention was directed towards the development of a nanocrystalline diamond growth process in the Lambda MPCVD reactor. This chapter will discuss the effect of argon concentration on the growth rate and grain size of polycrystalline diamond deposition.

#### **5.1: Background**

Polycrystalline diamond (PCD) is essentially a film of coalescing large diamond crystals. The film is characterized as microcrystalline (MCD) diamond when the grain sizes are reduced to a few microns. Nanocrystalline diamond (NCD) can be described as a polycrystalline diamond film with very fine grains, typically below 100nm and has been observed as small as 5-15nm [2]. This film of ultra fine diamond crystals can be deposited onto a wide range of substrates including glass, silicon, polycrystalline diamond, and several metals [2]. Nanocrystalline diamond is expected to play a large role in the development and progress of several emerging applications including: MEMS and NEMS devices, optical coatings, thermal management, electrochemistry, and bioelectronics.

Unlike the columnar growth of typical PCD, the grain size of NCD does not scale with film thickness. Due to the Ar-rich plasma, NCD continuously re-nucleates during growth [2]. Consequently, the very fine grains lead to a large density of grain boundaries in the film (~10% of the film volume). This leads to a greater proportion of non-diamond or  $sp^2$  carbon incorporation in the film [2]. In addition, the Ar-rich plasma used in NCD growth results in very low amounts of atomic hydrogen in the plasma, leading to negligible etching of  $sp^2$  carbon. In contrast, for typical PCD and MCD growth (using a hydrogen-methane plasma) there exist a continuous etching of  $sp^2$  carbon by atomic hydrogen. This causes the re-nucleation effect (observed in the Ar-rich plasma) to be suppressed [2]. Because of the difference in  $sp^2$  carbon between NCD and PCD, the electrical conduction mechanisms are quite different. Due to the low proportions of  $sp^2$  to  $sp^3$  carbon, PCD and MCD are efficient for electrochemistry applications, where  $sp^2$  carbon would negatively influence the electrode stability. However, it is possible to generate a highly n-type material with NCD by the addition of nitrogen to the gas phase. This type of electrical transport is dominated by grain boundary conduction, while n-type conduction is very difficult to achieve with PCD and MCD [2]. Therefore, a large interest in the development of nanocrystalline diamond growth has sparked due to its unique electrical advantages over PCD, MCD, or even single crystal diamond.

## **5.2: Growth Rate vs. Argon Concentration**

All runs were done in the Lambda Technologies MPCVD reactor described in Chapter 2. Typical PCD, MCD, and NCD growth is carried out on seeded substrates. However, for this study, 5mm x 5mm x 0.4mm PCD substrates were used for simplicity as no seeding process needed to be developed. Hydrogen, methane, and argon were used as the process gases.

Substrates were cleaned with acetone in an ultrasonic bath for 15 minutes. For all growths, configuration 3 was used with a 7mm raised and tapered molybdenum seed holder. Pressure was maintained at 120 Torr, methane concentration was fixed at 1%, and the growth time was 4 hours. Temperature was held at 1100°C. However, at higher argon concentrations (>30%), there appeared to be some sort of interference with the pyrometer, making accurate temperature measurements impossible at high concentrations of argon in the gas phase. Therefore, when the temperature could not be read, the input power was fixed at 2500W. Table 5-1 details the runs conducted for this study and the resulting growth rates. Note that Poly-19 utilized an argon concentration of 98%, which required a mixed cylinder containing 90% argon and 10% hydrogen in place of a pure hydrogen cylinder due to limitations associated with the hydrogen mass flow controller. Figure 5-1 plots the growth rate as function of argon concentration.

Table 5-1: Growth Results for Various Argon Concentrations

Run	Ar %	H <sub>2</sub> %	CH <sub>4</sub> %	Flow (Ar/H <sub>2</sub> /CH <sub>4</sub> ) (sccm)	Avg. Growth Rate (μm/hr)
Poly-13	95	4	1	570/30/6	0.59
Poly-14	85	14	1	170/30/2	6.14
Poly-15	0	99	1	0/198/2	3.15
Poly-16	90	9	1	270/30/3	2.79
Poly-17	70	29	1	100/43/1.5	7.48
Poly-18	30	69	1	100/233/3.5	4.37
Poly-19	98	1	1	270/30/3	0.20
Poly-20	99	0	1	198/0/2	0.35

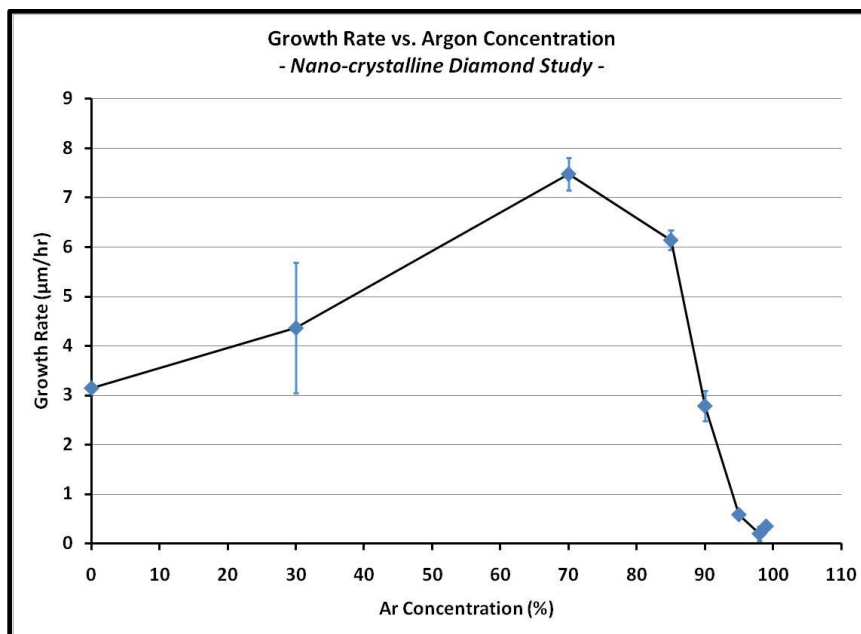


Figure 5-1: Nanocrystalline Diamond Growth Rate vs. Argon Concentration. The increase in growth rate up to 70% Ar is due to the enhanced dissociation of methane by argon ions. Above 70% Ar however the growth rate drops off significantly due to detachment of the plasma from the substrate. Growth rate was averaged from the two measurement techniques. Error bars indicate the standard deviation of the data.

From Table 5-1 and Figure 5-1, it is obvious that the growth rate is significantly affected by the argon concentration. Growth using purely hydrogen and methane resulted in a growth rate of  $3.15\mu\text{m/hr}$ . Growth rate increases with the addition of argon up to  $7.48\mu\text{m/hr}$  at 70% argon. Growth rate then decreases sharply at argon concentrations greater than 70%. At 98% argon, the growth rate essentially disappears, depositing only graphitic particles onto the substrate surface. This will be subsequently discussed and shown in the optical images of section 5.3.

The increase in growth rate with the addition of argon to the gas phase can be attributed to the increase in the C2 to H $\alpha$  peak ratios with increasing argon concentration. Figure 5-2 compares the OES data for 0%, 30%, 70%, and 98% argon and Figure 5-3 plots the C2/H $\alpha$  peak ratios.

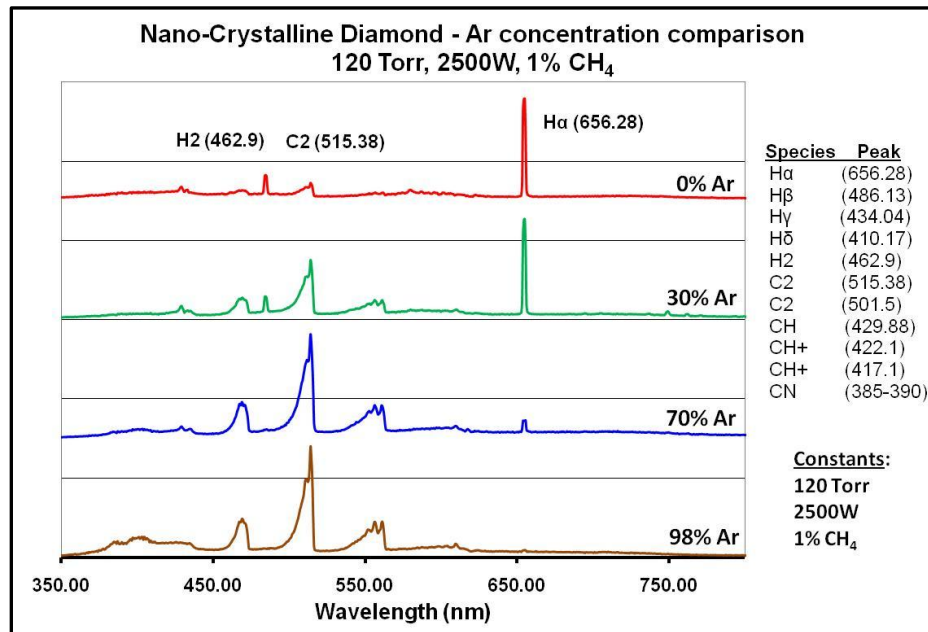


Figure 5-2: OES Spectra at Different Argon Concentrations. As the Ar concentration is increased the C2 peak increases while the H $\alpha$  peak decreases, leading to reduced contributions from atomic hydrogen etching and promoting secondary nucleation

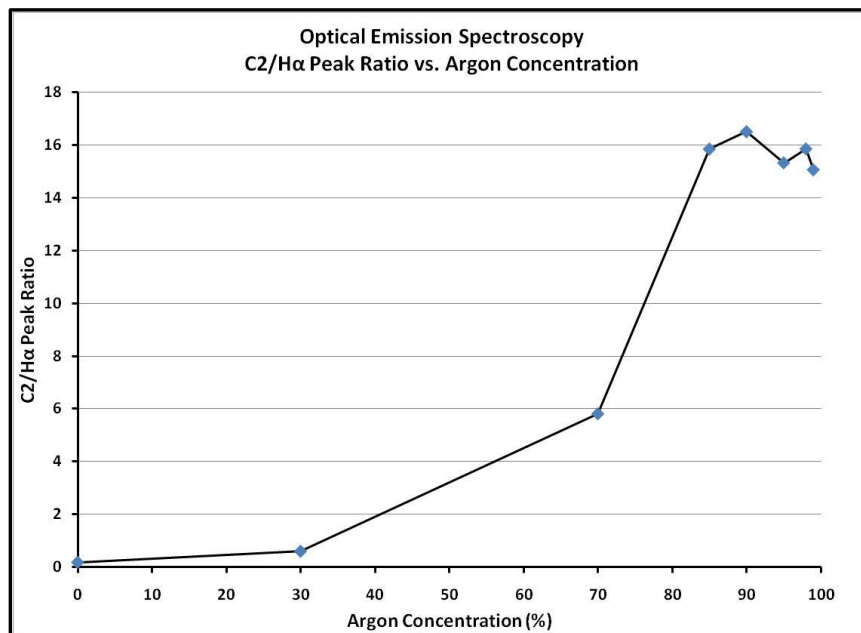


Figure 5-3: OES C2/H $\alpha$  Peak Ratios vs. Argon Concentration

The C2 peak increases significantly with increasing argon concentration while the H $\alpha$  peak decreases until it essentially disappears. This could explain the increased growth rate with increasing argon content. The addition of argon to the source gases promotes a higher density of active carbon species in the gas phase, which is believed to be the cause of the secondary nucleation behavior of NCD [49]. Therefore, there are far greater carbon radicals that can contribute to growth than in the case of a purely hydrogen and methane gas mixture. Also, the decreasing concentration of hydrogen in the gas phase leads to less hydrogen etching. Thus, growth (rather than etching) dominates. The sharp drop off at argon concentrations greater than 70% may be explained by the plasma behavior. When there is still a considerable amount of hydrogen in the gas phase, the plasma remains in contact or close to the substrate. Increasing argon concentrations causes the plasma to move towards the top of the bell jar, bringing it out of contact with the substrate. As we have seen from Chapter 3, poor plasma-substrate contact leads to poor growth rates.

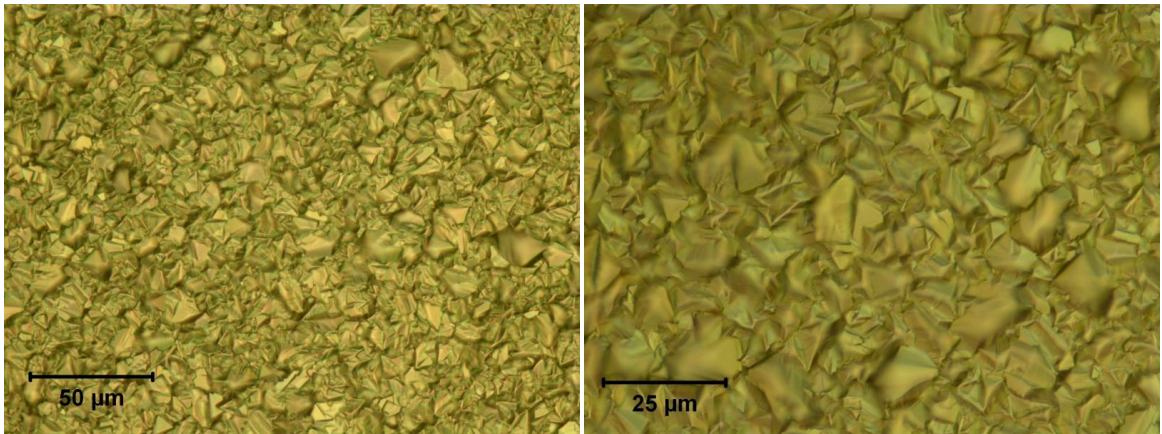
### **5.3: Effects of Argon Concentration on Grain Size and Morphology**

As explained previously, the effect of the argon plasma on the grain size of polycrystalline diamond films can be significant. A hydrogen-rich plasma will preferentially etch non-diamond sp<sup>2</sup> phases and grow columnar grains whose grain size increases with film thickness. On the other hand, an argon-rich plasma will not etch graphitic phases and will promote continuous re-nucleation, leading to ultra fine grains that are independent of film thickness. Depending on the percentage of argon in the gas phase, the nucleation behavior, and indeed the grain size, can vary considerably [49]. Here, the effect of argon concentration on the

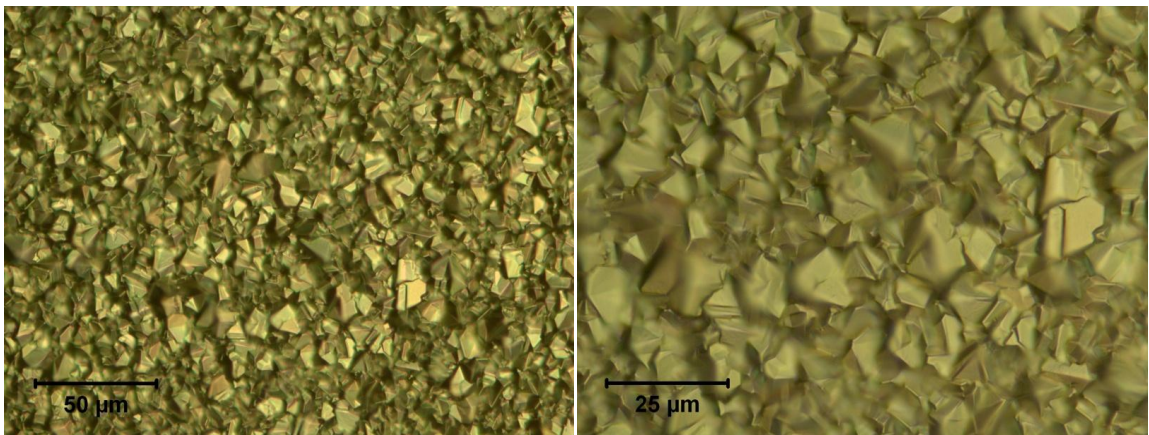
morphology and grain size of NCD films deposited on PCVD substrates is examined. Figure 5-4 shows 500x and 1000x images for argon concentrations of 0, 30, 70, 85, 90, 95, 98 and 99% Ar.

### 500x Images

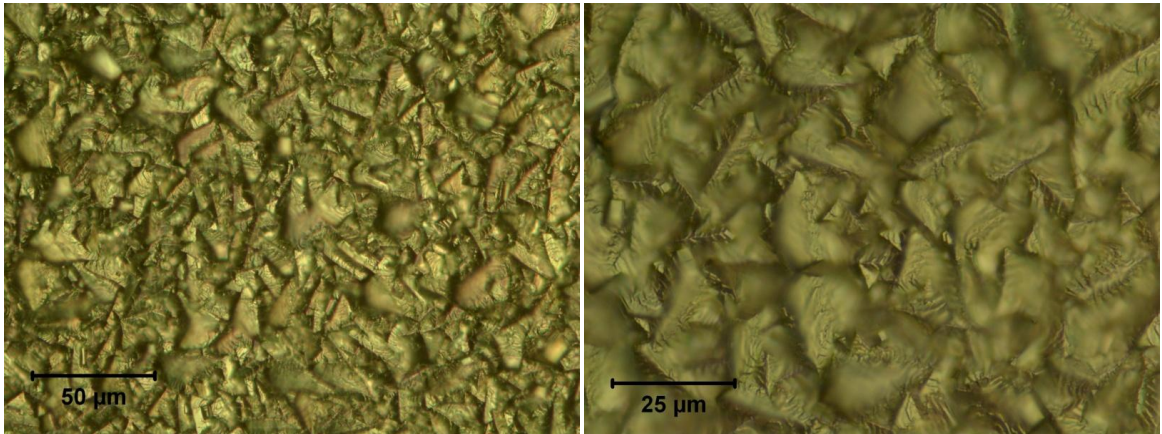
### 1000x Images



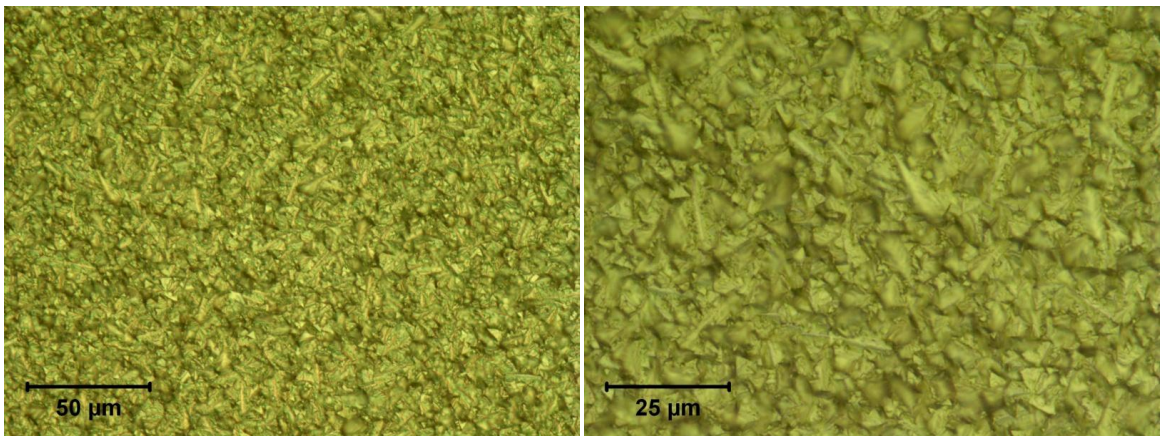
**0% Ar; Thickness: 12.59μm**



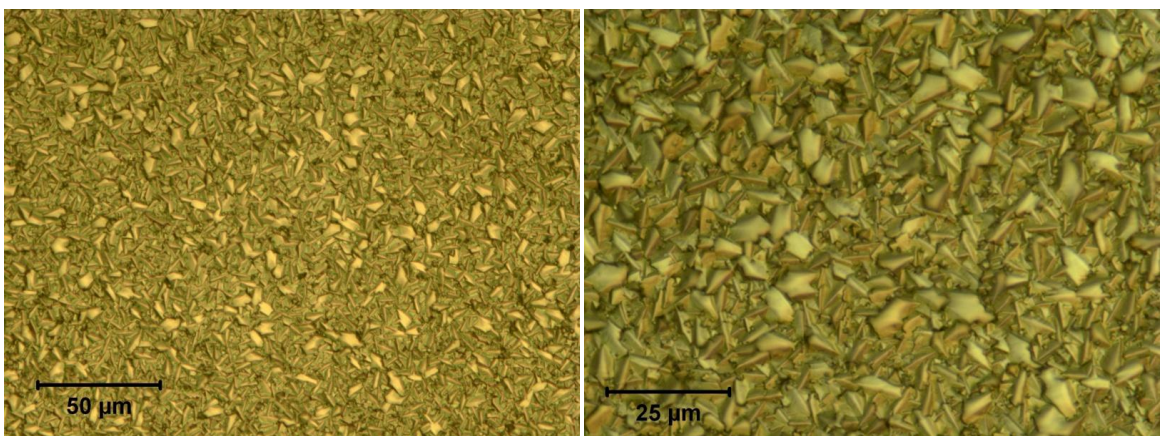
**30% Ar; Thickness: 17.46μm**



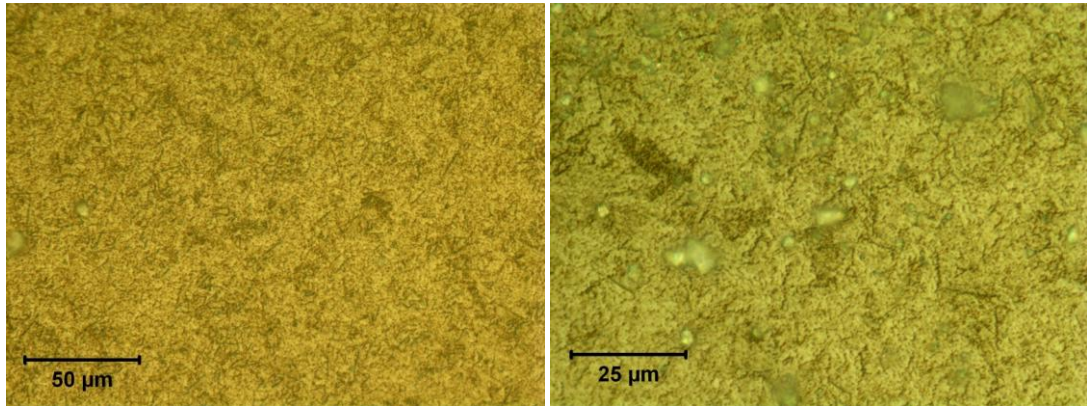
**70% Ar; Thickness: 29.93μm**



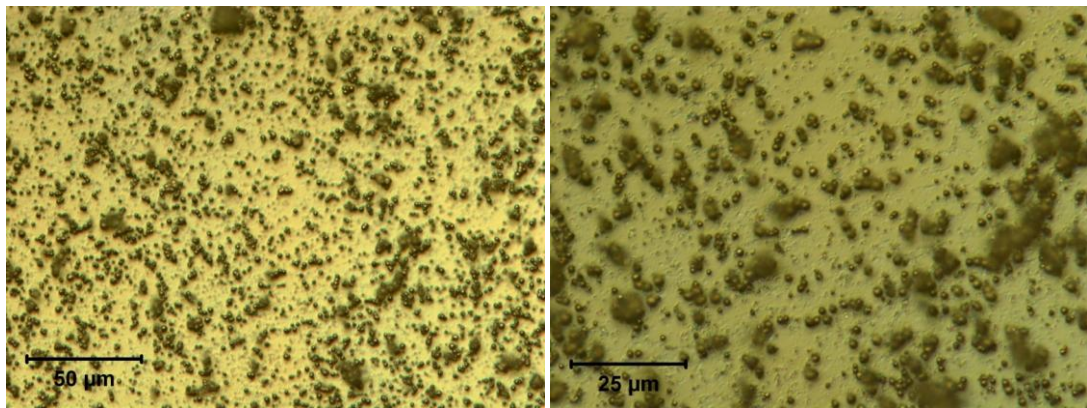
**85% Ar; Thickness: 24.57μm**



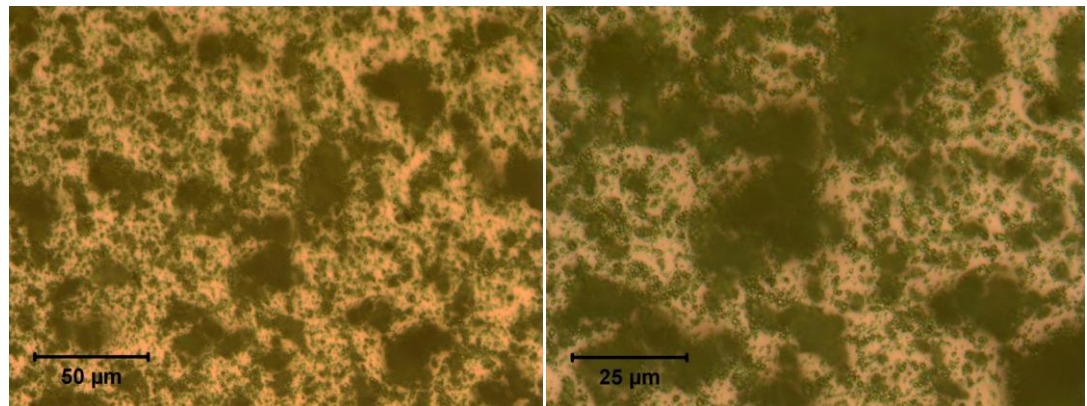
**90% Ar; Thickness: 11.14μm**



**95% Ar; Thickness: 2.35μm**



**98% Ar; Thickness: 0.80μm**



**99% Ar; Thickness: 0.80μm**

Figure 5-4: Optical Images of morphology development. Left: 500x, Right: 1000x. Grain increases in size with increasing argon concentration up to 70% Ar due to columnar grain growth. Above 85% Ar, grain size decreases significantly due to secondary nucleation. At 98% and 99% however, NCD did not nucleate onto the surface.

The grain size and morphology do not seem to change much with a moderate addition of argon to the gas phase. Even at a concentration of 70% Ar, the grains are very similar to the argon-free growth process. Above 70% however, the grain size begins to decrease. A decrease in growth rate was also observed above 70% argon. At 85% and 90%, a transition from polycrystalline diamond growth to microcrystalline diamond growth occurs. At 95% argon, grain sizes approaching the nano-scale are observed. These transitions between PCD, MCD, and NCD are fairly consistent with literature [49]. However, the growth rate at 95% was very low so it cannot be assumed that the grains wouldn't enlarge with increasing film thickness, indicating microcrystalline growth. Above 95% there appeared to be no nucleation of diamond on the substrate. Instead, macro-particles began to nucleate randomly within the plasma and coated the substrate (along with the rest of the susceptor). This was especially true for 99% argon. Figure 5-5 shows pictures of the susceptor after growth runs using 98% and 99% argon. Dark carbon deposits are observed covering a large portion of the susceptor and substrate surface. This coating was easily wiped off and did not adhere to the substrate. Therefore, it can be assumed that no NCD deposition took place at argon concentrations greater than 95%.



Figure 5-5: Carbon Deposition on Susceptor. Left: 98% Ar, Right: 99% Ar

#### 5.4: Raman Characterization and Summary of Results

From section 5.2 and 5.3, it is obvious that the concentration of argon has a significant impact on the growth rate and film morphology. In this section, Raman microscopy will be used to determine if nanocrystalline diamond was truly deposited, or if microcrystalline diamond dominates. The OES data shown in Figure 5-2 and 5-3 show that the C2 and H $\alpha$  peaks should be favorable for nanocrystalline growth which requires high carbon radical concentrations to promote a high re-nucleation rate and low atomic hydrogen concentrations that would suppress sp<sup>2</sup> formation.

Figure 5-6 shows Raman spectra taken for all concentrations of argon explored in this chapter. Figure 5-7 shows the Raman spectra taken for 98% and 99% argon. These two peaks were kept separate because they cannot be considered diamond films and do not follow the same trend. High resolution scans were used to detail the most relevant peaks.

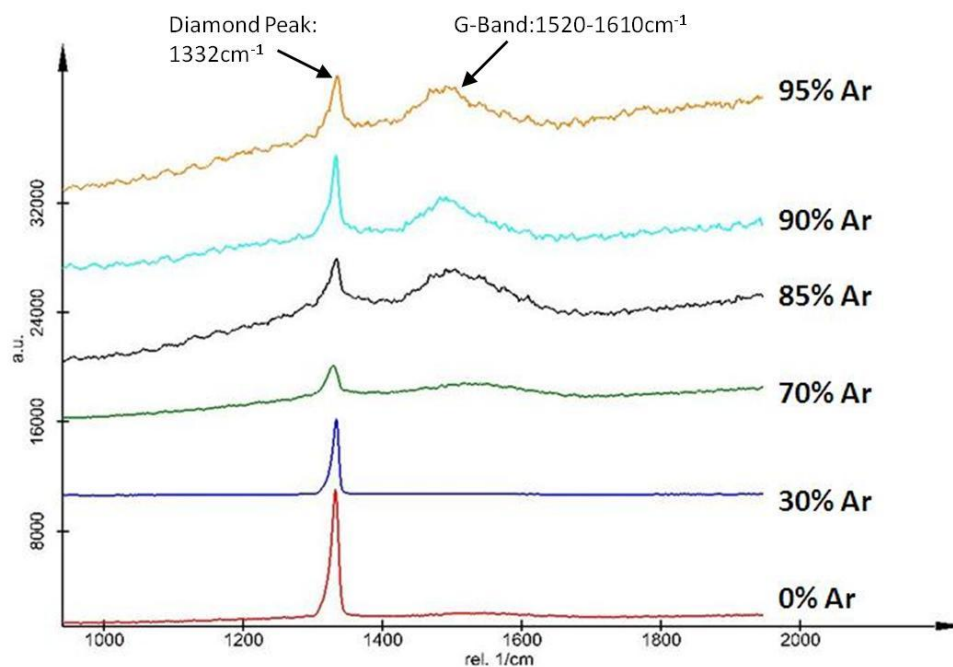


Figure 5-6: Raman Spectra for Varying Argon Concentrations. The intensity of the G-band increases significantly as the argon concentration increases above 70%. This is attributed to the increasing concentration of grain boundary containing  $sp^2$  carbon phases as grain size is reduced

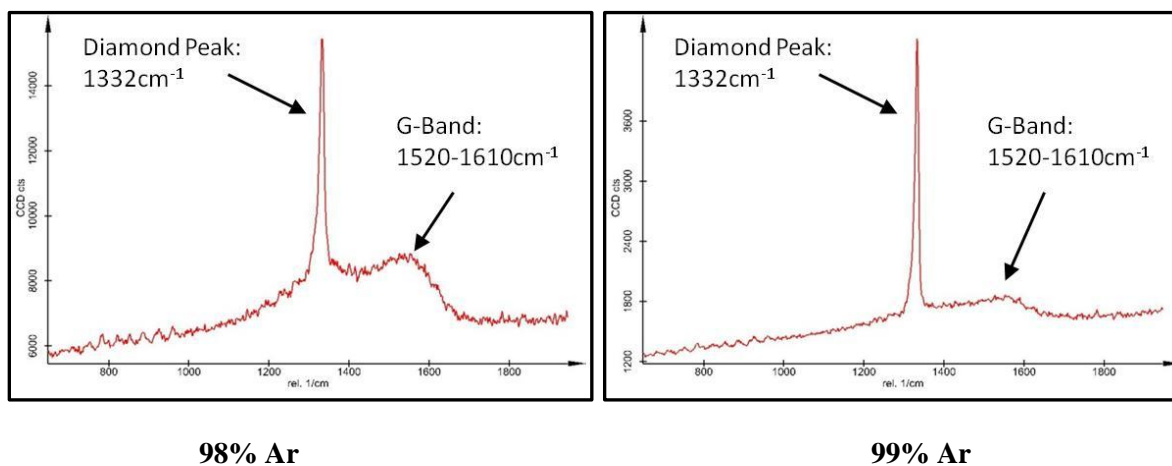


Figure 5-7: Raman Spectra for 98% and 99% Argon. The sharp diamond peak and weak G-band may be due to the signal from the polycrystalline diamond substrate.

At 0% argon, the diamond peak at  $1332\text{cm}^{-1}$  is very well defined. Though a slight graphitic region from  $1520\text{-}1610\text{cm}^{-1}$  can be observed, it is clear that the high concentration of atomic hydrogen contained in the hydrogen-methane plasma preferentially etched most of the  $\text{sp}^2$  carbon during deposition. At 30% argon, there is still a high concentration of atomic hydrogen in the gas phase to etch most  $\text{sp}^2$  carbon, depositing a diamond film with little graphitic incorporation. In fact, the graphitic region in this case is actually less pronounced than with no argon addition. This may be explained by the relatively low ionization energy of argon compared to other species in the hydrogen-methane plasma. An addition of argon would increase the total number of free electrons and excited Ar atoms which would lead to an increase in collisions between molecules. This in turn would lead to an increase in atomic hydrogen as well as active carbon radicals, leading to an increase in growth rate while still containing enough atomic hydrogen to etch  $\text{sp}^2$  carbon.

At 70% argon, the g-band (correlated to  $\text{sp}^2$  bonded graphitic carbon) begins to become more prominent. Here, the concentration of atomic hydrogen in the plasma is decreased enough that its contribution to  $\text{sp}^2$  carbon etching is significantly reduced and secondary nucleation is increased. This trend is observed up to 95% argon, where the g-band becomes more and more distinct with increasing argon concentration. The increased intensity of the G-band is related to the increase in the density of grain boundaries, which contain graphitic carbon phases, as the grain size of the film decreases. At 98% and 99%, the g-band decreases significantly and the diamond peak is more intense. Here, the films were very thin and non-continuous. It appears that the signal is from the polycrystalline diamond substrate rather than the dark particles (most likely graphitic soot).

Though the film morphology and Raman spectra follow an expected trend up to 95% argon, it cannot be assumed that nanocrystalline diamond was actually grown. None of the Raman data presented here compare well to Raman spectra reported in literature for

nanocrystalline diamond films. A truly nanocrystalline film should have a weak diamond peak with a larger G-band [49]. Also, a peak at  $1140\text{cm}^{-1}$  is said to be indicative of nanocrystalline growth. This peak was not observed in the present study. Therefore, Raman indicates that the material is not truly nanocrystalline diamond, rather the spectra is typical of microcrystalline diamond. This also appears to be the case as observed optically in Figure 5-4 where the grain size appears microcrystalline up to 90% argon and appears to approach nanocrystalline diamond only at 95%.

The large separation between the plasma and the substrate at high argon concentrations may be responsible for the failure to deposit nanocrystalline diamond. Figure 5-8 shows an example from literature indicating the importance of plasma-substrate contact.

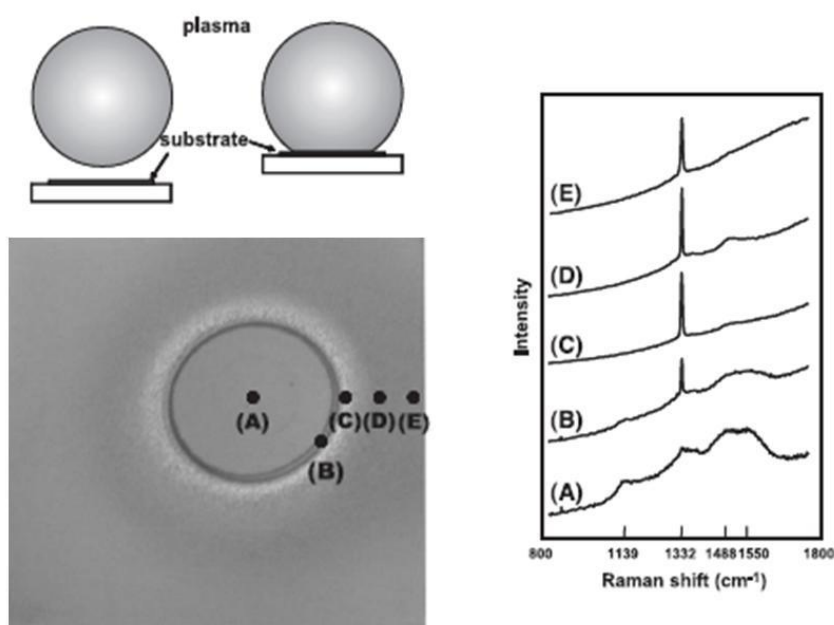


**Figure 5-8:** Effect of plasma-substrate contact on the deposition of nanocrystalline diamond. Point “A” indicates a region where the plasma was in contact with the substrate. Here the Raman spectra suggests nanocrystalline diamond deposition with a weak D-peak, large G-band, and a peak at  $1140\text{cm}^{-1}$ . In regions where the plasma was not in contact with the substrate, the  $1140\text{cm}^{-1}$  peak disappears and the D-peak becomes more intense, indicating microcrystalline diamond deposition [49].

Because of the relatively low ionization energy of argon and the top to bottom propagation of the microwave cavity, the plasma formed very easily near the top of the bell jar instead of on the surface of the substrate. In the literature, nanocrystalline diamond only formed when the plasma and the substrate were in contact, as shown in Figure 5-8 [49]. This was due to the significant decrease in the flux of carbon radicals to the surface as the separation between the plasma and the substrate increased, especially at high pressures due to the lower diffusivity of species through the plasma sheath at high pressure [49]. Strong emission from the C<sub>2</sub> peak of OES data is correlated with the high re-nucleation (or secondary nucleation) rate required for nanocrystalline growth [49]. Due to the poor plasma-substrate contact however, the high C<sub>2</sub> peaks observed in the plasma are not indicative of the carbon radical concentrations on the surface of the substrate. Therefore, the C<sub>2</sub>/H $\alpha$  ratio at the substrate surface would be less than the ratio observed with OES.

It seems that truly nanocrystalline diamond could not be obtained in the present state of research. Modifications to the susceptor to push the substrate closer to the plasma may be necessary as well as experimentation with the reactor geometry settings; which were kept constant in the present study to preserve continuity. A lower growth pressure may be required as well to promote enhanced diffusivity of the gas species from the plasma to the substrate; especially if good plasma-substrate contact cannot be established. Also, electrical biasing of the substrate may prove to be useful by accelerating the ions, and thus the plasma, into contact with the substrate. The deposition of large dark particles onto the substrate at 98% and 99% argon does not agree with literature and seems unusual. It can be concluded that the plasma's separation from the substrate is responsible for this "soot" deposition. These particles did not adhere to the substrate and the Raman data is suspicious. Further research at such high argon concentrations needs to be explored.

## Chapter 6

### Conclusions

Diamond is a material of great interest for a wide range of technological and scientific applications. In particular, diamond possesses some exceptional properties (described in Chapter 1) ideal for several key electronic devices. Two applications of direct interest are M-i-P Schottky diodes and neutron detectors. These devices rely on the extremely high intrinsic hole mobility of single crystal diamond. However, defects, impurities, and surface features (such as hillocks) severely reduce the efficiency and potential of such devices. Current growth techniques have yet to fully conquer these limitations.

This thesis has attempted to improve the quality of homoepitaxial diamond in an effort to work towards overcoming the material-related limitations associated with diamond electronics. This was done by first understanding the growth process to a point where the geometrical factors of the electromagnetic field of a microwave cavity could be controlled to generate ideal growth conditions. Secondly, the misorientation was altered in an effort to improve the as-grown surface morphology of homoepitaxial diamond, leading to an overall reduction in crystallographic defects and impurities. Finally, reactive ion etching was explored as a pre-growth substrate treatment process to remove surface defects (induced from mechanical polishing) that could otherwise lead to dislocation propagation and hillock formation. Nanocrystalline diamond, having unusual doping properties as well as MEMS and NEMS applications, was explored as an additional investigation but was not successfully deposited. However, it was shown that the grain size of polycrystalline films can be controlled with argon concentration and approached nanocrystalline scale.

## 6.1: Growth Kinetics and Optimal Reactor Geometry

There are many factors that influence the growth behavior of homoepitaxial diamond. Control of these factors is a key to realizing desired growth characteristics. Chapter 3 explored the dependence of pressure and methane concentration on the growth rate and morphology of (100) single crystal diamond for three different susceptor configurations. Figures 3-22 and 3-23 showed these dependencies. It became very clear that the susceptor configuration played a large role in the diamond nucleation behavior and growth kinetics. Optical emission spectroscopy (OES) proved to be very beneficial for understanding the dissociation behavior of the plasma for each susceptor configuration. OES plots were shown in Figures 3-14 to 3-19. The growth rate as well as the surface morphology differed greatly depending on the plasma density, the contact between the plasma and substrate, and the cooling to the substrate.

Configuration 1 gives an example of poor plasma-substrate contact. Because the diffusivity of gas species from the plasma to the substrate decreases as the plasma sheath (or distance of separation) is increased, the overall concentration of active species at the substrate surface is much lower than in the plasma. OES data (Figures 3-20 and 3-21) showing a high C2/H $\alpha$  ratio for configuration 1 is therefore misleading. Not only would the overall concentration of active gas species be lower at the substrate surface, but the ratios of C2/H $\alpha$  would be lower as well. Atomic hydrogen, being lighter and faster, would be more likely to reach the surface than the heavier methyl radicals, leading to a lower C2/H $\alpha$  ratio at the surface than observed with OES. In fact, susceptor configuration 2 (having good plasma-substrate contact) had a higher growth rate even though the C2/H $\alpha$  ratios observed with OES were lower than for susceptor configuration 1. This was because the concentration of active gas species at the substrate surface was in fact higher for susceptor configuration 2 than for susceptor configuration 1. The improved plasma-substrate contact of susceptor configuration 2 would create a smaller plasma sheath and

thus a higher flux of active gas species to the surface. Therefore, it is obvious that the contact between the plasma and the substrate plays an important role in terms of regulating the flux of atomic hydrogen and carbon radicals to the surface and indeed the overall growth behavior.

Plasma density (or the density of free electrons in the plasma) also plays an important role in determination of the growth rate and growth behavior of single crystal diamond. Equations **3-2** and **3-3** showed how an increase in the plasma density leads to an increase in the dissociation rate of methane, which in turn creates a higher concentration of reactive carbon radicals and atomic hydrogen in the gas phase, promoting higher growth rates. The easiest way to obtain high plasma densities is to improve the cooling to the substrate to allow for higher forward microwave power inputs. By removing as much molybdenum susceptor material between the substrate and the cooling stage, configuration 3 accomplished this and accordingly produced films with growth rates approaching 18 $\mu\text{m/hr}$  without the addition of nitrogen or oxygen. In this growth configuration, the methane concentration had a significant effect on the surface morphology. Figure **4-4** showed images of growths done with susceptor configuration 3 at different methane concentrations. The high plasma density created a very high concentration of atomic hydrogen. At low  $\text{CH}_4$  concentrations (1-2%), it seems that a competition between growth and hydrogen etching was taking place, leaving etch pits in some areas. As the  $\text{CH}_4$  concentration was increased, the morphology moved towards step flow growth. Also, it seems that the high growth rates associated with susceptor configuration 3 promoted step-flow growth even without substrate misorientation. Figure **3-24** showed optical images from three runs, one for each susceptor configuration, done under identical process conditions. Only susceptor configuration 3 resulted in step-flow growth morphology while configurations 1 and 2 promoted hillock formation. This could be due to the high overall growth rate beating out locally enhanced growth rates at dislocation sites. In other words, the available concentration of carbon species that could participate in growth was so high that the surface reaction rates were comparable or higher than

the hillock nucleation rate. Therefore, steps propagated faster in the [110] direction than hillocks could in the [100] direction, covering any dislocation sites before they could nucleate into hillocks.

Based on the results from Chapter 3, it is understood that the plasma density should be high, the plasma should be in good contact with the substrate, and the cooling to the substrate should be adequate enough to obtain a high microwave power input. Therefore, the susceptor configuration which satisfies all these criteria is configuration 3. Figure 6-1 shows the three susceptor configurations and their respective advantages and disadvantages.

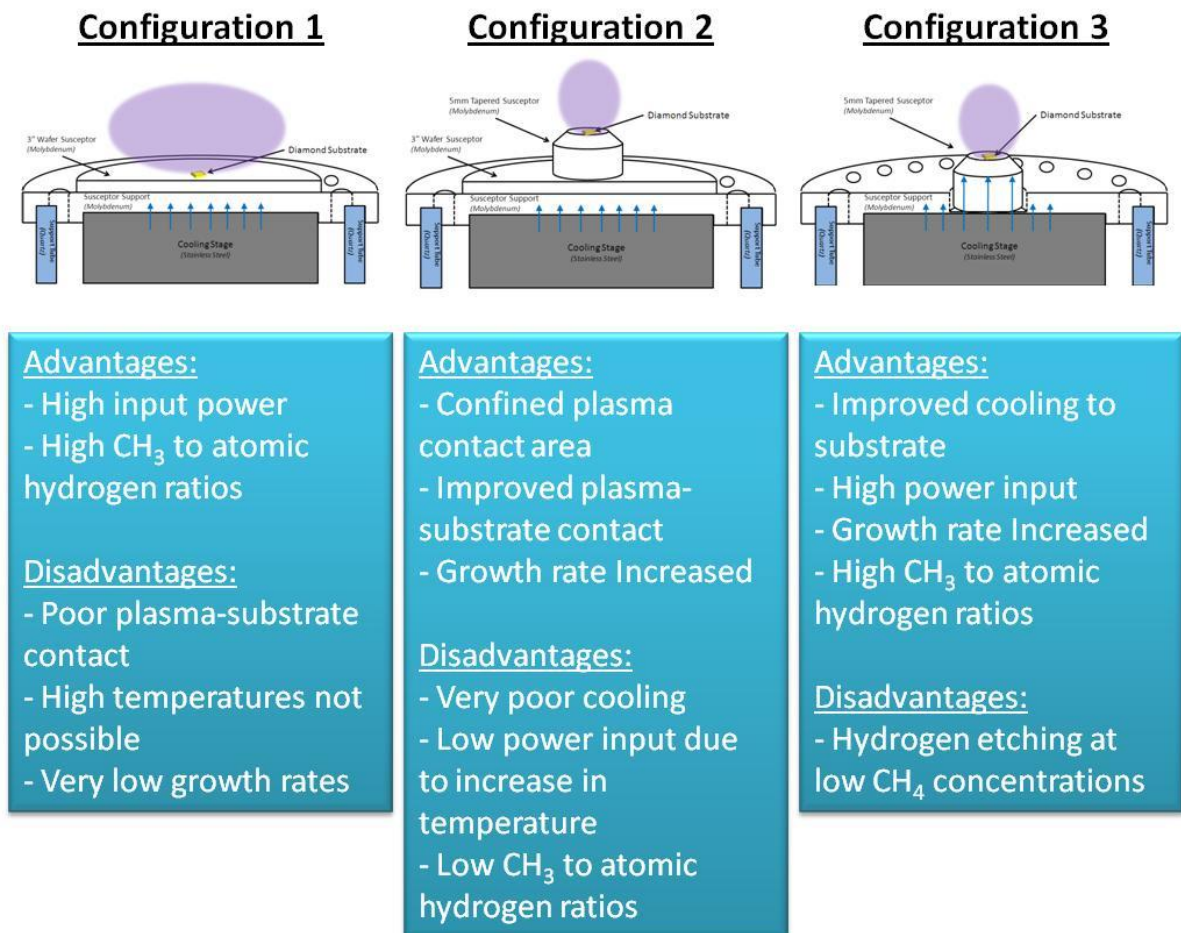


Figure 6-1: Susceptor configuration comparison. The increased substrate cooling combined with the confinement of the plasma volume over the substrate resulted in susceptor configuration 3 being the ideal configuration for high plasma density and high growth rates.

The optimal process parameters for susceptor configuration 3 proved to be a pressure of 120 Torr, a methane concentration of 8%, and a forward power of 2300W creating a substrate temperature of  $\sim 1100^{\circ}\text{C}$ . These parameters led to a step-flow growth mode with growth rates approaching  $20\mu\text{m/hr}$ .

## **6.2: Secondary Ion Mass Spectrometry Analysis**

Secondary Ion Mass Spectrometry (SIMS) was used to characterize impurity concentrations in single crystal diamond films and is described in section 2.3. For this thesis, SIMS analysis was used to measure impurity concentrations of silicon, nitrogen, molybdenum, and boron. Silicon is expected to be incorporated into diamond during the MPCVD process through the hydrogen etching of the quartz bell jar and molybdenum can be introduced from the etching of the susceptor. Nitrogen can be introduced from the source gases (mainly hydrogen). Boron levels were measured (for the first sample only) due to its strong effect on the electrical properties of diamond. Due to the high cost of this analytical technique, SIMS was only done on two samples. Both samples were sent to Evans Analytical Group in Sunnydale, California for the analysis. The first sample was grown on an on-axis substrate with susceptor configuration 1. The growth conditions were: a pressure of 120 Torr, a forward power of  $\sim 2500\text{W}$  giving a temperature of  $1050^{\circ}\text{C}$ , and a methane concentration of 4%. This sample represented the initial growth conditions using the stock reactor configuration. Conversely, the second sample was grown under the ideal conditions established throughout this thesis. This sample was an off-axis substrate that was etched under the optimal RIE pressure of 25mTorr for 1 hour. Growth was then carried out with susceptor configuration 3 under the following growth conditions: a pressure of 120 Torr, a forward power of 2300W giving a temperature of approximately  $1100^{\circ}\text{C}$ , and a

methane concentration of 8%. With the optimal growth conditions, morphology observations and Raman spectroscopy concluded that the crystalline quality was enhanced over the base conditions through the development of a step-flow growth mode. SIMS analysis will show if the purity of the intrinsic layer is also improved from the base condition. Figure 6-2 shows 50x optical images of the two samples that were sent for SIMS analysis and Figure 6-3 shows the SIMS data. The average impurity concentrations for each element are shown on the SIMS data plots (Figure 6-3).

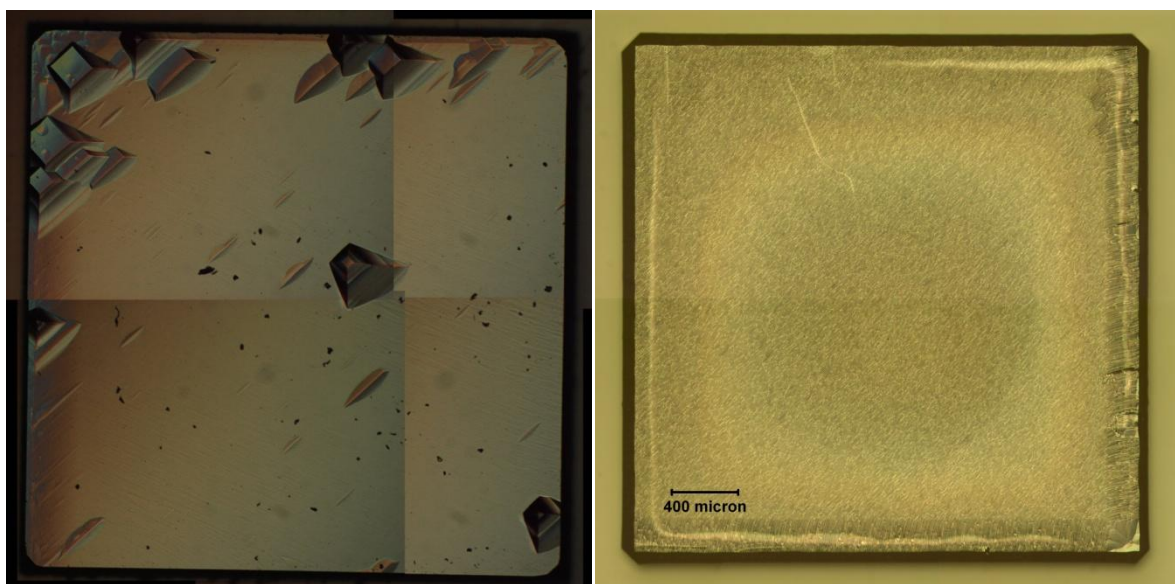


Figure 6-2: 50x optical images of samples sent out for SIMS analysis. Right: CVD-05 used an on-axis substrate, susceptor configuration 1, 120 Torr, 2500W (1050°C), and 4% CH<sub>4</sub>. Left: OA-13 was etched at 25mTorr for 1 hour, used an off-axis substrate, susceptor configuration 3, 120 Torr, 2300W (1100°C), and 8% CH<sub>4</sub>. The step flow morphology of OA-13 (Left image) is expected to incorporate fewer impurities than the hillocks observed in CVD-05 (Right image).

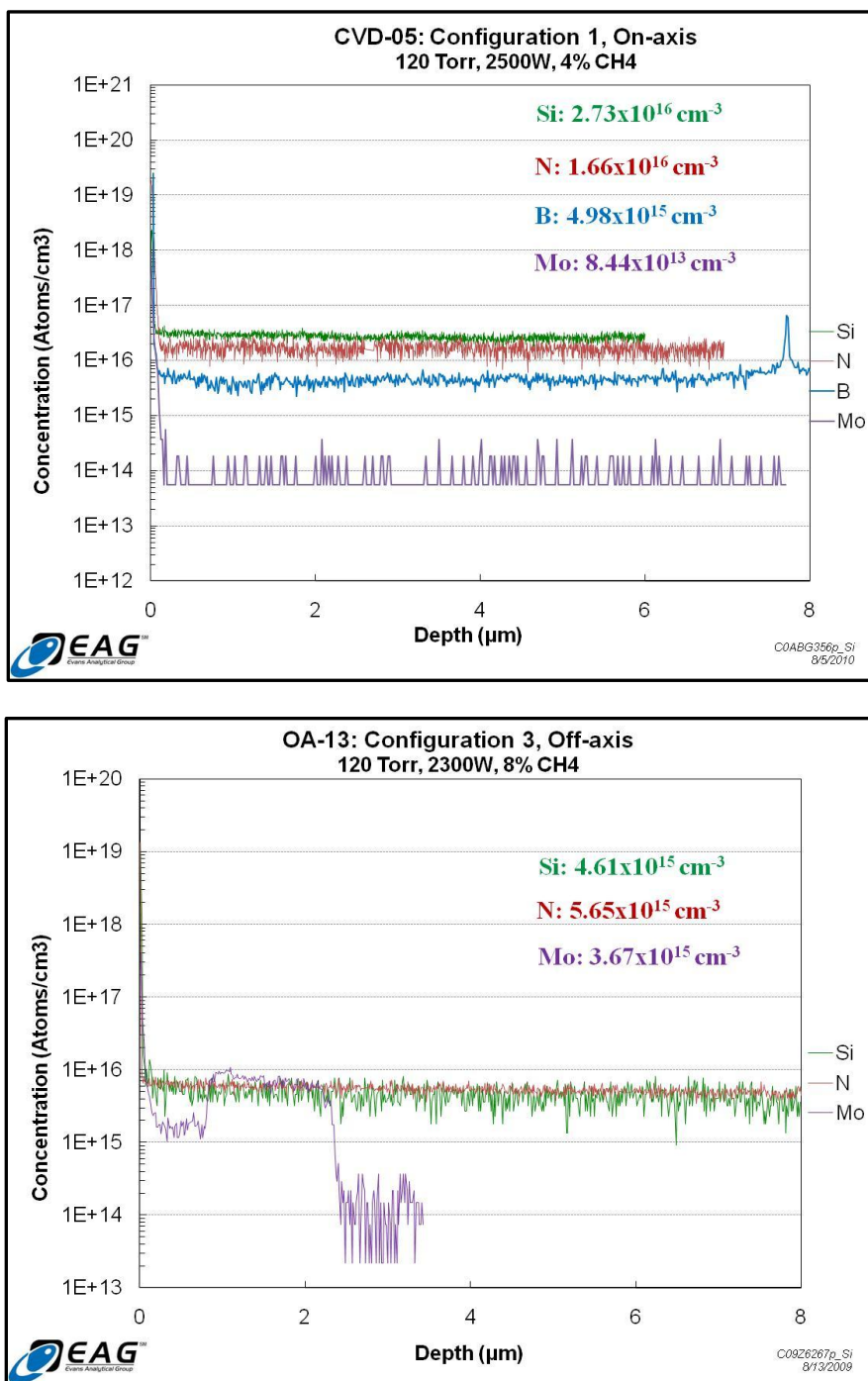


Figure 6-3: SIMS profiles of nitrogen, silicon, and boron impurities in CVD-05 (top plot) and OA-13 (bottom plot). CVD-05 used an on-axis substrate, susceptor configuration 1, 120 Torr, 2500W (1050°C), and 4% CH<sub>4</sub>. OA-13 was etched at 25mTorr for 1 hour, used an off-axis substrate, susceptor configuration 3, 120 Torr, 2300W (1100°C), and 8% CH<sub>4</sub>. The off-axis and etched sample (OA-13) shows slightly lower Si and N impurity levels but higher Mo levels.

From Figure 6-3, the use of off-axis substrates, a pre-growth etching technique, and the optimal growth conditions decreased the nitrogen and silicon impurity concentrations by an order of magnitude from the base conditions. However, the impurity concentrations of silicon and nitrogen are still higher than desired. A hydrogen purifier may need to be installed to reduce the concentration of nitrogen in the hydrogen source gas. The reactor geometry settings (specifically the stage height) may be lowered to reduce hydrogen etching of the quartz bell jar to reduce silicon incorporation. Also, the molybdenum impurity concentration increased for the off-axis case. This could be due to the use of susceptor configuration 3. The enhanced plasma density directly over the substrate and susceptor may etch the molybdenum susceptor more readily and enhance incorporation of Mo into the diamond film.

### **6.3: Off-axis vs. On-axis Growth and RIE Surface Treatment**

Section 4.1 investigated the effects of substrate misorientation on the growth behavior of single crystal diamond in an effort to improve the post-growth surface morphology and thus, reduce hillock formation, defect formation, and impurity incorporation. As explained in section 4.3, the misorientation creates a higher probability that incoming carbon radicals will nucleate onto a crystallographic step edge rather than between steps or onto a hillock forming dislocation. As a result, step-flow growth almost always was the preferred growth mode on off-axis substrates except at low methane concentrations as explained in section 6.1. Step flow growth is the preferred growth mode as it maintains crystallinity and homogenous doping (important for p-type boron doping). Conversely, hillocks can coalesce and form dislocations. Also, hillocks can lead to inhomogeneous doping. Also, Figure 4-2 showed that the growth rate is increased by using

misoriented substrates due to the increase in crystallographic steps which act as available nucleation sites.

Mechanical polishing of the substrates by the manufacturer usually incorporates scratches, micro-fractures, and metal contaminants on the (100) diamond surface. Reactive ion etching (RIE) was shown in section 4.2 to remove such damaged surface layers from off-axis substrates that could act as unwanted nucleation sites and lead to hillock growth or defect incorporation. RIE surface treatment was shown to improve the post-growth surface morphology of off-axis (100) diamond by improving the starting surface roughness and quality. RIE treatment on on-axis substrates however led to the formation of etch pits which degraded the deposited surface morphology. Therefore, RIE was concluded to be beneficial only for misoriented substrates.

The etching pressure had a significant effect on the post-etch surface roughness of the off-axis substrates. Too much chemical reactive etching or not enough ion bombardment led to an aggressive etch and pitting, roughening the substrate surface. At 25 mTorr however, the surface roughness actually decreased, as shown previously in Figure 4-6. Therefore, for the gas concentrations and input power used in this study, 25 mTorr seemed to be the optimal pressure for an adequate balance of the two etching mechanisms.

Raman results, specifically center of mass and full width half maximum data shown in Appendix E, show that there is no significant degradation to the material after RIE treatment or after film deposition. In fact, the disappearance of defect and impurity peaks in the Raman spectra indicates that the deposited homoepitaxial film is actually of a higher crystalline quality and purity than the substrate, as shown previously in Figure 4-17. This indicates that the growth conditions and use of misoriented substrates does indeed improve the crystalline quality of the films.

#### 6.4: Control of Polycrystalline Grain Size

Unlike traditional polycrystalline diamond, whose grains increase in size as they grow in a columnar fashion, nanocrystalline diamond is independent of thickness due to its secondary nucleation behavior. The very small grain sizes of nanocrystalline diamond lead to a high density of grain boundaries (up to 10% of the entire volume). When doped with nitrogen, these grain boundaries exhibit n-type conduction. Polycrystalline and single crystal diamond are very difficult to dope as n-type; therefore nanocrystalline diamond offers some unique properties that make it ideal for certain applications.

In Chapter 5, deposition of nanocrystalline diamond on polycrystalline diamond substrates was attempted by introducing an argon-rich plasma chemistry. It was shown that an addition of argon to the gas phase improved the ionization of methane and hydrogen significantly, as shown in OES scans in Figures 5-2 and 5-3. This occurs because argon has a relatively low ionization energy and thus creates a very high concentration of free electrons in the plasma. A higher concentration of free electrons of course creates a higher dissociation rate of methane and hydrogen, creating a higher concentration of carbon radicals and atomic hydrogen (Equation 3-3).

Therefore, the growth rate was increased as the argon concentration increased up to 70% (Figure 5-1). However, the atomic hydrogen present in the gas phase at these concentrations was still enough to etch the majority of  $sp^2$  carbon, promoting columnar growth rather than nanocrystalline secondary nucleation. Above 70% argon, the plasma started to detach from the substrate notably, decreasing the growth rate. The decreased hydrogen concentrations however led to finer grains (Figure 5-4), consistent with the literature. However, Raman data (Figure 5-6) did not show a Raman response indicative of nanocrystalline diamond, even at 95% argon. Above 95% argon the plasma was completely coupled to the quartz bell jar and far from the substrate surface. In this case, it appears that diamond did not nucleate onto the substrate surface. Instead, a

dark soot material (nucleating in the plasma) covered the substrate and susceptor. Literature suggests that the contact between the substrate and the plasma plays an important role in the nucleation behavior of nanocrystalline diamond [49]. Additional experiments are required to try and bring the plasma into better contact with the substrate by altering the susceptor geometry or adjusting the microwave chamber geometry settings.

Although truly nanocrystalline diamond could not be achieved in the present study, microcrystalline diamond films approaching the nano-scale were obtained. It was shown that the microstructure is indeed affected by the argon concentration in the gas phase, decreasing with increased argon addition. Raman has shown that, as expected,  $sp^2$  carbon content increases with increasing argon concentrations. Based on the results up to 95% argon, it was expected that nanocrystalline diamond would indeed be achieved at higher concentrations. However, it seems that the plasma contact issue at such high argon concentrations is the only thing holding back the nucleation of truly nanocrystalline diamond.

## **6.5: Future Work**

The present research for this thesis has successfully improved the crystalline quality, growth rate, and purity of intrinsic (100) homoepitaxial diamond by optimizing the reactor geometry, using misoriented substrates, and improving the substrate surface through reactive ion etching. However, a great deal of research in several key areas needs to be addressed in order to realize efficient diamond based M-i-P devices.

First, boron doping is required for the conductive p-type layer of an M-i-P Schottky device. Doping concentrations greater than  $10^{18} \text{ cm}^{-3}$  are required for sufficient conduction. Currently, research in the Freeport facility of the Penn State Electro Optics Center is working towards the development of a growth process of the p-type layer. Initial studies have looked into

solid source doping with boron nitride, boron carbide, and pure boron as well as gas phase doping using  $\text{BCl}_3$  as the source gas. Integration of the p-type layer and the intrinsic layer may prove to be difficult and must be carefully studied. Boron will contaminate a reactor, making it very difficult to deposit subsequent diamond films without boron incorporation. Therefore, the p-type layer and the intrinsic region must be deposited in separate reactors. In addition, difficulties may arise from deposition of the intrinsic layer onto the boron-doped p-type layer. During the initial stages of deposition, hydrogen etching could incorporate boron into the reactor. Therefore, a third reactor may be required to deposit a buffer layer before being placed into the high-purity intrinsic MPCVD reactor.

Boron doping may alter the post-growth morphology significantly. This would mean that the starting surface for intrinsic deposition may differ from the surfaces used in this study. Therefore, a post-growth surface treatment would probably need to be developed for processing of the p-type layer. Post-growth surface processing would also be required after the intrinsic layer is deposited. The final surface must be very smooth in order to deposit the contacts to the M-i-P device. Mechanical polishing would most likely be used to macroscopically smooth and planarize the surface. An RIE step may also be required to remove any surface defects or micro-fractures induced from the mechanical polishing step.

Finally, electrical characterization must be performed on the p-type layer, intrinsic layer, and the final M-i-P device to quantify the electrical properties of each layer as well as the overall device performance.

The present study has presented growth processes and substrate treatment techniques for the improved deposition of high quality, high purity (100) homoepitaxial diamond for the active intrinsic layer of diamond based M-i-P devices. However, a significant amount of research still needs to be completed to better understand the many technological limitations associated with diamond electronics.

## References

- [1] M. Brezeanu, T. Butler, G.A.J. Amaratunga, F. Udrea, N. Rupesinghe, S. Rashid, *On-state behavior of diamond Schottky diodes*. *Diamond & Related Materials*. 2008. **17**: p. 736-740.
- [2] Koizumi, Satoshi., Christoph E. Nebel, and Milos Nesladek, eds. Physics and Applications of CVD Diamond. Weinheim: WILEY-VCH Verlag GmbH & Co. KGaA, 2008.
- [3] S.J. Rashid, A. Tajani, L. Coulbeck, M. Brezeanu, A. Garraway, T. Butler, N.L. Rupesinghe, D.J. Twitchen, G.A.J. Amaratunga, F. Udrea, P. Taylor, M. Dixon, J. Isberg, *Modelling of single-crystal diamond Schottky diodes for high-voltage applications*. *Diamond & Related Materials*. 2006. **15**: p. 307-323.
- [4] D. Lattanzi, M. Angelone, M. Pillon, S. Almagora, M. Marinelli, E. Milani, G. Prestopino, A. Tucciarone, C. Verona, G. Veron-Rinati, S. Popovichev, R.M. Montecali, M.A. Vincenti, A. Murari, *Single crystal CVD diamonds as neutron detectors at JET*. *Fusion Eng. and Design*. 2009.
- [5] M. Angelone, D. Lattanzi, M. Pillon, M. Marinelli, E. Milani, A. Tucciarone, G. Verona-Rinati, S. Popovichev, R.M. Montecali, M.A. Vincenti, A. Murari, *Development of single crystal diamond neutron detectors and test at JET tokamak*. *Nucl. Instr. and Methods in Phys. Res. A*. 2008. **595**: p. 616-622.
- [6] G.J. Schmid, J.A. Koch, R.A. Lerche, M.J. Moran, *A neutron sensor based on single crystal CVD diamond*. *Nucl. Instr. and Methods in Phys. Res. A*. 2004. **527**: p. 554-561.
- [7] C. De Angelis, M. Casati, M. Bruzzi, S. Onori, M. Bucciolini, *Present limitations of CVD diamond detectors for IMRT applications*. *Nucl. Instr. and Methods in Phys. Res. A*. 2007. **583**: p. 195-203.
- [8] J.H. Kaneko, T. Tanaka, T. Imai, Y. Tanimura, M. Katagiri, T. Nishitani, H. Takeuchi, T. Sawamura, T. Iida, *Radiation detector made of a diamond single crystal grown by a chemical vapor deposition method*. *Nucl. Instr. and Methods in Phys. Res. A*. 2003. **505**: p. 187-190
- [9] F. Foulon, P. Bergonzo, V.N. Amosov, Yu. Kaschuck, V. Frunze, D. Tromson, A. Brambilla, *Characterization of CVD diamond detectors used for fast neutron flux monitoring*. *Nucl. Instr. and Methods in Phys. Res. A*. 2002. **476**: p. 495-499.
- [10] R.D. Mavunda, Y.I. Zakari, T.L. Nam, R.J. Keddy, *The presence of defects and their influence on the performance of CVD diamond as an alpha-particle radiation sensing element*. *Appl. Rad. and Iso*. 2008. **66**: p. 1128-1137.

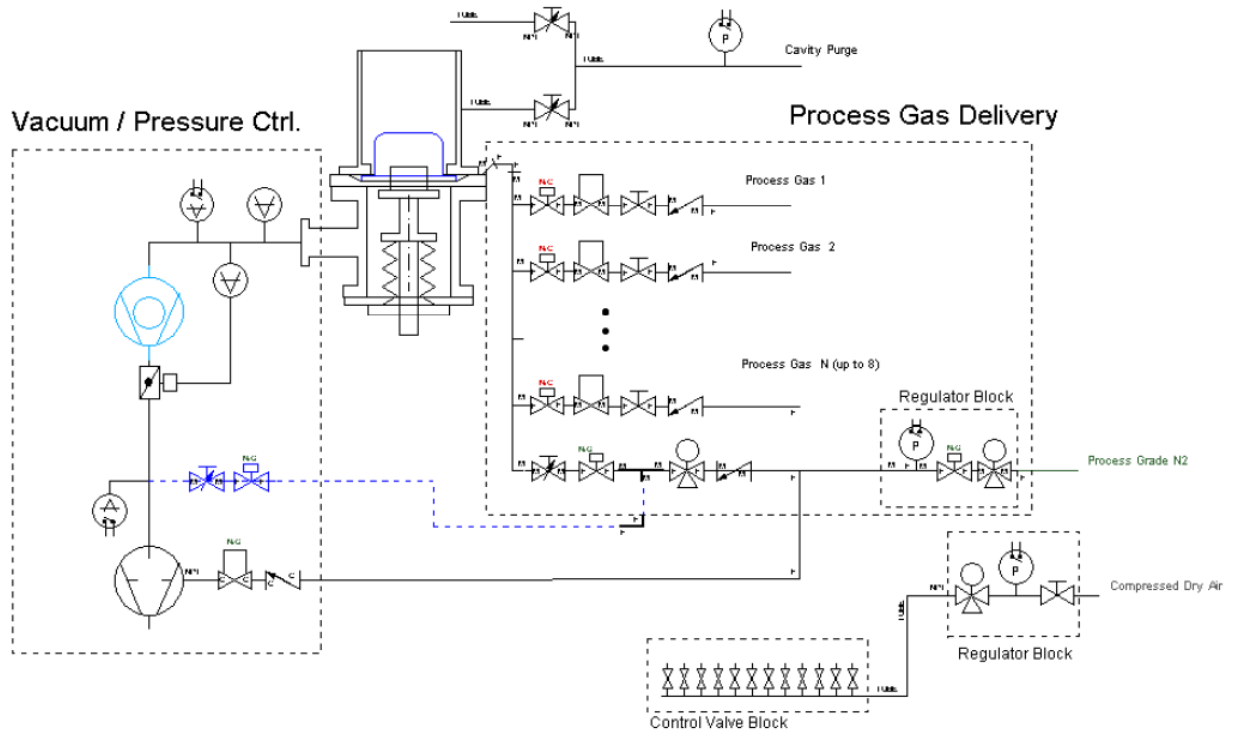
- [11] C. Tuve, M. Angelone, V. Bellini, A. Balducci, M.G. Donato, G. Faggio, M. Marinelli, G. Messina, E. Milani, M.E. Morgada, M. Pillon, R. Potenza, G. Pucella, G. Russo, S. Santagelo, M. Scoccia, C. Sutura, A. Tucciarone, G. Verona-Rinati, *Single crystal diamond detectors grown by chemical vapor deposition*. Nucl. Instr. and Methods in Phys. Res. A. 2007. **570**: p. 299-302.
- [12] M. Marinelli, E. Milani, G. prestopino, M. Scoccia, A. Tucciarone, G. Verona-Rinati, *High performance LiF-diamond thermal neutron detectors*. Appl. Phys. Letters. 2006. **89**.
- [13] P. Lardon, C. Mer, P. Delacour, B. Bazin, D. Tromson, S. Normand, M. Nesladek, F. Foulon, P. Bergonzo, *Investigations of high quality diamond detectors for neutron fluency monitoring in a nuclear reactor*. Diamond and Related Materials. 2006. **15**: p. 815-821.
- [14] M. Marinelli, E. Milani, G. Prestopino, A. Tucciarone, C. Verona, G. Verona-Rinati, M. Angelone, D. Lattanzi, M. Pillon, R. Rosa, E. Santoro, *Synthetic single crystal diamond as a fission reactor neutron flux monitor*. Appl. Phys. Letters. 2007. **90**.
- [15] M. Bruzzi, M. Bucciolini, S. Lagomarsino, D. Menichelli, S. Miglio, S. Pini, M. Scaringella, S. Sciortino, *Deep levels in CVD diamond and their influence on the electrical properties of diamond-based radiation sensors*. Phys. Stat. Sol. 2002. 193. **3**: p. 563-571.
- [16] A. Stolz, M. Behravan, M. Regmi, B. Golding, *Heteroepitaxial diamond detectors for heavy ion beam tracking*. Diamond and Related Materials. 2006. **15**: p. 807-810.
- [17] P. Bergonzo, D. Tromson, C. Descamps, H. Hamrita, C. Mer, N. Tranchant, M. Nesladek, *Improving diamond detectors: A device case*. Diamond and Related Materials. 2007. **16**: p. 1038-1043.
- [18] F. Silva, et al., *High quality, large surface area, homoepitaxial MPACVD diamond growth*. Diamond & Related Materials. 2009. **18**: p. 683-697
- [19] Yu. A. Mankelevich, P.W. May, *New Insights into the mechanisms of CVD diamond growth: Single crystal diamond in MW PECVD reactors*. Diamond & Related Materials. 2008. **17**: p. 1021-1028
- [20] D.G. Goodwin, *Scaling laws for diamond chemical-vapor deposition. I. Diamond surface chemistry*. Journal of Applied Physics. 1993. **74**: p. 6888-6894
- [21] D.G Goodwin, *Scaling laws for diamond chemical-vapor deposition. II. Atomic hydrogen transport*. Journal of Applied Physics. 1993. **74**: p. 6895-6906
- [22] I. Friel, S.L. Clewes, H.K. Dhillon, N. Perkins, D.J. Twitchen, G.A. Scarsbrook, *Control of surface and bulk crystalline quality in single crystal diamond grown by chemical vapor deposition*. Diamond & Related Materials. 2009. **18**: p. 808-815
- [23] A. Tallaire, M. Kasu, K. Ueda, T. Makimoto, *Origin of growth defects in CVD diamond epitaxial films*. Diamond & Related Materials. 2008. **17**: p. 60-65

- [24] Badzian, Andrzej. June 2010. Personal Communication.
- [25] W.J.P van Enkevort, G. Janssen, J.J. Schermer, L.J. Giling, *Step-related growth phenomena on exact and misoriented {001} surfaces of CVD-grown single-crystal diamonds*. Diamond & Related Materials. 1995. **4**: p. 250-255
- [26] T. Bauer, M. Schreck, H. Sternshulte, B. Strizker, *High growth rate homoepitaxial diamond deposition on off-axis substrates*. Diamond & Related Materials. 2005. **14**: p. 266-271
- [27] P. K. Tyagi, A. Misra, K.N. Narayanan Unni, P. Rai, M.K. Singh, U. Palnitkar, D.S. Misra, F. Le Normand, M. Roy, S.K. Kulshreshtha, *Step growth in single crystal diamond grown by microwave plasma chemical vapor deposition*. Diamond & Related Materials. 2006. **15**: p. 304-308
- [28] H. Miyatake, K. Arima, O. Maida, T. Teraji, T. Ito, *Further improvement in high crystalline quality of homoepitaxial CVD diamond*. Diamond & Related Materials. 2007. **16**: p. 679-684
- [29] C. Wang, M. Irie, T. Ito, *Growth and characterization of hillock-free high quality homepitaxial diamond films*. Diamond & Related Materials. 2000. **9**: p. 1650-1654
- [30] A. Tallaire, J. Achard, F. Silva, R.S. Sussman, A. Gicquel, *Homoepitaxial deposition of high-quality thick diamond films: effect of growth parameters*. Diamond & Related Materials. 2005. **14**: p. 249-254.
- [31] J. Achard, A. Taillaire, R. Sussman, F. Silva, A. Gicquel, *The control of growth parameters in the synthesis of high-quality single crystalline diamond by CVD*. Journ. of Cryst. Growth, 2005. **284**: p. 396-405.
- [32] Q. Liang, C.S. Yan, Y. Meng, J. Lai, S. Krasnicki, H.K. Mao, R.J. Hemley, *Recent advances in high-growth rate single-crystal CVD diamond*. Diamond & Related Materials. 2009. **18**: p. 698-703.
- [33] T. Nakai, K. Arima, O. Maida, T. Ito, *High-quality diamond films grown at high deposition rates using high-power-density MWPCVD method with conventional quartz-type chamber*. Journ. of Cryst. Growth. 2007. **309**: p. 134-139.
- [34] J. Achard, F. Silva, A. Tallaire, X. Bonnin, G. Lombardi, K. Hassouni, A. Gicquel, *High quality MPACVD diamond single crystal growth: high microwave power density regime*. Journ. of Phys. D: Appl. Phys. 2007. **40**: p. 6175-6188.
- [35] Q. Liang, C.Y. Chin, J. Lai, C.S. Yan, Y. Meng, H.K. Mao, R.J. Hemley, *Enhanced growth of high quality single crystal diamond by microwave plasma assisted chemical vapor deposition at high gas pressures*. Appl. Phys. Letters. 2009. **94**.
- [36] J.W. Steeds, A. Gilmore, J.A. Wilson, J.E. Butler, *On the nature of extended defects in CVD diamond and the origin of compressive stresses*. Diamond & Related Materials. 1998. **7**: p. 1437-1450.

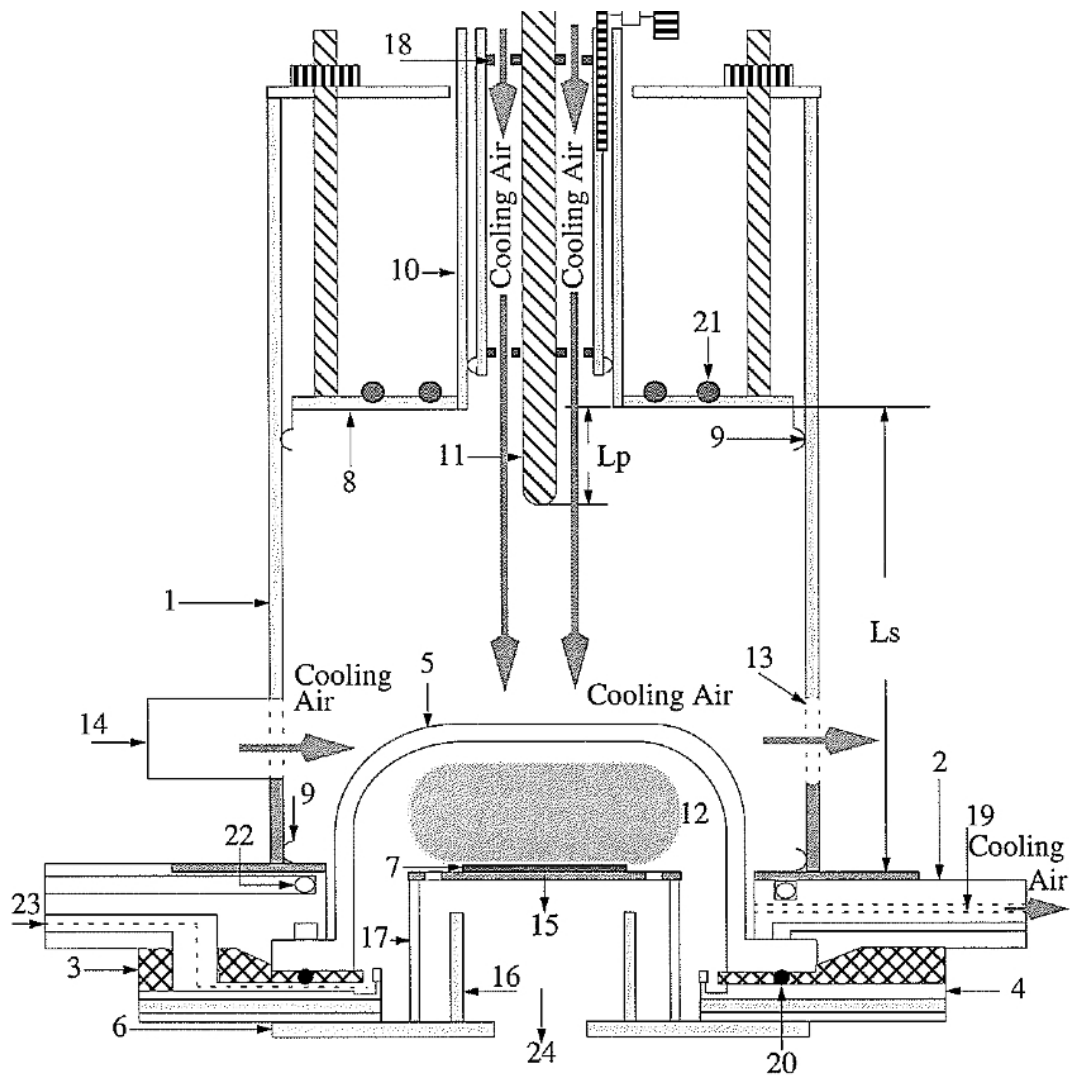
- [37] M.G. Donato, G. Faggio, M Marinelli, G. Messina, E. Milani, A. Paoletti, S. Santangelo, A. Tucciarone, G. Verona Rinati, *High quality CVD diamond for detection applications: structural characterization*. Diamond & Related Materials. 2001. **10**: p. 1788-1793.
- [38] N. Fujita, R. Jones, S. Oberg, P.R. Briddon, *Theoretical investigation on the interaction of nitrogen with dislocations in single crystal CVD diamond*. Diamond & Related Materials. 2008. **17**: p. 123-126.
- [39] C.L. Lee, E. Gu, M.D. Dawson, I. Friel, G. A. Scarsbrook, *Etching and micro-optics fabrication in diamond using chlorine-based inductively-coupled plasma*. Diamond & Related Materials. 2008. **17**: p. 1292-1296.
- [40] D.T. Tran, T.A. Grotjohn, D.K. Reinhard, J. Asmussen, *Microwave plasma-assisted etching of diamond*. Diamond & Related Materials. 2008. **17**: p. 717-721.
- [41] G.F. Ding, H.P. Mao, Y.L. Cai, Y.H. Zhang, X. Yao, X.L. Zhao, *Micromachining of CVD diamond by RIE for MEMS applications*. Diamond & Related Materials. 2005. **14**: p. 1543-1548.
- [42] Y. Ando, Y. Nishibayashi, K. Kobashi, T. Hirao, K. Oura, *Smooth and high-rate reactive ion etching of diamond*. Diamond and Related Materials. 2002. **11**: p. 824-827.
- [43] Schroder, Dieter K. Semiconductor Material and Device Characterization 3<sup>rd</sup> ed. Hoboken: John Wiley & Sons, Inc, 2006.
- [44] Smith, Donald L. Thin-Film Deposition: Principles & Practice. New York: McGraw-Hill, 1995.
- [45] D. Takeuchi, H. Wantanabe, S. Yamanaka, H. Okushi, K. Kajimura, *Homoepitaxial diamond films grown by step-flow mode in various misorientation angles of diamond substrates*. Diamond and Related Materials. 2000. **9**: p. 231-235.
- [46] K. Hayashi, S. Yamanaka, H. Wantanabe, T. Sekiguchi, H. Okushi, K. Kajimura, *Diamond films epitaxially grown by step-flow mode*. Journal of Crystal Growth. 1998. **183**: p. 338-346.
- [47] Zaitsev, Alexander M. Optical Properties of Diamond: A Data Handbook. Berlin: Springer-Verlag, 2001.
- [48] Lee, Naesung. "Microwave Plasma-Assisted Chemical Vapor Deposition and Characterization of (001) Homoepitaxial Diamond Films." PhD Thesis. The Pennsylvania State University, 1996.
- [49] Y.K. Liu, Y. Tzeng, C. Liu, P. Tso, I.N. Lin. *Growth of microcrystalline and nanocrystalline diamond films by microwave plasmas in a gas mixture of 1% methane/5% hydrogen/94% argon*. Diamond and Related Materials. 2004. **13**: p. 1859-1864.

## Appendix A

### Lambda Technologies MPCVD Reactor Schematics



System Block Diagram



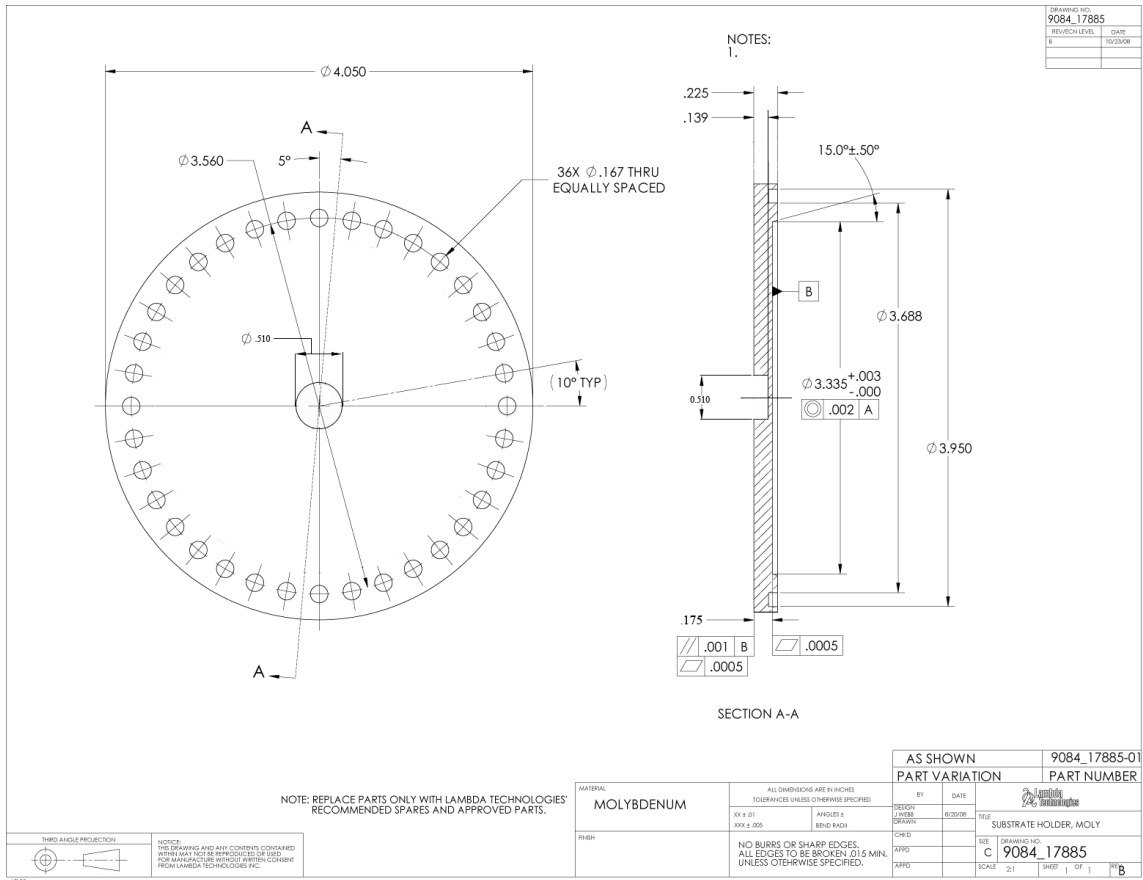
#### Legend

(1) Cavity Side Wall	(2) Baseplate	(3) Annular Plate
(4) Distribution Plate	(5) Quartz Dome	(6) Holder-baseplate
(7) Substrate	(8) Sliding Short	(9) Finger Stock
(10) Coaxial Waveguide	(11) Excitation Probe	(12) Plasma discharge
(13) View Window (grid)	(13) Air Blower Outlet	(14) Air Blower Inlet
(15) Flow Pattern Regulator	(15) Substrate Holder	(16) Metal Tube
(17) Quartz Tube	(18) Teflon Pieces	(19) Optical Access Port
(20) Seal O-ring	(21) Cooling Sliding Short	(22) Cooling Baseplate
(23) Gas Inlet	(24) Gas Outlet	

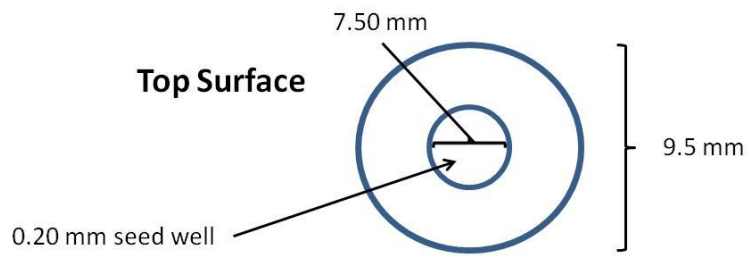
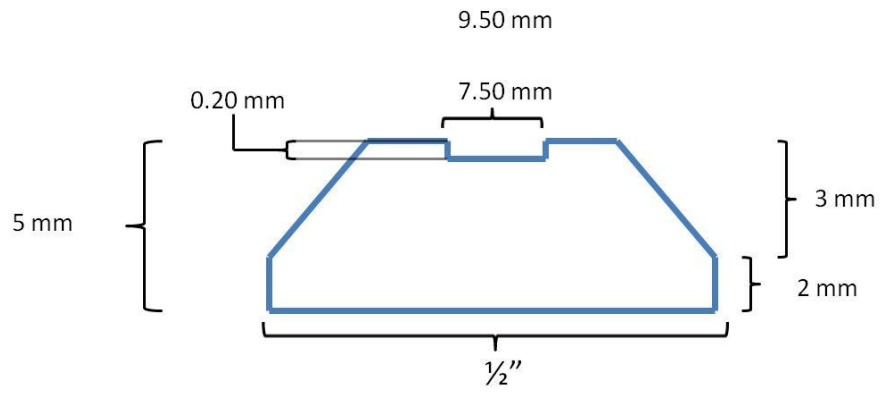
Cross Section of MPCVD Reactor – Tunable Microwave Cavity

Appendix B

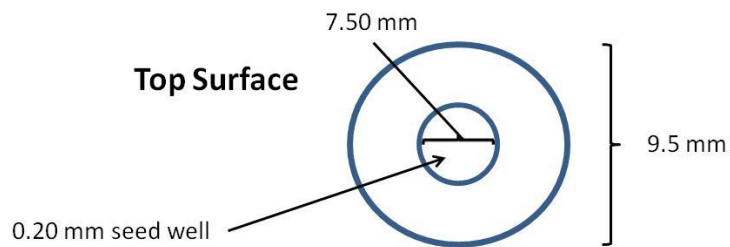
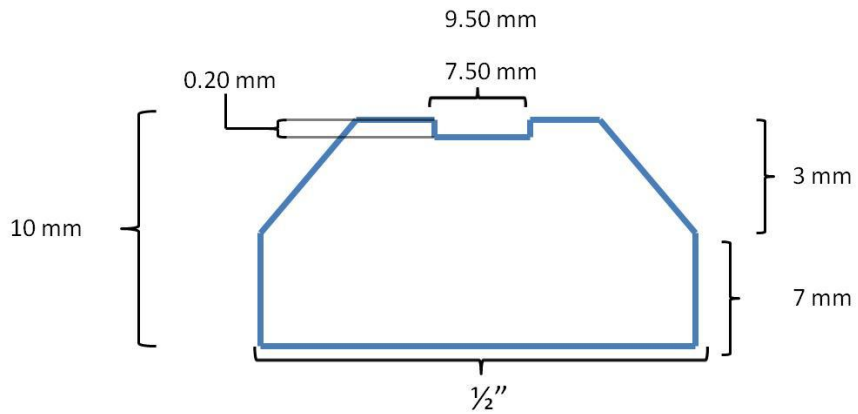
Molybdenum Susceptor Schematics and Configuration Images



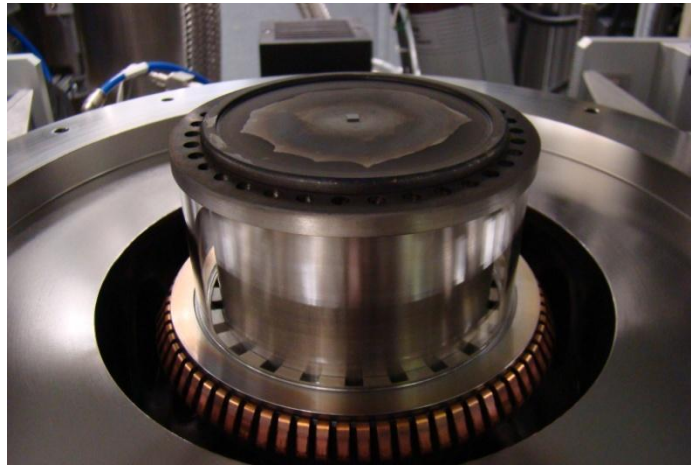
Redesigned molybdenum base plate for Susceptor Configuration 3



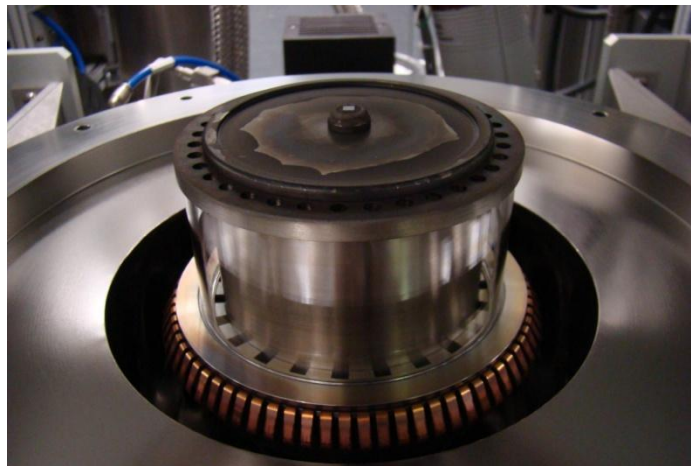
5mm raised and tapered molybdenum seed holder



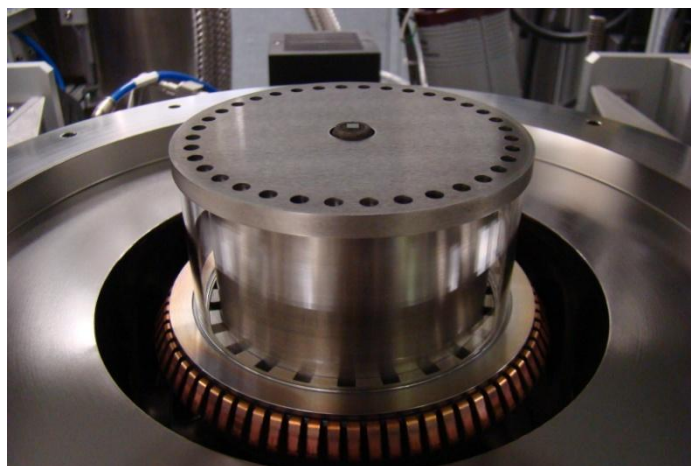
10mm raised and tapered molybdenum seed holder



**Susceptor Configuration 1**



**Susceptor Configuration 2**



**Susceptor Configuration 3**

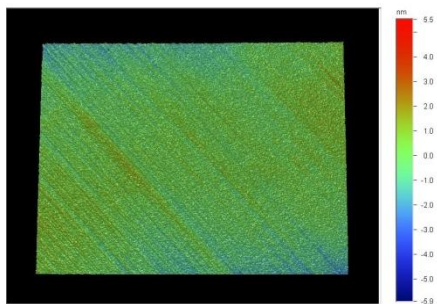
Appendix C

Wyko Optical Profiler Images: Off-axis Etching Study

OA-01

Etch Pressure: N/A; CH<sub>4</sub> Concentration: 8%

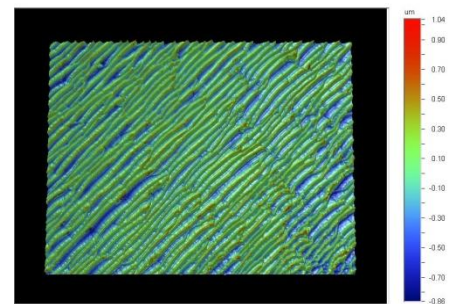
**Pre-Etch**  
Ra = 0.535nm



**Post-Etch**  
Ra = N/A

N/A

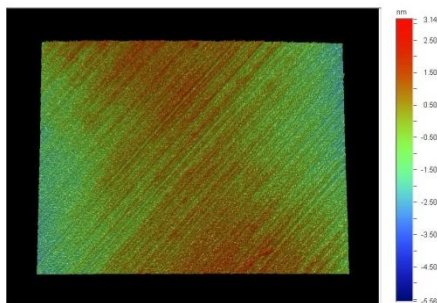
**Post-Growth**  
Ra = 177.097nm



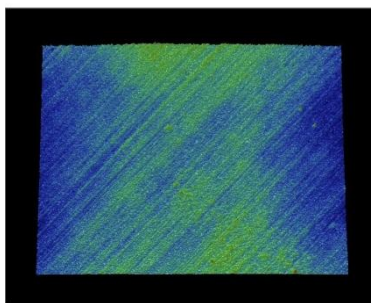
OA-02

Etch Pressure: 25mtorr; CH<sub>4</sub> Concentration: 8%

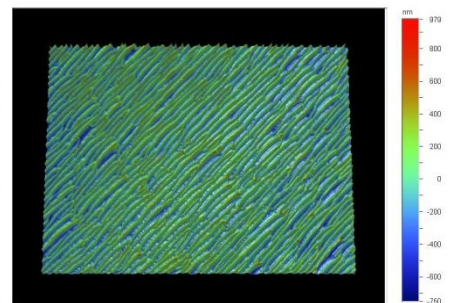
**Pre-Etch**  
Ra = 0.785nm



**Post-Etch**  
Ra = 0.723nm

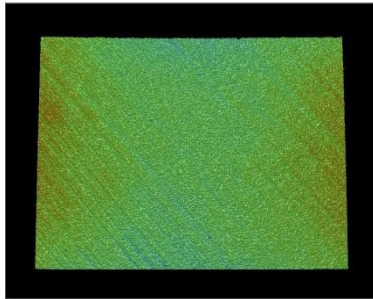


**Post-Growth**  
Ra = 148.785nm

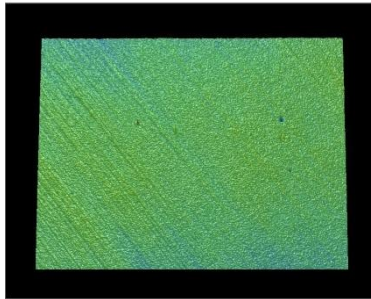


**OA-03**  
Etch Pressure: 25mtorr; CH<sub>4</sub> Concentration: 4%

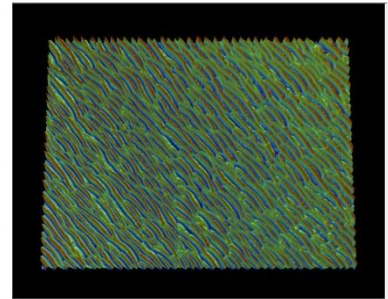
**Pre-Etch**  
Ra = 0.910nm



**Post-Etch**  
Ra = 0.633nm

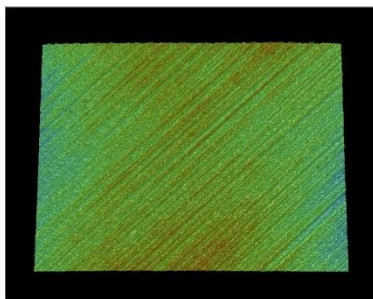


**Post-Growth**  
Ra = 179.390nm

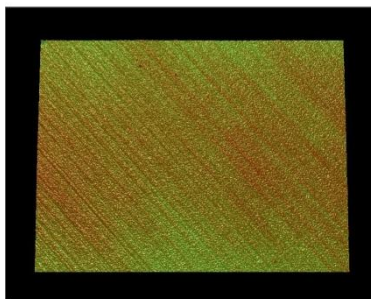


**OA-04**  
Etch Pressure: 25mtorr; CH<sub>4</sub> Concentration: 2%

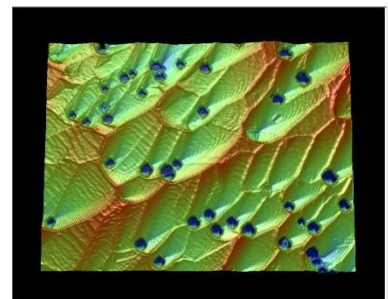
**Pre-Etch**  
Ra = 0.675nm



**Post-Etch**  
Ra = 0.643nm

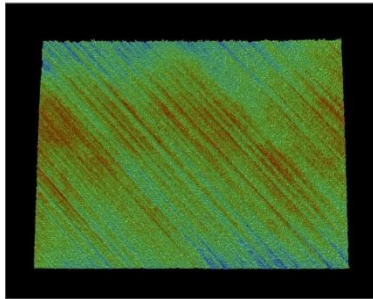


**Post-Growth**  
Ra = 368.960nm

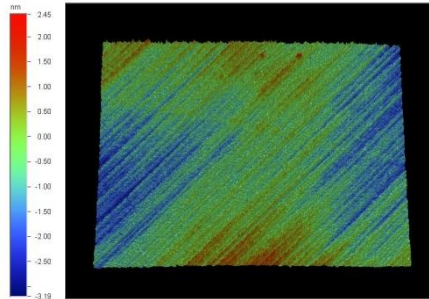


**OA-05**  
**Etch Pressure: 5mtorr; CH<sub>4</sub> Concentration: 4%**

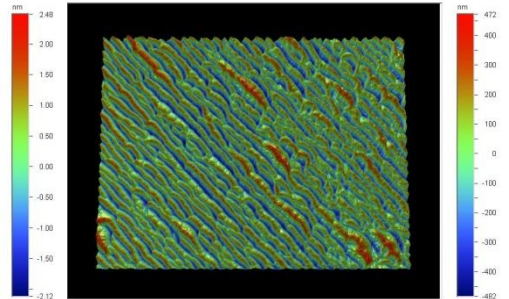
**Pre-Etch**  
Ra = 0.393nm



**Post-Etch**  
Ra = 0.537nm

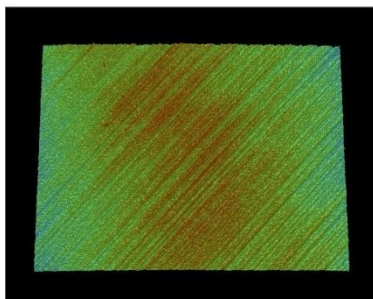


**Post-Growth**  
Ra = 135.707nm

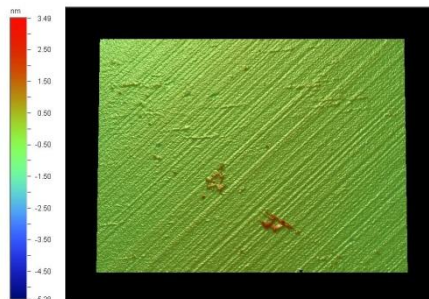


**OA-06**  
**Etch Pressure: 50mtorr; CH<sub>4</sub> Concentration: 4%**

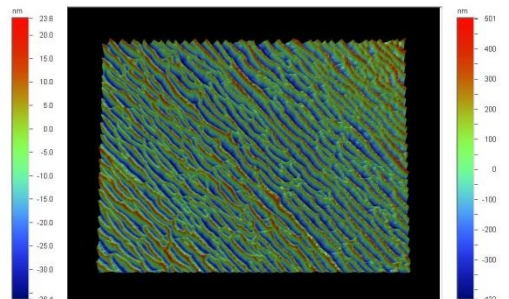
**Pre-Etch**  
Ra = 0.637nm



**Post-Etch**  
Ra = 0.897nm

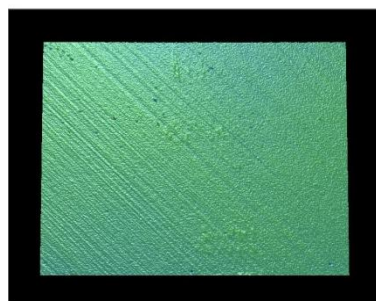


**Post-Growth**  
Ra = 159.630nm

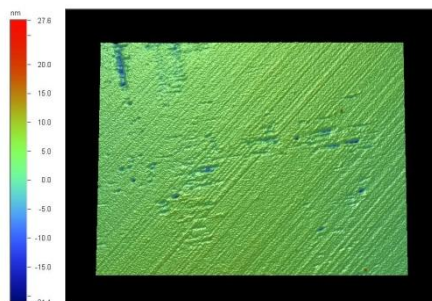


**OA-07**  
Etch Pressure: 75mtorr; CH<sub>4</sub> Concentration: 4%

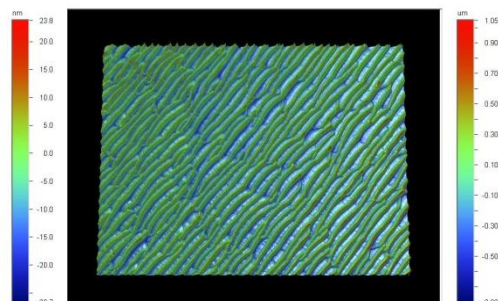
**Pre-Etch**  
Ra = 0.593nm



**Post-Etch**  
Ra = 0.955nm

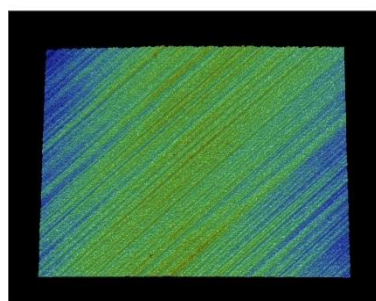


**Post-Growth**  
Ra = 183.463nm

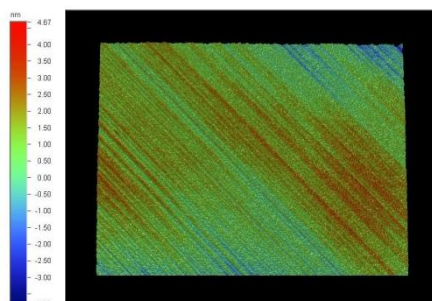


**OA-09**  
Etch Pressure: 25mtorr; CH<sub>4</sub> Concentration: 1%

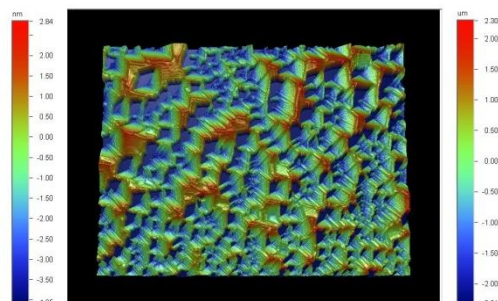
**Pre-Etch**  
Ra = 0.677nm



**Post-Etch**  
Ra = 0.560nm

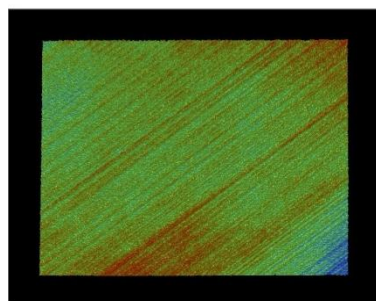


**Post-Growth**  
Ra = 556.333nm



**OA-10**  
Etch Pressure: 25mtorr; CH<sub>4</sub> Concentration: 3%

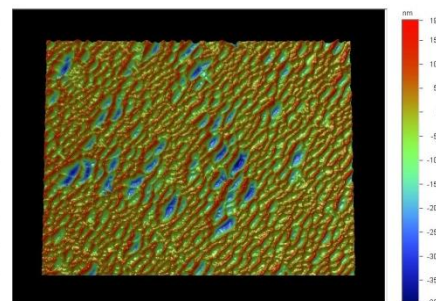
**Pre-Etch**  
Ra = 0.457nm



**Post-Etch**  
Ra = 0.480nm

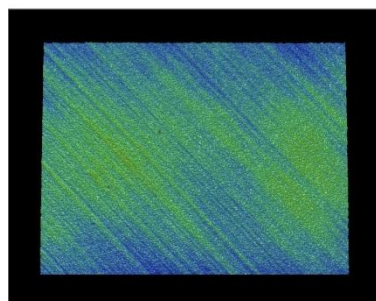


**Post-Growth**  
Ra = 61.743nm



**OA-11**  
Etch Pressure: N/A; CH<sub>4</sub> Concentration: 4%

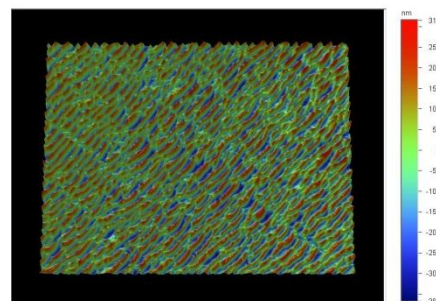
**Pre-Etch**  
Ra = 0.687nm



**Post-Etch**  
Ra = N/A

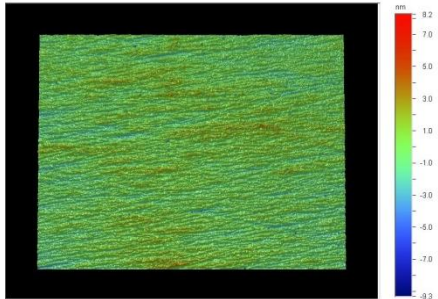
N/A

**Post-Growth**  
Ra = 111.59nm



**CVD-28**  
**Etch Pressure: N/A; CH<sub>4</sub> Concentration: 4%**

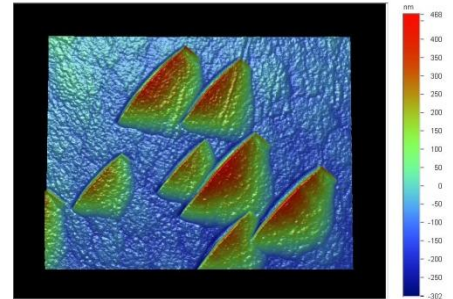
**Pre-Etch**  
 Ra = 0.737nm



**Post-Etch**  
 Ra = N/A

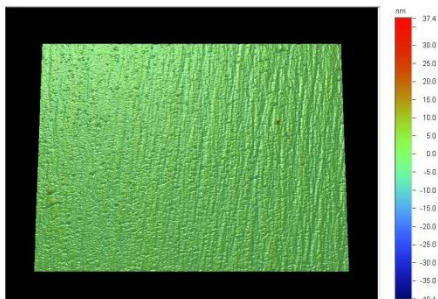
**N/A**

**Post-Growth**  
 Ra = 92.073nm



**CVD-29**  
**Etch Pressure: N/A; CH<sub>4</sub> Concentration: 8%**

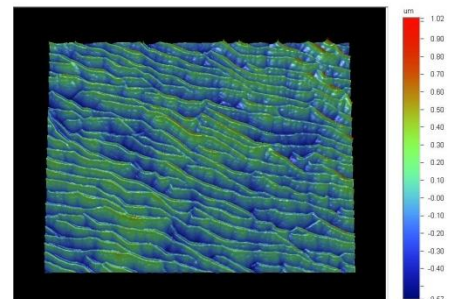
**Pre-Etch**  
 Ra = 0.747nm



**Post-Etch**  
 Ra = N/A

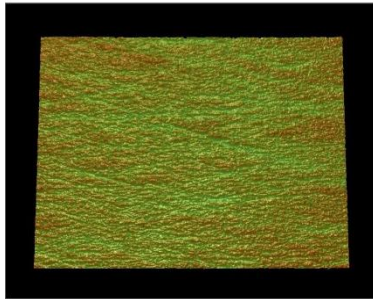
**N/A**

**Post-Growth**  
 Ra = 124.717nm

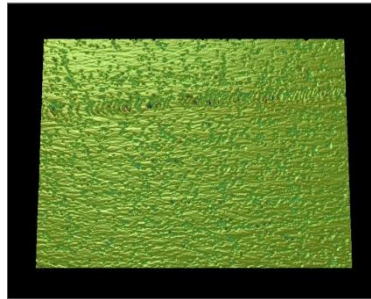


**CVD-30**  
Etch Pressure: 25mtorr; CH<sub>4</sub> Concentration: 4%

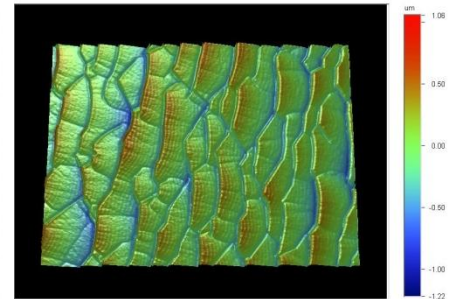
**Pre-Etch**  
Ra = 0.947nm



**Post-Etch**  
Ra = 3.360nm

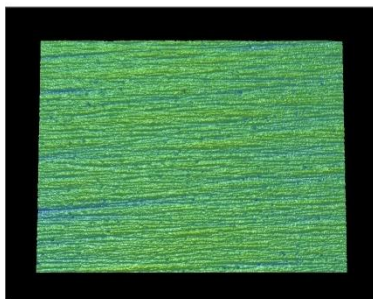


**Post-Growth**  
Ra = 195.773nm

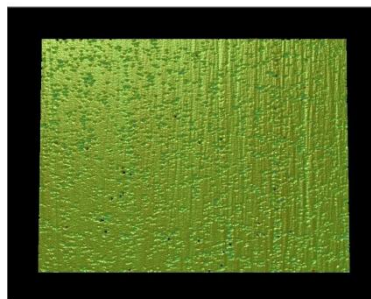


**CVD-31**  
Etch Pressure: 25mtorr; CH<sub>4</sub> Concentration: 8%

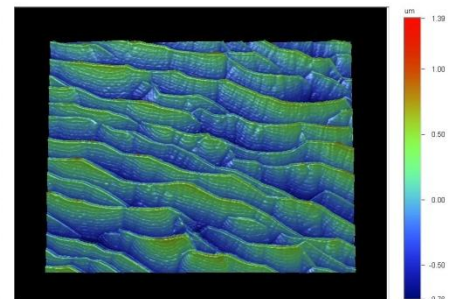
**Pre-Etch**  
Ra = 0.853nm



**Post-Etch**  
Ra = 2.060nm



**Post-Growth**  
Ra = 194.587nm

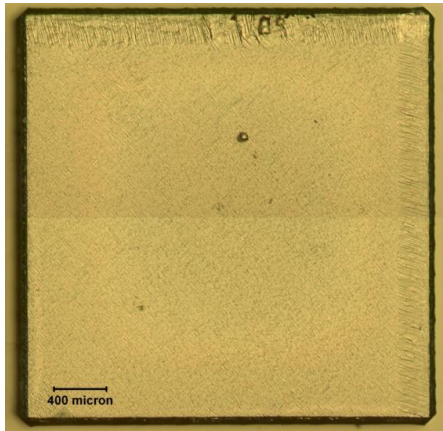


## Appendix D

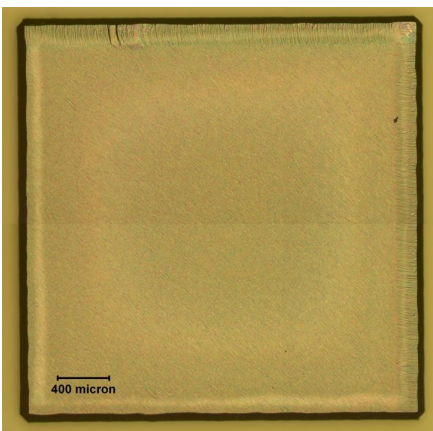
## Optical Images: Off-axis Etching Study

## 50x Images

**OA-01**  
Etch Pressure: N/A  
CH<sub>4</sub> Concentration: 8%  
Growth Rate: 16.994 $\mu$ m/hr



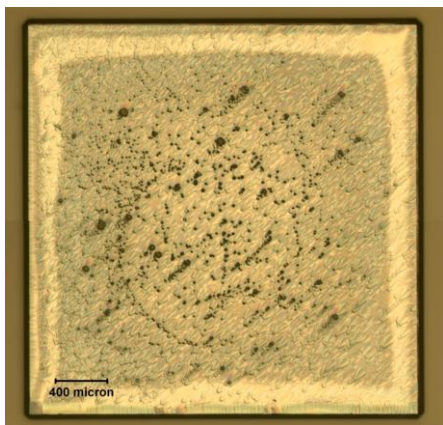
**OA-02**  
Etch Pressure: 25mtorr  
CH<sub>4</sub> Concentration: 8%  
Growth Rate: 15.260 $\mu$ m/hr



**OA-03**  
Etch Pressure: 25mtorr  
CH<sub>4</sub> Concentration: 4%  
Growth Rate: 7.642 $\mu$ m/hr



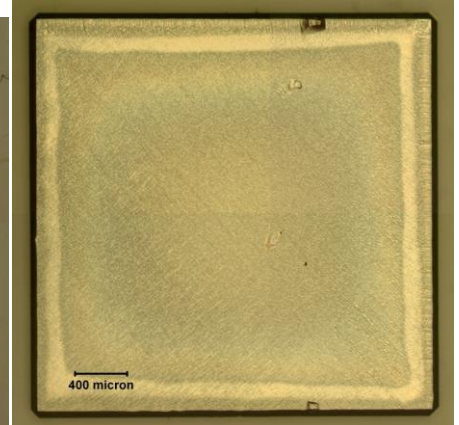
**OA-04**  
Etch Pressure: 25mtorr  
CH<sub>4</sub> Concentration: 2%  
Growth Rate: 4.530 $\mu$ m/hr



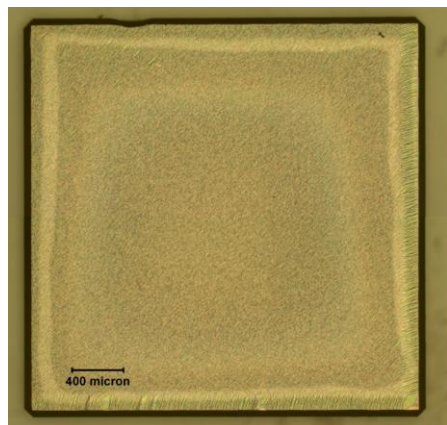
**OA-05**  
Etch Pressure: 5mtorr  
CH<sub>4</sub> Concentration: 4%  
Growth Rate: 5.14 $\mu$ m/hr



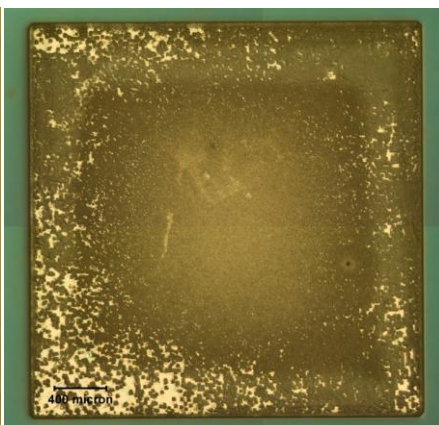
**OA-06**  
Etch Pressure: 50mtorr  
CH<sub>4</sub> Concentration: 4%  
Growth Rate: 6.370 $\mu$ m/hr



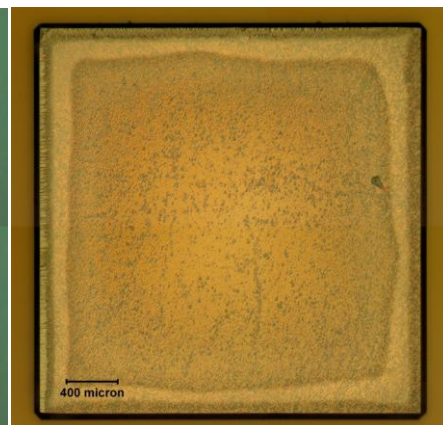
**OA-07**  
Etch Pressure: 75mtorr  
CH<sub>4</sub> Concentration: 4%  
Growth Rate: 7.360 $\mu$ m/hr



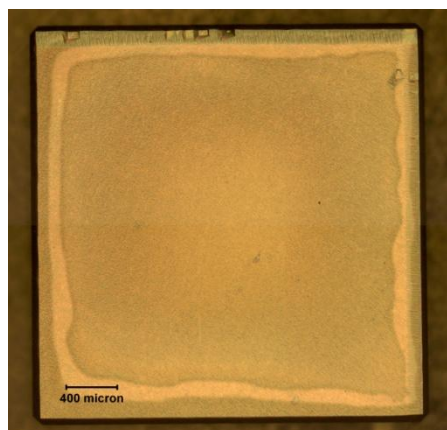
**OA-09**  
Etch Pressure: 25mtorr  
CH<sub>4</sub> Concentration: 1%  
Growth Rate: 1.469 $\mu$ m/hr



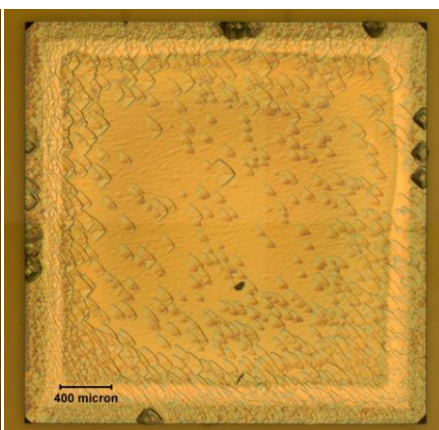
**OA-10**  
Etch Pressure: 25mtorr  
CH<sub>4</sub> Concentration: 3%  
Growth Rate: 5.140 $\mu$ m/hr



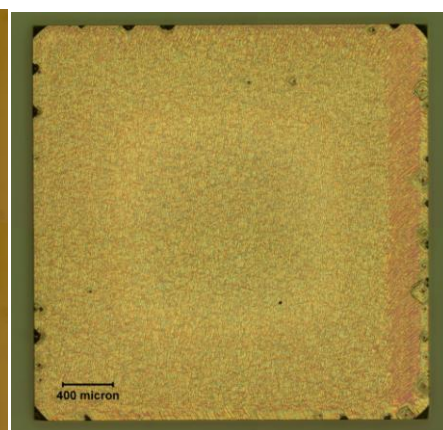
**OA-11**  
Etch Pressure: N/A  
CH<sub>4</sub> Concentration: 4%  
Growth Rate: 7.442 $\mu$ m/hr



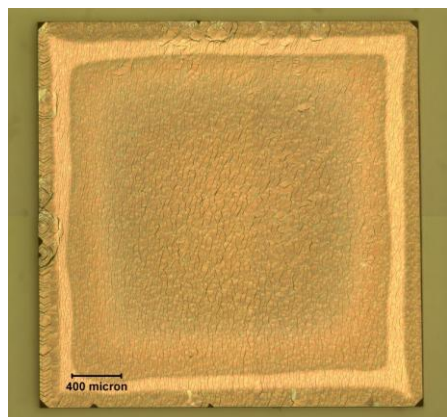
**CVD-28**  
Etch Pressure: N/A  
CH<sub>4</sub> Concentration: 4%  
Growth Rate: 4.627 $\mu$ m/hr



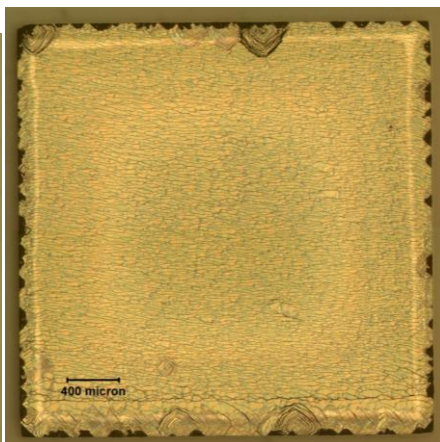
**CVD-29**  
Etch Pressure: N/A  
CH<sub>4</sub> Concentration: 8%  
Growth Rate: 12.965 $\mu$ m/hr



**CVD-30**  
Etch Pressure: 25mtorr  
CH<sub>4</sub> Concentration: 4%  
Growth Rate: 5.995 $\mu$ m/hr

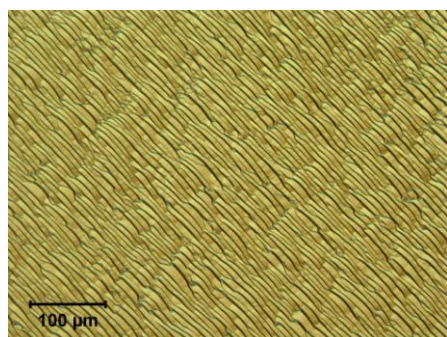


**CVD-31**  
Etch Pressure: 25  
CH<sub>4</sub> Concentration: 8%  
Growth Rate: 12.003 $\mu$ m/hr

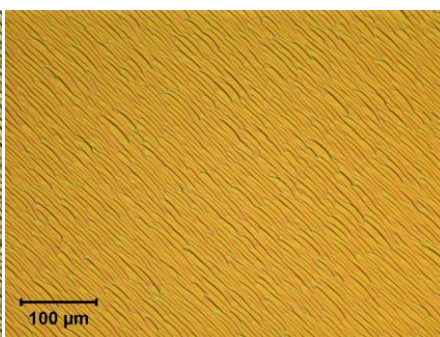


## 200x Images

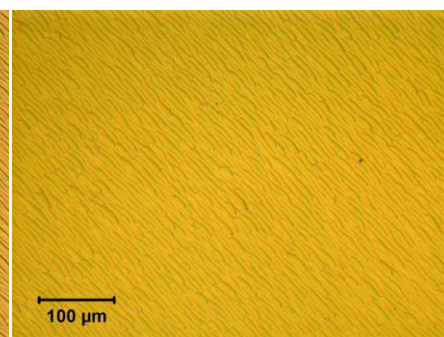
**OA-01**  
Etch Pressure: N/A  
CH<sub>4</sub> Concentration: 8%  
Growth Rate: 16.994 $\mu$ m/hr



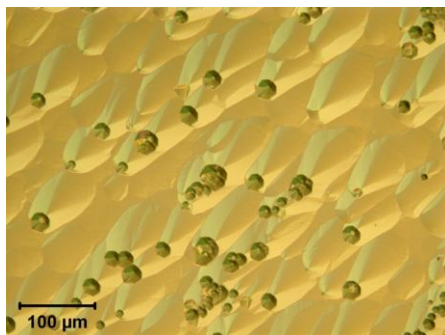
**OA-02**  
Etch Pressure: 25mtorr  
CH<sub>4</sub> Concentration: 8%  
Growth Rate: 15.260 $\mu$ m/hr



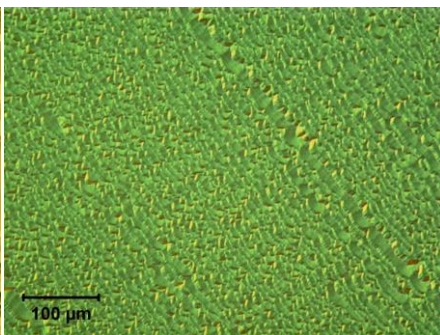
**OA-03**  
Etch Pressure: 25mtorr  
CH<sub>4</sub> Concentration: 4%  
Growth Rate: 7.642 $\mu$ m/hr



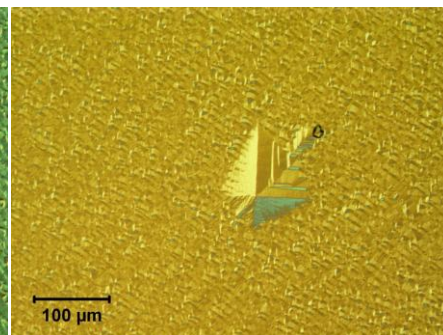
**OA-04**  
 Etch Pressure: 25mtorr  
 CH<sub>4</sub> Concentration: 2%  
 Growth Rate: 4.530 $\mu$ m/hr



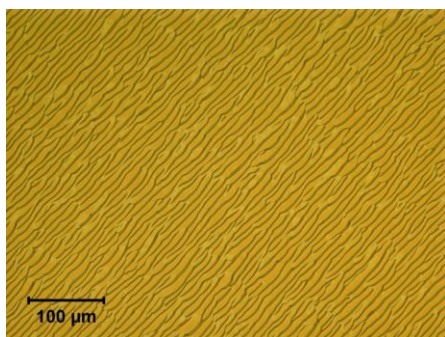
**OA-05**  
 Etch Pressure: 5mtorr  
 CH<sub>4</sub> Concentration: 4%  
 Growth Rate: 5.14 $\mu$ m/hr



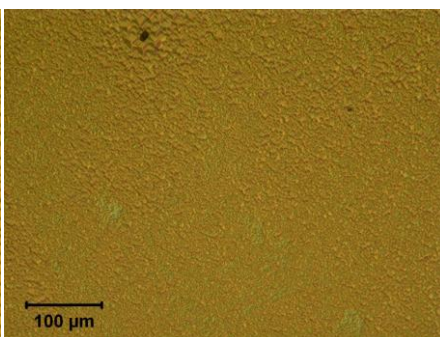
**OA-06**  
 Etch Pressure: 50mtorr  
 CH<sub>4</sub> Concentration: 4%  
 Growth Rate: 6.370 $\mu$ m/hr



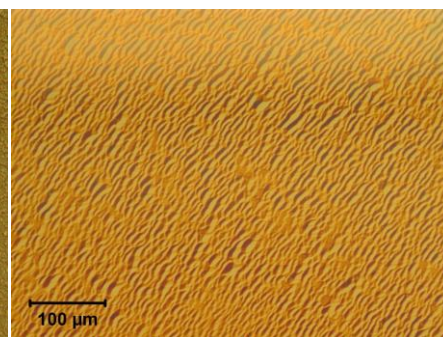
**OA-07**  
 Etch Pressure: 75mtorr  
 CH<sub>4</sub> Concentration: 4%  
 Growth Rate: 7.360 $\mu$ m/hr



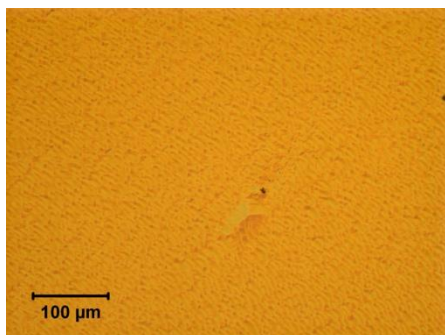
**OA-09**  
 Etch Pressure: 25mtorr  
 CH<sub>4</sub> Concentration: 1%  
 Growth Rate: 1.469 $\mu$ m/hr



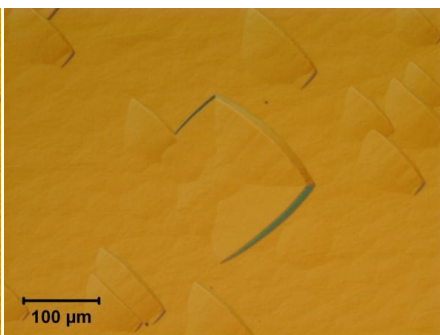
**OA-10**  
 Etch Pressure: 25mtorr  
 CH<sub>4</sub> Concentration: 3%  
 Growth Rate: 5.140 $\mu$ m/hr



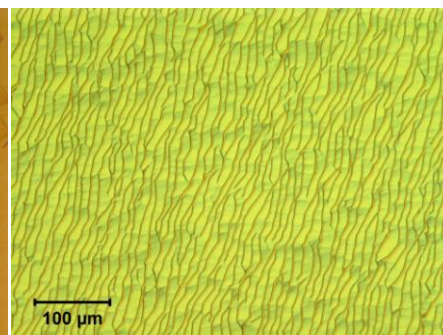
**OA-11**  
 Etch Pressure: N/A  
 CH<sub>4</sub> Concentration: 4%  
 Growth Rate: 7.442 $\mu$ m/hr



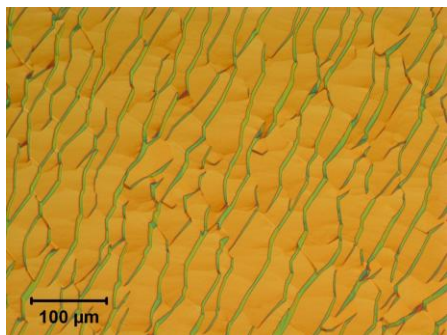
**CVD-28**  
 Etch Pressure: N/A  
 CH<sub>4</sub> Concentration: 4%  
 Growth Rate: 4.627 $\mu$ m/hr



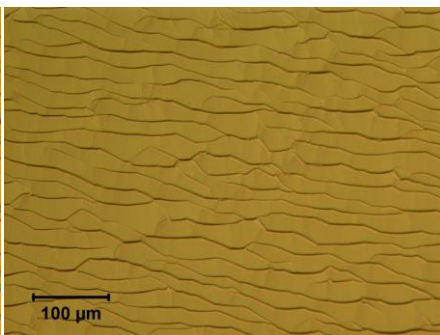
**CVD-29**  
 Etch Pressure: N/A  
 CH<sub>4</sub> Concentration: 8%  
 Growth Rate: 12.965 $\mu$ m/hr



**CVD-30**  
Etch Pressure: 25mtorr  
CH<sub>4</sub> Concentration: 4%  
Growth Rate: 5.995 $\mu$ m/hr

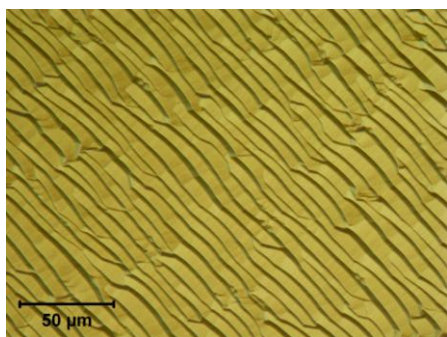


**CVD-31**  
Etch Pressure: 25  
CH<sub>4</sub> Concentration: 8%  
Growth Rate: 12.003 $\mu$ m/hr

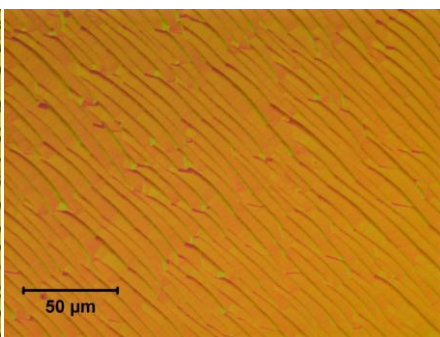


## 500x Images

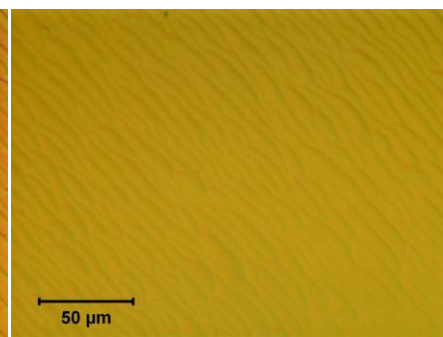
**OA-01**  
Etch Pressure: N/A  
CH<sub>4</sub> Concentration: 8%  
Growth Rate: 16.994 $\mu$ m/hr



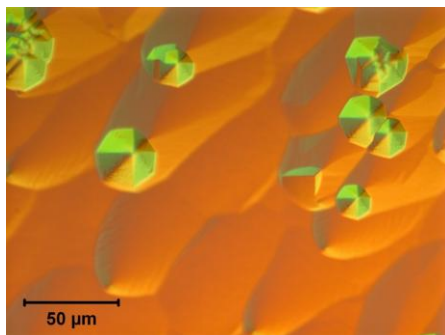
**OA-02**  
Etch Pressure: 25mtorr  
CH<sub>4</sub> Concentration: 8%  
Growth Rate: 15.260 $\mu$ m/hr



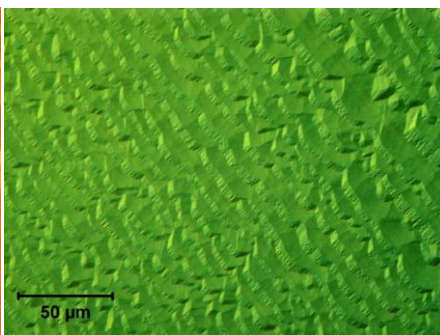
**OA-03**  
Etch Pressure: 25mtorr  
CH<sub>4</sub> Concentration: 4%  
Growth Rate: 7.642 $\mu$ m/hr



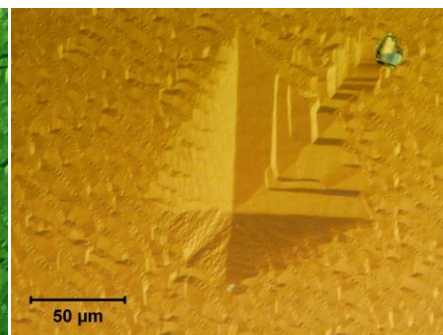
**OA-04**  
**Etch Pressure: 25mtorr**  
**CH<sub>4</sub> Concentration: 2%**  
**Growth Rate: 4.530 $\mu$ m/hr**



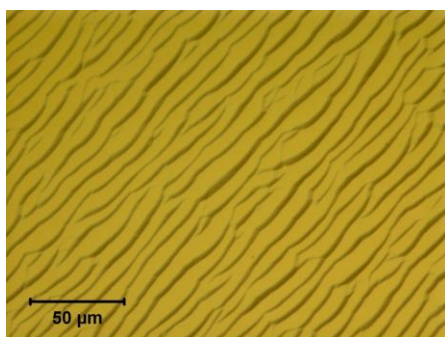
**OA-05**  
**Etch Pressure: 5mtorr**  
**CH<sub>4</sub> Concentration: 4%**  
**Growth Rate: 5.14 $\mu$ m/hr**



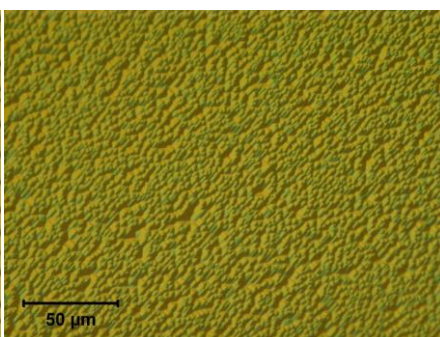
**OA-06**  
**Etch Pressure: 50mtorr**  
**CH<sub>4</sub> Concentration: 4%**  
**Growth Rate: 6.370 $\mu$ m/hr**



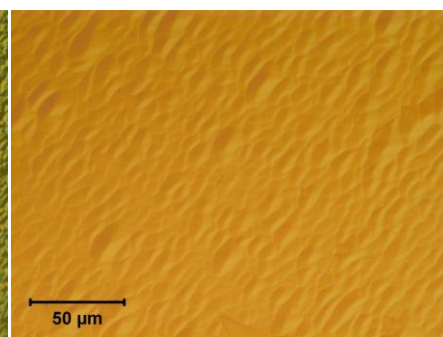
**OA-07**  
**Etch Pressure: 75mtorr**  
**CH<sub>4</sub> Concentration: 4%**  
**Growth Rate: 7.360 $\mu$ m/hr**



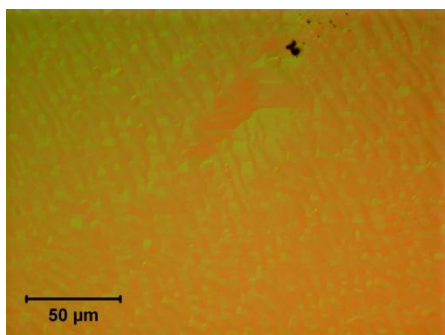
**OA-09**  
**Etch Pressure: 25mtorr**  
**CH<sub>4</sub> Concentration: 1%**  
**Growth Rate: 1.469 $\mu$ m/hr**



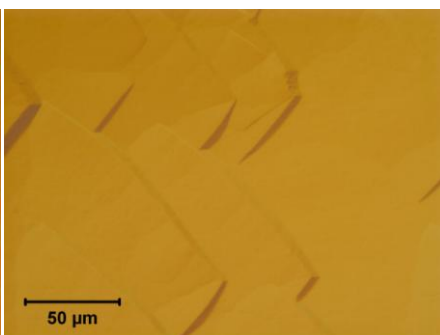
**OA-10**  
**Etch Pressure: 25mtorr**  
**CH<sub>4</sub> Concentration: 3%**  
**Growth Rate: 5.140 $\mu$ m/hr**



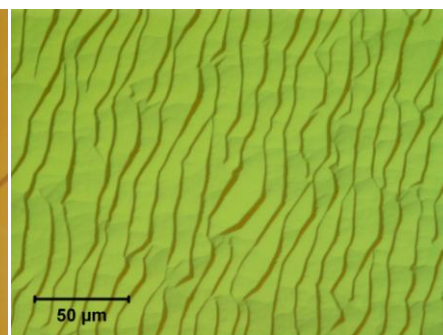
**OA-11**  
**Etch Pressure: N/A**  
**CH<sub>4</sub> Concentration: 4%**  
**Growth Rate: 7.442 $\mu$ m/hr**



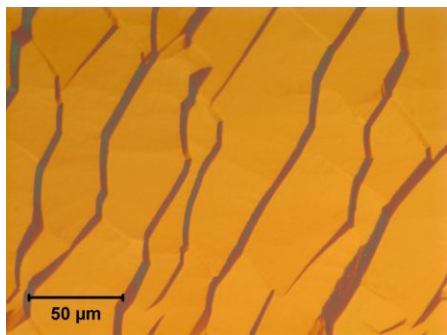
**CVD-28**  
**Etch Pressure: N/A**  
**CH<sub>4</sub> Concentration: 4%**  
**Growth Rate: 4.627 $\mu$ m/hr**



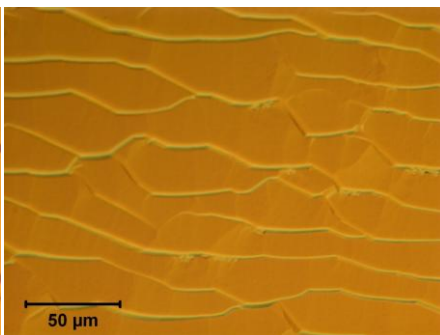
**CVD-29**  
**Etch Pressure: N/A**  
**CH<sub>4</sub> Concentration: 8%**  
**Growth Rate: 12.965 $\mu$ m/hr**



**CVD-30**  
Etch Pressure: 25mtorr  
CH<sub>4</sub> Concentration: 4%  
Growth Rate: 5.995 $\mu$ m/hr

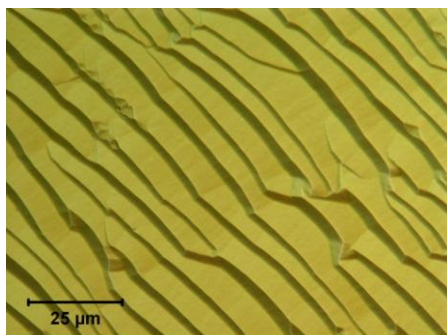


**CVD-31**  
Etch Pressure: 25  
CH<sub>4</sub> Concentration: 8%  
Growth Rate: 12.003 $\mu$ m/hr

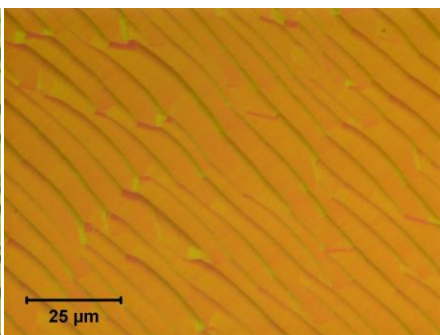


### 1000x Images

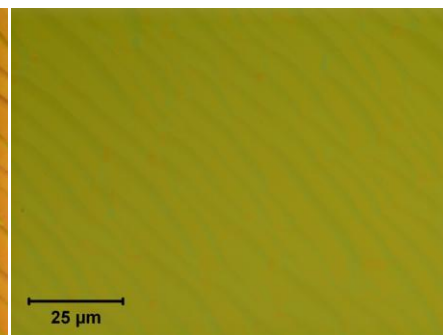
**OA-01**  
Etch Pressure: N/A  
CH<sub>4</sub> Concentration: 8%  
Growth Rate: 16.994 $\mu$ m/hr



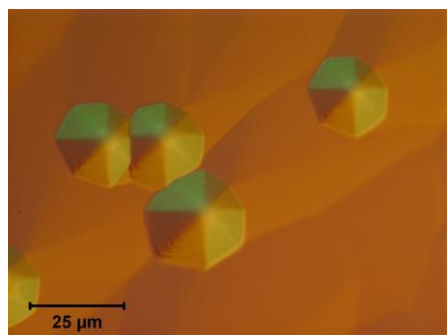
**OA-02**  
Etch Pressure: 25mtorr  
CH<sub>4</sub> Concentration: 8%  
Growth Rate: 15.260 $\mu$ m/hr



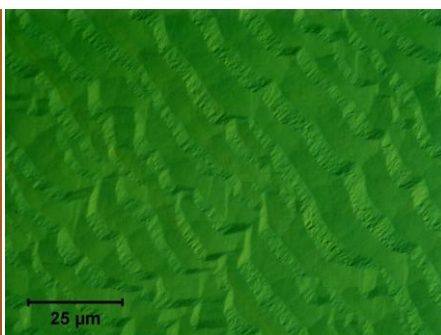
**OA-03**  
Etch Pressure: 25mtorr  
CH<sub>4</sub> Concentration: 4%  
Growth Rate: 7.642 $\mu$ m/hr



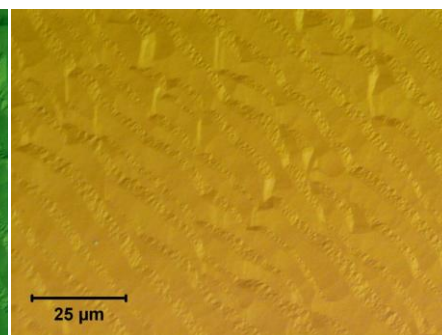
**OA-04**  
 Etch Pressure: 25mtorr  
 CH<sub>4</sub> Concentration: 2%  
 Growth Rate: 4.530 $\mu$ m/hr



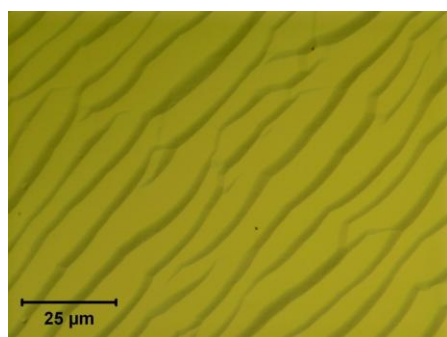
**OA-05**  
 Etch Pressure: 5mtorr  
 CH<sub>4</sub> Concentration: 4%  
 Growth Rate: 5.14 $\mu$ m/hr



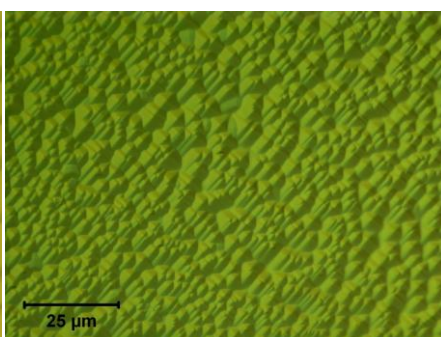
**OA-06**  
 Etch Pressure: 50mtorr  
 CH<sub>4</sub> Concentration: 4%  
 Growth Rate: 6.370 $\mu$ m/hr



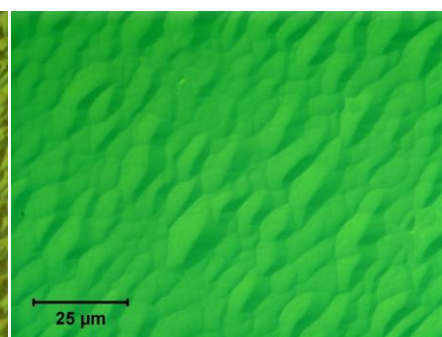
**OA-07**  
 Etch Pressure: 75mtorr  
 CH<sub>4</sub> Concentration: 4%  
 Growth Rate: 7.360 $\mu$ m/hr



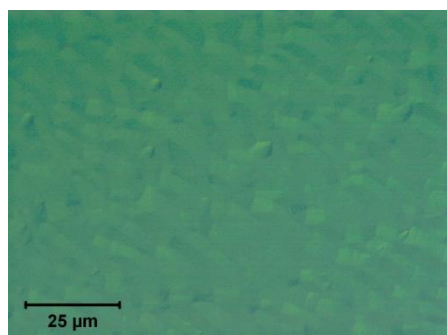
**OA-09**  
 Etch Pressure: 25mtorr  
 CH<sub>4</sub> Concentration: 1%  
 Growth Rate: 1.469 $\mu$ m/hr



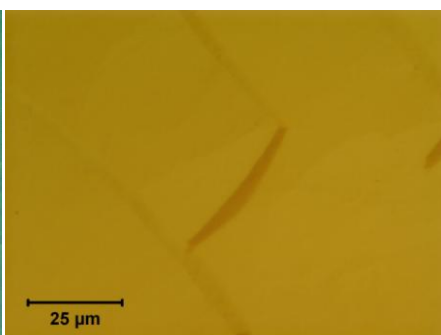
**OA-10**  
 Etch Pressure: 25mtorr  
 CH<sub>4</sub> Concentration: 3%  
 Growth Rate: 5.140 $\mu$ m/hr



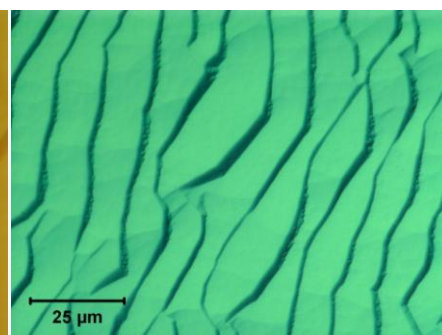
**OA-11**  
 Etch Pressure: N/A  
 CH<sub>4</sub> Concentration: 4%  
 Growth Rate: 7.442 $\mu$ m/hr

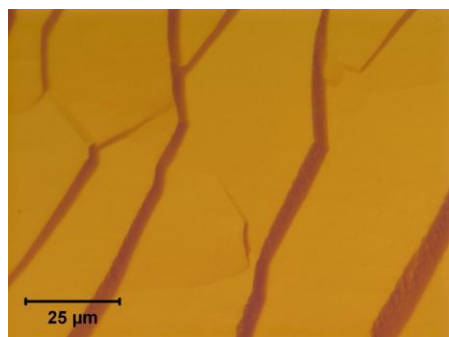
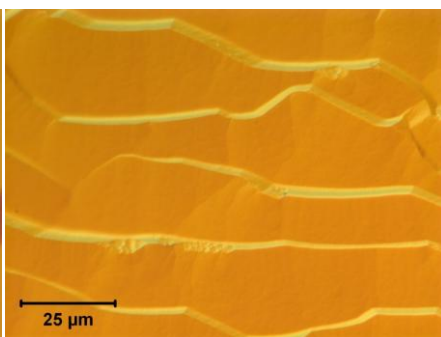


**CVD-28**  
 Etch Pressure: N/A  
 CH<sub>4</sub> Concentration: 4%  
 Growth Rate: 4.627 $\mu$ m/hr



**CVD-29**  
 Etch Pressure: N/A  
 CH<sub>4</sub> Concentration: 8%  
 Growth Rate: 12.965 $\mu$ m/hr



**CVD-30****Etch Pressure: 25mtorr****CH<sub>4</sub> Concentration: 4%****Growth Rate: 5.995 $\mu$ m/hr****CVD-31****Etch Pressure: 25****CH<sub>4</sub> Concentration: 8%****Growth Rate: 12.003 $\mu$ m/hr**

## Appendix E

## Raman Spectroscopy Quantitative Results: Off-axis Etching Study

**Full Width Half Maximum – High Resolution**

Sample	Etch Pressure	Growth CH4 %	Substrate FWHM	St. Dev	Post-Etch FWHM	St. Dev	Post-Growth FWHM	St. Dev
OA-01	N/A	8	<b>8.834</b>	0.12	N/A	N/A	<b>9.102</b>	0.104
OA-02	25	8	<b>8.834</b>	0.12	<b>8.972</b>	0.15	<b>8.784</b>	0.11
OA-03	25	4	<b>8.834</b>	0.12	<b>8.972</b>	0.15	<b>8.783</b>	0.133
OA-04	25	2	<b>8.834</b>	0.12	<b>8.972</b>	0.15	<b>8.841</b>	0.124
OA-05	5	4	<b>8.834</b>	0.12	<b>8.784</b>	0.121	<b>11.51</b>	0.795
OA-06	50	4	<b>8.834</b>	0.12	<b>8.751</b>	0.11	<b>9.092</b>	0.175
OA-07	75	4	<b>8.834</b>	0.12	<b>8.754</b>	0.104	<b>8.574</b>	0.134
OA-09	25	1	<b>8.861</b>	0.171	<b>8.47</b>	0.064	<b>9.297</b>	0.131
OA-10	25	3	<b>8.681</b>	0.12	<b>8.472</b>	0.05	<b>9.326</b>	0.071
CVD-28	N/A	4	<b>9.129</b>	0.087	N/A	N/A	<b>8.802</b>	0.182
CVD-29	N/A	8	<b>9.129</b>	0.087	N/A	N/A	<b>8.918</b>	0.052
CVD-30	25	4	<b>9.183</b>	0.164	<b>8.752</b>	0.145	<b>9.404</b>	0.071
CVD-31	25	8	<b>9.183</b>	0.164	<b>8.794</b>	0.054	<b>9.541</b>	0.058

**Center of Mass – High Resolution**

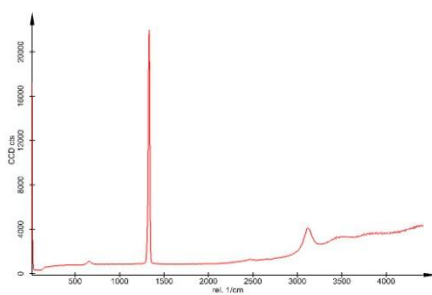
Sample	Etch Pressure	Growth CH4 %	Substrate COM	St. Dev	Post-Etch COM	St. Dev	Post-Growth COM	St. Dev
OA-01	N/A	8	<b>1329.817</b>	0.029	N/A	N/A	<b>1330.226</b>	0.099
OA-02	25	8	<b>1329.817</b>	0.029	<b>1329.72</b>	0.044	<b>1329.678</b>	0.0484
OA-03	25	4	<b>1329.817</b>	0.029	<b>1329.72</b>	0.044	<b>1329.748</b>	0.0431
OA-04	25	2	<b>1329.817</b>	0.029	<b>1329.72</b>	0.044	<b>1329.671</b>	0.0291
OA-05	5	4	<b>1329.817</b>	0.029	<b>1330.033</b>	0.042	<b>1332.386</b>	0.427
OA-06	50	4	<b>1329.817</b>	0.029	<b>1329.978</b>	0.07	<b>1331.113</b>	0.118
OA-07	75	4	<b>1329.817</b>	0.029	<b>1330.025</b>	0.04	<b>1329.91</b>	0.031
OA-09	25	1	<b>1330.074</b>	0.051	<b>1330.423</b>	0.014	<b>1329.937</b>	0.066
OA-10	25	3	<b>1330.116</b>	0.041	<b>1330.512</b>	0.019	<b>1330.512</b>	0.019
CVD-28	N/A	4	<b>1329.897</b>	0.024	N/A	N/A	<b>1330.216</b>	0.097
CVD-29	N/A	8	<b>1329.897</b>	0.024	N/A	N/A	<b>1330.115</b>	0.046
CVD-30	25	4	<b>1329.698</b>	0.054	<b>1330.057</b>	0.091	<b>1330.057</b>	0.091
CVD-31	25	8	<b>1329.698</b>	0.054	<b>1330.032</b>	0.018	<b>1330.032</b>	0.018

## Appendix F

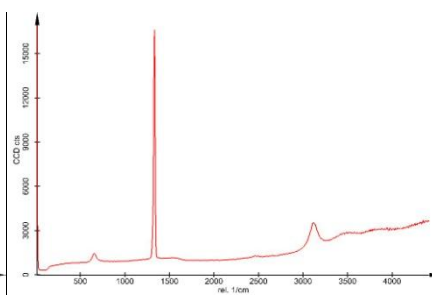
## Raman Results: Pre-etch, Post-etch, and Post-growth comparison

Off-Axis Substrates Etched at 25 mtorr. Effect of Methane ConcentrationOA-02: 8% CH<sub>4</sub>

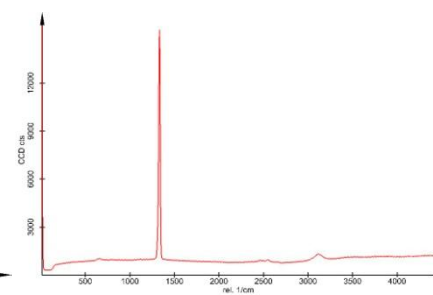
Pre-etch



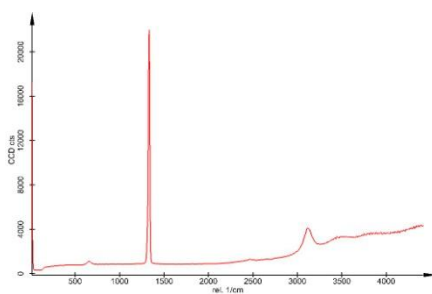
Post-etch



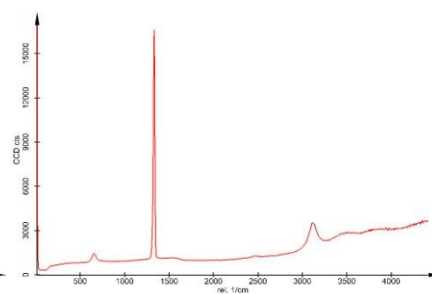
Post-growth

OA-03: 4% CH<sub>4</sub>

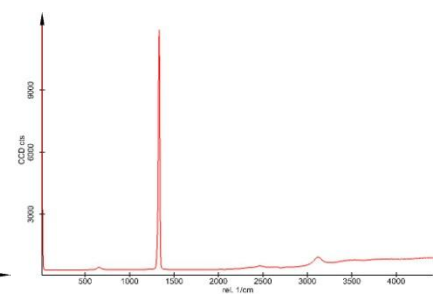
Pre-etch

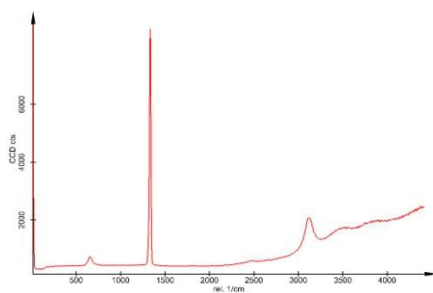
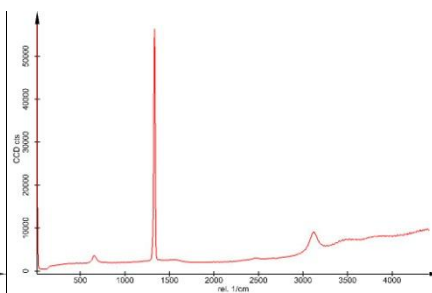
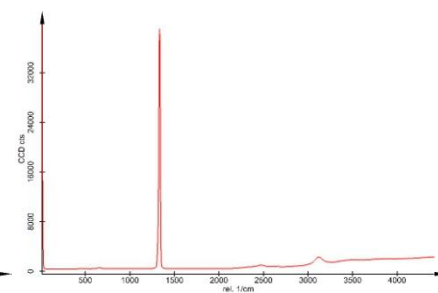
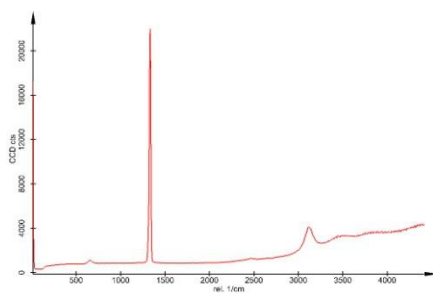
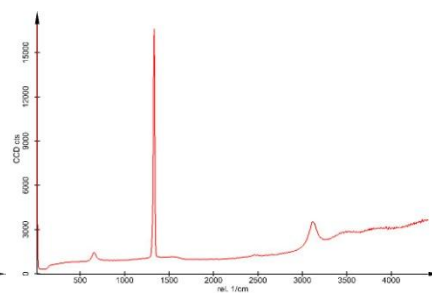
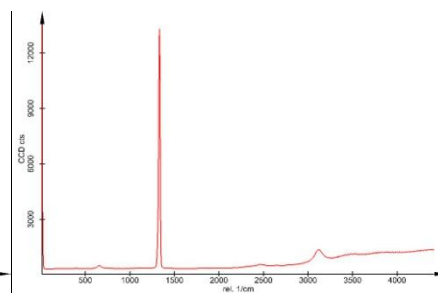
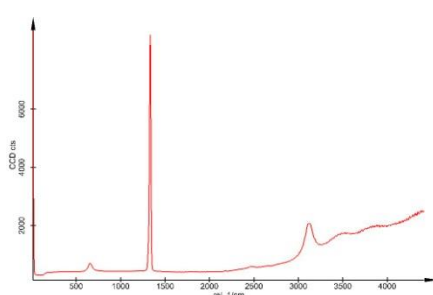
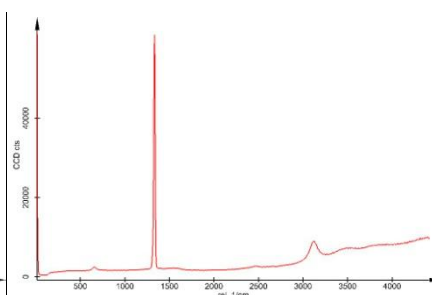
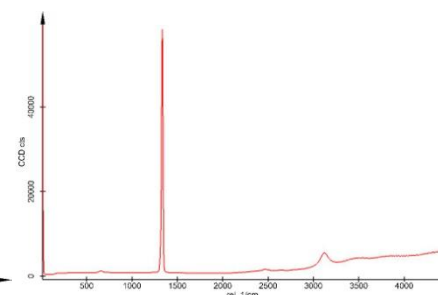


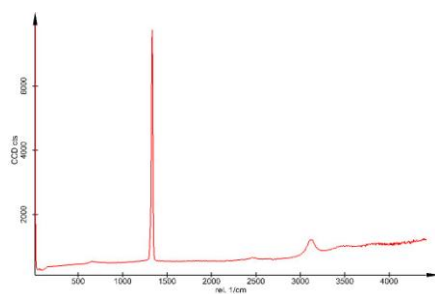
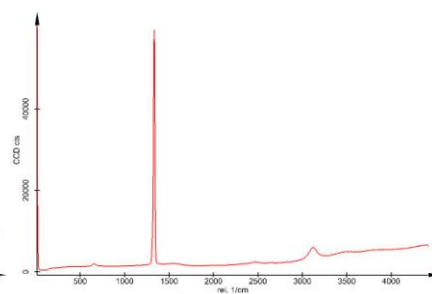
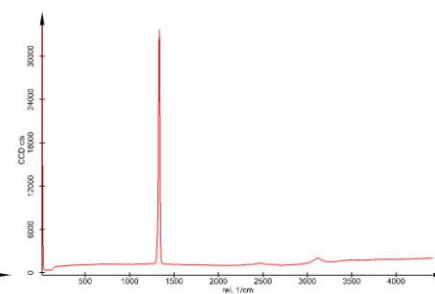
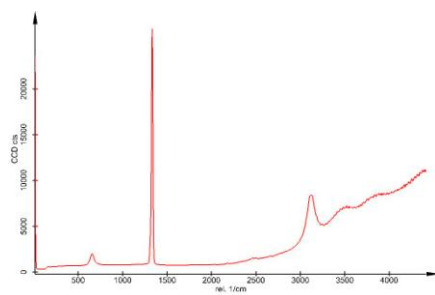
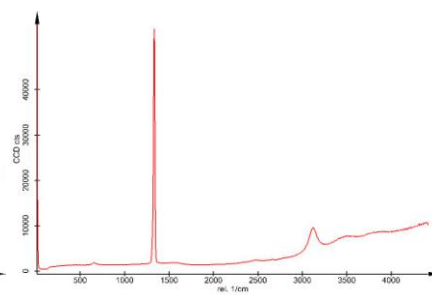
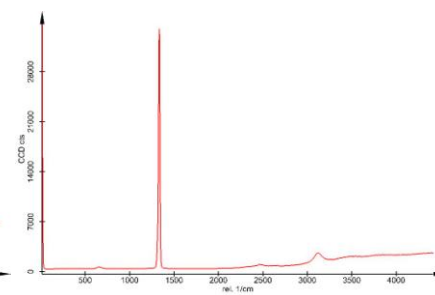
Post-etch



Post-growth



**OA-10: 3% CH<sub>4</sub>****Pre-etch****Post-etch****Post-growth****OA-04: 2% CH<sub>4</sub>****Pre-etch****Post-etch****Post-growth****OA-09: 1% CH<sub>4</sub>****Pre-etch****Post-etch****Post-growth**

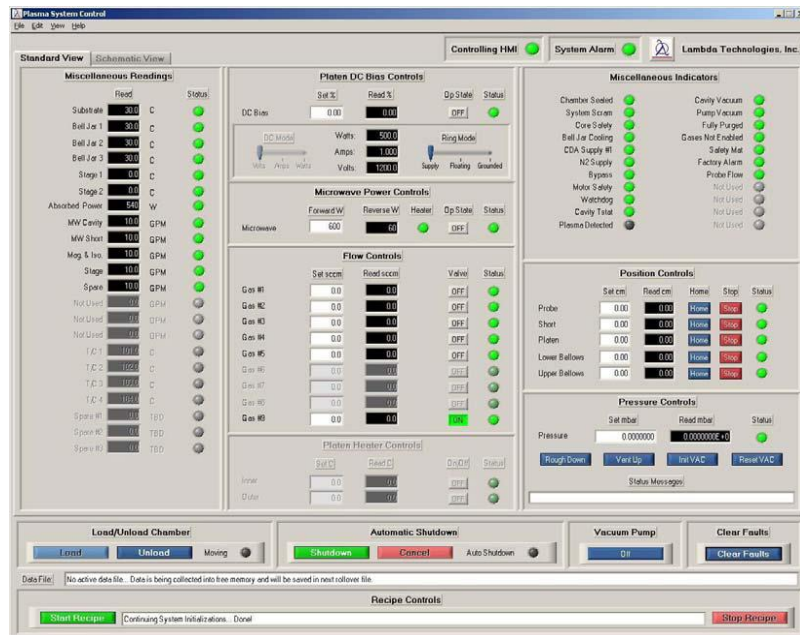
**On-Axis Substrates Etched at 25 mtorr. Effect of Methane Concentration****CVD-31: 8% CH<sub>4</sub>****Pre-etch****Post-etch****Post-growth****CVD-30: 4% CH<sub>4</sub>****Pre-etch****Post-etch****Post-growth**

## Appendix G

### Reactor Operation and Growth Run Procedure

The following section details the standard procedure for initiation and operation of the Lambda Technologies MPCVD reactor for a typical diamond deposition run.

First, the system must be turned on. Verify that the emergency stop buttons are released and check to make sure the main AC breaker to the system is on. Press the green “ON” button on front of the tool to turn on the system. When the computer turns on, double click the “diamotek” icon; the CIP and HMI programs will then launch. Figure 2-18 shows the main interface for the controlling HMI software. If the computer does not start up when the green “ON” button is pressed, the UPS (located at the very bottom of the front panel) may need to be manually turned on. To do this, hold the circle button on the UPS for two seconds, release, then hold again for two seconds, release, then press the straight line button once.



Panel view operation window for diamotek HMI (human-machine interface).

Next, verify that the process gas sources are flowing to the reactor. Verify that there is sufficient hydrogen, methane, and other process gas cylinder pressure to run the experiment. Make sure the valves to the reactor are open to allow flow of gases. Then, turn on the compressed air supply. Next, cooling water needs to be supplied to the reactor. Open the house coolant lines located in the chase, and turn on the water to water heat exchanger beside the MPCVD reactor. Be sure that the water filter on the house side does not need replaced before doing this step.

At this point, the samples are ready to be loaded into the growth chamber. In most cases, the sample should have been cleaned using the standard cleaning step previously described. Make sure all system faults are resolved in the HMI program. Then press the “UNLOAD” button in the HMI and allow the chamber to vent to atmosphere. The stage will begin to lower after atmospheric pressure has been established. Allow the chamber to come to a complete stop before proceeding. Place the substrate onto the molybdenum or graphite susceptor; the susceptor can be removed from the system to do this step if necessary. After the sample is loaded on the susceptor, press the “LOAD” button in the HMI and allow the chamber to fully close. Next, evacuate the process chamber by pressing the “ROUGH DOWN” button in the HMI.

The HMI program can be set-up to automatically control the growth process. This is done through user-edited “recipes”. To set up a recipe, click from the menu: Edit→Recipe (or press F2). A recipe is created by adding “events” from the pull down menu in the edit recipe screen. Events include: Roughdown, Vent, Set Pressure, Set Microwave Power, Set Flow Gas #, Set Position Probe, Set Position Short, Set Position Lower Bellows, Set Time, Pulsed Strike, Ramp, and Automatic Shutdown. Press “Add Event” or “Insert Event” to add a event to the recipe. Previously inserted events can be edited by selecting the event from the current recipe, modifying the parameters, and then clicking “Replace Event”. Events can be removed by selecting them from the recipe and clicking “Delete Event”. Changes apply to the currently opened recipe file. Be sure to use “open” or “save as” to create a new recipe.

After a recipe has been selected, a growth run can be started by pressing the “Start Recipe” button on the main HMI screen. This will begin the automated growth process. During automatic mode, the parameters may be adjusted if needed to establish the desired conditions. This can be either done by typing the desired parameter value into the level settings box for each parameter (the box to the left of the measured value box), or by opening the “Jog Panel” to the right of a particular parameter. Jog panels are available for: Position (short, probe, lower bellows), pressure, gas flow, and microwave power.

For termination or shut down procedure, the automatic shutdown (part of a standard recipe) should ramp down the pressure and microwave power until it eventually turns off the microwave, stops gas flow, and roughs down the chamber to vacuum. Automatic shutdown parameters can be edited in the recipe editor just as any recipe can. Click “Open Recipe” and chose “shutdown.evt”. After the run is completed, close the manual process gas valve to the system as well as at the cylinders. Close the house coolant valves and turn the water to water heat exchanger off. Water flow errors will pop up after the heat exchanger is shut off, leave them be until the next run and clear the errors after the coolant water supply is returned. Unload the chamber the same way as described for loading, remove the sample, then close the chamber (caution: wait at least 10 minutes to do this as the susceptor will still be hot). To fully shut down the entire system, be sure all gas flows are off, shut off the compressed air supply, vent the system to atmosphere, close the HMI application, and press the red “OFF” button on the front panel of the tool.

At anytime the user deems the machines operation may threaten personal or equipment safety, the system can be immediately shut down via an “Emergency Stop”. There are two emergency stop buttons (one in the front, one in the back of the tool). Pressing either button will immediately shut down the power for all subsystems except for the control computer and monitor (connected to the UPS).